Design, Analysis, and Applications of Optically-Activated Antennas and Dielectric Lenses Using Photosensitive Semiconducting Materials

Andre Sarker Andy

A thesis submitted in partial fulfilment of the requirements for the degree of Doctor of Philosophy

School of Electronic Engineering and Computer Science
Queen Mary University of London
London E1 4NS, United Kingdom

June 2018

© Queen Mary University of London

DECLARATION

I hereby declare that the content of the work presented in this thesis is original and has not been submitted in whole or in part for consideration for any other degree or qualification in this, or any other university. This dissertation is my own work and all references have been cited accordingly.

Andre Sarker Andy
June 2018

TO MY FAMILY.

ABSTRACT

The primary objective of the research is to investigate photosensitive semiconducting materials, mainly organic, and utilise them in antenna front-end systems and dynamic lenses for sub-THz applications. Mechanisms such as phase-shifting and photo-conductive switching are introduced in EM-devices to alter the antenna performance and behaviour. Using such mechanisms the devices are able to attain frequency, radiation pattern and polarisation reconfigurability. The common inorganic semiconductor, Si, and organic semiconductors such as poly 3-hexylthiophene (P3HT), [6,6]-Phenyl C61 butyric acid methyl ester (PCBM) have been extensively studied and used in the exemplar EM-devices developed for this thesis.

In this research, novelty is deployed with the use of photosensitive semiconductors as a means of 'tuning' dielectrics to control the propagation of the emerging beam-field of an antenna. Both organic and inorganic photosensitive semiconductors have been implemented in this work. The research begins by exploring the physical properties of such photosensitive semiconductors at microwave frequencies. Medium-resistivity Si was characterised using a conventional microstrip transmission line and the conductivity of the Si piece in dark and active states were estimated by matching its transmission characteristics with the modelled Si in CST Studio Suite. Thereafter the modelled Si was used in an antenna design to estimate the reconfigurability of the device.

However, inorganic semiconductors are being replaced with organic semiconductors because of their inflexibility in device fabrication. Organic polymers, on the other hand, are light in weight, can be cast onto any surface, when blended with an organic solvent, and also photo-excited using white light. Organic polymer heterojunction 95% P3HT: 5% PCBM was characterised and changes in the real and imaginary parts of the complex dielectric constant of the organic blend are measured in the range of –0.05 to –0.55 and +0.01 to +0.52 respectively, over the sub-THz frequency-domain.

In order to demonstrate EM-control of a wave using a photo-sensitive material, a two-element patch antenna array using organic polymer P3HT-PCBM is fabricated and the functionality for antenna beam steering examined. Non-optimum illumination of the organic layer on the antenna patches, led to an asymmetric and perturbed beam steer. Hence, a novel optically triggered antenna has been proposed at S-Band (2 – 4 GHz),

where sodalime glass is being used as lower substrate, ITO (Indium Tin Oxide), transparent to white-light, as the ground plane and transmission lines along with patches are modelled onto the upper substrate layer (P3HT:PCBM). The estimates of the dielectric changes in the organic polymer blend due to optical excitation were used as inputs in the modelled device to show the proof-of-concept for beam steering with such a phase-shifting device. In addition, the antenna design also demonstrated that with a small change in the real part of the permittivity of the substrate it is possible to generate a maximum beam steer of 5°, using an effective phase-shifting design in CST Studio Suite.

At millimetre-wave or sub-terahertz frequencies, small changes in the dielectric with excitation-region depth comparable to the wavelength are plenty to manipulate the emerging wave of an antenna or lens. Hence, an optically-activated dynamic lens is proposed and designed to dynamically control millimetre-wave transmission using optical illumination. The lens acts as a graduated gateway for phase transmission by adjusting the spatial permittivity across the lens. A nearfield measurement system is used to analyse the performance of the lens over the WR-10 (75 – 110 GHz) waveband. The phase distribution of the electric field across the face of the plane organic lens shows a similar pattern in the spatial phase-distribution of the lens plane in the active state as that projected by the illuminating source, allowing for projection-angle-induced cosine errors. Hence the dynamic operation of the lens can be beneficial for beam controlling applications in imaging, surveillance and remote sensing in the mm-wave frequency-domain.

ACKNOWLEDGEMENT

First and foremost I would like to express my sincere gratitude towards my primary supervisor Dr Robert S. Donnan for his expert guidance and unconditional support during the 4 years of my PhD study. I would like to equally thank Dr Theo Kreouzis, my second supervisor, for his unparalleled contribution in my work. Having two such academic mentors as advisors has benefited me to rapidly gain immense knowledge and expertise in the fields of material science and electromagnetics over the last 4 years.

I would like to thank Dr Khalid Rajab, who was my accessor for the first 2 years of my PhD. I am indeed grateful for his valuable suggestions in my research and encouragement to collaborate with his PhD students. I would also like to thank Dr Rostyslav Dubrovka for employing me in his research as a research assistant and supporting me throughout the last few months of my PhD study. I'm also thankful for his motivation and technical insight delivered in my PhD work.

I would also like to thank the lab managers and technicians who were involved in the fabrication and measurements of the prototypes of my designs. From the School of Physics and Astronomy, I would like to thank Dr Ken Scott, and Mr. Geoff Gannaway for their assistance in using the glove-box and the clean room and Mr. George Neville, and Mr. Geoff Simpson for their unconditional support in fabricating the samples, and their supporting-holders. From School of Engineering and Computer Science (EECS), I would like to thank the previous, Dr Massimo Candotti, and the current, Dr Max Munoz Torrico, antenna lab managers for their immense support in the antenna lab during measurements. I would also like to thank the electronics lab manager Mr KoK Ho Huen, and technician Mr Dave Wilkinson for their unconditional assistance and support with the electronics-related jobs.

I would like to thank the Head of Antennas Group (Director of Research, 2014), Prof Clive Parini, for accepting my application for EECS PhD Studentship. I would also like to thank the Queen Mary Doctoral College Postgraduate Research Initiative Fund (PGRIF) for providing me funding to support my living expenses, as a studentship, during my study in Queen Mary. I thank Prof Simon Dixon and Mrs Melissa Yeo, who were involved in commencing and monitoring my studentship throughout the PhD program.

I would also like to thank all my colleagues from my department (EECS), especially the ones who eventually became my close friends. I would like to take the opportunity to thank the post-doctoral research assistants in my group, Dr Oleksandr Sushko and Dr Melusine Pigeon, who were always willing to help me with any sort of advice or guidance needed to progress in my research. I would also like to thank Dr Yang Zeng, Dr Majid Naeem and Dr Deepak Singh Nagarkoti, for their selfless contribution in my research. Amongst close friends, I would like to thank Mr Peter Alizadeh, who has been a true lab partner throughout the 4 years of my PhD. Mr Ardavan Rahimian, a loyal friend, never failed to be there when needed. Mr Ahmed K. Aziz, Ms Syeda Fizzah Jilani, and Mr Shaker Alkaraki for amusing me with their positive attitude, enthusiasm and food supplies throughout the years and Mr Xingjian Zhang for his endless contribution in assisting me with MATLAB coding. I would also like to take the opportunity to thank my colleagues from School of Physics and Astronomy. Firstly, I would like to thank my dear friends from Physics, Mr James W. E. Kneller, my physics laboratory partner, for his immense support in the lab, and Mr Dominico Trotta, for being a stress-reliever with his jokes and funny gestures during the writing-up stage of my PhD. I would also like to thank other colleagues from physics, Ms Xiao Qi Liu, and Mr Shankui Chang, who assisted me with fabrication techniques such as photo-lithography, drop-casting and hot-press.

Lastly I would like to thank my family. My parents were always supportive of me pursuing the highest level of education. Never did they stop me to support mentally whenever I was stuck in my research or my experiments failed miserably. They always backed me up with immense mental strength. My only sister, who lives in Canada now, has also been a huge support for me throughout my whole PhD. When she was here, in London, she used to cook good food for me and bring it for me when I was ill or was extremely occupied meeting stage-report or conference deadlines. I must say without the contribution of my family, progressing this far would be quite impossible.

Thank you all!

LIST OF PUBLICATIONS

JOURNALS

1) **A. S. Andy**, J. W. E. Kneller, O. Sushko, M. Torrico, R. Dubrovka, C. Parini, T. Kreouzis, and R. Donnan, "Beam Manipulation of Sub-THz Waves Using Dynamic Organic Lens," IEEE Transactions on Terahertz Science and Technology, *to be submitted*.

2) **A. S. Andy**, J. W. E. Kneller, O. Sushko, R. Dubrovka, C. Parini, K. Scott, T. Kreouzis, and R. S. Donnan, "Estimation of dark and active dielectric constants in the sub-THz frequency domain of an optically tunable organic semiconductor blend of poly(3-hexylthiophene) and phenyl-C61-butyric acid methyl ester," Applied Physics Express, vol. 11, pp. 061601-5, 2018

3) S. Alkaraki, **A. S. Andy**, Y. Gao, K. Tong, Z. Ying, R. S. Donnan, and C. Parini, "Compact and Low Cost 3D-Printed Antennas Metalized using Spray-Coating Technology for 5G mm-Wave Communication Systems," IEEE Antennas and Wireless Propagation Letters, *accepted.*

CONFERENCE PROCEEDINGS

1) **A. S. Andy**, P. Alizadeh, O. Sushko, M. M. Torrico, T. Kreouzis, R. Donnan, C. Parini, and R. Dubrovka, "Characterisation of a Quasi-Optical Transmissometer for Precise Measurement of a Sub-THz Multenna," in Loughborough Antenna and Propagation Conference, Loughborough, UK, Nov. 2017, pp. 1-4

2) P. Alizadeh, O. Sushko, M. Pegion, **A. S. Andy**, J. W. E. Kneller,T. Kreouzis, R. S. Donnan, C. G. Parini, and R. Dubrovka, "Quasi-optical measurements of a THz multiplying antenna," in 38th ESA Antenna Workshop on Innovative Antenna Systems and Technologies for Future Space Missions, Netherlands, Oct. 2017, pp. 1–4.

3) **A. S. Andy**, J. W. E. Kneller, O. Sushko, R. Dubrovka, C.G. Parini, T. Kreouzis, and R. S. Donnan, "Dynamic Organic Lens Using Photosensitive Semiconductor (P3HT:PCBM) for Millimetre-Wave Applications," in 41st International Conference on Infrared, Millimetre, and Terahertz Waves (IRMMW-THz), Cancun, Mexico, Aug. 2017, pp. 1–2.

4) R. Dubrovka, O. Sushko, M. Pegion, P. Alizadeh, **A. S. Andy**, J. W. E. Kneller, T. Kreouzis, R. S. Donnan, and C. G. Parini, "Measurements of non-linear sub-THz quasi-optical devices," in 11th International Conference on Antenna Theory and Techniques (ICATT), Kyiv, Ukraine, May 2017, pp. 9–13.

5) **A. S. Andy**, J. W. E. Kneller, R. Dubrovka, T. Kreouzis, and R. S. Donnan, "Antenna Array Control via Integrated Optically- Activated Organic Semiconductor for S-Band Applications," in 46th European Microwave Conference (EuMC), London, UK, Oct. 2016, pp. 1–4.

6) **A. S. Andy**, P. Alizadeh, K. Z. Rajab, T. Kreouzis, and R. S. Donnan, "An Optically-Switched Frequency Reconfigurable Antenna for Cognitive Radio Applications," in 10th European Conference on Antennas and Propagation (EuCAP), Davos, Switzerland, Apr. 2016, pp. 1–4.

7) P. Alizadeh, **A. S. Andy**, C. Parini, and K. Z. Rajab, "A Reconfigurable Reflectarray Antenna in Ka- Band Using Optically Excited Silicon," in 10th European Conference on Antennas and Propagation (EuCAP), Davos, Switzerland, Apr. 2016, pp. 1–5.

8) **A. S. Andy**, O. Sushko, T. Kreouzis, and R. S. Donnan, "Optically-Tunable Organic Semiconductor Heterojunction P3HT-PCBM for Millimetre-Wave Applications," in 40th International Conference on Infrared, Millimetre, and Terahertz Waves (IRMMW-THz), Hong Kong, Aug. 2015, pp. 1–2.

9) Y. Zeng, **A. S. Andy**, T. Kreouzis, X. Chen, and R. S. Donnan, "Beam profile measurement of THz pulses in a TDS system," in 40th International Conference on Infrared, Millimetre, and Terahertz Waves (IRMMW-THz), Hong Kong, Aug. 2015, pp. 1–2.

10) **A. S. Andy**, R. Dubrovka, T. Kreouzis, and R. S. Donnan, "An Optically Controlled Phase Shifter for Antenna Array Beam Steering," in 9th European Conference on Antennas and Propagation (EuCAP), Lisbon, Portugal, Apr. 2015, pp. 1–4.

TABLE OF CONTENTS

LIST OF FIGURES

CHAPTER 2

CHAPTER 3

CHAPTER 4

CHAPTER 5

CHAPTER 6

LIST OF TABLES

CHAPTER 2

CHAPTER 3

CHAPTER 4

CHAPTER 6

ABBREVIATIONS

2D	**2-Dimensional**
3D	**3-Dimensional**
Al	**Aluminium**
AlAs	**Aluminium Arsenide**
AUT	**Antenna Under Test**
CAI	**Coded-Aperture Imaging**
CPW	**Coplanar Waveguide**
CW	**Continuous Wave**
DC	**Direct Current**
DLP	**Digital Light Processing**
EM	**Electromagnetic**
EO	**Electro-Optic**
FET	**Field-Effect Transistors**
GaAs	**Gallium Arsenide**
Ge	**Germanium**
H_2O	**Water Vapour**
HOMO	**Highest Occupied Molecular Orbital**
InAs	**Indium Arsenide**
InP	**Indium Phosphate**
IR	**Infrared**
IRED	**Infrared Emitting Diodes**
ITO	**Indium Tin Oxide**
LED	**Light Emitting Diode**
LHCP	**Left-Hand Circular Polarisation**
LP	**Linear Polarisation**
LT	**Low Temperature**

LUMO	**Lowest Unoccupied Molecular Orbital**
MEMS	**Microelectromechanical Systems**
mm	**Millimetre**
N_2	**Nitrogen**
ND	**Neutral Density**
O_2	**Oxygen**
OLED	**Organic Light-Emitting Diodes**
OPV	**Organic Photovoltaic**
P3HT	**Poly-3-Hexylthione**
PCA	**Photoconductive Antenna**
PCBM	**Phenyl C61 Butyric Acid Methyl Ester**
PICA	**Planar Inverted Cone Antenna**
piFZPA	**Photo-Injected Fresnel Zone Plate Antenna**
PNA	**Programmable Network Analyser**
PV	**Photovoltaic**
QO	**Quasi-Optical**
RF	**Radio Frequency**
RFID	**Radio Frequency Identification**
RHCP	**Right-Hand Circular Polarisation**
RR	**Regioregular**
Si	**Silicon**
sub-THz	**Sub-Terahertz**
SUT	**Sample Under Test**
THz	**Terahertz**
ToF	**Time-of-Flight**
UWB	**Ultra-wideband**
VNA	**Vector Network Analyser**
ZnTe	**Zinc-Telluride**

Chapter 1 Introduction

1.1 Overview

An antenna is an interface between a guided wave and an un-guided wave. It acts as a transducer that converts electromagnetic fields into alternating current and vice-versa. It is required to transfer data or signals over a wireless communication link. However, with the increase in the number of wireless applications at present, there is a high demand for advancements in antenna technology. In order to satisfy such demands, multi-functional antennas are required where reconfigurable or tuneable antennas serve as best replacements [1].

In wireless communication, at recent times, the popular wireless devices in use are mobile phones, personal digital assistants, and laptops. These devices tend to suffer from unpredictable or harsh electromagnetic conditions due to inadequacies in signal reception or interference in the operating frequency band. Reconfigurable antennas offer advanced functionalities for the device to avoid frequency collision or signal blockage. By tuning different operational parameters of the antenna, such as the resonant frequency, impedance bandwidth, polarisation and radiation pattern, the antenna can adjust to the system requirements caused by environmental change [2]. This improves the system performance and ensures better service through higher data transmission. An antenna that is unable to adjust to a new operating environment cannot maintain optimum system performance.

Reconfigurability in antennas usually requires use of active loading elements such as PIN or varactor diodes. These active elements in turn require several biasing lines accompanied by high biasing voltages [3]. PIN diodes have lower biasing voltages compared to varactor diodes [4]. Microelectromechanical systems (MEMS), have shown better performance as electronic switches when compared to PIN diodes and FET

transistors [5]. Additionally these switching elements have been used in both low and high frequency applications. However, despite the merits of electronic switching elements, the external biasing required for activating these switches can cause interference with the radiation of the antenna and hence deteriorates the antenna performance significantly.

Optically-controlled switches or materials, on the other hand, have some inherent advantages over electronic control, such as high isolation between the controlling signal (the optical signal) and the controlled signal (the radiated signal) of the device. As a result, they provide high immunity to electromagnetic interference [6, 7]. In addition to high isolation from electromagnetic coupling between the radiating wave and the controlling elements, the switching of these optically driven photoconductive switches is extremely fast offering nanosecond switching times. Furthermore, these switches offer not only electrical, but thermal isolation between the antenna and the control circuitry.

1.2 Motivation and Objectives

Photosensitive semiconductors are considered as one of the primary choices for use as tuneable materials in optically-driven reconfigurable antennas. Semiconductors, when illuminated by light with sufficient photon energy exceeding their band gap energy, generate electron-hole pairs. This initiates a change in the physical parameters such as permittivity and conductivity of the semiconductor material. As a result, reconfigurability in a microwave device or antenna can be achieved by manipulating the optically dependent properties of the tuneable semiconductor. Photoconductivity is one of the main approaches for attaining optical control over a device fabricated using a semiconducting material. A significant change in the photoconductivity of high-resistivity silicon (Si) can be obtained with low levels of optical power [8]. Si-based photoconductive switches has been widely used in optically controlled devices such as phase-shifters, frequency selective surfaces and reconfigurable antennas, enabling changes to their operating performance.

A new application of optically-pumped reconfigurable antenna systems in cognitive radio systems has been demonstrated by Tawk *et. a.l.* [9]. A cognitive radio system is a smart radio system where the sensing unit continuously searches for an idle frequency band and dynamically assigns that band to the user of the radio device, minimising interference with other wireless systems. In order to achieve such operation of the device,

there must be a wideband radio unit that searches the wireless channel for unused carrier frequencies, and a "reconfigurable transmit/receive antenna" to perform the data transfer over the unused frequency bands. Another major focus of using optically-activated materials for antenna systems has been on the development of beam steering techniques [10]. Phase-shifters have been readily employed in antenna arrays to implement beam steering. Conventionally, phase-shifting in antenna arrays is achieved with the use of electronic or mechanical switches. However, optically-controlled phase-shifters have proved to have advantages over their counterparts [11, 12].

Conventional reconfigurable antenna arrays require separate phase-shifters for each radiating element to off-set the initiation of radiation among neighbouring radiating elements. Nevertheless, these phase-shifting electronic units introduce system-interference, whereas optically-controlled phase-shifters are inherently isolated from the antenna's radiation field. Most optically-controlled phase-shifters are based on the photoconductive effect of inorganic-semiconductors (Si). Light with a wavelength of 880 nm is used to tune the conductivity of Si by generating electron-hole pairs which in turn alter the propagation characteristics of the wave in the medium. However, Tang *et al.* have designed an optically controlled phase shifter employing the organic semiconductor P3HT, poly (3-hexylthiophene), for the first time [13]. This p-type organic semiconductor has been demonstrated as a tuneable dielectric.

Photosensitive organic semiconductors such as P3HT are typically used in organic photovoltaics (OPVs). These are low dielectric materials and have a band-gap of ~ 1.9 eV, which is sufficient for the photon energy of white-light to excite the material and generate electron-hole pairs. Additionally, P3HT has a relatively high carrier mobility of the order 10^{-4} $cm^2V^{-1}s^{-1}$ [14]. This order of drift mobility of the induced charge carriers contributes to the optically excited dielectric changes making the organic semiconductor an appropriate choice for use in optically-driven phase-shifters. These polymers also offer mechanical flexibility and their fabrication process is less complex when compared to their inorganic counterparts. Since the relative permittivity of photosensitive organic polymers such as P3HT can be tuned using external optical illumination, the EM properties of the electromagnetic wave propagating through the medium can be manipulated in a similar manner as using Si. The changes, due to excitation, in the physical properties of these polymers are not as high as in inorganic semiconductors, e.g dielectric constant changes of a typical high-resistivity Si range from 11.9 to 8.9. However, small changes in the dielectric constant are often found to be useful at high

frequencies (sub-THz and THz) in the field of electromagnetics. The regime of the electromagnetic spectrum between 30 and 300 gigahertz (GHz) (with corresponding wavelengths between 10 and 1 mm) is defined as millimetre-wave (mm-wave) frequency domain. In this frequency domain, a small portion of the spectrum is also known as sub-THz, i.e., 100 – 300 GHz (0.1 – 0.3 THz). Any frequency above 300 GHz (0.3 THz) up to 3 THz is considered as THz frequencies.

Mm-wave frequency domain is of great interest to the antenna engineering community because of high bandwidth (in terms of data transmission), less interference at such frequencies since most of the commercial applications take place at microwave frequencies, and very high directive beams. The applications at mm-wave frequencies are plenty. They span from radio astronomy and telecommunications to medical applications. In radio astronomy, mm-wave frequencies are used for earth observation, universe studies, exoplanets studies and solar system with the use of radiotelescopes and interferometers. In addition, indoor wireless communication systems as well as automotive radar systems operate at frequencies between 60 – 90 GHz. There are several military applications including controlling and tracking of missiles, drones and helicopters. In telecommunication, 5^{th} generation (5G) applications require use of massive multiple input multiple output (MIMO) systems. The antennas used in these systems require high gain, narrow beamwidth, and low sidelobes in different directions. Proposed systems demonstate use of a phased antenna arrays at the mm-wave (60–100 GHz) region. Lastly, mm-wave frequencies are also lucrative for radar imaging systems. For high resolution or 3 dimensional (3D) imaging both lower mm-wave and sub-THz frequencies are used. Along with imaging applications, mm-wave frequencies can also be useful to resonate biological macromolecules and biofilm and understand their oscillating frequency, which is of great interest to medical communities.

If organic semiconductors are used for sub-THz and THz applications, it is vital that their complex dielectric properties are known, both in the dark and under illumination. The dielectric properties of P3HT and related donor–acceptor blends can be found in literature below 10 GHz [15] and above 1 THz, but not in the sub-THz region. Studies determining the dark and active conductivities of a 1:1 P3HT:PCBM blend using THz time-domain spectroscopy (THz-TDS) [16-18] observe frequency dependent conductivities. This makes 1:1 blends unsuitable for EM applications due to the high resulting absorption at sub-THz and THz frequencies. To counter high absorption, we reduce the amount of acceptor by blending 5% PCBM with a matrix of 95% P3HT,

providing donor-acceptor interfaces to aid exciton dissociation without increasing the overall conductivity. This can lead to low loss optically tuneable EM devices based on the blend. The physical properties of these sub-THz low-loss dielectric organic semiconductors need to be known for device modelling at such frequencies. Potential devices using such photosensitive organic semiconductors are investigated in this research and the possible applications of such devices discussed in Chapter 5 and 6. The target application lies in the sub-THz region of the electromagnetic spectrum and is based on changes in the dielectric within a photogenerated region resulting in spatially modulated phase changes of the emerging EM waves, as demonstrated using inorganic semiconductors [19-20]. The flexibility of the organic semiconductor can potentially provide advantages over the current beam control mechanisms in QO systems. In this research, these polymers are presented in an entirely new and unconventional application, namely the control and tuning of Radio Frequency (RF) devices.

1.3 Research Contributions

In this work, several major contributions have been made regarding the use of photosensitive tuneable materials in antenna engineering. The research started with characterising inorganic semiconductor Si using a simple microstrip transmission line (see Appendix D for more details on micorstrip transmission line). The estimate for the conductivity of a medium-resistivity Si has been made by matching the simulated results of the transmission of an optically-switched microstrip line to that of measured. In addition, the expected conductivity values of high-resistivity Si have been used in the modelled design of an antenna to analyse the performance of an optically-switched cognitive radio system.

Additionally, the organic polymer P3HT as a base polymer, has been introduced as an optically-tuneable material to control the main beam of an antenna array. A donor-acceptor organic system was established, a bulk-heterojunction formed by blending 5% PCBM with a matrix of 95% P3HT, to increase the photo-carrier generation during optical excitation. Characterisation of such a heterojunction was performed using a quasi-optical transmissometer. The tuneable dielectric range between dark and active states of the heterojunction was estimated in the WR-10 (75 – 110 GHz) frequency-domain. In order to demonstrate an application of such a dielectric change in the organic blend, a two-element patch antenna array was fabricated and measured with the organic polymer covering the patch assembly. Illumination of the organic layer was directed from the front

end, failing to ensure a non-impeding condition during measurements. As a result, a multi-layered model of an antenna array comprising of copper, organic blend, sodalime glass ITO (indium tin oxide) was proposed. Glass and ITO, being transparent to visible light, allow optimum illumination of the organic layer. The measured dielectric changes of the organic blend were used as the data input required to show the proof-of-concept for beam steering with the antenna array. This antenna design demonstrated that with a small change in the real part of the permittivity ($\Delta\varepsilon = 0.1$) of the substrate it is possible to generate a significant beam steer (5° in this case), using an effective phase-shifting design.

The final investigation of this research was on a tuneable photosensitive organic lens, capable of manipulating a millimetre (mm)-wave, or sub-terahertz (THz), beamfield for imaging applications. Demonstration of such a concept was presented through numerical modelling and a fabricated device design. With numerical analysis it has been shown that a photo-sensitive planar lens is able to output a pattern dynamically, in terms of its spatial complex electric field distribution, when triggered with patterned illumination. Since the dielectric changes observed in the active state of these organic semiconductors are small the change in the phase of the complex electric field across the lens plane is close to the noise floor of the measurement system. Consequently, a sensitive measurement system such as an electro-optic probe operating in THz frequencies should be able to detect such phase changes with minimum system (phase) noise.

1.4 Organisation of Report

The thesis is organised in six additional chapters as follows:

Chapter 2 presents the literature review on optically-activated antennas and dielectric lenses. Description of how reconfigurability is attained in optically-activated antennas using the tuning characteristics of photosensitive semiconducting materials is provided. The employment of organic semiconductors in antenna engineering has been exemplified. Lastly a critical review of the existing designs on optically-tuneable dielectric lenses has been made.

Chapter 3 outlines the principle behind the mechanism of triggering a photosensitive material and altering the physical characteristics of an electromagnetic wave propagating through it is explained. Two different processes, phase-shifting and photoconductivity, to attain tuneability in antennas using photosensitive materials have

been detailed in this chapter. A comparative analysis has been made between inorganic semiconductors and organic semiconductors in terms of their physical properties. Measurement of the mobility and the change in the carrier concentration due to optical excitation of the organic blend (95% P3HT: 5% PCBM) has been shown.

Chapter 4 demonstrates characterisation of photosensitive semiconducting materials using EM transmission-only techniques. The measurement methods used to characterise these materials are thoroughly discussed. A novel matching technique using a microstrip transmission line and its transmission characteristics for estimating the dark and active state conductivities of a photosensitive semiconducting material at microwave frequencies has been demonstrated. Additionally, the dielectric constant of the organic blend (95% P3HT: 5% PCBM) has been estimated using two different measurement systems and compared. Lastly, reversible and reproducible changes in the real and imaginary parts of the complex dielectric constant of the organic blend have been measured.

Chapter 5, discusses development of the illumination techniques in the designs of the existing optically-activated antennas using inorganic semiconductors and the employment of photosensitive organic semiconductors in antenna engineering to enable beam steering. Firstly a prototype design of an optically-switched cognitive radio using inorganic semiconductor (Si) is presented. Secondly, a novel optically-activated two-element patch antenna array using organic semiconductor blend (95% P3HT: 5% PCBM) has been presented for beam-steering applications.

Chapter 6 discusses the performance analysis of a novel optically-tuneable dynamic organic lens. The performance of the lens has been analysed using numerical analysis as well as measurements using a NSI planar scanner. Lastly, the possible applications of the dynamic organic lens have been presented.

Chapter 7 includes the conclusion of the work done in this research and provides some potential future works.

References

[1] Y. Tawk, "Analysis, design and implementation of front-end reconfigurable antenna systems (FERAS)," PhD, The University of New Mexico, New Mexico, 2011.

[2] J. T. Bernhard, *Reconfigurable Antennas*. Fort Collins, CO: Morgan and Claypool, 2007.

[3] D. Patron, K. R. Dandekar, and A. S. Daryoush, "Optical Control of Pattern-Reconfigurable Planar Antennas," *2013 IEEE International Topical Meeting on Microwave Photonics (Mwp),* pp. 33-36, 2013.

[4] C. Luxey, L. Dussopt, J. L. Le Sonn, and J. M. Laheurte, "Dual-frequency operation of CPW-fed antenna controlled by pin diodes," *Electronics Letters,* vol. 36, pp. 2-3, Jan 6 2000.

[5] D. E. Anagnostou, G. Z. Zheng, M. T. Chryssomallis, J. C. Lyke, G. E. Ponchak, J. Papapolymerou, *et al.*, "Designg fabrication, and measurements of an RF-MEMS-based self-similar reconfigurable antenna," *IEEE Transactions on Antennas and Propagation,* vol. 54, pp. 422-432, Feb 2006.

[6] A. J. Seeds and A. A. A. Desalles, "Optical Control of Microwave Semiconductor-Devices," *IEEE Transactions on Microwave Theory and Techniques,* vol. 38, pp. 577-585, May 1990.

[7] Y. Tawk, A. R. Albrecht, S. Hemmady, G. Balakrishnan, and C. G. Christodoulou, "Optically Pumped Frequency Reconfigurable Antenna Design," *IEEE Antennas and Wireless Propagation Letters,* vol. 9, pp. 280-283, 2010.

[8] S. Pendharker, R. K. Shevgaonkar, and A. N. Chandorkar, "A Novel T-shaped Optically Controlled Microwave Phase Shifter," *2011 IEEE International Conference on Microwaves, Communications, Antennas and Electronic Systems (Comcas 2011),* 2011.

[9] Y. Tawk, S. Hemmady, C. G. Christodoulou, J. Costantine, and G. Balakrishnan, "A Cognitive Radio Antenna Design Based on Optically Pumped Reconfigurable Antenna System (OPRAS)," *2011 IEEE International Symposium on Antennas and Propagation (Apsursi),* pp. 1116-1119, 2011.

[10] C. J. Panagamuwa, A. Chauraya, and J. C. Vardaxoglou, "Frequency and beam reconfigurable antenna using photoconducting switches," *IEEE Transactions on Antennas and Propagation,* vol. 54, pp. 449-454, Feb 2006.

[11] M. El Khaldi, F. Podevin, O. Exshaw, A. Vilcot, and A. M. E. Safwat, "Improvement of performance of optically controlled microstrip phase shifters," *Iet Microwaves Antennas & Propagation,* vol. 1, pp. 427-432, Apr 2007.

[12] W. Li, W. H. Sun, W. T. Wang, and N. H. Zhu, "Optically controlled microwave phase shifter based on nonlinear polarization rotation in a highly nonlinear fiber," *Optics Letters,* vol. 39, pp. 3290-3293, Jun 1 2014.

[13] H. Y. Tang, R. S. Donnan, and T. Kreouzis, "An optically controlled phase shifter employing the organic semiconductor poly(3-hexylthiophene)," *Applied Physics Letters*, vol. 91, Nov 12 2007.

[14] K. M. Coakley, B. S. Srinivasan, J. M. Ziebarth, C. Goh, Y. X. Liu, and M. D. McGehee, "Enhanced hole mobility in regioregular polythiophene infiltrated in straight nanopores," *Advanced Functional Materials,* vol. 15, pp. 1927-1932, Dec 2005.

[15] X. Ai, M. C. Beard, K. P. Knutsen, S. E. Shaheen, G. Rumbles, and R. J. Ellingson, "Photoinduced charge carrier generation in a poly(3-hexylthiophene) and methanofullerene bulk heterojunction investigated by time-resolved terahertz spectroscopy," *Journal of Physical Chemistry B,* vol. 110, pp. 25462-25471, Dec 21 2006.

[16] J. Obrzut and K. A. Page, "Electrical conductivity and relaxation in poly(3-hexylthiophene)," *Physical Review B,* vol. 80, Nov 2009.

[17] P. D. Cunningham and L. M. Hayden, "Carrier dynamics resulting from above and below gap excitation of P3HT and P3HT/PCBM investigated by optical-pump terahertz-probe spectroscopy," *Journal of Physical Chemistry C,* vol. 112, pp. 7928-7935, May 29 2008.

[18] P. Parkinson, J. Lloyd-Hughes, M. B. Johnston, and L. M. Herz, "Efficient generation of charges via below-gap photoexcitation of polymer-fullerene blend films investigated by terahertz spectroscopy," *Physical Review B,* vol. 78, Sep 2008.

[19] T. F. Gallacher, R. Sondena, D. A. Robertson, and G. M. Smith, "Optical Modulation of Millimeter-Wave Beams Using a Semiconductor Substrate," *IEEE Transactions on Microwave Theory and Techniques,* vol. 60, pp. 2301-2309, Jul 2012.

[20] L. J. Cheng and L. Liu, "Optical modulation of continuous terahertz waves towards cost-effective reconfigurable quasi-optical terahertz components," *Optics Express,* vol. 21, pp. 28657-28667, Nov 18 2013.

Chapter 2 Literature Review on Optically-Activated Antennas and Dielectric Lenses

Optically-activated antennas and lenses, in recent years, have gained sufficient attention for being considered as possible replacements for electronically-driven microwave and millimetre (mm)-wave reconfigurable devices. The applications of such devices lie in day-to-day wireless communication, space applications, imaging, surveillance and remote sensing. In this chapter detail of existing optically-activated microwave and mm-wave devices has been critically reviewed. These devices are dependent on the tuneable materials used in the design to attain reconfigurability in their output. As a result, the behaviour, in terms of physical properties, of the material must be known in order to understand the operation and the efficiency of these devices.

The performance of a reconfigurable antenna or dielectric lens is dependent on the way the tuning at the output is achieved. In conventional reconfigurable antennas, the reconfigurability is achieved using either electronic or mechanical switching. Electronic switches such as PIN-diodes and FETs require biased voltage lines to activate them, which in turn interfere with the radiating field of the antenna. Additionally, mechanical switches are very complicated to fabricate for which they tend to hamper flexibility in device manufacturing. Optical switches on the other hand provide immunity from electromagnetic (EM) interference since there is high isolation between the controlling signal and the radiating signal of the antenna. In addition, they are as light weight as thin film FETs, easier to fabricate and can achieve high switching speeds (up to picoseconds) between on and off states when triggered using picosecond optical excitation source [1, 2].

Inorganic semiconductors, mainly silicon (Si) and low-temperature grown gallium arsenide (LT-GaAs), are commonly used in optically-activated devices. These devices include optically-switched microstrip transmission lines, coplanar waveguides and phase shifters [2-4]. Optically-activated signal attenuators have also been designed using optically-controlled waveguide or transmission lines [5]. Additionally, several optically-activated tuneable antennas have been designed, using photoconductive switches. These mainly include frequency-reconfigurable antennas, polarization-reconfigurable antennas and radiation pattern reconfigurable antennas [6-8]. A cognitive radio system using such antennas has also been proposed [9]. Furthermore, photoconductive microwave switches, based on Si, have been demonstrated to be used in a reconfigurable antenna array for mm-wave applications [10, 11].

Optically-tuneable organic semiconductor, such as poly(3-hexylthiophene), or P3HT, has been previously used as a substrate in a phase shifting device and as a patch in a reconfigurable antenna [12, 13]. Organic semiconductors offer several advantages over their inorganic counterparts. They are light-weight, flexible, non-brittle, and can be easily triggered by a white-light LED source, since there absorption spectrum lies within the visible region. However, the drawbacks of these carbon-based polymers can be summarised as follows: i) due to inherent low mobility of free charge carriers within them, the changes in conductivity, or dielectric constant, between dark (no light) and active states (with illumination), is very low ii) These polymers tend to suffer from environmental instability, particularly due to photo-oxidation. Hence, there is a continuing search for an improved doped or blended (p-type and n-type) polymer by the opto-electronics community. Also very little has been reported about the dielectric constants of these photosensitive polymers at mm-wave frequencies. In Chapter 4 precise determination of the dielectric constants of such polymers is reported at mm-wave and THz frequencies.

The concept of an optically-activated lens operating at mm-wave and THz frequencies is uncommon. These devices could be considered as reconfigurable or tuneable components in quasi-optical (QO) sub-THz or THz systems for controlling the angular power pattern of a transmitted beam field. The functionality of such devices include sub-THz or THz wave switching, attenuation, focusing and beam steering. Optically-tuneable flat lenses reported till date have been fabricated using inorganic semiconductor Si [14, 15]. It has been reported that using a patterned illumination, manipulation of an EM wave is possible at the optically-triggered flat-lens interface.

Using a controlled or patterned illumination the beam field can be correspondingly manipulated in terms of its power-pattern, polarisation, and steering.

2.1 Optically-activated transmission lines

Optically-activated, reconfigurable, antennas mostly tend to derive their tuneability from integrated photoconductive switches. The performance of these switches can be tested using a microstrip or coplanar waveguide (CPW) transmission line (see Appendix D for more details on coplanar waveguides). The photoconductive switch is usually positioned over the gap structure of such devices. In other cases, the microstrip line or the CPW structure is fabricated onto a Si substrate and the gap is illuminated using a point-source. Both microstrip transmission lines and CPW devices have been proven to be effective in determining the performance of a photoconductive semiconducting material in both microwave and mm-wave frequencies [7, 16-18]. The source of illumination for the photoconductive switches for these optically-activated microwave devices is conventionally a continuous-wave (CW) laser. In order to trigger a Si switch for example, different wavelengths, 488 nm [16], 785 nm [19], 808 nm [20], 830 nm [17], 980 nm [7], of the excitation light has been reported. Besides wavelength, the incident power at the switch interface is equally responsible for generating electron-hole pairs in the active plasma region of the semiconductor. Incident light at the switch interface ranging in power from 20 to 500 mW over an area of 40 mm^2 has been reported to be sufficient for successfully triggering a Si switch [21].

Several models of the optically-switched transmission line have been reported [7, 8, 20]. Fig. 2.1 shows prototypes of optically-switched transmission lines using Si as a photoconductive switch. These transmission lines are primarily used to test the functionality of a photoconductive switch under illuminated conditions and estimate the isolation between dark and active states of the device. Isolation, by definition, is the difference between the transmission of the microstrip line in dark and active states. The isolation determines the optimal performance of the switch when integrated into the antenna design. An isolation circa 10 – 15 dB between dark and active states is essential for the switch to behave as an on-off switch and imbue a microwave device with reconfigurability. Typical gap lengths ranging from 0.25 – 1.5 mm are used in such devices. The thickness of the Si switch or substrate is chosen based on the plasma depth of the photosensitive semiconducting material used. In the active plasma region, electron concentration of these materials becomes negligible above a depth of 0.4 mm [17].

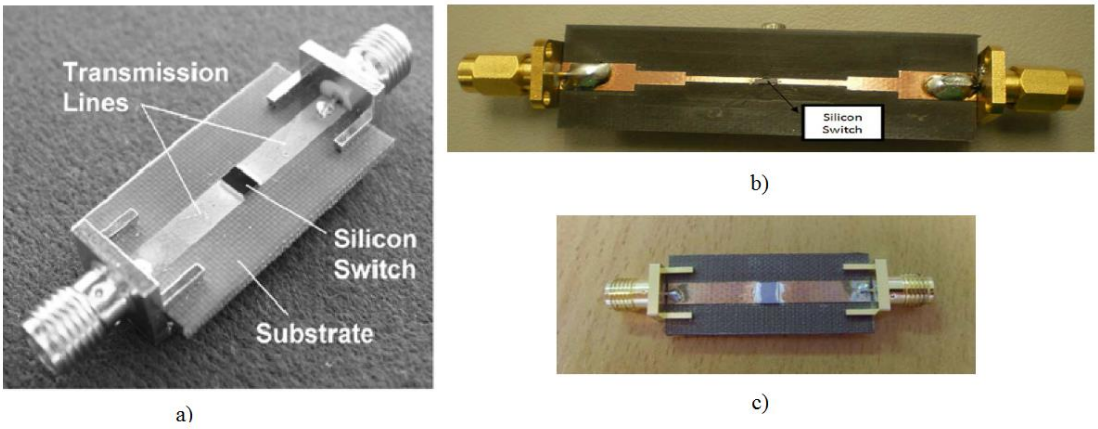

Fig. 2.1. Optically-switched transmission lines reported in literature by a) Panagamuwa et al. [7] b) Tawk et al. [6] c) Su et al. [8].

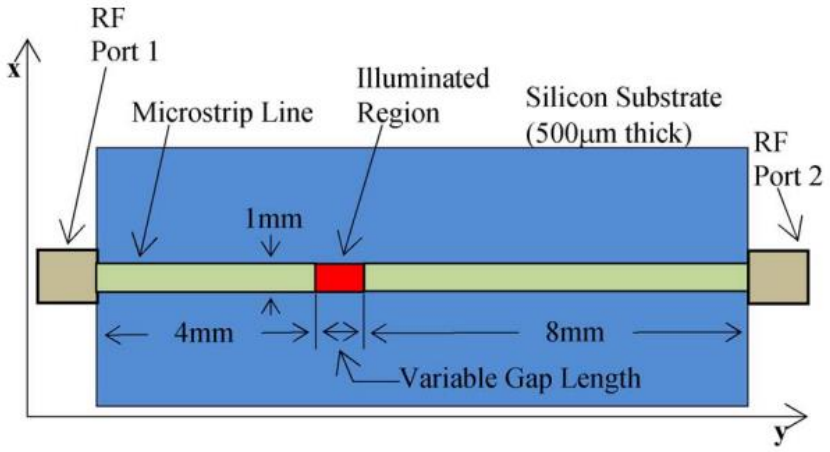

(a)

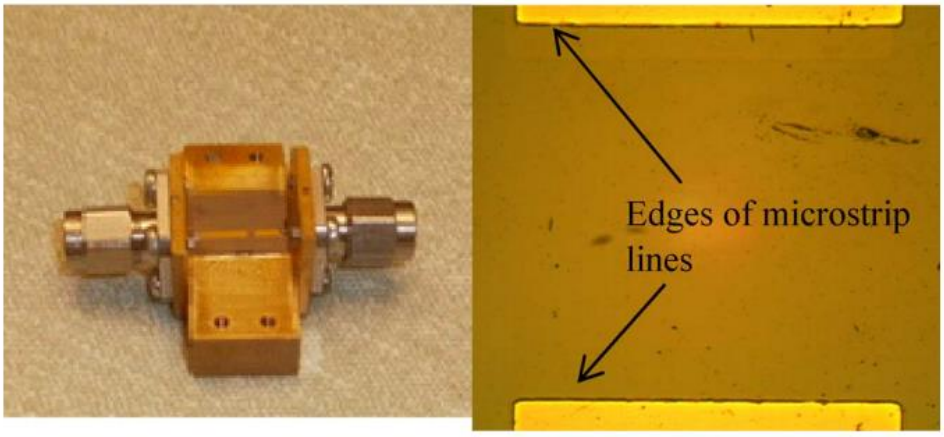

(b)

Fig. 2.2. a) A microstrip line transmission line modelled on Si substrate with a gap width of 0.4 mm and variable gap length. b) Fabricated prototype of the optically-switched microstrip transmission line, reproduced from Gamlath *et al*. [17].

Gamlath *et al*. have successfully characterised the plasma region of a Si substrate using a microstrip transmission line up to mm-wave frequencies (50 GHz in this case). Fig. 2.2a shows the prototype used for modelling the plasma region using EM modelling software, CST [22]. The design was fabricated on a Si substrate and a high power illumination point-source was directed onto the gap in the transmission line (see Fig. 2.2b). The illuminated region was modelled as electron-hole plasma. A matching technique was used, to match simulated and measured results, by precisely modelling the plasma region. The main aim of this study was to develop a new model for the optically-generated plasma region by closely matching simulated results with the measured results of the optically-switched transmission line. However, at higher frequencies, typically 30 – 50 GHz, the trend of the measured transmission coefficient in S-parameters (S21) (see Appendix D for more details on S-parameters) deviated, an average estimation over the frequency range, 8 dB away from that of the modelled structure. This model is demonstrated in a way that the microwave properties of the inhomogeneous plasma layer can be adapted to other inorganic semiconductors such as GaAs.

2.2 Optically-activated phase shifters

Optically-controlled phase shifters are devices that take advantage of illumination to create a shift in phase between the input and output signal of the device or, between multiple outputs. Generally, semiconducting materials, such as Si, are used as a switches or substrates in these devices. When external irradiance of an appropriate wavelength is incident onto the target region of the tuneable dielectric, factors such as signal propagation, velocity and impedance of the EM wave propagating in that very region change, which translate into a change in phase. By exploiting these parameters, phase shifters can be coupled with antennas or dielectric lens structures for applications such as beam-steering, pattern-shaping or modulation.

2.2.1 Tuneable phase shifters using photosensitive inorganic semiconductors

An optically-controlled microstrip phase-shifter has been reported by El Khaldi *et al.*, in which phase-shifting is obtained by optically controlling the gap capacitance in the design of Fig. 2.3 [4]. The concept of phase shifting is realised with the use of a photosensitive semiconducting material (Si in this case), where photoinduced changes in the physical parameters of the semiconducting material (permittivity and conductivity) result in a change in the strength and phase velocity of the electromagnetic wave

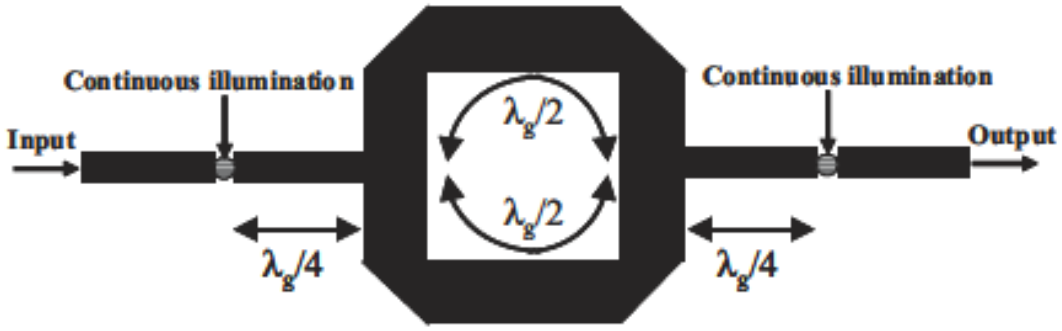

Fig. 2.3. Top view of an optically-controlled microstrip ring-based phase-shifter, showing two gap structures in the transmission line where continuous spot-illumination is applied to alter the phase between dark (no illumination) and active states at the output of the device, reproduced from El Khaldi *et al*. [4].

propagating through it. The presence of the photoinduced plasma region, or photo-active region, alters the wave velocity compared to the dark state, resulting in a phase shift at the output. In this work, a microstrip ring resonator has been designed with a width of 869 µm and a length equal to λ_g, the RF wavelength in silicon, two quarter-wave transmission lines and two gaps at each end of length 20 µm (see Fig. 2.3). A SDL5431 laser diode (λ = 840 nm) coupled into a single mode optical fibre is used to generate a constant cylindrical spot beam of diameter 50 µm. In Fig. 2.4a continuously variable 0° – 127° phase shift is observed under very low optical power [0 mW – 3 mW] at 12 GHz. The variation of the magnitude of S21, at one given frequency, is about 5dB in the 9 – 12 GHz band. However, with this design, insertion loss has very small variation; return loss results indicated mismatch of the transmission (see Fig. 2.4b) and so another design was proposed, called rat-race hybrid phase-shifter.

The rat-race hybrid phase-shifter uses similar technology and materials to that of the ring-based phase-shifter, except for the gap length, that was fixed at 50 µm. Unlike the previous design, four ports are used in the present design and during the 'off'-state (without illumination) the propagating signals at ports 3 and 4 have opposite phases for which there is no transmission at port 2. Port 4 is extended in length to a quarter-wave as shown in Fig. 2.5, so that the reflected signals from the gap get sum to a null at port 1and to a maximum at port 2 (output). The dispersive scattering parameters of this design are calculated employing the even- and odd-mode technique demonstrated by Reed *et al.* [23]. By using such a technique and taking into account the additional stub length of $\lambda/4$ at port 4, the expressions for the return loss coefficient (S_{11}) and the overall transmission

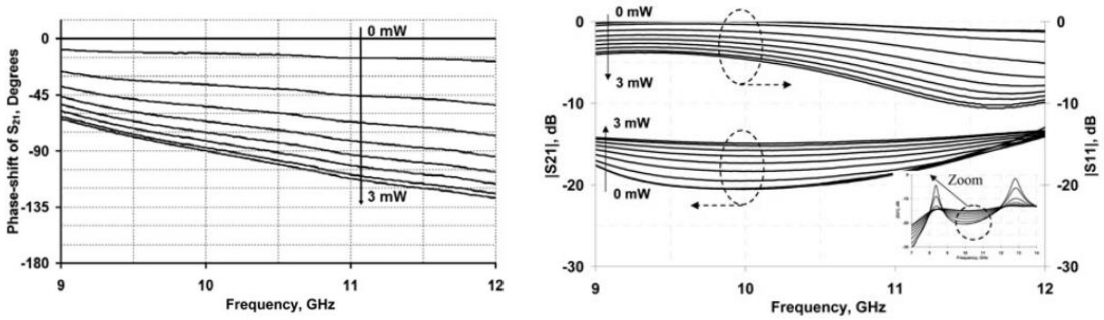

a) b)

Fig. 2.4. Measured a) phase-shift of parameter S_{21} annd b) magnitude of parameters S_{11} and S_{21} of the optically-controlled microstip ring resonator, reproduced from El Khaldi *et al*. [4].

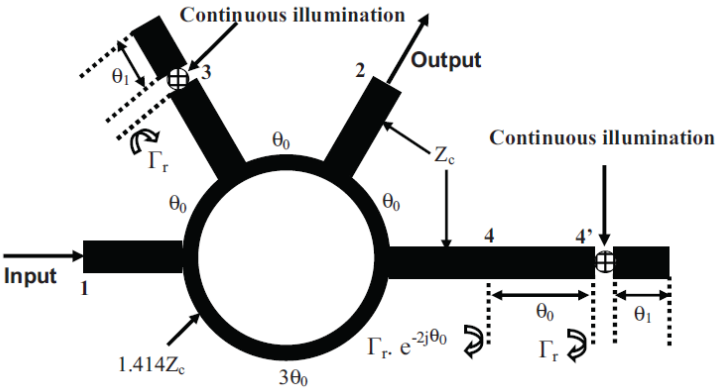

Fig. 2.5. Top view of the hybrid rat-race phase-shifter showing two gap structures in the transmission line where continuous spot-illumination is applied to alter the phase between dark (no illumination) and active states at the output of the device, reproduced from El Khaldi *et al*. [4].

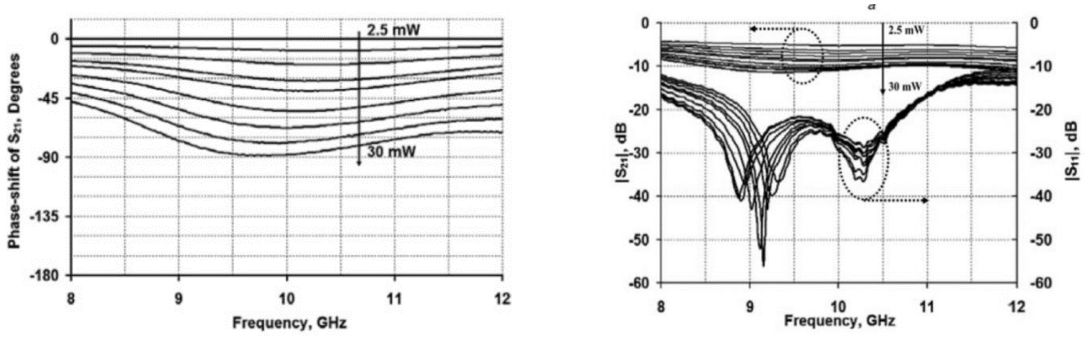

a) b)

Fig. 2.6. Measured a) phase shift of transmission coefficient b) magnitude of transmission coefficient at different illumination intensities of the hybrid rat-race phase-shifter, reproduced from El Khaldi *et al*. [4].

coefficient (S_{21}), are derived. The measured magnitude and phase of transmission from port 1 to port 2 is shown in Fig. 2.6a and b. It is observed that with this design a maximum of 90º phase shifting is obtained and the insertion loss is better than in the previous design and the transmission too varies over a workable range.

2.2.2 Tuneable phase-shifters using photosensitive organic semiconductors

The organic semiconductor P3HT is a photosensitive organic polymer that can be used as a tuneable dielectric material. When illuminated, its effective permittivity is altered in response to the excitation region in the polymer. The underpinning theory is described in Section 3.1 of Chapter 3. The excitation region due to illumination influences the propagation factors (impedance, wavevector, velocity etc) of the EM waves in the polymer. Where one region is illuminated and another not, a relative phase offset results. Fig. 2.7a shows the schematic diagram of an optically-induced phase-shifter employing

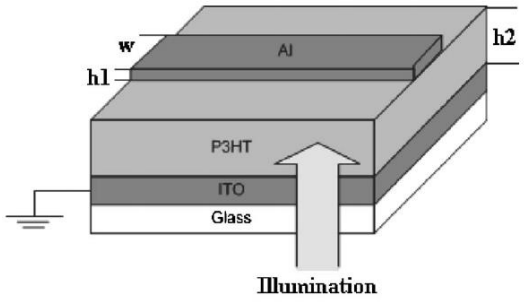

a)

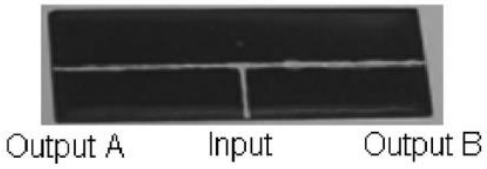

b)

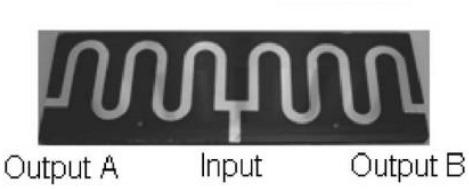

c)

Fig. 2.7. a) Schematic diagram of the optically-controlled phase-shifter employing organic semiconductor poly-3-hexylthiophene (P3HT). The transmission line (aluminium) is vacuum deposited onto the P3HT substrate (75 × 25 mm^2), indium tin oxide (ITO) acts as the ground floor, and glass the transparent (to visible light) support for the entire structure b) the first fabricated prototype is a transmission line with meandering conductor strips. c) the second fabricated proto prototype is a transmission line with meandering conductor strips, reproduced from Tang et al. [12].

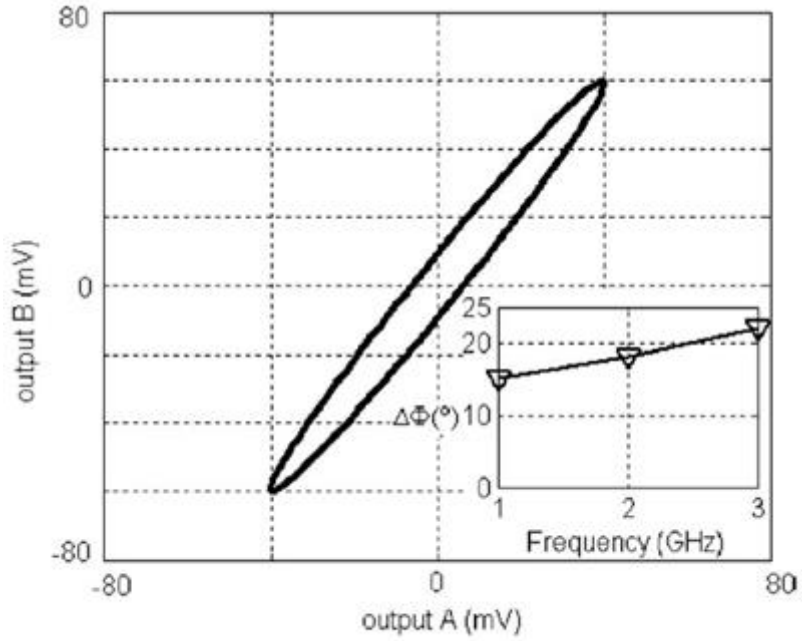

Fig. 2.8. Measured Lissajous curves for illumination conditions of a meandering conductor strip transmission line where an 18° differential phase shift is observable for a 2 GHz signal, reproduced from Tang *et al.* [12].

an organic semiconductor illuminated using a tungsten filament microscope light source of optical power 90 mW. Tang *et al.* report a maximum of 9° ± 1° phase shift is achievable using a conducting straight strip (see Fig. 2.7b) of transmission line and a maximum of 18° ± 1° using a meandering transmission line. (see Fig. 2.7c). Fig 2.8 shows its maximum possible output, in terms of phase shift. Based on such a design, prototype optically-activated antennas have been proposed in Section 5.2 of Chapter 5. More advanced and complex designs involving a two-element patch antenna array using integrated optically-activated phase shifters for beam-steering applications have been reported. Clear beam-steer has been observed with such prototype designs, modelled using measured physical properties of these organic semiconducting materials.

2.3 Optically-activated antennas using photosensitive semiconducting materials

Optically-activated reconfigurable antennas are mainly based on two principal operating mechanisms. The first mechanism is phase-shifting, which is initiated using the concept of complex permittivity in the plasma region, in other words the illuminated region. The change in permittivity of the active region creates a phase offset between

Table 2.1 Selected technologies for the implementation of reconfigurable antennas and qualitative assessment of a few related properties ('+', '0', and '–' symbols refer to good, neutral, and poor respectively), reproduced from [26].

Type	Technology	Maturity - reliability	Integration (incl. biasing)	D/A control	Complexity (cost)	Loss (microwave / THz)	Bias power consumption	Linearity	Switching time
Lumped elements	PIN diodes	+	-	D	+	-/-	-	0	+
	Varactor diodes	+	-	A	+	-/-	+	-	+
	RF-MEMS	0	+	D[1]	+	+/0	+	+	0
Hybrid	Ferro-electric thin film	0	+	A	0	0/-	+	0	+
Tunable materials	Liquid crystal	0	0	A	0	-/+	0	0	-
	Graphene	-	+	A	0	-/+	+	-	+
	Photo-conductive	0	-	A	0	-/-	-	-	+
Mechanical	Fluidic	0	-	A	0	0/+	+	0	-
	Micromotors	-	0	A	-	+	0	+	-

active and non-active regions. The second mechanism is attaining reconfigurability via photoconductivity. Photoconductive semiconductor switches are used to control the onand off states of the optically-activated microwave devices. Tested photoconductive microwave switches are then incorporated in the antenna design to attain frequency, polarisation, and beam reconfigurability. In comparison to the existing switching technologies in reconfigurable antennas, optically-activated switches tend be advantageous over the others in terms of fast switching time (see Table. 2.1).

2.3.1 Tuneable antennas using photosensitive inorganic semiconductors

Optically controlled reconfigurable antennas mostly tend to derive their tuneability from integrated photoconductive switches. The performance of these switches can be tested using microstrip or coplanar waveguide transmission lines, before incorporating the switches in the real design [6-7]. This is done by investigating the gap structure of a transmission line. A photoconductive switch can either be modelled as an area of illumination on the gap structure of the transmission line, where Si is used as the substrate, or the gap structure can be occupied by a Si switch, in which case the substrate can be of any other dielectric, for example FR-4. In the latter case to account for such switches in a real antenna design, dimensions as well as positioning of the Si switch must be well

modelled in the transmission line design to get efficient functioning of the optically switched transmission line.

Several models of the optically switched transmission line have been reported in literature [5, 6, 7]. Fig. 2.9 shows prototype designs of optically-switched transmission lines using Si as a photoconductive switch. The primary objective of this device is to test the functioning of the photoconductive switch at active state, and also to estimate the isolation between active and dark states of the device. The insertion loss of an optically-switched transmission line in the active state is expected to be above 3 dB for optimum operation of the switch in the frequency domain 1 – 9 GHz. The isolation of insertion loss between dark and active states determines the tuneability of the optical switch. A typical value for the isolation for optimum operation of these optically reconfigurable switches is around 8 – 10 dB in the frequency domain 1 – 9 GHz.

Reconfigurable antennas using optically-activated switches have been reported by a significant number of authors in the literature. Tawk *et al.* have proposed a unique optically-activated, frequency reconfigurable, antenna design, in which the antenna consists of an outer annulus about an inner circular patch [6]. These two structures are separated by a 1mm gap but connected using two high-resistivity Si switches as shown in Fig. 2.10a. The Si switches were illuminated using optical fibre cables connected to a laser source (see Fig. 2.10b). During the dormant or off-state, the circular ring is active and the antenna resonates at a frequency between 18 and 19 GHz; during on-state, the circular patch links up with the annulus to generate a second resonance at 12 GHz. This shows the dual frequency operation of this reconfigurable antenna (see Fig. 2.11b).

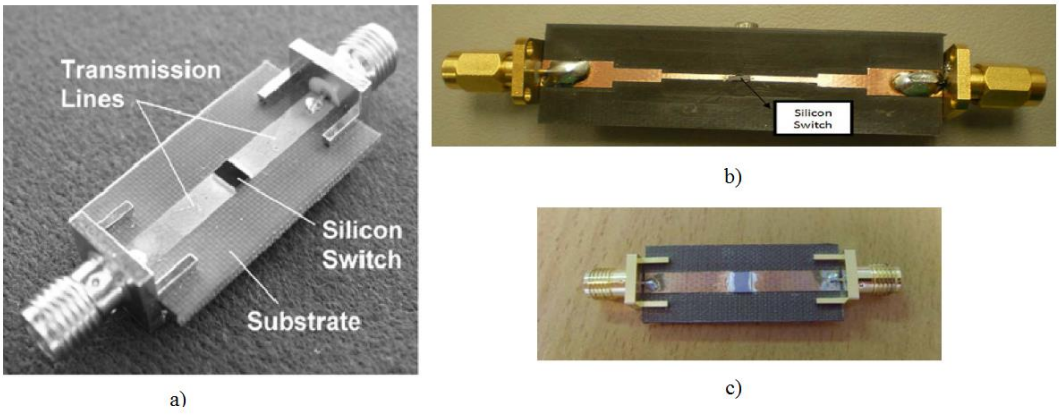

Fig. 2.9.Optically switched transmission lines reported in literature by a) Panagamuwa et al [7] b) Tawk et al [6] c) Hansheng Su et al [8].

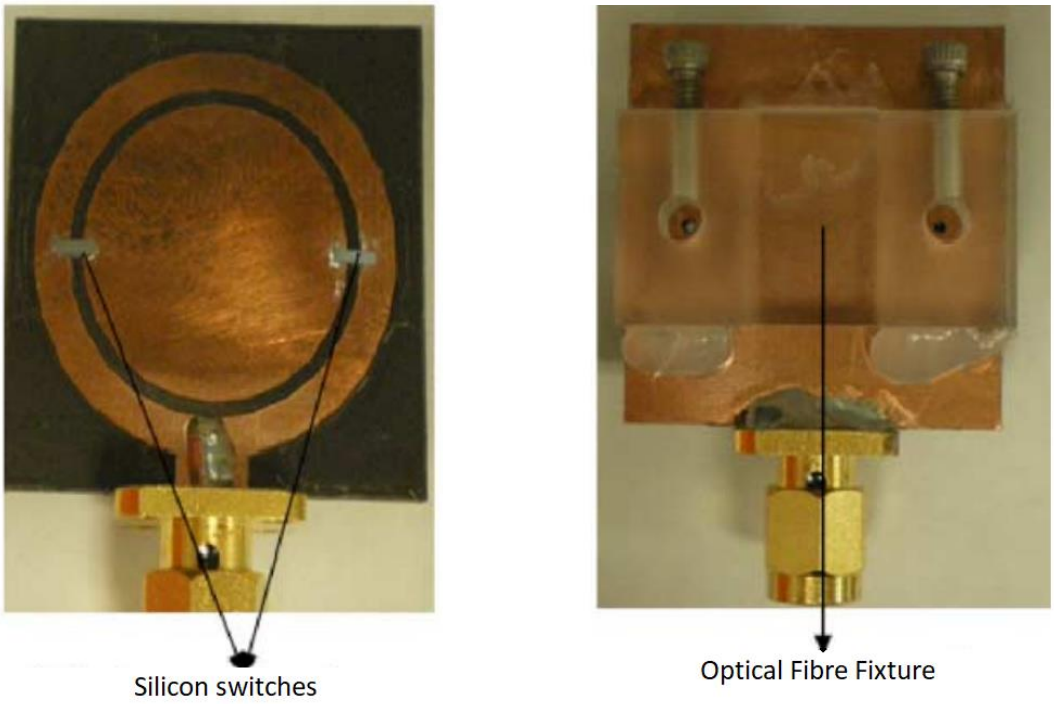

a) b)

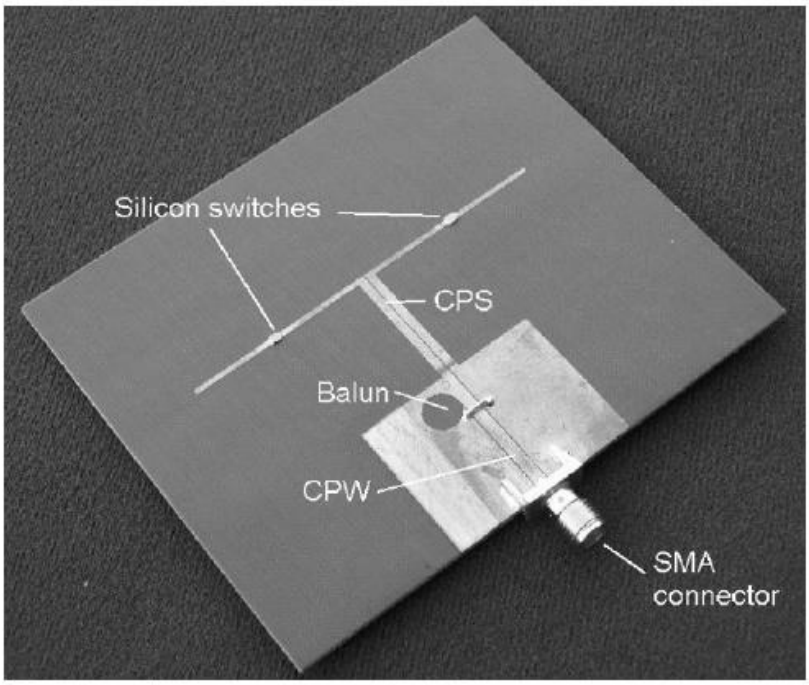

c)

Fig. 2.10. Optically-controlled frequency reconfigurable antenna a) top view showing the silicon switches b) antenna bottom part showing the optical fibre fixtures for illumination c) Optically-switched frequency and beam reconfigurable antenna, reproduced from Panagamuwa and Tawk *et al.* [6, 7].

Another promising work on optically-controlled reconfigurable antennas was demonstrated by Panagamuwa *et al.* [7]. This design is comprised of two Si switches placed on gaps of the dipole arms equidistant from the centre feed (see Fig. 2.10c). During the off-state, the dipole antenna resonates at 3.15 GHz corresponding to a shorter electrical length. When the dipole resonates at longer electrical length, associated with the on-state, the resonant frequency drops to 2.26GHz (see Fig. 2.11a). Additionally, the radiation pattern is tuned between on and off-states of the reconfigurable antenna. The radiation patterns have shown a beam-steer of 12º off boresight when the right switch was on and a beam-steer of 7º when the left switch was on. This asymmetric behaviour of the beam-steer accounted for the asymmetry in the balun and coplanar waveguide ground planes in relation to the dipole arms.

A polarisation reconfigurable antenna was designed by Hansheng Su *et al.* to demonstrate the transition from linearly to circularly polarised radiation using four Si switches. Design of such a tuneable antenna is shown in Fig. 2.12a, where the antenna patch is truncated at its four corners. The corners have been separated from the patch with

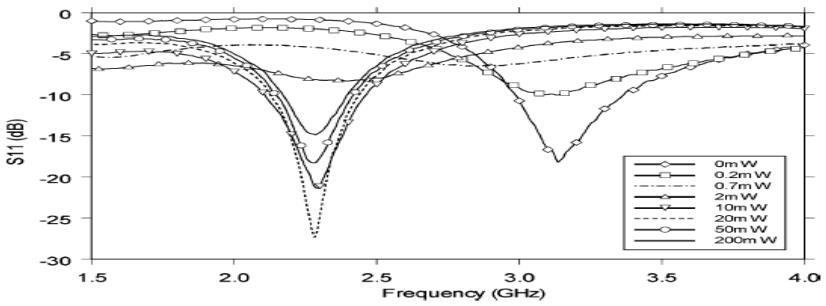

a)

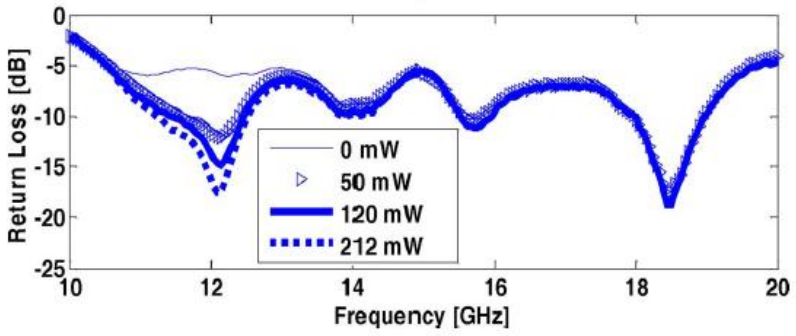

b)

Fig. 2.11. Measured return loss results for a) Optically- controlled frequency reconfigurable antenna shown in Fig. 2.10a. b) Optically-switched frequency and beam reconfigurable antenna shown in Fig. 2.10c, reproduced from Panagamuwa and Tawk *et al.* [6, 7].

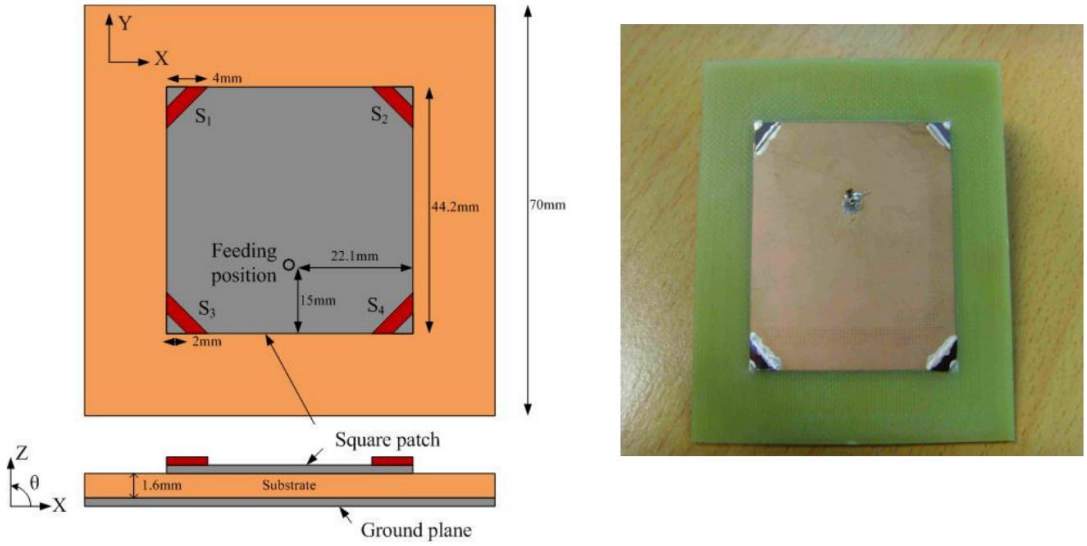

a) b)

Fig. 2.12. Optically-tuned polarisation reconfigurable antenna a) the geometry of the design showing the positioning of the Si switches S_1, S_2, S_3, and S_4 to attain polarisation reconfigurability b) the prototype of the polarisation reconfigurable antenna fabricated on FR-4 substrate and the Si switches attached to the truncated edges of the patch using silver epoxy, reproduced from Su *et al.* [8].

a 1.4 mm gap. Four Si switches are placed in the gap between the corners and the truncated patch. These switches can be turned on and off separately giving rise to 16 different combinations, where the output is either right-hand circular polarisation (RHCP) or left-hand circular polarisation (LHCP), or linear polarisation (LP). Fig. 2.12b shows the positioning of the switches, according to which RHCP is selected when S1 & S4 are on and S2 & S3 are at off-state. Similarly, for LHCP, switches S2 & S3 are kept on, while S1 & S4 are off. For LP, all the switches are either off or on [8].

2.3.2 Tuneable antennas using photosensitive organic semiconductors

Designs of optically-activated antennas using inorganic semiconductors discussed in the previous section are more commonly found in the literature. Most of these antenna designs involve use of Si as the photosensitive material. The first optically-controlled phase-shifter using an organic semiconductor was designed by Tang *et al.* [12]. It was demonstrated that photo-active organic materials could be used as phase-shifters to control the propagation of a signal along a transmission line. Exposure of the photosensitive organic material to light results in a change of permittivity in the lit region. As a result, the change between illuminated and non-illuminated regions results in a change in relative phase at the output.

Furthermore, Sathi *et al.* have demonstrated the use of the organic semiconductor, P3HT, as a radiating patch in a simple patch antenna structure [13, 24]. Although the mobility of carriers in the organic polymers are relatively low compared to their inorganic counterparts, Sathi *et al.* have managed to demonstrate a feasibility test of using such photosensitive organic polymers as the conductor of a patch antenna in the active state. Fig. 2.13 shows the prototype design for the frequency reconfigurable antenna composed of organic semiconducting polymer. High power irradiances from 1 to 8 Wcm^{-2} were used to illuminate the polymer patch using an adjustable white-light source (see Fig. 2.13). However, there were no tests performed on the temperature dependency of the conductivity of the polymer. Such high light intensities, used in this work, are expected to change the conductivity of the material over the temperature range. The efficiency of the fabricated microstrip antenna in the active state was very poor, being about 50%. By comparison the standard patch has an efficiency of circa 97% [24]. This emphasized the fact that the low charge-carrier mobility within the polymers cannot be modelled as a photoconductive material for EM applications, since even with irradiances of 8 Wcm^{-2} in the active state, the efficiency of the antenna is almost half of that of a metallic patch antenna. As a result, in this research, organic semiconductor P3HT has been modelled solely as a low-loss tuneable dielectric. The dielectric loss of this semiconducting polymer is carefully measured and the change in the relative permittivity of the polymer

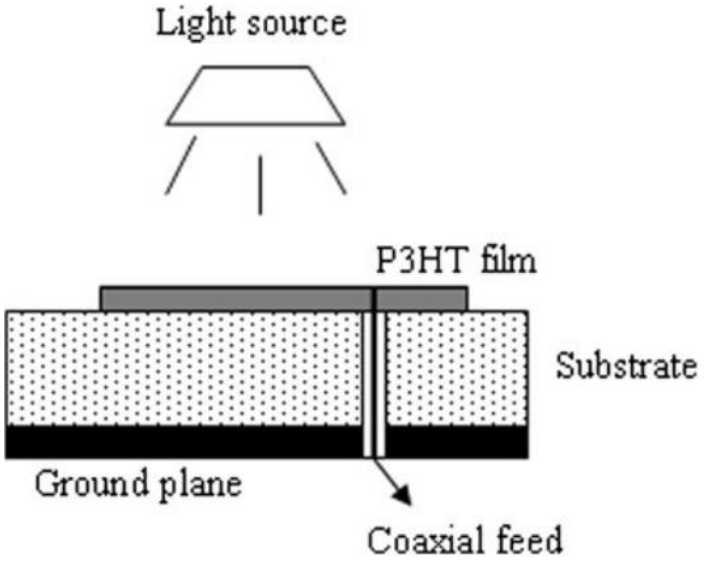

Fig. 2.13. Configuration of the rectangular P3HT antenna, where the antenna is excited using a coaxial line feed. The top layer of the structure is a 100 μm film of poly-3-hexylthione (P3HT) polymer followed by a 1.8 mm Ultralam 2000 substrate and copper ground plane, reproducedfrom Sathi *et al.* [13].

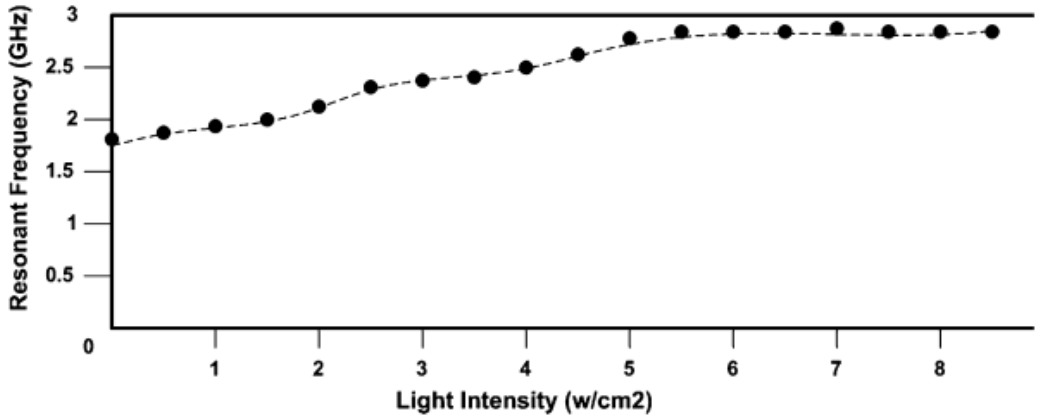

Fig. 2.14. Change in the resonant frequency of the rectangular P3HT antenna due to varied illumination projected from an ordinary white-light projector with tuneable light intensity from 0.5 Wcm^{-2} to 10 Wcm^{-2}, reproduced from Sathi *et al.* [13].

is taken into consideration to manipulate the main beam of an antenna and dielectric lens for beam-steering, beam-shaping and modulating applications. Fig. 2.14 shows the change in the resonant frequency of the reconfigurable antenna upon illumination.

2.4 Dynamic dielectric lenses using photosensitive semiconducting materials

Dynamic operation of mm-wave or THz beams provides improved reliability, speed and flexibility to several EM applications. These applications include imaging, surveillance and remote sensing, and reconfigurable antenna systems [14]. However, these applications require beam controlling devices, and at these frequencies either the performance of the present electronic methods is poor or, the cost of fabricating such devices is very high. One of the most desirable component for any advanced mm-wave or THz circuits and systems is a tuneable quasi-optical (QO) device enabling functions such as wave switching, attenuating, focusing and steering.

Several tuneable lenses for a wide range of applications have been reported in literature [14, 15, 25]. Gallacher *et al.* have demonstrated that by projecting a patterned illumination on a photosensitive flat lens, the incident beam field can be manipulated accordingly. The photosensitive tuneable lens can be used in beam-steering applications, by changing the relative permittivity over the front face of a flat lens. Fig. 2.15a shows the experimental setup for measuring the output of the photo-injected Fresnel zone plate antenna (piFZPA) [14]. The PiFZA is comprised of a 675 μm thick 150 mm diameter high-resistivity Si wafer and the antenna assembly consisted of a 94 GHz Gunn oscillator.

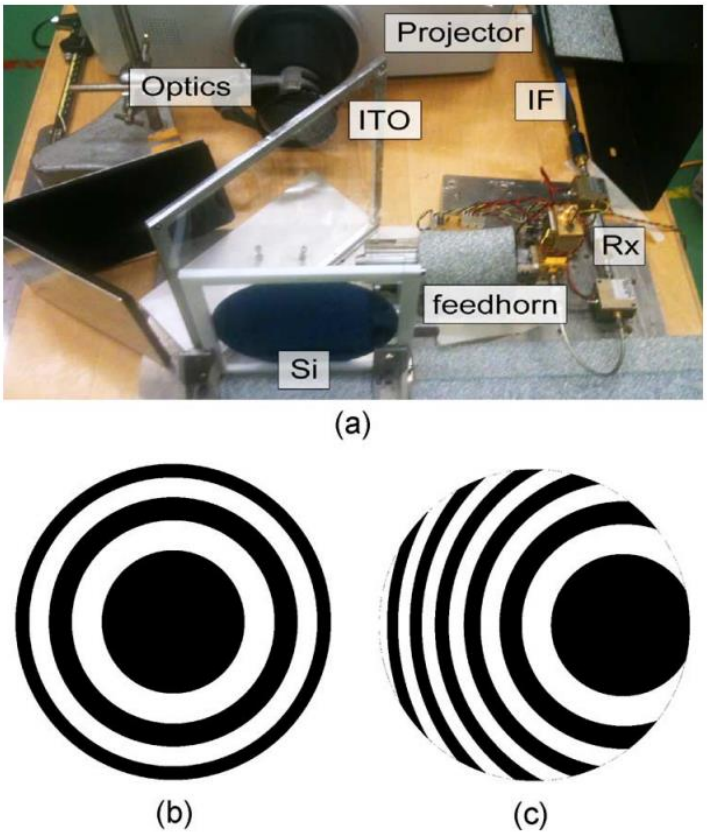

Fig. 2.15. (a) Photograph of the transmission-type photo-injected Fresnel zone plate antenna (piFZPA) configured in receive mode. (b) Example projected Fresnel zone plate mask for beam forming on-axis; and (c) example projected Fresnel zone plate mask for off-axis beam forming at 10º from boresight, reproduced from Gallacher *et al.* [14]

The illuminating pattern was projected using a Sanyo projector using a white-light source of radiance 70 $mWcm^{-2}$ (at λ = 550 nm). Fig. 2.15b, c show the different illuminating patterns projected onto the Si lens face in order to steer the main beam of the antenna off boresight. Changing the illuminating pattern altered the mainlobe of the transmitting antenna assembly, allowing for dynamic beamforming. A beam-steer of 14.5º off boresight using such a setup was reported (see Fig. 2.16).

Similarly, modulation of an EM wave using illuminating reconfigurable patterns on Si flat lenses in the THz frequencies was realised by Cheng *et al.* [15]. They have demonstrated modulation of THz waves by projecting programmable illuminating patterns using a digital light processing (DLP) projector. A photo-induced polarizer, Si wafer, with tuneable polarization angle has been used to demonstrate a cost-effective reconfigurable QO THz component. These photo-active Si wafers have a low insertion

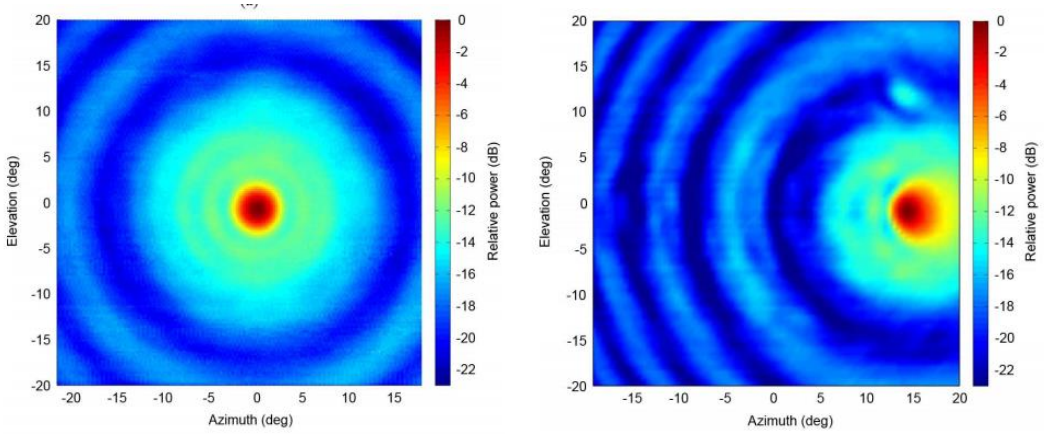

a) b)

Fig. 2.16. (a) Measured farfield antenna radiation pattern of the piFZPA configured in receive mode with (a) the beam pointing on-axis b) the beam steered 14.5º off-axis, reproduced from Gallacher *et al.* [14].

loss at THz frequencies, for which they can be used as tuneable dielectric lenses. The photo-generated electron-hole pair plasma region in the active state of the lens can be used to manipulate incident THz waves (see Fig. 2.17).

Several types of modulations were demonstrated by using patterns such as uniform light with different grey-scale intensities, linear wire-grid with varied orientations, and a 4 × 4 reconfigurable array. The illuminating patterns were generated to implement THz intensity modulation. The experiment was performed using a frequency-domain THz spectrometer with the source being a WR-1.5 horn antenna connected to a series of nonlinear Schottky diode frequency multipliers and the THz detector was a zero-bias Schottky diode and a lens-coupled sinuous antenna for ultra-broadband operation (0.1-1 THz). The THz beam was collimated and focused twice through two sets of off-axis ellipsoidal mirrors before focusing onto the detector. The 200 µm Si flat lens was positioned between the final parabolic mirror and the detector. An indium tin oxide (ITO) plate was positioned at 45º to direct the beam paths of THz wave and photo-excitation light in two different directions, one towards the Si lens plane and the other towards the detector.

A unique imaging technique, coded-aperture imaging (CAI), was used where a single THz detector in combination with a series of N × N coded aperture masks is required for an image with N × N resolution. N^2 measurements were performed and the same number of linear equations are solved to reconstruct the targeted object image. It is reported that this optical modulation mechanism can be applied to generate extremely

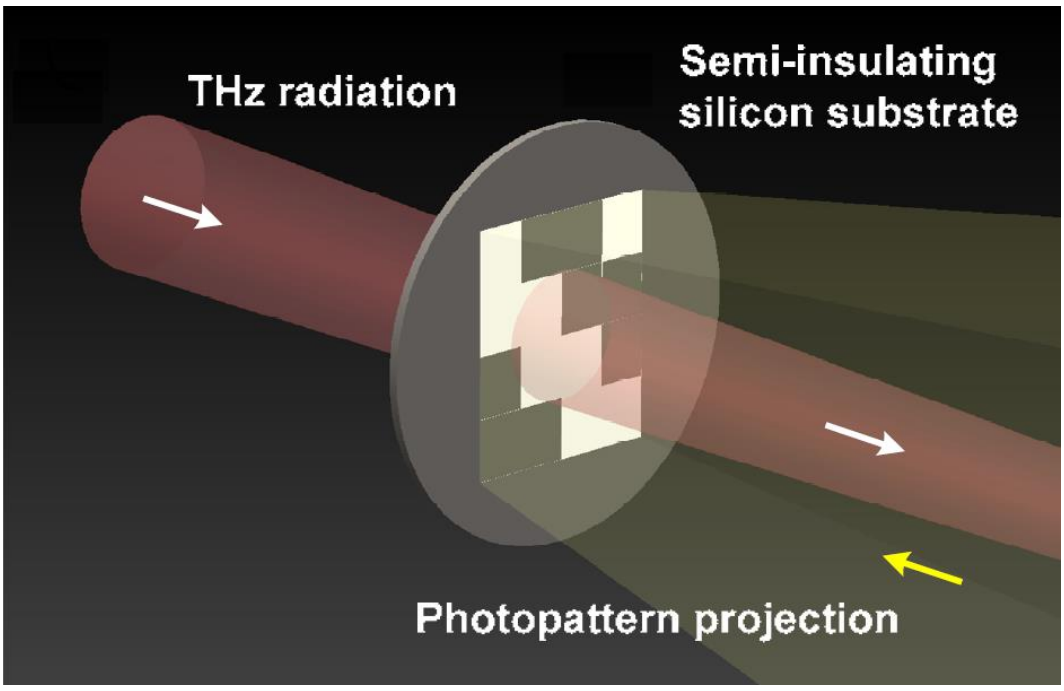

Fig. 2.17. Render of the key component in the proposed system that enables reconfigurable THz modulation. Reconfigurable patterns projected onto the semi-insulating silicon substrate using a digital light processing (DLP) projector generating reconfigurable conductive patterns on the silicon to interact with the incident THz beam, reproduced from Cheng *et al.* [15].

large–scale coded masks (e.g., 1024 × 768, only limited by the resolution of the DLP projector and carrier diffusion lengths in the Si wafer) for CAI without increasing costs further. The authors mention that demonstration of such room temperature CAI using the photo-induced reconfigurable aperture arrays (directly illuminated by a commercial DLP) and a single Schottky diode detector may lead to the realization of compact, low-cost THz cameras for manifold applications.

2.5 Summary

Optically-activated antennas and dielectric lenses are devices that make use of a photosensitive semiconducting material to obtain reconfigurability in the output. The tuning characteristics are derived from the type of tuneable semiconducting material used. These devices can be designed to have controllable characteristics for changing the frequency of operation, steer the main beam or alter the polarisation at the output of the device. Compared to the conventional reconfigurable devices, using electronic or mechanical means of attaining tuneability, optically-activated devices provide better immunity from electromagnetic interference. They are easier to fabricate compared to electronically-reconfigurable devices and are usually light weight and compact.

In the last two decades, inorganic photosensitive semiconductors have been extensively studied and used in EM applications. However, there is always a constant need for flexible materials and ease in device fabrication. As a result, organic semiconductors have been considered as an ideal replacement. Although the use of photosensitive organic semiconductors in the field of electromagnetics has been demonstrated in only a few cases, exploiting their mechanical flexibility in tuneable dielectrics, there remains a scope for further investigation into the material properties of such semiconductors to explore wider EM applications.

References

[1] A. M. Johnson and D. H. Auston, "Microwave Switching by Picosecond Photoconductivity," *IEEE Journal of Quantum Electronics,* vol. Qe11, pp. 283-287, 1975.

[2] D. A. M. Khalil and A. M. E. Safwat, "On the improvement of the performance of the optically controlled microwave switch," *IEEE Transactions on Microwave Theory and Techniques,* vol. 45, pp. 1358-1361, Aug 1997.

[3] W. Platte and B. Sauerer, "Optically Cw-Induced Losses in Semiconductor Coplanar Wave-Guides," *IEEE Transactions on Microwave Theory and Techniques,* vol. 37, pp. 139-149, Jan 1989.

[4] M. El Khaldi, F. Podevin, O. Exshaw, A. Vilcot, and A. M. E. Safwat, "Improvement of performance of optically controlled microstrip phase shifters," *Iet Microwaves Antennas & Propagation,* vol. 1, pp. 427-432, Apr 2007.

[5] J. R. Flemish and R. L. Haupt, "Optimization of a Photonically Controlled Microwave Switch and Attenuator," *IEEE Transactions on Microwave Theory and Techniques,* vol. 58, pp. 2582-2588, Oct 2010.

[6] Y. Tawk, A. R. Albrecht, S. Hemmady, G. Balakrishnan, and C. G. Christodoulou, "Optically Pumped Frequency Reconfigurable Antenna Design," *IEEE Antennas and Wireless Propagation Letters,* vol. 9, pp. 280-283, 2010.

[7] C. J. Panagamuwa, A. Chauraya, and J. C. Vardaxoglou, "Frequency and beam reconfigurable antenna using photoconducting switches," *IEEE Transactions on Antennas and Propagation,* vol. 54, pp. 449-454, Feb 2006.

[8] H. S. Su, I. Shoaib, X. D. Chen, and T. Kreouzis, "Optically Tuned Polarisation Reconfigurable Antenna (Invited)," *2012 IEEE Asia-Pacific Conference on Antennas and Propagation (Apcap),* pp. 265-+, 2012.

[9] Y. Tawk, S. Hemmady, C. G. Christodoulou, J. Costantine, and G. Balakrishnan, "A Cognitive Radio Antenna Design Based on Optically Pumped Reconfigurable Antenna System (OPRAS)," *2011 IEEE International Symposium on Antennas and Propagation (Apsursi)*, pp. 1116-1119, 2011.

[10] I. F. da Costa, S. A. Cerqueira, D. H. Spadoti, L. G. da Silva, J. A. J. Ribeiro, and S. E. Barbin, "Optically Controlled Reconfigurable Antenna Array for mm-Wave Applications," *IEEE Antennas and Wireless Propagation Letters*, vol. 16, pp. 2142-2145, 2017.

[11] M. R. Chaharmir, J. Shaker, M. Cuhaci, and A. R. Sebak, "Novel photonically-controlled reflectarray antenna," *IEEE Transactions on Antennas and Propagation*, vol. 54, pp. 1134-1141, Apr 2006.

[12] H. Y. Tang, R. S. Donnan, and T. Kreouzis, "An optically controlled phase shifter employing the organic semiconductor poly(3-hexylthiophene)," *Applied Physics Letters*, vol. 91, Nov 12 2007.

[13] V. Sathi, N. Ehteshami, and J. Nourinia, "New frequency-reconfigurable microstrip antenna composed of organic semiconductor polymer," *Organic Electronics*, vol. 13, pp. 1192-1196, Jul 2012.

[14] T. F. Gallacher, R. Sondena, D. A. Robertson, and G. M. Smith, "Optical Modulation of Millimeter-Wave Beams Using a Semiconductor Substrate," *IEEE Transactions on Microwave Theory and Techniques*, vol. 60, pp. 2301-2309, Jul 2012.

[15] L. J. Cheng and L. Liu, "Optical modulation of continuous terahertz waves towards cost-effective reconfigurable quasi-optical terahertz components," *Optics Express*, vol. 21, pp. 28657-28667, Nov 18 2013.

[16] S. Lee, Y. Kuga, and R. A. Mullen, "Experimental results for a CW-mode optically controlled microwave switch on a silicon-based coplanar waveguide," *Microwave and Optical Technology Letters*, vol. 36, pp. 257-262, Feb 20 2003.

[17] C. D. Gamlath, D. M. Benton, and M. J. Cryan, "Microwave Properties of an Inhomogeneous Optically Illuminated Plasma in a Microstrip Gap," *IEEE Transactions on Microwave Theory and Techniques*, vol. 63, pp. 374-383, Feb 2015.

[18] P. Alizadeh, A. S. Andy, C. Parini, and K. Z. Rajab, "A Reconfigurable Reflectarray Antenna in Ka-Band Using Optically Excited Silicon," *2016 10th European Conference on Antennas and Propagation (Eucap)*, 2016.

[19] G. Poesen, G. Koers, J. Stiens, G. Carchon, W. De Raedt, and R. Vounckx, "Photo-induced millimeter wave losses in coplanar waveguide on high resistivity silicon," *Microwave and Optical Technology Letters*, vol. 49, pp. 808-810, Apr 2007.

[20] Y. Tawk and C. G. Christodoulou, "A New Reconfigurable Antenna Design for Cognitive Radio," *IEEE Antennas and Wireless Propagation Letters*, vol. 8, pp. 1378-1381, 2009.

[21] H. Su, "Development of optically controlled FSS and antenna using photoconductive approach," PhD Thesis, Queen Mary University of London, London, 2012.

[22] "Computer Simulation Technology," 2017 ed: Dassault Systemes.

[23] G. J. W. J. Reed, "A Method of Analysis of Symmetrical Four-Port Networks," *IRE Transactions on Microwave Theory and Techniques*, vol. 4, 1956.

[24] N. Ehteshami and V. Sathi, "New Optically Controlled Frequency-Agile Microstrip Antenna," *Journal of Electronic Materials*, vol. 42, pp. 162-167, Jan 2013.

[25] S. Busch, B. Scherger, M. Scheller, and M. Koch, "Optically controlled terahertz beam steering and imaging," *Optics Letters*, vol. 37, pp. 1391-1393, Apr 15 2012.

[26] S. V. Hum and J. Perruisseau-Carrier, "Reconfigurable Reflectarrays and Array Lenses for Dynamic Antenna Beam Control: A Review," *IEEE Transactions on Antennas and Propagation*, vol. 62, no. 1, pp. 183-198, Jan. 2014.

Chapter 3 Physical Properties of Optically-Tuneable Photosensitive Semiconducting Materials

In antenna engineering, reconfigurability is defined as the ability of an electromagnetic device to alter its operating characteristics. These characteristics may concern operating frequency, radiation pattern and polarisation. In other words, the definition of reconfigurability originates from the reversible adjustment of the impedance and radiation pattern of an antenna. Reconfigurability in antennas requires use of active loading elements such as PIN or varactor diodes that require several biasing lines accompanied by high biasing voltages [1]. PIN diodes have lower biasing voltage compared to varactor diodes [2]. Microelectromechanical systems (MEMS), have shown better performance compzared to PIN diodes and FET transistors, in terms of switching components in RF circuits, with the advantage of being used for both low and high frequency applications [3].

However, even after considering all the merits involved in using these types of switching elements, the external cabling required for the biasing network to turn the switches on and off causes electromagnetic interference with the radiation of the antenna and hence deteriorates the antenna performance significantly. Optical control, on the other hand, has some inherent advantages over electronic control, such as high isolation between the controlling signal (optical) signal and the controlled (radiating) signal. As a result optically controlled systems provide higher immunity to electromagnetic interference [4]. In addition to the high isolation from electromagnetic coupling between the radiating wave and the switching devices, the switching of these optically driven photoconductive switches is extremely fast and of the orders of nanoseconds. These

switches offer not only electrical, but thermal isolation between the antenna and the control circuitry [5].

Conventionally, most of the optically-controlled antenna designs reported in literature are based on inorganic-semiconductors, such as silicon (Si). In most designs high-resistivity Si is used as a photo-conductive switch to control the RF behaviour of microwave devices and antennas. In this study, organic semiconductors have been introduced in antenna engineering for the first time, following the experiment performed by Tang *et al*. where the use of optically tuneable organic polymer, P3HT, in a phase-shifting device was demonstrated [6]. Organic semiconductors inherently have low mobility [7, 8], hence, the electrical conductivity of the material in the excited state is much lower compared to their inorganic counterparts. Thus, the useful parameter in the excited state of such organic polymers is the real part of the relative permittivity. This is because, in the excited (or active) state the dielectric properties of the material are addressed, which in turn can be used to tune the RF behaviour of the antenna, when used as a substrate of an antenna or lens structure.

3.1 Change in complex permittivity in plasma region of inorganic semiconductors

When energy greater than the band-gap of a semiconducting material is incident on its surface, it generates free carriers known as electron-hole pairs. Optical illumination of suitable wavelength (~3eV) is similarly capable of exciting a photosensitive semiconducting material whose bandgap is lower than the excitation energy. The region so formed due to the absorption of light is referred as the electron-hole plasma region (see Fig. 3.1). The induced electron-hole plasma region spreads throughout the dielectric block. Consequently, this induces a complex permittivity shift in the plasma or active region, which attains a different value of permittivity compared to that of the region left un-illuminated. This phenomenon, in photosensitive inorganic semiconductors can be explained using classical electron-hole plasma theory [9]. The polymer will thus have a complex permittivity in the active region as the following:

$$\varepsilon_r = \varepsilon' - j\varepsilon'' \tag{3.1}$$

where, $\varepsilon'$is the real part of the plasma complex permittivity due to bound charges and ε'' is the imaginary part of the permittivity representing ohmic and frictional losses [10]. Since the electromagnetic fields in this region is described by the Maxwell equations, Ampere's Law may firstly be considered, i.e.

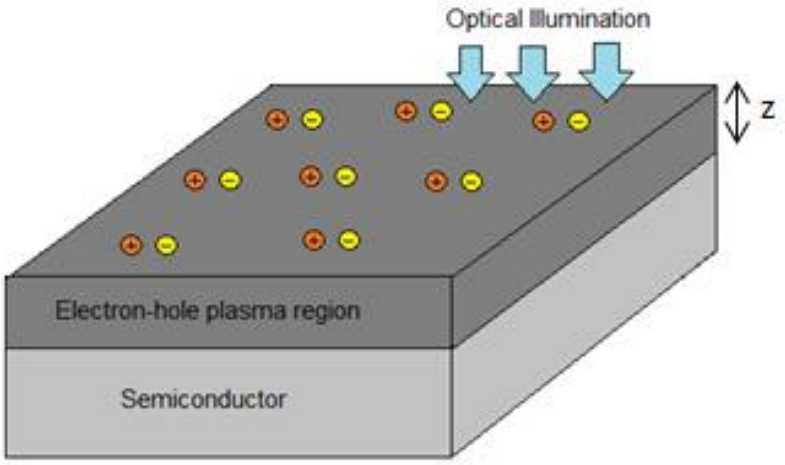

Fig. 3.1. Photo induced electron-hole plasma generated in the semiconducting material, with plasma depth, z, due to absorption of photons, with energy greater than the bandgap of the material, during optical illumination.

$$\nabla \text{ X } \vec{H} = \vec{J} + \frac{\partial \vec{D}}{\partial t} \tag{3.2}$$

Initially, for a lossless semiconducting material without any external field applied, the electrical conductivity is considered to be zero. And the displacement vector can be written as

$$\vec{D} = \varepsilon_o \vec{E} + \vec{P} \tag{3.3}$$

in which ε_o is the permittivity of free space, and $\vec{P}$ is the polarisation. Now using the definition of polarisation, the susceptibility of the material can be expressed in terms of bound and fixed charges.

$$\vec{P} = \varepsilon_o (X_b + X_f)\vec{E} \tag{3.4}$$

where X_b and X_f are the electrical susceptibilities due to bound and free charges, respectively. Substituting Eqn. (3.4) into (3.3) yields:

$$\vec{D} = \varepsilon_o \vec{E} + \varepsilon_o (X_b + X_f)\vec{E} \tag{3.5}$$

where,

$$\vec{D} = \varepsilon_o \varepsilon_r \vec{E}. \tag{3.6}$$

From (3.5) and (3.6) we have

$$\varepsilon_r = 1 + \mathrm{X}_b + \mathrm{X}_f = \varepsilon_L + \mathrm{X}_f \tag{3.7}$$

where, ε_L is the permittivity of the host lattice which represents the contribution of the bound charges. The equation of motion of charge carriers in a semiconducting material is given by

$$m^* \left(\frac{d^2}{dt^2} + \frac{1}{\tau}\frac{d}{dt}\right) \delta\,\vec{r} = -e\vec{\mathrm{E}} \tag{3.8}$$

where τ is the collision time, $\delta\,\vec{r}$ is the spatial displacement and m^* is the effective mass of the charge carrier. The charge of a single electron is denoted by e and the applied electric vector is given by $\vec{\mathrm{E}}$. The polarisation due to free chargers can be written as

$$\overrightarrow{\mathrm{P}_f} = \Delta n e\,\delta\,\vec{r} \tag{3.9}$$

Δn is the carrier density of the plasma region. From (3.8) and (3.9)

$$\overrightarrow{\mathrm{P}_f} = \frac{\Delta n e^2}{m^*}\frac{1}{(-\omega^2 + j\frac{\omega}{\tau})}\vec{\mathrm{E}} = \varepsilon_o \mathrm{X}_f \vec{\mathrm{E}}\,; \tag{3.10}$$

and from (3.7) and (3.10)

$$\varepsilon_r = \varepsilon_L + \frac{\Delta n e^2}{m^* \varepsilon_o (-\omega^2 + j\frac{\omega}{\tau})}\,, \tag{3.11}$$

τ being the collision time related to carrier mobility μ as

$$\tau_e = \frac{\mu_e m_e}{e}, \tau_h = \frac{\mu_h m_h}{e} \tag{3.12}$$

where, m_e and m_h are effective mass of electrons and holes respectively, and $\mu_e$and μ_h are the electron and hole mobilities.

Introducing the plasma frequency given by $\omega_p = \sqrt{\frac{\Delta n e^2}{\varepsilon_o m^*}}$ with the collision frequency given by $v = 1/\tau$, (3.11) can now be written as

$$\varepsilon_r = \varepsilon' - j\varepsilon'' = \varepsilon' - j\frac{\sigma}{\varepsilon_o \omega} = \varepsilon_L - \frac{\omega_p^2}{\omega^2 + v^2} - j\frac{v}{\omega}\frac{\omega_p^2}{\omega^2 + v^2} \tag{3.13}$$

Eqn. 3.13, in terms of τ, can be expressed as

$$\varepsilon_r = \varepsilon_L - \frac{\omega_p^2 \tau^2}{1 + \omega^2 \tau^2} - j\frac{1}{\omega\tau}\frac{\omega_p^2 \tau^2}{1 + \omega^2 \tau^2} \tag{3.14}$$

In general, the collision time of organic and inorganic semiconductors is about $\tau \approx 10^{-13}s$, for which $\omega\tau \ll 1$. Therefore,

$$\varepsilon_r = \varepsilon_L - \omega_p^2\tau^2 - j\left(\frac{\omega_p^2}{\omega}\right)\tau \tag{3.15}$$

If we want to find out the contribution of each type of carriers, equation (3.15) can be written as

$$\varepsilon_r = \varepsilon_L - \omega_p^2\tau_e^2 - \omega_p^2\tau_h^2 - j\left(\frac{\omega_p^2}{\omega}\tau_e + \frac{\omega_p^2}{\omega}\tau_h\right) \tag{3.16}$$

collision time τ is related to carrier mobility μ as

$$\tau_e = \frac{\mu_e m_e}{e}, \tau_h = \frac{\mu_h m_h}{e} \tag{3.17}$$

Hence substituting Equation (2.17) in plasma frequency equation (2.16) we get

$$\varepsilon_r = \varepsilon_L - (m_e\mu_e^2 + m_h\mu_h^2)\frac{\Delta n}{\varepsilon_o} - j\frac{e(\mu_e+\mu_h)\Delta n}{\varepsilon_o\omega} \tag{3.18}$$

where Δn is the density of photo generated carriers, m_e and m_h are effective mass of electrons and holes respectively, and $\mu_e$and μ_h are the electron and hole mobilities.

Equation (3.18) shows the dependence of both real and imaginary part of permittivity of the semiconducting material on the photo-generated carrier density Δn of the plasma region. Photo-induced carrier density Δn of the plasma region on the other hand is proportional to the illumination intensity. Hence we can conclude that with higher orders of illumination intensity, permittivity of a photo-sensitive material can be altered by increasing the charge carrier density of the plasma region. This equation also tells us that permittivity of the material is also proportional to the mobility of electrons μ_e and the mobility of holes μ_h which are considered to be physical properties of the material. Eqn. 3.18 can be modified to formulate an equation that describes the change in permittivity of a semiconducting material, due to external optical illumination, thus

$$\Delta\varepsilon = -(m_e\mu_e^2 + m_h\mu_h^2)\frac{\Delta n}{\varepsilon_o} - j\frac{e(\mu_e+\mu_h)\Delta n}{\varepsilon_o\omega} \tag{3.19}$$

where $\Delta\varepsilon$ is the change in permittivity of the semiconductor due to external optical illumination. The magnitude of the real part of $\Delta\varepsilon$ has a significant effect on the overall permittivity ε_r of the plasma region compared to the imaginary part. This phenomenon

will be graphically explained in detail in Section 3.5. However, for a high mobility semiconductor, like Si, changing the operating RF frequency from microwave to millimetre-wave, increases the imaginary part of the complex permittivity of the material. This accounts for frequency dependent dielectric losses, in terms of conductivity, which results due to the photoconductive effect of these photosensitive semiconductors, as detailed in Section 3.4.

3.2 Plasma depth of optically-tuneable inorganic semiconductors

The plasma region so formed due to excess carrier generation, Δn, depletes exponentially with depth into the semiconductor. The absorption depth of the semiconductor is essentially the depth at which the intensity of the incident energy drops to 1/e of its initial value. However, for inorganic semiconductors, the generated excess carriers recombine from conduction to valence band at one point depending on their carrier life-time. The concept of diffusion is explained as an extended region formed beyond the absorption depth. This length is referred to as the diffusion length, L_n. Using the general equations of continuity and charge neutrality along with equations for generation and recombination rate of the excess charge carriers, we can define change in carrier generation, Δn, in terms of depth, z , which is essentially the depth from the semiconductor surface [11]:

$$\Delta n = \frac{\tau q_e I_0}{hf(L_n + \tau s)}\left\{e^{-z/L_n}\right\} \tag{3.16}$$

where, τ is the recombination time, q_e is a constant representing the combined effect of quantum efficiency and carrier generation efficiency, I_0 is the illumination intensity at the incident surface, hf being the incident energy and s is the surface recombination velocity (typical values in Si-based solar cells for the surface recombination velocity lie in the range of 10^2-10^3 cms^{-1}) [12]. The recombination time is the average time it takes for the excess carriers to recombine, not to be confused with scattering time, which is the average time in which the wave vector is changing (the drift velocity of a carrier is average because of the scattering time). We can therefore express the change in the complex permittivity of the excess carriers as a function of depth, z, by substituting (3.16) into (3.11), thus

$$\Delta\varepsilon = \frac{\tau q_e I_0 e^2}{m^* \varepsilon_o\, hf(L_n+\tau s)(-\omega^2 + j\frac{\omega}{\tau})}\left\{e^{-z/L_n}\right\} \tag{3.17}$$

Eqn. 3.17, relates the complex permittivity to the depth of the plasma region. With the established relation between change in the dielectric constant of a photosensitive semiconducting material and its plasma depth, it is possible to estimate the plasma depth by measuring the change in permittivity of organic samples of different thicknesses. The absorption and depth of the excitation region depends on the optical wavelength and the physical properties of the illuminated substrate. The photo-induced permittivity and conductivity in the excitation region vary with depth.

The theoretical analysis of diffusion of excess carriers has been shown by Jarome et al, which has been used by Avanish *et al*. to establish equations concerning the change in conductivity and permittivity of the plasma region with increase in plasma depth [13, 14]. These equations relating the carrier concentration, real part of dielectric constant and conductivity have been derived from the classical plasma theory as explained in Section 3.1. The change in both conductivity and permittivity of the active plasma region with increase in the substrate depth is depicted in Fig. 3.2. At a certain substrate depth, i.e. the plasma depth of the inorganic semiconductor, the real part of the dielectric constant tends to zero, meaning there is no change in the permittivity after the plasma depth. We see the same trend in the conductivity vs substrate graph, where the conductivity of the active plasma region gradually decreases and becomes zero after the plasma depth. These graphs show the importance of plasma depth, while using them in a modelled EM device such as an optically-activated antenna. In Section 4.1 we try to use the concept of plasma depth to model an active plasma region in an optically-switched transmission line using commercially available electromagnetic modelling software CST Studio Suite.

Additionally, a microstrip parallel-line coupler phase shifter was designed by El-Khladi et al, where an analysis was carried out based on the diffusion-controlled distribution of photoconductivity in the electron-hole plasma region derived from quasi-static analysis by Walter *et al.* [15]. The simulation software, Atlas of Silvaco, has been used to analyse the relation between conductivity in the plasma region and the plasma-penetration depth [16]. In addition a similar analysis of the plasma region using the same simulation software was carried out by J.D. Arnould *et al.* [17]. This time the electron concentration of the plasma region was examined as a function of the depth of the plasma region as shown in Fig. 3.3 b). Both these pieces of work shows that the plasma layer is inhomogeneous and hence requires accurate modelling of the microwave properties of the optically-illuminated plasma.

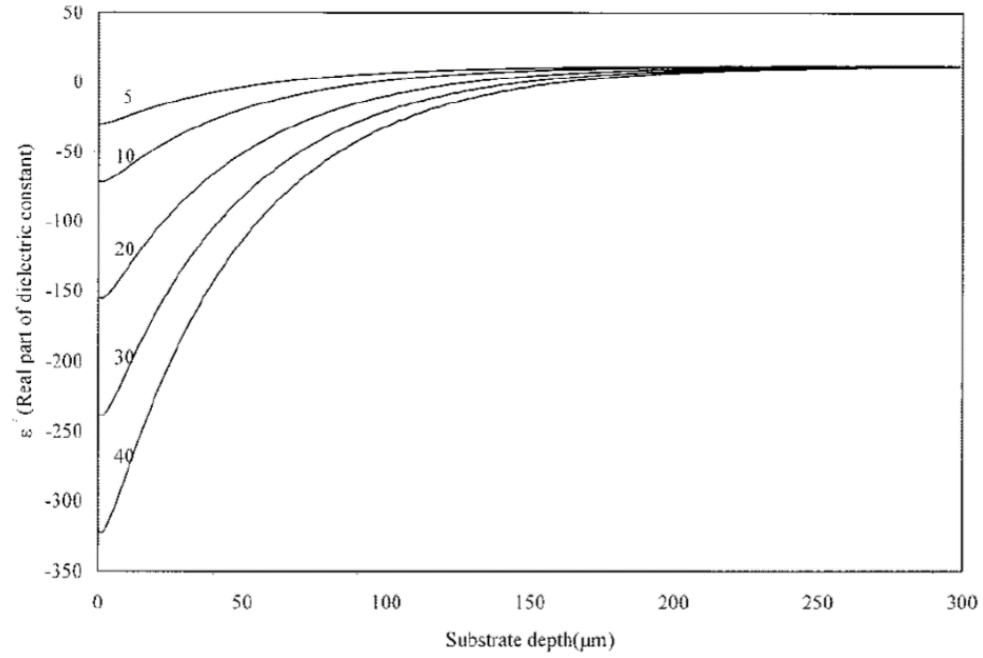

a)

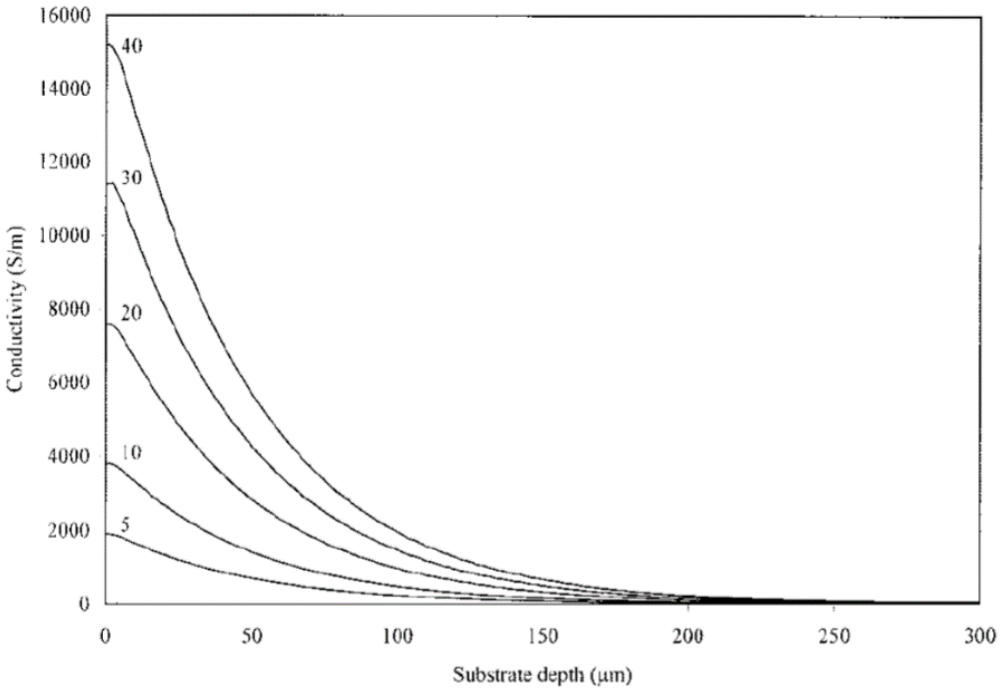

b)

Fig. 3.2. Variation of a) real part of dielectric constant b) conductivity with substrate depth in a silicon substrate illuminated by a lase`q`qr spot of diameter 250 μm at different power levels with frequency of operation 6-8 GHz, reproduced from [13].

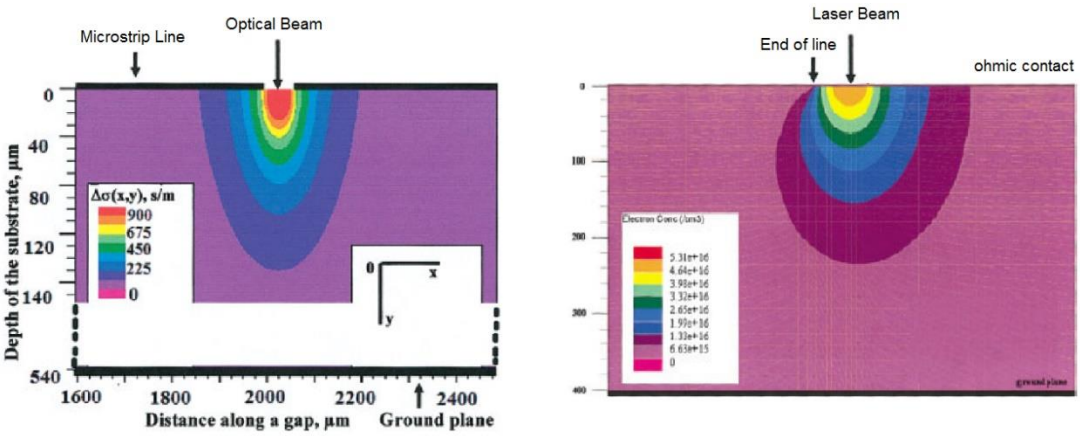

a) b)

Fig. 3.3. a) Silicon conductivity as a function of depth of plasma region under 24 mW irradiance, reproduced from [16] b) Electron concentration as a function of depth of plasma region, reproduced from [17].

3.3 Phase shifting mechanism in optically-tuneable materials

The generation of free carriers in a photo-sensitive material in turn leads to an effective change in the permittivity of the active region as (3.18). The phase velocity of the propagating wave in the plasma region differs from that in non-illuminated areas resulting in a phase lag in the propagation of the wave. This can be described mathematically by (3.19).

$$v_p = \frac{c}{\sqrt{\varepsilon_r \mu_r}} \tag{3.18}$$

where v_p is the phase velocity of the wave propagating in the plasma region; c is the speed of light ~ 3.0×10^8 m/s; ε_r is the permittivity of the plasma region; and, μ_r is the permeability of the plasma region equal to 1.

Now considering a propagating wave in a simple microstrip line structure, we can analyse how the phase of the wave can be altered by looking at the difference in phase between the input and output. The phase in a microstrip structure is dependent on three factors: the magnetic permeability of the dielectric μ_r, electric permittivity of the dielectric ε_r and the length of transmission l. Hence, a ferrite phase-shifter alters the magnetic permeability of the dielectric, μ_r, a PIN diode phase-shifter switches from off to on state to alter the length of the transmission line and the dielectric phase-shifter changes the relative permittivity of the dielectric to achieve the desired phase shift [18].

The phase, ϕ of a propagating wave in a dielectric material with electric permittivity, ε_r and magnetic permeability, $\mu_r = 1$, and length, *l*, of propagation is given by,

$$\phi = kl \tag{3.19}$$

where $k = 2\pi\lambda_r$ is the wavenumber, λ_r is wavelength of the wave in the medium and $\lambda_r = \lambda_0 / \sqrt{\mu_r \varepsilon_r}$. Hence from Eqn. 3.19 it is evident that the phase of a wave propagating in a dielectric medium is dependent on the relative permittivity of that medium. The shift in phase of the propagating wave can therefore be altered by tuning either the permeability or the permittivity of the medium in which the wave is propagating.

3.4 Photoconductivity in optically-tuneable materials

One of the principal aspects of the electronic properties of a semiconductor is the electronic band gap of the material [19]. The concept of a bandgap in a semiconductor can be understood from Fig 3.4. In semiconductors, a gap exists between the conduction and valence bands. In the conduction band, electrons move freely throughout the crystal, and so establish a current. On the other hand, in valence band, electrons are immobile, and hence limit conduction. This is because electrons in the valence band exist in bound electronic states due to molecular bonding of the constituent atoms of the crystal. No electronic states exist in between these bands and the gap between the bands is termed as forbidden or an energy gap region E_g.

The process of photo-generation occurs when a photon is incident on a semiconducting material whose energy is equal to or greater than the bandgap energy of the material. Its energy transfers to an electron promoting it from the valence band to an unoccupied level in the conduction band, creating electron-hole pairs during the process (see Fig. 3.4). In the case where the energy of white light, ranging from 1.8 to 3.1 eV, is sufficient to surpass the bandgap energy of the material that is illuminated, electron-hole pairs will be generated. When external energy *hf*, *h* being Planck's constant [h= 6.63 X 10^{-34} Js], and *f* represents the frequency of the incident photon equal to E_g, then excited electron moves from the valance band to the lowest state of conduction band, whereas when $hf > E_g$, the electron is supplied surplus energy enabling it to move to a higher state in the conduction band. An excess energy (hf- E_g) is dissipated as heat as shown in Fig 3.4 [20]. However, if the external energy is less than bandgap of the material, the photon will not be absorbed, instead will pass through the material.

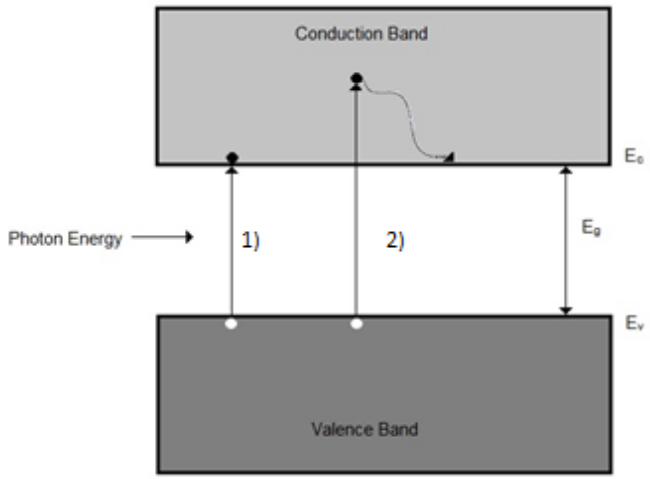

Fig. 3.4. Band diagram of a typical semiconducting material. Two cases shown in the diagram: 1) $hf = E_g$ 2) $hf > E_g$.. Photon energy greater than the band gap of the optically-excited material generates increased numbers of electrons and holes resulting in increased conductivity.

When a photo-sensitive semiconducting material is illuminated using an external optical source that has photon energy $hf > E_g$ of the material, electron-hole pairs are generated leading to an electron current in the conduction band and hole movement in the valence band. This current leads to the photoconductivity of the material. The general expression for conductivity of a material is given as

$$\sigma = e(n_e\mu_e + n_h\mu_h) \tag{3.20}$$

where e is the electronic charge of a carrier; n_e and n_h are the carrier concentrations of electrons and holes, and $\mu_e$and μ_h are the electron and hole mobilities respectively in the material. Mobility could be defined as the motion of charge carriers in the presence of an applied external field. Now photoconductivity could be expressed in terms of excess carriers generated due to external photon energy applied to a semiconducting material as:

$$\Delta\sigma = e(\Delta n_e\mu_e + \Delta n_h\mu_h). \tag{3.21}$$

From the above equation we can now state that the increased conductivity $\Delta\sigma$ is a result of increased charge carriers Δn_e and Δn_h. From (3.21) it is also observed that not only is the photoconducitivity of a material proportional to the charge carrier density but also to its carrier mobilities. The carrier density of the material is in turn dependent on the inherent material properties of the semiconductor as well as the property of the incident excitation electromagnetic wave. These properties include the intensity of light, carrier lifetime of the material (recombination), absorption coefficient and initial carrier concentration.

The most well know semiconductors to be used in photo-conductive devices are inorganic semiconductors. The commonly used inorganic semiconductors include silicon (Si), germanium (Ge), gallium arsenide (GaAs), indium arsenide (InAs), aluminium arsenide (AlAs), and indium phosphate (InP). The primary reason behind choosing inorganic semiconductors in many photo-conductive applications is the high carrier mobility of such elements or compound semiconductors. For instance, the electron mobility of GaAs could reach up to 8500cm^2 V^{-1}s^{-1}, almost a six times higher mobility than that of silicon ($\mu_{silicon} = 1400\text{cm}^2\text{V}^{-1}\text{s}^{-1}$) [21]. High mobility of the material increases the photoconductivity value $\Delta\sigma$ which results in faster operation of a photo-active device.

The choice of a semiconductor for an electronic application is extremely vital. According to the requirements of the operation of an electronic device, the semiconducting material has to be chosen wisely. For instance, an application requiring fast switching speed between on and off states of a photoconductive switch, the device would require GaAs whose carrier mobility is six times that of Si [22]. On the other hand, Si, being an indirect band-gap semiconductor can have a longer carrier lifetime, meaning the recombination process in such semiconductors is longer. This accumulates more carriers in the plasma region for longer periods, assisting in photoconductivity. Thus Si serves as the best option for photoconductive devices requiring a large tuneable range.

In order to understand photoconductivity in a broader perspective, the time a carrier takes to remain in an excited energy state before recombination needs to be considered. The lifetime of carriers in a material is defined as the average time taken by the carriers to recombine once existed to a higher order state. Hence the number of carriers generated n_e and n_h due to external illumination (P_0) in the plasma region can be expressed in terms of electron and hole lifetimes τ_e and τ_h. The maximum number of electrons and holes generated due to illumination (P_0) in one second is given by P_0/hf, where the photon energy (hf) is fully absorbed. At the excited state, the number of generated carriers are estimated by,

$$\Delta n_e = \frac{\tau_e P_o}{hf} \qquad \text{and} \tag{3.22}$$

$$\Delta n_h = \frac{\tau_h P_o}{hf} \tag{3.23}$$

Therefore (3.21) can be re-written as

$$\Delta\sigma = e(\tau_e\mu_e + \tau_h\mu_h)\,{}^{P_o}/_{hf}. \tag{3.24}$$

From (3.24) it is evident that semiconductors with longer carrier lifetimes, correlate with greater photoconductivity. Hence, Si, having a higher carrier lifetime compared to other inorganic semiconductors, along with a high electron mobility of 1400cm^2 V^{-1}s^{-1}, makes it an ideal material to be used in photoconductive switches. Although GaAs has higher carrier mobility compared to Si, the bandgap being direct, cannot restrict recombination once the carriers are excited to a higher state and hence results in a very short carrier lifetime, which decreases the overall photoconductive effect.

3.4 RF properties of optically-tuneable materials

When an optical source of optimum wavelength with illumination energy greater than the bandgap of the semiconducting material is incident on it, the charge carrier density of the material increases [23]. However, the overall effect of the increase in the charge carrier density and the decrease in the mobility of the semiconductor result in an increase in the conductivity of the semiconductor. Additionally, (3.11) and (3.21) show the dependence of the permittivity and conductivity of the semiconducting material on the carrier density and the mobility of the material. This theoretical relation between carrier density of Si at different light intensities and the change in both conductivity and permittivity of the material has been analysed by Tawk *et al.* as shown in Figs. 3.5 and 3.6.

In the mechanism of optical tuning, besides the wavelength of the incident light on the semiconducting material, the intensity of the light source is also an equally significant property for determining the change in the physical processes of the semiconducting material due to illumination. By definition, the irradiance of light, E, over a particular receiving area is defined as the ratio of the power of light to that area. A photon, in general, has an energy E_p equal to $h\nu$; now, the quantum flux ϕ, or photon flux, can be defined as the number of photons. In other words it can be expressed as the ratio of the irradiance of the light source to the energy per photon [$\phi = E/E_p$]. As a result at a given wavelength of light, at higher irradiance, the photon flux is expected to be high or, in other words, a greater number of photons is incident onto the surface of a semiconducting material.

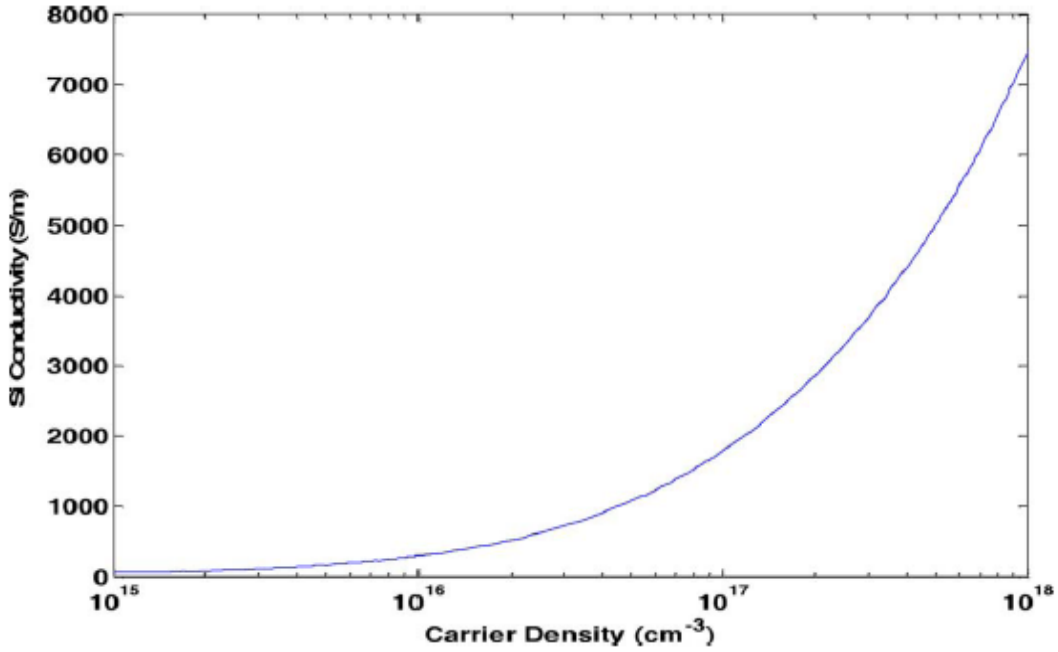

Fig. 3.5. Change in the conductivity of Si with respect to change in the carrier density due to optical illumination at 12 GHz, reproduced from Tawk *et al.* [23].

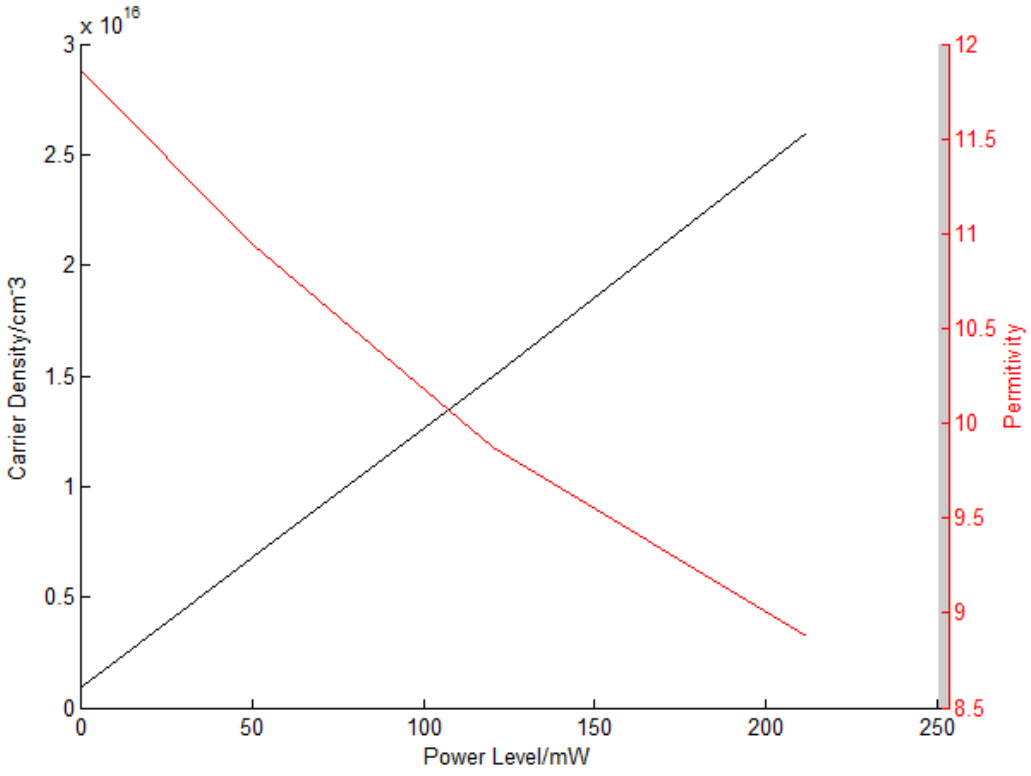

Fig. 3.6. Change in carrier density and permittivity of Si with respect to incident power level at 12 GHz, reproduced from Tawk *et al.* [23].

According to classical electron-hole plasma theory a greater number of photons, when absorbed, gives rise to an increased number of photo-induced carriers. As a result it can be concluded that the irradiance of the incident light source is a useful tuning parameter for altering the tuneability of a photosensitive semiconducting material. However increase in the number of photo-induced carriers reaches saturation at a certain level of irradiance, and remains almost constant throughout the higher levels of optical power. This can be explained using carrier recombination. At lower light intensity, the rate at which carriers are generated and excited to a higher state is much higher than the carrier recombination rate from a higher (conduction band) state back to a lower state (valence band). But as the light intensity increases, the generation and recombination rate becomes almost equal for which there is no further increase in the net number of photo-induced carriers.

3.6 Organic semiconductors as photosensitive materials

Organic polymers currently are the primary means of replacement for inorganic semiconductors. The developments in the optoelectronic properties of such polymers for the past two decades have outweighed the performance of electronics using inorganic semiconductors. Some significant contributions in electronic applications include organic light-emitting diodes (OLEDs), organic field-effect transistors (FETs) and organic photovoltaic cells (OPVs) [24-28]. However, the key to designing high performance optical and electronic devices using organic semiconductors is by understanding the electronic structure of these polymeric materials [29].

Organic semiconductors can be categorized mainly into two classes based on their molecular weight. They are small molecules (molecular weight less than 1000 Da) and polymer molecules with higher molecular weight (typically above 1000 Da) [30]. However, there are also short polymer chain molecules having fixed and defined number of repeating units classified as oligomers which also fall under the group of small molecules. Small molecules, if arranged in highly crystalline films, can form either crystals or polycrystalline films which have lower charge mobilities than their crystalline counterparts [30]. However, they are highly flexible and hence are deployed in organic semiconductor devices. Typical examples of small molecules include aluminium tris(8-

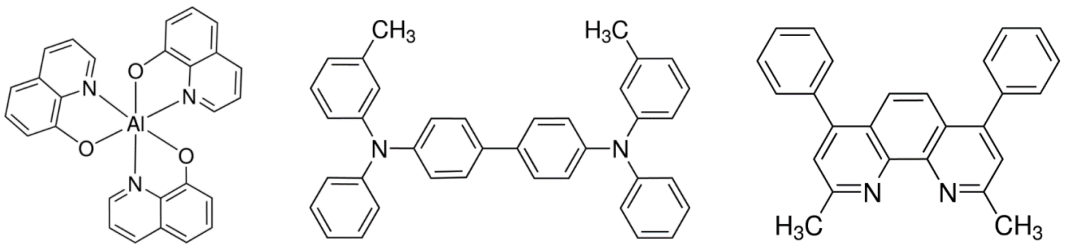

Alq_3 TPD BCP

a)

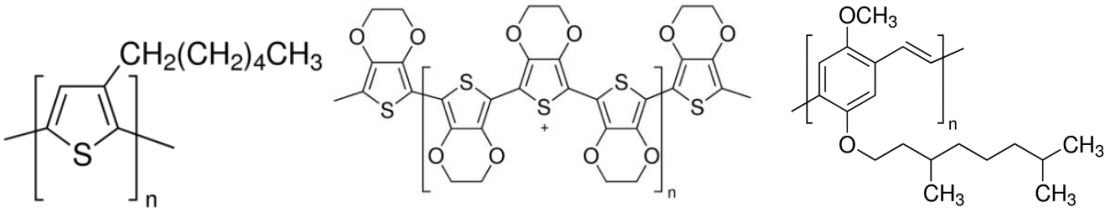

P3HT PEDOT:PSS MDMO-PPV

b)

Fig. 3.7. The chemical structure of organic semiconductors a) small molecule b) polymer

hydroxyquinoline) (Alq_3), N,N'-diphenyl-N,N'-bis(3-methylphenyl)-4,4'-diamine (TPD), and 2,9-dimethyl-4, 7- diphenyl-1, 10-phenanthroline (BCP). Fig. 3.7 a) shows the molecular structures of these small molecules.

Polymer molecules are comprised of a statistically distributed repeating monomer units forming macromolecules. Films of polymer molecules form crystalline or amorphous structures. The bonding between the repeating monomer units allows the polymer molecules to form non-straight chains intertwining with each other in the material. This gives rise to higher associated disorder of the polymer molecules when compared with small molecules. Some common examples of polymer molecules are poly(3-hexylthiophene-2,5-diyl) (P3HT), Poly(3,4-ethylenedioxythiophene)-poly(styrenesulfonate) (PEDOT:PSS), and Poly(2-methoxy-5-(3′,7′-dimethyloctyloxy)-1,4-phenylenevinylene) (MDMO PPV). The chemical structures of these polymers are shown in Fig. 3.7 b).

Organic semiconductors are carbon-based compounds that share similar physical properties to that of an inorganic semiconductor [31]. Unlike the covalently bonded molecules of inorganic semiconductors, the molecules in organic semiconductors are held together by weak van der Waals interactions. Organic semiconductors tend to form the sp^2-hybridisations where the sp^2-orbitals form a triangle within a plane and the pz-orbitals

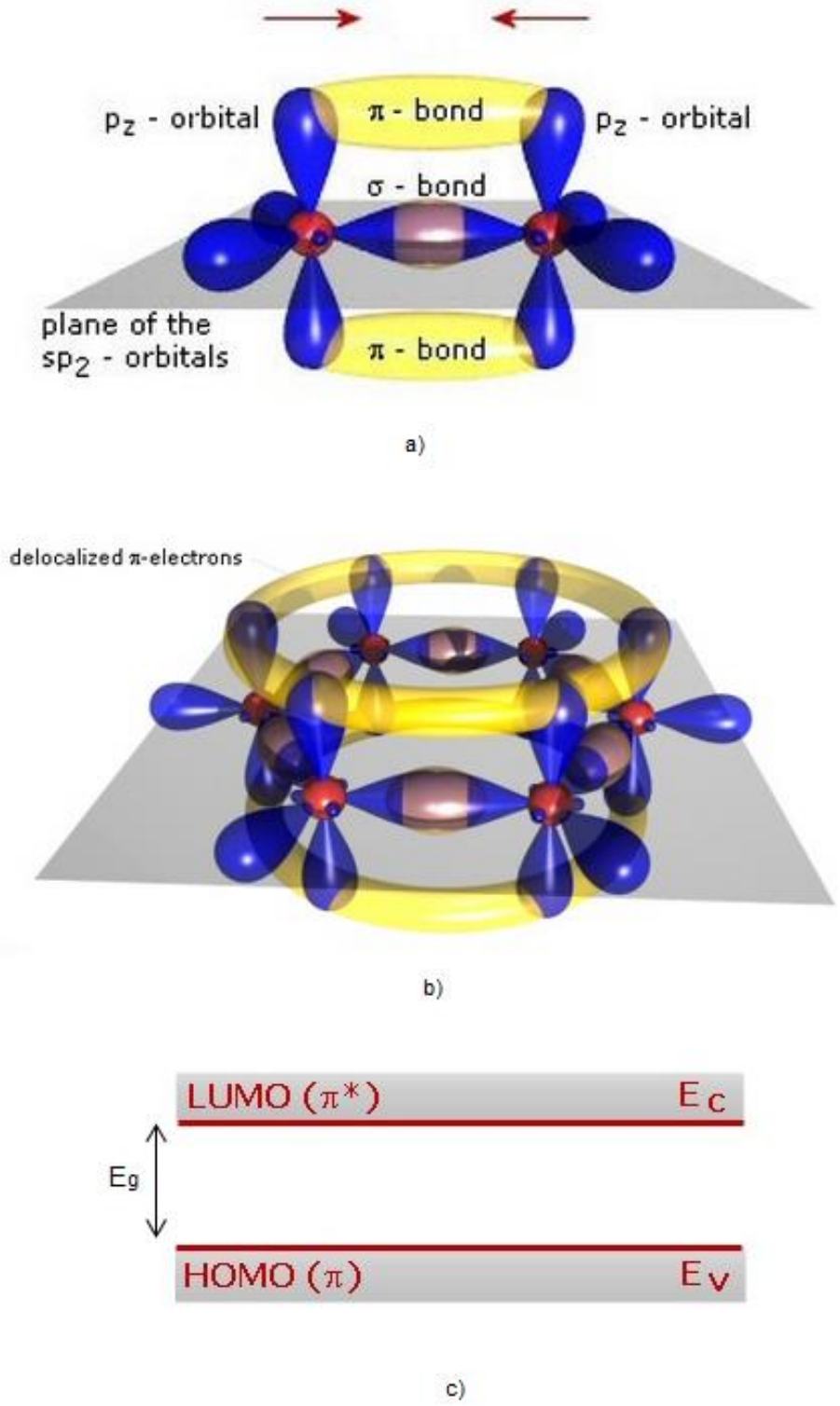

Fig. 3.8. a) Schematic view of π & σ-bonds in sp2 hybrid configuration b) delocalized π-electrons in a benzene ring c) The energy difference between the (π) and (π^*) bonds, is considered as the 'band-gap' of an organic semiconductor, reproduced from [32].

are orthogonal to the plane [32]. The sp^2-hybrid orientation, in these semiconductors, is such that between adjacent carbon atoms the sp^2-hybrid orbitals overlap to form σ-bonds and the pz-orbitals extend to form additional π-bonds with neighbouring molecules as shown in Fig. 3.8 a).

When the carbon atoms form larger molecules, the pz-orbitals tend to undergo continuous overlap causing the π-bonds to become delocalised and form an extended delocalised π-conjugated system, as depicted in Fig. 3.8 b). Now in a carbon-carbon bond, the π-bonds are relatively weaker than σ-bonds and therefore have less excitation energy for the bonding electrons. The highest π-bond orbital that is occupied is referred as HOMO (Highest occupied molecular orbital) and the lowest π* antibonding unoccupied orbital is referred as LUMO (Lowest unoccupied molecular orbital). These bonding and anti-boding orbitals are responsible for the electronic properties of the organic semiconductors. Some organic semiconductors tend to have smaller energy difference between HOMO and LUMO, giving rise to a lower band-gap, which can be of advantage, as it results in high absorption in visible spectral domain. Additionally, the bonding structure gives the organic semiconductors its unique flexibility, light weight and ease of device fabrication.

In organic semiconductors, excitons can be formed from electron-hole pairs with different total spin configurations. If the spins of electron and hole are random the triplet/singlet states will be generated in a ratio of 3:1 respectively. This phenomenon is explained in Fig. 3.9. The electrical excitation leads to 25% of the excitons forming singlets and 75% of the excitons forming triplets. In photovoltaic applications however, where the external energy is delivered in terms of photon energy, photo-induced excitation leads to the formation of singlet excitons only. Since single t excitons are short lived (i.e. the radiative recombination pathway is allowed) only as small fraction will dissociate into free charge carriers. These mobile charges can eventually meet and form singlet and triplet excitons. Due to Pauli's exclusion principle, the excitons which are triplets cannot recombine easily (radiatively) and an excitation region is created in the organic semiconductor.

When an incident photon is absorbed by an organic semiconductor, the photon absorption is characterised by an absorption length of $1/\alpha$ where α is the absorption coefficient. The absorption coefficient can be best described using the Beer-Lambert law, $I = Io\ exp(-\alpha x)$, where Io is the incident irradiance (power per unit area), I is the

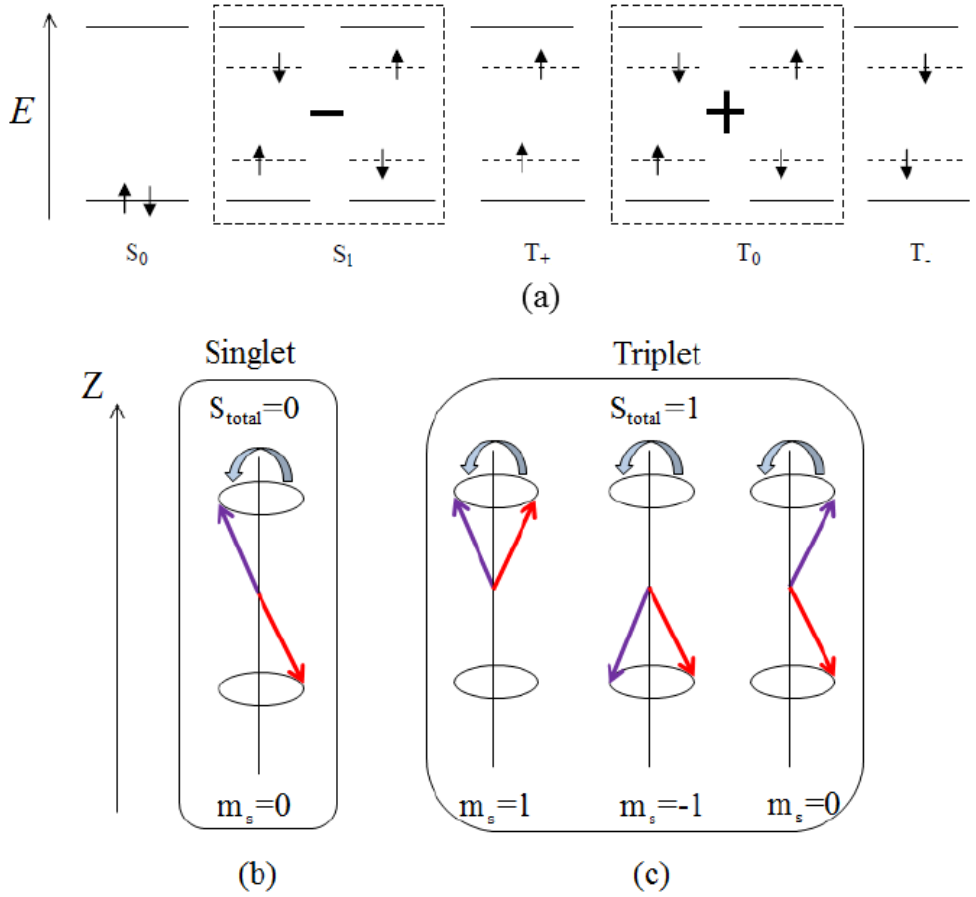

Fig. 3.9. Exciton spin arrangement a) Ground state (S_0), singlet state (S_1), and c) triplet states (T_+, T_-, T_0). The vertical axis in a) represents the energy (E) b) and c) indicate spin momentum and angular momentum of singlet and triplet states. The vertical axis in b) and c) is z-axis along which the B-field is aligned [33].

transmitted irradiance, α is the absorption coefficient in units of reciprocal length, and x is the thickness of the medium. For organic semiconductors, absorption coefficient, α is typically around 104~105 cm^{-1}, which results in an absorption length of at least 100 nm at visible light wavelength range [33].

A conduction electron (or hole) together with its self-induced polarization in a polar semiconductor or an ionic crystal forms a quasiparticle, which is called a polaron. We have already seen that by combining positive and negative excitations a neutral exciton is formed. However, charged excitations in organic semiconductors form positive and negative polarons. These polarons comprise of a charged molecule (positively or negatively) together with the distortion of the molecule compared to the neutral state. This phenomenon is explained in Fig. 3.10. The polaron binding energies (also known as

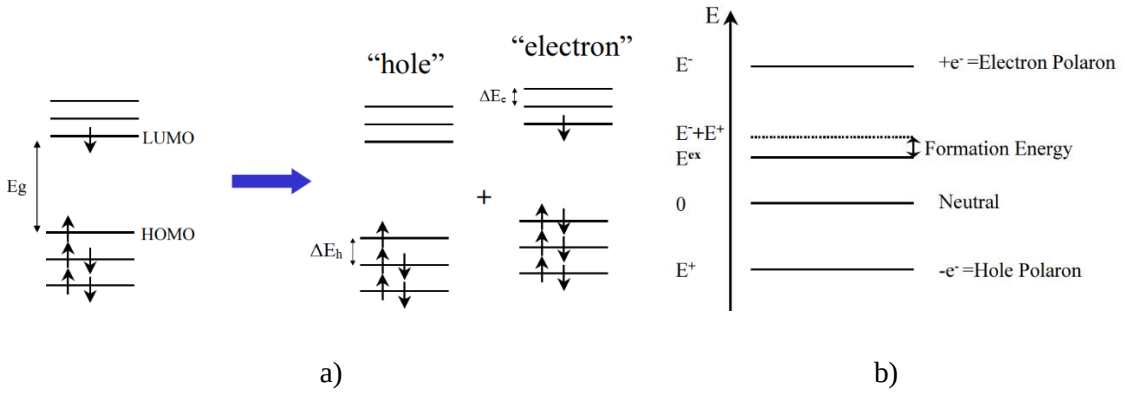

Fig. 3.10. a) Schematic description of the exciton dissociation into positive and negative polarons. b) Schematic description of the energy of a molecule in its neutral state and first positive(hole), negative (electron), and exciton states. The binding (formation) energy is shown as the decrease in the molecule energy after correlating separated electron and hole to form exciton reproduced from [34].

formation energy) ΔE_h and ΔE_e shown in Fig. 3.10 a) can be used to compare the intrachain exciton to an interchain exciton. The interchain exciton consists of two charges residing on different chains but which are still correlated. This is based on the asuumption that the interchain exciton can easily dissociate into non-correlated charge-polarons. Thebinding energy of the interchain exciton is on the order of kT, where k is the Boltzmann constant and T is the temperature. In semiconducting polymers, generally the states are energetically disordered with a width of the density of states, σ. Since the energetic disorder can be greater than the polaron binding energy, we can often ignore the effect of polarons while explaining the charge transport in organic semiconductors. To illustrate this we consider kT at room temperature to be ~ 25 meV, whereas typical energetic disorder parameters for polymers are σ ~ 100 meV.

The charge transport process in organic semiconductors differs from those in inorganic semiconductors. In inorganic semiconductors we know that the charge transport is described as the movement of electrons and holes in the conduction and valence bands respectively. In organic semiconductors, the intermolecular coupling leads to the localisation of neutral and charged excitations. As a result, the elementary transport step between molecules or segments of a conjugated polymer takes place via phonon-assisted hopping. In other words, this thermally activated 'hopping' of carriers take place to overcome the barrier within the disordered conjugated polymer structure allowing carrier transport within the semiconductor. As a result, with an applied bias, via an electric field,

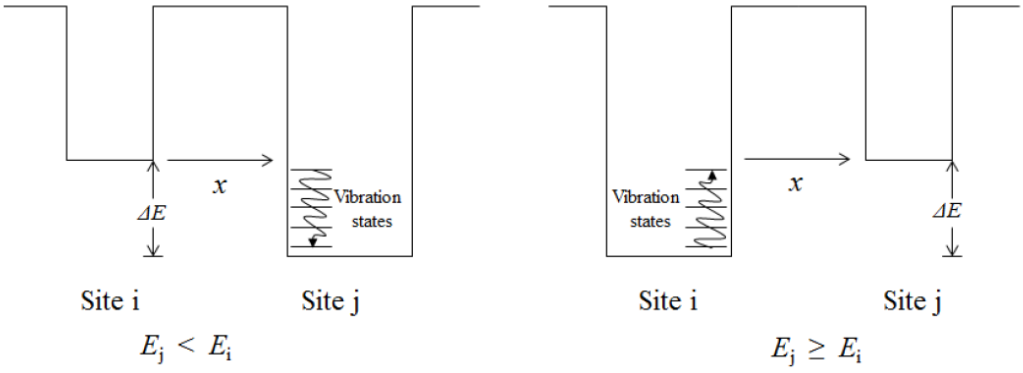

a) b)

Fig. 3.11. Schematic of Miller-Abraham model of hopping transport in organic semiconductors a) $\Delta E = E_j - E_i < 0$ b) $\Delta E = E_j - E_i \geq 0, r$ reproduced from [33]

the probability of the carrier overcoming the barrier increases. Fig. 3.11 describes the hopping process using the Miller-Abraham model. In order to understand the hopping transport in an energetically disordered environment, the hopping rate for an upward jump is accounted as the product of the attempt frequency, the probability for a carrier to get a certain amount of energy E, given by the Boltzmann distribution exp (-E/kT), and the probability to jump over a certain distance x, with the tunnelling factor exp (-2γx) given by:

$$v = v_0 \exp(-2\gamma x) \exp(-\frac{E}{kT}) \tag{3.25}$$

Similarly, for a downward jump, the charge carrier is considered to create a phonon to lose its energy. This is considered to be a reasonable assumption based on the rich phonon spectra of conjugated polymers. The downward jump rate is hence given by:

$$v = \exp(-2\gamma x) \tag{3.26}$$

Combined Miller-Abraham rate for carrier hooping is given by:

$$v_{ij} = \begin{cases} v_0 \exp(-2\gamma x) \exp(-\frac{E}{kT}) & E_{j-}E_i \geq 0 \\ \exp(-2\gamma x) & E_{j-}E_i < 0 \end{cases} \tag{3.27}$$

where, v_0 is the phonon vibration frequency, x is distance between site i and j, γ is the iverse localisation radius, $E_i$and E_j are the energy of site i and j.

The unpaired electron residing in the LUMO of a potential well can be thermally excited to higher vibrational energy levels and then tunnel to either the next higher or

lower energy potential's LUMO or a net current forms in the material. The charge carrier transport can be affected by the trap states, or traps, of the composite films. These traps originate from the structural defects and the impurity of the materials. They provide localised energy minima of variable depth for the charge carrier transport, which reduce the charge carrier mobility [35].

3.7 Organic-heterojunction P3HT: PCBM

Poly(3-hexylthiophene) (P3HT) is an ideal conjugated polymer for polymer-based photovoltaic (PV) cells. It has been reported that P3HT tends to have a higher mobility compared to most commercial organic semiconductors, because it forms a semi-crystalline lamellar structure during spin-casting [36]. Additionally, P3HT has a bandgap of 1.9 eV, suitable for photo-excitation of free carriers from HOMO to LUMO [37]. Furthermore, the carrier density of P3HT has been measured using ZnO nano-wire field-effect transistors coated with P3HT by Choe *et al.* and found to be of the order $10^{17}cm^{-3}$ [38]. Due to the low permittivity of P3HT the dielectric response varies with irradiance. The high drift mobility of induced charge carriers and its optical absorption properties make the semiconductor an appropriate choice as a photo-controlled phase shifter [39]. Although it is powdery in form, it can still be spray coated onto any hard surface when dissolved in organic solvents. Other popular methods of depositing P3HT onto substrates are by drop casting and spin-coating.

Organic semiconductors, when compared to their inorganic counterparts, have low dielectric constant and the localized electron and hole wave functions resulting in a high binding energy (1.0 – 1 .4 eV). In inorganic semiconductors, the binding energy is of the orders of a few meV [40]. As a result, during absorption of photons, there are more free carriers generated in the conduction band in inorganic semiconductors as the electron-hole pairs can dissociate easily. On the other hand organic semiconductors have strongly bound excitons that result in a low dissociation efficiency.

Exciton dissociation in organic semiconductors generates an electron-hole pairs. These electron-hole pairs must be kept separated to ensure free carrier flow in LUMO; in other words, to generate current in the excitation region. But since organic semiconductors generate a high binding energy between electron-hole pairs, it becomes a challenging task to overcome such a barrier. However, the use of two different organic materials with correctly-aligned levels can successfully solve this problem. The junction

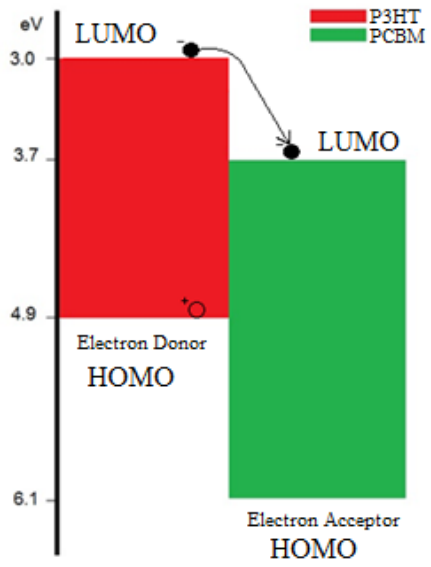

Fig. 3.12. Band alignment of a donor and acceptor system. In this case a heterojunction P3HT:PCBM is shown. In an organic heterojunction system, the excited charge carrier of the donor is trapped by the energy band of the acceptor, restricting the recombination process.

between the two organic materials with different band alignment is known as heterojunction. This is depicted in Fig 3.12 where a blend of P3HT and PCBM ([6, 6]-Phenyl C61 butyric acid methyl ester), is shown, with different band alignments. Organic materials have the tendency to relax from an excited state; additionally, the permittivity of these types of materials is expected to be low, i.e. very few states are expected to undergo dissociation. Hence by adding PCBM, the organic nature of P3HT is distorted and the dissociation of free electrons takes place easily, since the recombination process of an excited electron from conduction to valence band is to somewhat restricted. As a result, the number of photo-generated carriers in the excitation region of a P3HT:PCBM sample is expected to be more in number compared to a pure P3HT sample.

Most organic polymers tend to absorb in the U-V or visible range, depending on the electronic configuration of the material. It is possible to observe the absorption of electromagnetic wave by a photo-sensitive material by investigating the absorption coefficient of a thin film sample of the material under test. Fig. 3.13 shows the absorption spectrum of a 100 nm P3HT film, where a significant absorption is seen almost throughout the whole visible region. This confirms that white light is sufficient for the operation of optically controlled devices using P3HT. Additionally the graph also provides information of the bandgap of P3HT, as we observe the lowest absorption occurs provides at 640 nm, representing a bandgap of 1.93 eV.

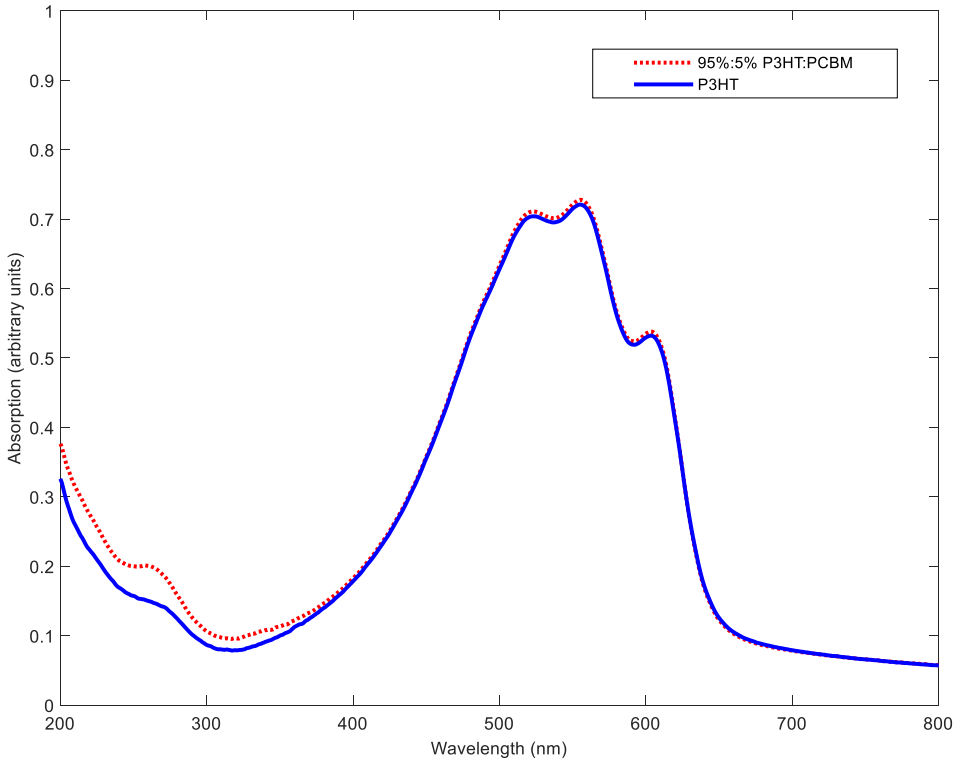

Fig. 3.13. Comparative absorption spectra of pure P3HT and the blend 95%:5% P3HT:PCBM measured using UV-VIS spectrophotometer.

3.8 Estimation of carrier concentration in optically-tuneable organic semiconductors

Photo-generated carriers can be measured in a photosensitive material by collecting electrons and holes at electrodes of an electric field source. When not illuminated, the photocurrent of a photosensitive material under an applied electric field is called the *dark current*. With the material being excited by an electromagnetic wave of appropriate wavelength while the electric field is still acting on it, the extra electron-hole pairs generated due to this excitation can be measured using an ammeter, since the photocurrent across the material is proportional to the number of photo-generated carriers.

According to Ohm's Law, the current density across a material can be expressed in terms of the number of carriers generated, Δn, as

$$J = \Delta n e v_d \tag{3.28}$$

where v_d is the drift velocity and e being the charge of an electron. Now drift velocity can be written in terms of the mobility of the material, μ and the applied electric field, E.

$$v_d = \mu E. \tag{3.29}$$

Assuming a uniform electric field throughout the material, and *d* being the thickness of the material and $\Delta\varphi$ the potential difference between the two electrodes across the thickness of the material.

$$E = \frac{\Delta\varphi}{d} = \frac{V_b}{d}. \tag{3.30}$$

Now expressing the current in terms of current density J and cross-sectional area of the electrodes, A, $I = JA$. Thus, substituting (3.29) and (3.30) into (3.28), we get

$$\Delta n = \frac{Id}{Ae\mu V_b} \tag{3.31}$$

where Δn represents the number of excess carriers due to photo-excitation. During measurements, the initial dark current was recorded for each of the biased voltages used from 0.5 to 3 volts. Table 3.1.shows the tabulated measured photocurrent readings at different light intensities and varied biased voltages.

The mobility of the organic blend is measured using a time-of-flight (ToF) technique on a thick (1.3 µm) device made by spin-coating multiple layers of a mixture of 95% P3HT: 5% PCBM (ITO) dissolved in dichlorobenzene (33 ml/mg) onto previously photolithographed indium tin oxide glass substrates. These substrates are cleaned using an ultrasonic cleaner (see Appendix B). A gold cathode is deposited on top of the organic layer via thermal evaporation. The device is loaded into a vacuum chamber and ToF measurements are carried out under a vacuum of 10^{-4} – 10^{-6} mbar (see Fig. 3.14 a). The ToF measurements included optical illumination by a frequency triple (355 nm)

Table 3.1. Photocurrent detected by the ammeter at different light intensities at varied biased voltages.

Intensity%	**Photocurrent/µA**					
	V_b=0.5V	**V_b =1V**	**V_b =1.5V**	**V_b =2.0V**	**V_b =2.5V**	**V_b =3V**
1	20	31	48	53	88	119
20	48	76	118	153	234	321
50	55	87	128	181	261	387
80	85	133	206	284	421	607
100	215	361	538	796	1219	1609

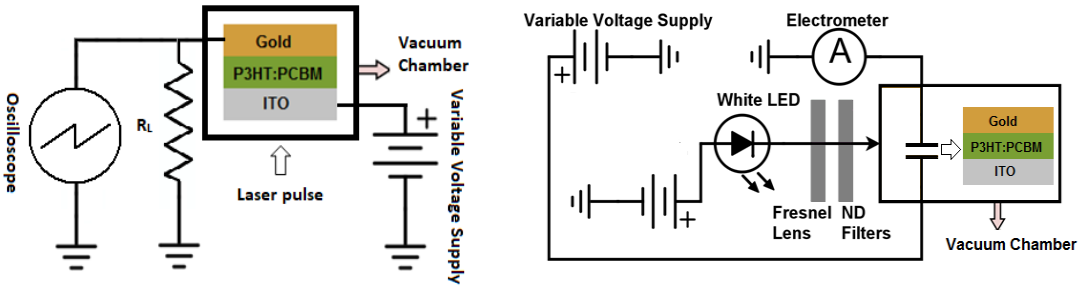

a) b)

Fig. 3.14. a) Carrier mobility measurement carried out using the time-of-flight (ToF) technique where the organic heterojunction (P3HT:PCBM) was illuminated using a BIG SKY Nd:YAG laser b) Schematic diagram of the experimental setup for measuring the carrier concentration of P3HT:PCBM where the photocurrent was measured using an electrometer under varying illumination intensity.

BIG SKY Nd:YAG laser; with the applied bias voltage being supplied via a DC-power supply (0 – 30 V). Fig. 3.15 shows a photocurrent transient time for a 95% P3HT: 5% PCBM device at V = 30 V. The arrival time is determined by the inflection point, $t_{Transit}$, because of the dispersive nature of the photocurrent. The insert shows the relationship of reciprocal of $t_{Transit}$ and the applied bias to determine an average hole mobility of 2×10^{-4} $cm^2V^{-1}s^{-1}$. The measured mobility of the organic blend matches the values reported in literature [41]. The photo-generated carriers in the blend are measured by the steady-state photocurrent through a device, as fabricated for ToF measurements, under DC bias (see Fig. 3.14b). The absorption peak of the organic blend is measured at a wavelength of 500±50 nm.

Consequently, illumination of the device, behind a Fresnel lens, is effected using a LED light source, whose unattenuated intensity, measured using an optical power meter, is 60 $mWcm^{-2}$. The device is kept in vacuum throughout the measurements. The intensity of light is varied using several neutral density (ND) filters allowing partial transmission onto the sample plane. The change in the photocurrent at each of the bias voltages (1.0 to 3.0 V) is recorded by subtracting the measured current from the dark-state current. By Ohm's Law, the current density across the blend is expressed in terms of the number of carriers, Δn, generated due to photo-excitation, and the drift velocity v_d of the carriers.

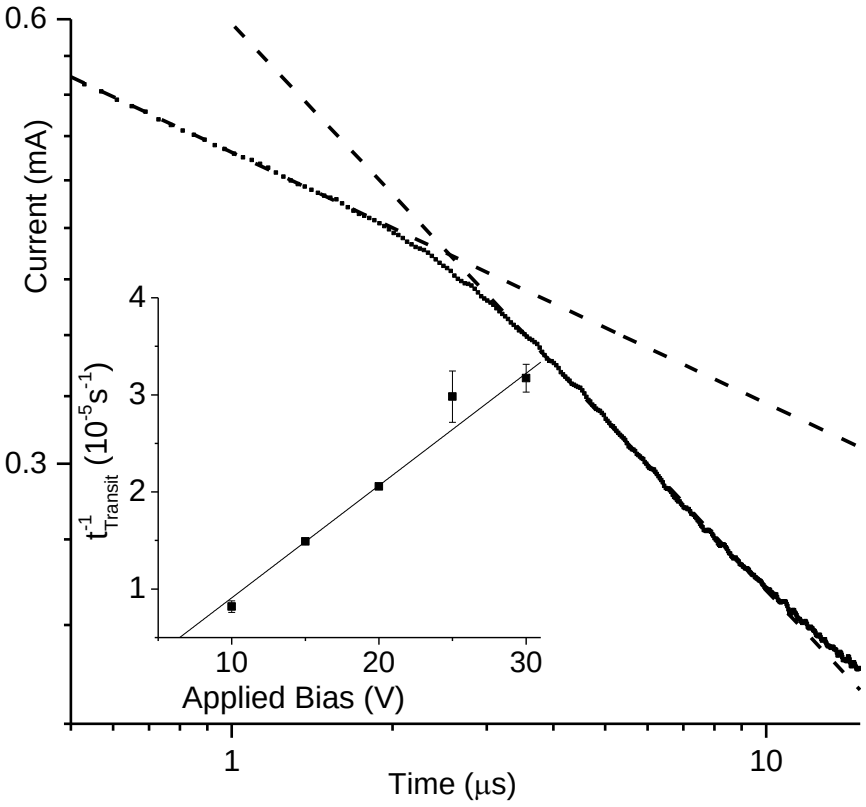

Fig. 3.15. Photocurrent transients of a 95% P3HT: 5% PCBM device of 1.3 μm thickness at V= 30V; Inset shows the inverse transit times scaling with various voltages.

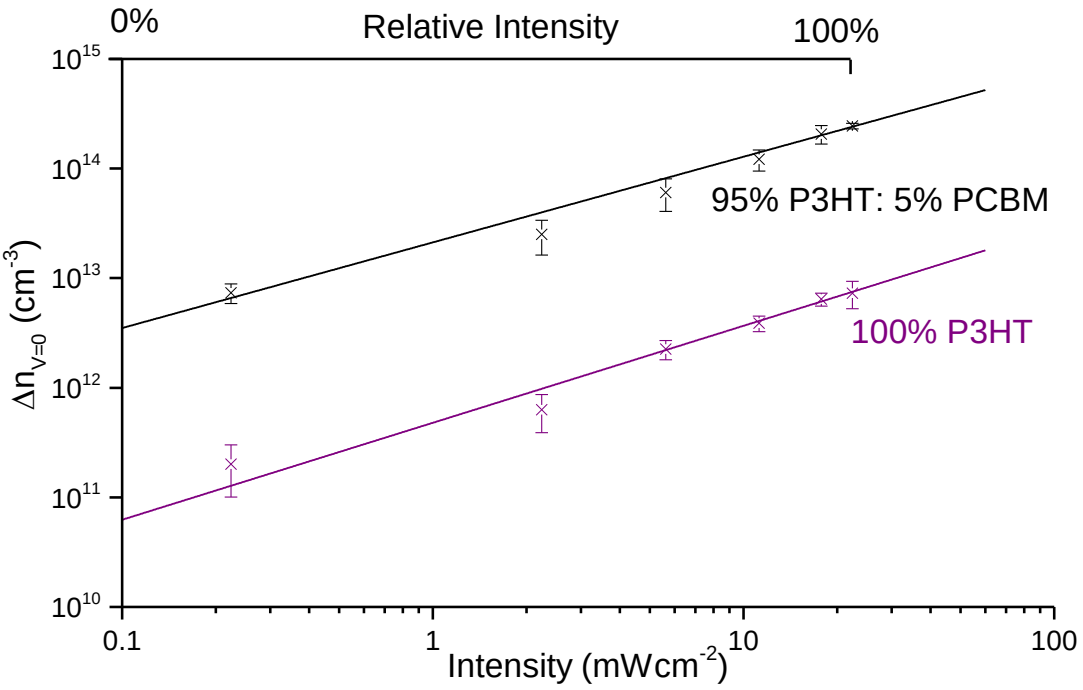

Fig. 3.16**.** Change in carrier concentration (Δn) of the organic polymer due to varying optical illumination at different direct current (DC) biased voltages (1.0 – 3.0 V).

Drift velocity is expressed as the product of the mobility μ (2×10^{-4} cm^2 V^{-1} s^{-1}) and the electric field E. Assuming a uniform electric field distribution throughout the material, with V_b being the potential difference between the electrodes, I the photo-current, and d being the thickness of the material, the number of excess carriers generated (Δn) by photo-excitation is calculated using (3.31).

The steady state photogenerated charge carrier concentrations have been calculated for two different samples under varying illumination and bias conditions and are depicted in Fig. 3.15. Δn for both the organic blend and the pure P3HT is essentially field independent at low bias. We can extrapolate to zero field (in order to make meaningful comparisons with unbiased samples measured and analysed using quasi-opitcal transmissometry and terahertz spectroscopy in Chapter-4) and Fig. 3.15 shows the zero field Δn values obtained for the organic blend and pure P3HT versus light intensity. The inclusion of 5% PCBM in the blend results in an approximately two order of magnitude increase in Δn, irrespective of illumination, compared to P3HT. The lines in Fig. 3.15 represent power laws of approximately 0.88 for P3HT and 0.78 for the blend. Δn values combined with light intensity measurements yield estimates for the photogeneration quantum efficiency of order 10^{-4} in agreement with literature for pure P3HT. Fig. 3.15 yields Δn values at 60 $mWcm^{-2}$ (as used in the QO and THz-TDS) in the range 10^{14} to 10^{15} cm^{-3} in the organic blend by extrapolation. These photogenerated carrier concentrations are lower than those reported in the literature (of order 10^{18} cm^{-3}) for P3HT:PCBM blends, probably due to the reduced electron acceptor content of our blends (5% versus 50%) [42]. Given the low PCBM content and the lack of clear ToF electron transients, we interpret the photoconduction as being hole dominated, with electrons trapped within isolated PCBM regions. The inclusion of 5% PCBM, however, increases Δn compared to pure P3HT.

3.9 Summary

Photosensitive semiconductors are considered as a primary choice for use as tuneable materials in optically-driven reconfigurable devices [43-45]. Semiconductors, stimulated by light with sufficient energy exceeding their band gap initiates change in their optical properties. Hence by manipulating these properties in an electromagnetic (EM) device employing photosensitive semiconductors, reconfigurability in the output of the device can be achieved. Most of these devices mainly use inorganic semiconductors

as means of tuning agents. Inorganic semiconductors, being delicate and brittle, are challenging to incorporate in millimeter-wave devices. In addition, they require high power infra-red illumination source to control the tuneability. As a result, the inflexibility of handling such semiconductors prevents them from being commercial and popular in electromagnetic applications.

Organic semiconductors, on the other hand, offer mechanical flexibility, ease in fabrication, and cost-effectiveness in large scale applications. The primary organic semiconductor chosen in this work is poly(3-hexylthiophene) or, P3HT. In addition, band-gap engineering has been performed, to increase the tuneability of the base polymer, by doping the p-type base polymer, P3HT, with an n-type dopant, phenyl-C61-butyric-acid-methyl ester (PCBM). Measurements of the change in the carrier concentration of the order of 10^{-15} cm^{-3} in the active state of the organic polymer provides sufficient information that there is a measurable change in the dielectric constant of the polymer. Hence, in order to estimate the dielectric changes of the organic polymer a free-space transmission-only measurement technique is considered to be the most appropriate choice. Chapter 4 details on the different measurement techniques used to characterize photosensitive semiconducting materials in microwave, millimeter-wave and terahertz frequencies.

References

[1] D. Patron, K. R. Dandekar, and A. S. Daryoush, "Optical Control of Pattern-Reconfigurable Planar Antennas," *2013 IEEE International Topical Meeting on Microwave Photonics (Mwp)*, pp. 33-36, 2013.

[2] C. Luxey, L. Dussopt, J. L. Le Sonn, and J. M. Laheurte, "Dual-frequency operation of CPW-fed antenna controlled by pin diodes," *Electronics Letters*, vol. 36, pp. 2-3, Jan 6 2000.

[3] D. E. Anagnostou, G. Z. Zheng, M. T. Chryssomallis, J. C. Lyke, G. E. Ponchak, J. Papapolymerou, *et al.*, "Designg fabrication, and measurements of an RF-MEMS-based self-similar reconfigurable antenna," *IEEE Transactions on Antennas and Propagation*, vol. 54, pp. 422-432, Feb 2006.

[4] A. J. Seeds and A. A. A. Desalles, "Optical Control of Microwave Semiconductor-Devices," *IEEE Transactions on Microwave Theory and Techniques*, vol. 38, pp. 577-585, May 1990.

[5] C. J. Panagamuwa, A. Chauraya, and J. C. Vardaxoglou, "Frequency and beam reconfigurable antenna using photoconducting switches," *IEEE Transactions on Antennas and Propagation,* vol. 54, pp. 449-454, Feb 2006.

[6] H. Y. Tang, R. S. Donnan, and T. Kreouzis, "An optically controlled phase shifter employing the organic semiconductor poly(3-hexylthiophene)," *Applied Physics Letters,* vol. 91, Nov 12 2007.

[7] M. M. Mandoc, L. J. A. Koster, and P. W. M. Blom, "Optimum charge carrier mobility in organic solar cells," *Applied Physics Letters,* vol. 90, Mar 26 2007.

[8] S. Tiwari and N. C. Greenham, "Charge mobility measurement techniques in organic semiconductors," *Optical and Quantum Electronics,* vol. 41, pp. 69-89, Jan 2009.

[9] C. H. Lee, P. S. Mak, and A. P. Defonzo, "Optical Control of Millimeter-Wave Propagation in Dielectric Wave-Guides," *IEEE Journal of Quantum Electronics,* vol. 16, pp. 277-288, 1980.

[10] U. S. Inan, *Numerical Electromagnetics: The FDTD Method.* , 1st Edition ed.: Cambridge University Press, 2011.

[11] C. D. Gamlath, D. M. Benton, and M. J. Cryan, "Microwave Properties of an Inhomogeneous Optically Illuminated Plasma in a Microstrip Gap," *IEEE Transactions on Microwave Theory and Techniques,* vol. 63, pp. 374-383, Feb 2015.

[12] F. A. Lindholm, J. J. Liou, A. Neugroschel, and T. W. Jung, "Determination of Lifetime and Surface Recombination Velocity of P-N-Junction Solar-Cells and Diodes by Observing Transients," *IEEE Transactions on Electron Devices*, vol. 34, pp. 277-285, Feb 1987.

[13] A. Bhadauria, Nasimuddin, A. K. Verma, E. K. Sharma, and B. R. Singh, "Optically controlled microstrip load and stub on silicon substrate," *Microwave and Optical Technology Letters,* vol. 39, pp. 271-276, Nov 20 2003.

[14] J. K. Butler, T. F. Wu, and M. W. Scott, "Nonuniform Layer Model of a Millimeter-Wave Phase-Shifter - Reply," *IEEE Transactions on Microwave Theory and Techniques,* vol. 34, pp. 1226-1227, Nov 1986.

[15] W. Platte and B. Sauerer, "Optically Cw-Induced Losses in Semiconductor Coplanar Wave-Guides," *IEEE Transactions on Microwave Theory and Techniques,* vol. 37, pp. 139-149, Jan 1989.

[16] M. El Khaldi, F. Podevin, and A. Vilcot, "Microstrip parallel-line coupler to perform broadband optically controlled phase-shifting," *Microwave and Optical Technology Letters,* vol. 47, pp. 570-573, Dec 20 2005.

[17] J. D. Arnould, R. Gary, and A. Vilcot, "3d photo-induced load modeling for optically controlled microwave microstrip line," *Microwave and Optical Technology Letters,* vol. 40, pp. 356-359, Mar 5 2004.

[18] D. C. Chang, B. H. Zeng, and J. C. Liu, "Mechanical Adjustable Phase Shifters for WiMAX BTS Antenna," *Apmc: 2008 Asia Pacific Microwave Conference (Apmc 2008), Vols 1-5,* pp. 995-998, 2008.

[19] T. Jenkins, *Semiconductor Science Growth and Characterization Techniques*: Prentice Hall, 1995.

[20] R. H. Bube, *Photoconductivity of Solids*: John Wiley & Sons, 1960.

[21] D. V. Morgan and M. J. Howes, *Gallium Arsenide: Material Devices and Circuits*. Chichester: Wiley, 1985.

[22] K. Ma, R. Urata, D. A. B. Miller, and J. S. Harris, "Low-temperature growth of GaAs on Si used for ultrafast photoconductive switches," *IEEE Journal of Quantum Electronics,* vol. 40, pp. 800-804, Jun 2004.

[23] Y. Tawk, A. R. Albrecht, S. Hemmady, G. Balakrishnan, and C. G. Christodoulou, "Optically Pumped Frequency Reconfigurable Antenna Design," *IEEE Antennas and Wireless Propagation Letters,* vol. 9, pp. 280-283, 2010.

[24] T. Wakimoto, H. Ochi, S. Kawami, H. Ohata, K. Nagayama, R. Murayama*, et al.*, "Dot-matrix display using organic light-emitting diodes," *Journal of the Society for Information Display,* vol. 5, pp. 235-240, 1997.

[25] S. E. Shaheen, R. Radspinner, N. Peyghambarian, and G. E. Jabbour, "Fabrication of bulk heterojunction plastic solar cells by screen printing," *Applied Physics Letters,* vol. 79, pp. 2996-2998, Oct 29 2001.

[26] D. Hertel and H. Bassler, "Photoconduction in amorphous organic solids," *Chemphyschem,* vol. 9, pp. 666-688, Apr 4 2008.

[27] J. L. Yang, D. H. Yan, and T. S. Jones, "Molecular Template Growth and Its Applications in Organic Electronics and Optoelectronics," *Chemical Reviews,* vol. 115, pp. 5570-5603, Jun 10 2015.

[28] O. Ostroverkhova, "Organic Optoelectronic Materials: Mechanisms and Applications," *Chemical Reviews,* vol. 116, pp. 13279-13412, Nov 23 2016.

[29] R. H. Friend, R. W. Gymer, A. B. Holmes, J. H. Burroughes, R. N. Marks, C. Taliani, *et al.*, "Electroluminescence in conjugated polymers," *Nature*, vol. 397, pp. 121-128, Jan 14 1999.

[30] H. E. Katz, Z. Boa and S. L. Gilat," Synthetic chemistry for ultrapure, processable, and high-mobility organic transistor semiconductors," Accounts of Chemical Research, vol.34, pp.359-369, 2001

[31] G. Horowitz, "Organic Semiconductors for New Electronic Devices," *Advanced Materials*, vol. 2, pp. 287-292, Jun-Jul 1990.

[32] *Dresden Integrated Center for Applied Physics and Photonic Materials*. Available: https://www.iapp.de/orgworld.de/?Basics:What_are_organic_semiconductors

[33] Hang Gu, "Magnetoresistance and Doping Effects in Conjugated Polymer-Based Organic Light Emitting Diodes", *PhD Thesis*, Queen Mary University of London. 2015.

[34] EE Dept. Technion -2000 [Online]. Available: http://webee.technion.ac.il/orgelect/Graduate_Files/charge_excitation.pdf

[35] P. Peumans, S. Uchida and S. R. Forrest , " Efficient bulk heterojunction photovoltaic cells using small-molecular-weight organic thin films", *Nature*, vol. 425, pp. 158-162, Sep 2003.

[36] K. M. Coakley, B. S. Srinivasan, J. M. Ziebarth, C. Goh, Y. X. Liu, and M. D. McGehee, "Enhanced hole mobility in regioregular polythiophene infiltrated in straight nanopores," *Advanced Functional Materials*, vol. 15, pp. 1927-1932, Dec 2005.

[37] R. D. McCullough, P. C. Ewbank, and T. A. Skotheim, *Handbook of Conducting Polymers*. New York: Marcel Dekker, 1998.

[38] M. Choe, B. H. Lee, W. Park, J. W. Kang, S. Jeong, K. Cho, *et al.*, "Characteristics of light-induced electron transport from P3HT to ZnO-nanowire field-effect transistors," *Applied Physics Letters*, vol. 103, Nov 25 2013.

[39] S. A. Choulis, Y. Kim, J. Nelson, D. D. C. Bradley, M. Giles, M. Shkunov, *et al.*, "High ambipolar and balanced carrier mobility in regioregular poly(3-hexylthiophene)," *Applied Physics Letters*, vol. 85, pp. 3890-3892, Oct 25 2004.

[40] A. C. Mayer, S. R. Scully, B. E. Hardin, M. W. Rowell, and M. D. McGehee, "Polymer-based solar cells," *Materials Today*, vol. 10, pp. 28-33, Nov 2007.

[41] S. Barard, M. Heeney, L. Chen, M. Colle, M. Shkunov, I. McCulloch, *et al.*, "Separate charge transport pathways determined by the time of flight method in bimodal polytriarylamine," *Journal of Applied Physics*, vol. 105, Jan 1 2009.

[42] A. D. Chepelianskii, J. P. Wang, and R. H. Friend, "Low-Temperature Transport Properties of Photogenerated Charges in Organic Materials," *Physical Review Letters*, vol. 112, Mar 26 2014.

[43] T. F. Gallacher, D. A. Robertson, and G. M. Smith, "The Photo-Injected Fresnel Zone Plate Antenna: Optoelectronic Beam Steering at mm-Wave Frequencies," *IEEE Transactions on Antennas and Propagation*, vol. 61, pp. 1688-1696, Apr 2013.

[44] R. S. R. Ribeiro, P. Dahal, A. Guerreiro, P. Jorge, and J. Viegas, "Optical fibers as beam shapers: from Gaussian beams to optical vortices," *Optics Letters*, vol. 41, pp. 2137-2140, May 15 2016.

[45] A. Karvounis, B. Gholipour, K. F. MacDonald, and N. I. Zheludev, "All-dielectric phase-change reconfigurable metasurface," *Applied Physics Letters*, vol. 109, Aug 1 2016.

Chapter 4 Characterisation of Photosensitive Semiconducting Materials Using Electromagnetic Transmission-Only Techniques

Tuneable materials play an essential role in controlling the functionality of an electromagnetic device. By adjusting the frequency, radiation pattern and polarisation of the device, it can serve multi-purpose applications. Tuneable materials such as photo-sensitive semiconductors, liquid crystals, ferro-electric materials, and graphene, are commonly used to tune characteristics of microwave devices [1]. In order to effectively use the physical properties of these tuneable materials in an antenna or lens structure, characterisation of the material is required to ascertain parameters such as the permittivity, permeability, and the tangent loss of the material. In addition, it is necessary to characterise the material at the frequency in which the device is operating. Hence, during antenna modelling using a suitable simulation tool such as CST [2], computational analysis is expected to be very accurate and close to measured results since the precise physical property of the material is used.

There are several methods for measuring the electrical or magnetic characteristics of materials using electromagnetic techniques. Several methods have been developed in time- or frequency-domain, where the techniques are restricted to constraints such as material thickness, single resonant frequency and systematic error due to temperature, pressure or vibration. The most well-known Vector Network Analyser (VNA)-driven techniques established for measuring material properties are based on transmission line methods; the open ended coaxial probe, free-space propagation; or, resonant cavity techniques [3]. The complex reflection and transmission coefficients measured using these techniques are then post-processed with known parameter extraction techniques to

convert from raw s-parameter to material dielectric properties. These techniques can be summarised as follows: the Nicolson-Ross-Weir technique, the NIST iterative technique, the new non-iterative technique, and the short circuit line technique.

One of the biggest challenges that exists in the characterisation of semiconducting materials is to accurately estimate the material properties of thin films. Thin films ranging from microns to nanometres in thickness often demand the use of high frequency electromagnetic characterisation techniques, to precisely determine optical constants [4, 5]. This is because at higher frequencies, the wavelength of the electromagnetic wave becomes comparable to the thickness of the samples under test. This results in the need for more physically accurate formulations of materials in order for their electromagnetic properties to be estimated. However, in the case of photosensitive semiconducting materials, characterising them in both the dark (without illumination) and active (with illumination) states is challenging, even when using a free-space electromagnetic material characterisation technique. This is because characterisation of photosensitive semiconducting materials requires a provision for illumination to estimate its active state physical properties. In this chapter several different techniques, both free-space and non-free-space, for material characterisation of photosensitive semiconducting materials shall be discussed in detail.

Several measurement techniques for characterising photosensitive inorganic semiconductors involving a microstrip line device, have been reported in the literature over the last two decades and relevant applications in antenna and microwave engineering proposed [6-8]. However, with the emergence of organic photosensitive semiconductors, offering both mechanical flexibility in device fabrication and illumination of the semiconductor itself, have led to several possible applications of such materials have being reported [9-11]. Characterisation of such photosensitive materials has been reported in terms of conductive behaviour at THz frequencies [12-16]. This is done to precisely determine the change in conductivity to illumination of high-conductivity or highly-doped photosensitive organic semiconductors for opto-electronic applications. As a result, an EM application using such a blend at sub-THz or THz frequencies is less likely to be successful due to its high absorption at these frequencies. In this chapter, the electromagnetic (EM) behaviour of a low loss, low-doped, photo-sensitive organic semiconductor is extensively studied and its physical properties determined for the first time at sub-THz and THz frequencies. The possible applications of such a low-loss optically-tuneable organic blend lie in high-frequency EM applications. These

applications are discussed in detail in Chapter 5 and 6, using the extracted physical properties of such semiconducting materials from the high-frequency measurements.

4.1 Electromagnetic transmission-only measurement techniques for photosensitive semiconducting material characterisation

In characterisation of dielectric materials, transmission-only measurement techniques are generally free-space based. The primary advantage of using electromagnetic free-space techniques over other measurement techniques is that it is non-contact, non-destructive and wide-band. These measurements are performed using a VNA-driven free-space transmission setup in a chamber or an optical bench [17, 18]. The system offers a broadband characterisation of the material under test. In addition, measurements using such a setup requires almost no sample preparation in comparison to other techniques. However, when it comes to determining the loss tangent of low loss materials, a cavity resonator operating at a single frequency proves to be more accurate [19]. When reporting the characterisation of dielectric measurements, it is of greater interest for the audience to observe a wide band dispersive response of the material under test, instead of a single frequency response.

At high frequencies, popular choices for the evaluation and determination of material dielectric properties are non-free-space waveguiding, coplanar waveguide (CPW) transmission line, or free-space transmissometer based techniques [20-22]. Amongst these high frequency material characterisation techniques, free-space transmissometer techniques are suitable for characterisation of materials under profiled beam illumination [17, 23] . Unlike the direct waveguiding techniques, where the sample under test (SUT) is enclosed in a waveguide structure, free-space transmissometer systems allow exposure of the SUT to illumination from a light source or detection of the temperature of the surface of the SUT using a pyrometer. Similarly, although the CPW transmission line structure is one of the most popular devices for material characterisation in microwave and millimetre-wave frequency-domain, it fails to accurately measure the properties of the SUT above W-band (75 – 110 GHz). This is because at high frequencies (above 100 GHz), the width of the transmission line becomes very narrow for commercially available low dielectric substrates.

In high frequency free-space measurements, broadband characterization of isotropic or anisotropic materials under various incident angles and polarizations are possible. This technique is usually categorized into reflection–transmission [24, 25], reflection-only [26, 27] and transmission-only methods, depending on the experimental set-up [28, 29]. For accurate free-space measurements in the methods mentioned above, an important consideration is that the size of the SUT, set normal to the incident wave, must be larger than the electromagnetic beam-waist, so that no diffraction from the edges of the sample will result. In this Chapter, we have used transmission-only techniques to characterise the photosensitive semiconducting materials. This is because, in reflection-transmission methods, the computational analysis becomes extremely complex. In reflection-only methods, multiple reflections occurring at boundaries between layers in multi-layered samples need to be considered and minimized, and the surface condition of the material becomes crucial for wave reflection at high frequencies [19]. Yang et al. have successfully estimated the complex permittivity of a SUT at millimetre-wave frequencies using a VNA-driven quasi-optical (QO) transmissometer [29]. A method of continuous-frequency dispersive analysis, such as used by Sun *et al.* [30] used a Fabry-Perot transferfunction to establish an initial-guess value of the permittivity of the SUT at both

Table. 4 .1. Table showing the properties of the samples investigated in Chapter-4.

Sample	Semiconductor	Characterisation method	Substrate	Film Thickness
Sample-1	Inorganic (Si)	Optically-switched transmission line (curve fitting method)	Taconic (TLY-5)	0.16 mm
Sample-2	Organic (%95:5% P3HT:PCBM)	THz-Spectroscopy	105 µm glass	40 µm
Sample-3	Organic (%95:5% P3HT:PCBM)	THz-Spectroscopy	105 µm glass	6 µm
Sample-4	Organic (48.45 mg:2.55 mg P3HT:PCBM)	Quasi-optical Transmissometry	70 µm Mylar	230 µm
Sample-5	Organic (15 mg P3HT: 0.8 mg PCBM)	Quasi-optical Transmissometry	70 µm Mylar	70 µm
Sample-6	Organic (%95:5% P3HT:PCBM)	Quasi-optical Transmissometry	105 µm glass (Encapsulated in Nylon)	40 µm
Sample-7	Organic (%95:5% P3HT:PCBM)	Quasi-optical Transmissometry	105 µm glass (Encapsulated in Nylon)	6 µm

Sub-THz and THz frequencies, has been performed and detailed in sections 4.3 and 4.4. In addition to free-space transmission measurements, a unique matching-technique, matching realised between simulated and measured results to extract physical properties of a SUT, using a microstrip transmission has been established, to characterise photo-sensitive crystalline semiconductors in microwave frequencies. Characterisation of both inorganic and organic photosensitive semiconductors have been reported in this chapter and the properties of the samples have been tabulated in Table 4.1.

4.2 Semiconductor characterisation using optically-switched microstrip transmission line

In free-space material characterisation, the SUT is considered as a transmission line element. A transfer function is constructed, in terms of S-parameters of the transmission line, and is used to extract the dielectric properties of the SUT. A microstrip line, similarly, can measure the transmission across a SUT positioned at the centre of the transmission line structure (See Fig. 4.1). In this section, a matching-technique method has been described to extract the direct current (DC) conductivity of an unknown sample of Si using an optically-switched microstrip transmission line. In this technique illumination of the photosensitive SUT is traditionally achieved using infra-red (IR) lasers [6]. Two ways of guiding the illumination to the SUT are by either using fibre optics [31] or direct illumination [32]. However, the use of IR-LEDs to produce an irradiance at the

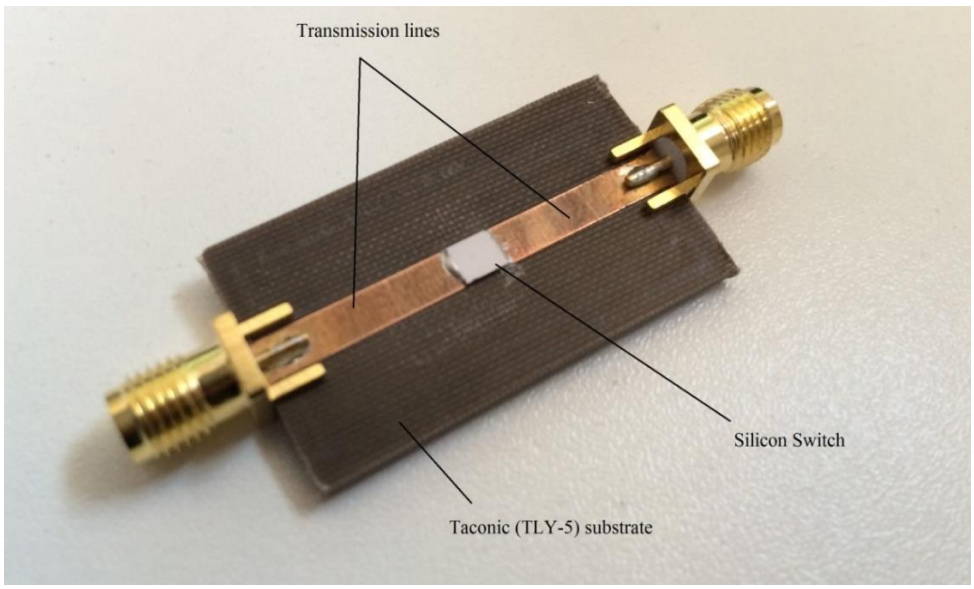

Fig. 4.1. Optically switched microstrip transmission line with 3.5mm × 4mm medium-resistivity Si switch embedded between two microstrip traces.

SUT interface similar to that of the IR-lasers are reported in [33, 34]. Laser-based sources are bulky and are not fully practical for an application focused design, but do allow the silicon to operate with excellent on-state characteristics. IR-LED sources, on the other hand provide a means to reduce the form factor of the illumination source, and hence the overall system becomes flexible and compact.

In optically-controlled reconfigurable antennas the switching component used is mostly comprised of high-mobility inorganic semiconductors Si or GaAs. Recall Chapter 3 which covers why Si serves as the best as option for use as a photoconductive switch in optically activated antennas. Chapter 5 will discuss in detail why Si is chosen as a photoconductive switch in some antenna systems [35]. Both medium and high-resistivity Si is examined to observe its suitability for use in specific antenna applications. The performance of these switches is usually tested using microstrip or coplanar waveguide transmission lines, before incorporation of the switches into the physical system [36].

A photoconductive switch can either be modelled as the cross-sectional area on the Si substrate between the microstrip tracks (gap-structure), or the gap structure can be occupied by a Si switch, in which case the substrate can be of any other dielectric, for example FR-4. In the latter case, in order to account for such switches in a real antenna design, dimensions, as well as the positioning of the Si switch, along with a low dielectric material, must be chosen and well-modelled in the transmission line design to get efficient operation of the active state of the optical switch. An optically-switched transmission line is designed using CST (see Fig. 4.2). The length of the switch is chosen to be 3.5 mm and the width 4.0 mm. A thickness, 0.16 mm, for the switch is measured using a micrometer screw gauge. An optimum gap length of 1.5 mm in the transmission line is considered to achieve an isolation of 8 dB between dark and active states.

A medium-resistivity (8 Ω-cm) Si wafer of thickness 0.16 mm is used as the optical switch (sample 1) during measurements. A Si switch with dimensions 3.5 x 4.0 mm^2 is placed over the 1.5 mm gap and glued to the microstrip tracks using silver epoxy. The optically-switched transmission line is fabricated using Taconic (TLY-5) substrate. Optical illumination of the Si switch is supplied by 880 nm infrared emitting diodes (IREDs). The radiance of each of the LEDs is measured using a digital photo-meter (see Fig. 4.3). In CST, a semiconductor can either be modelled as an insulator with appropriate loss tangent of the semiconductor in terms of electrical conductivity or a lossy metal where the electrical conductivity can be varied. CST uses Drude model to account for

conductivities in a semiconductor or lossy metal. In this piece of work, the dark state of Si is modelled as an insulator with a permittivity of 11.8. The dark-state electrical conductivity of the medium-resistivity Si is estimated by running a parametric sweep with conductivity values from 1 to 10 Sm^{-1} until the simulated results matched to measured. This technique has been used by Gamleth et al to form a general model for the inhomogeneous plasma in inorganic semiconductors and also characterise the region [21]. We used a similar matching-technique approach to evaluate dark and active conductivities. Dark-state DC conductivity is matched at 5 Sm^{-1}. Similarly, for the active state, the measured transmission graph is used to match the simulated results. In order to account for the active state of Si, the performance of the switch at different light intensities is analysed (see Fig. 4.4). Three IREDs were used to illuminate the switch at different light intensities and the transmission of the optically-switched line is measured using a PNA-L [37]. Each LED can be individually switched on, with a maximum total output power of 160 $mWcm^{-2}$ when all three LEDs are illuminated.

To minimise the power lost due to the divergent nature of the LEDs, the light source is placed very close to the sensitive power-meter when measuring its maximum output power. This is also replicated when taking transmission measurements of the transmission line. Three measured illumination powers are achievable with this illumination source: 93 $mWcm^{-2}$, 125 $mWcm^{-2}$ and 160 $mWcm^{-2}$, for one, two and three LEDs illuminated respectively, measured at 1 mm distance from the light sensor. The

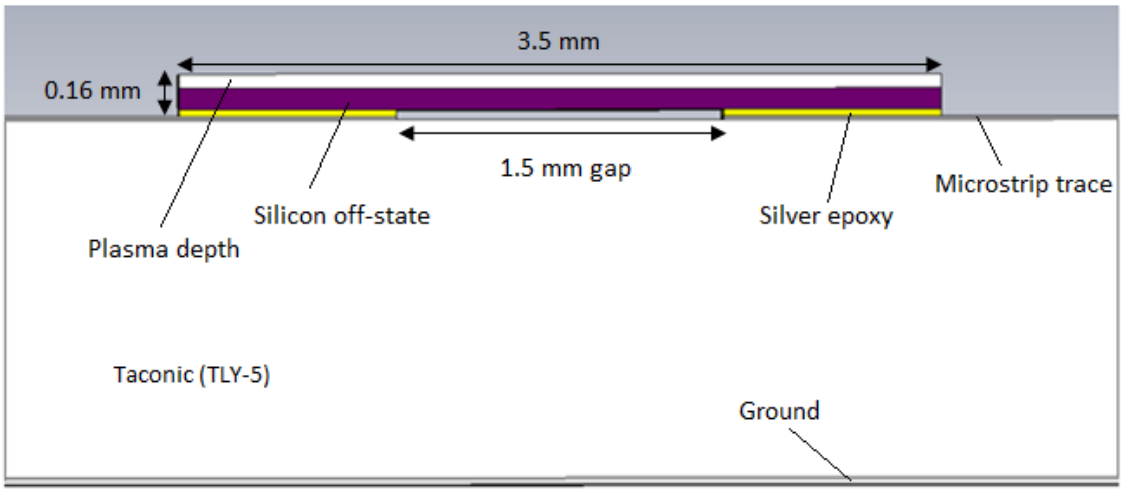

Fig. 4.2. Side view of the modelled Si switch on the optically-switched transmission line showing the plasma depth of the active region.

transmission (S_{21}) measured due to maximum irradiance of the optical source on the Si switch is considered as the active state transmission of the microstrip transmission line. The measured active state data is used as a reference to match the simulation in order to estimate the approximate value of conductivity and depth of the plasma layer for the active state. The plasma layer, as shown in Fig. 4.2 is modelled to account for the distribution of photo-generated carriers in the switch. The layer area is modelled with dimensions of 4.0 x 3.5mm^2 and its depth is varied from 50 to 100 μm. Additionally, a silver layer is modelled beneath the Si switch to account for the silver epoxy paste used to attach the switch to the microstrip traces during fabrication. A conductivity of 5 Sm^{-1} for dark-state and 70 Sm^{-1} for the active, with a plasma depth of 65 μm, in simulation, have shown a perfect match with the measured transmission (see Fig. 4.5). However, theisolation between the transmission for active and dark states of the medium-resistivity Si is not as high as that in high-resistivity Si. The maximum active state conductivity of high -resistivity silicon (5 kΩ-cm) in the frequency-domain 2−10 GHz is noted as 168 Sm^{-1} and that for the dark state as 4.25 x 10^{-4} Sm^{-1} by Gamlath *et al*. [21]. This high isolation between active and dark states effectively improves the performance of the frequency-reconfigurable antenna.

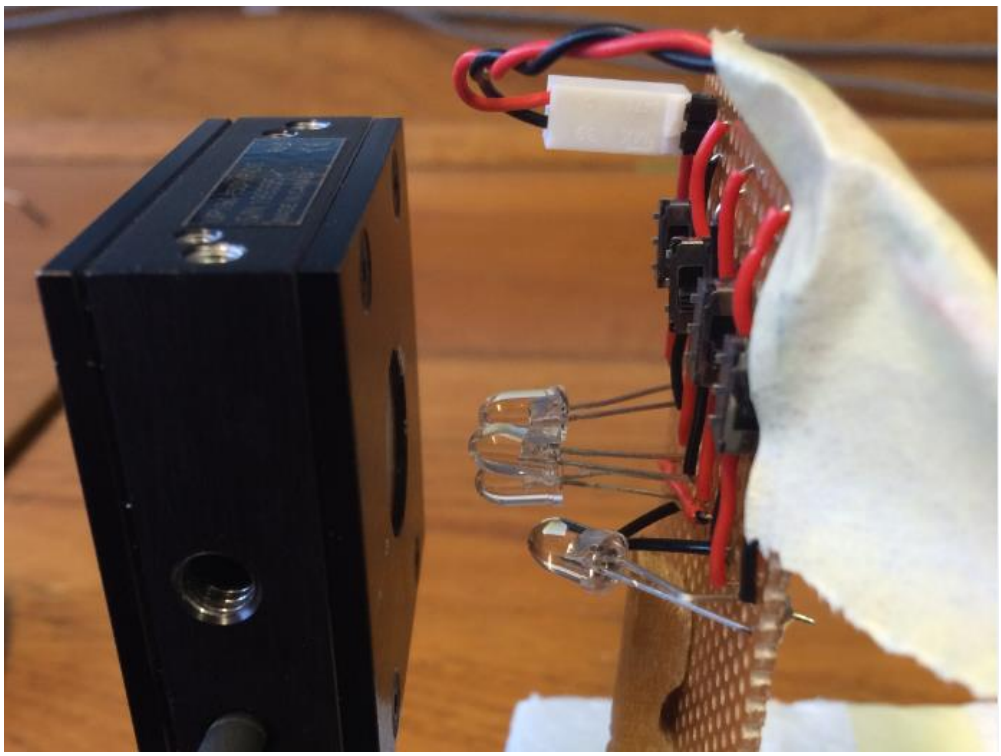

Fig. 4.3. Illumination intensity of the array of IREDs measured using a sensitive power-meter.

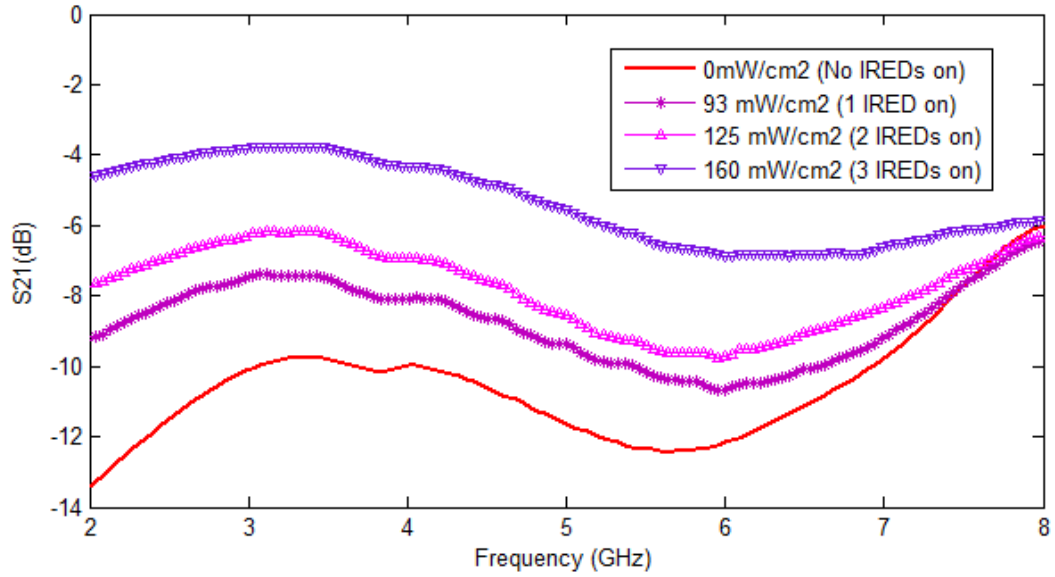

Fig. 4.4. Measured Transmission of an optically switched microstrip transmission line using medium-resistivity Si at different intensities using 880 nm IREDs. The four traces show improvement in transmission (S21) due to higher radiances shone onto the Si switch.

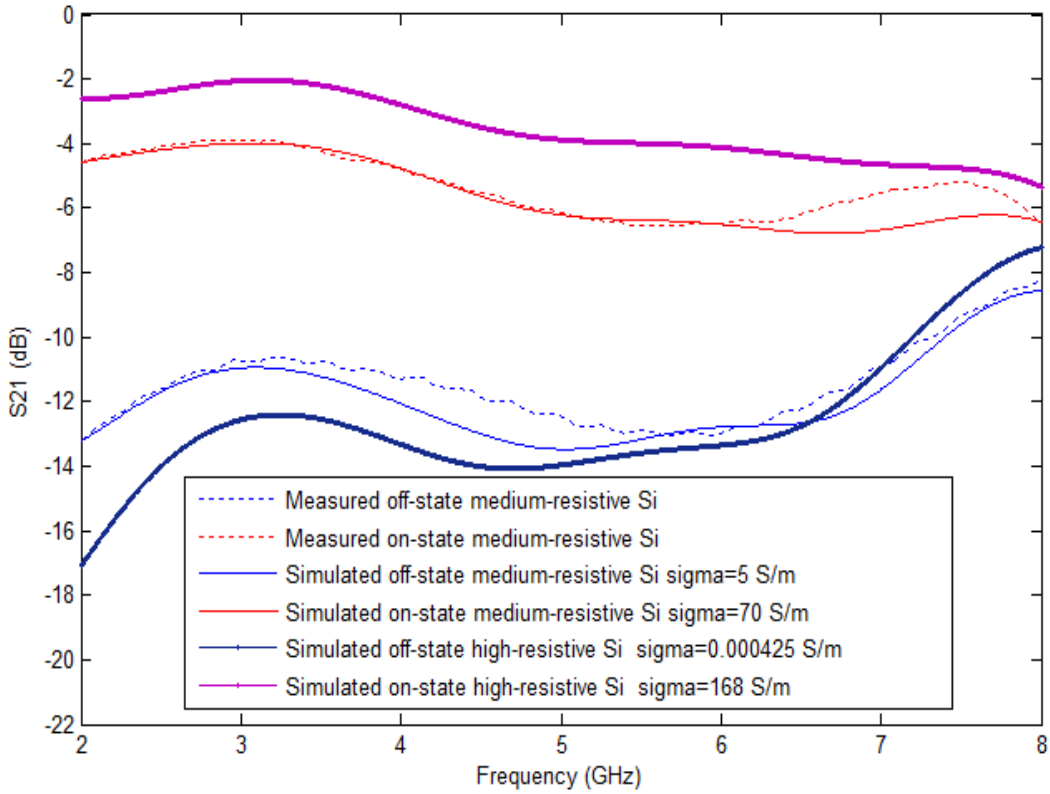

Fig. 4.5. Comparison between measured and simulated results of the fabricated and modelled optically-switched transmission line.

4.3 Estimation of dielectric constants of thin-film semiconducting polymer blends using Terahertz time-domain spectrometry

One of the well-known methods for extracting material properties at high frequencies is terahertz (THz) time-domain spectroscopy (TDS) [38-40]. The generation and detection of THz waves in a TDS measurement setup can be obtained using several different combinations of sources and detectors. A photoconductive antenna (PCA), as a source, and an electro-optic (EO) crystal, as a detector, is commonly employed in most TDS setups. Alternatively, a photoconductive detector and an EO receiver can also be used [41]. The THz-TDS measurement setup generally consists of a femto-second laser that produces femto-second pulses and with the help of a beam-splitter the pulses are separated in two different optical paths; pump-beam and probe-beam. The pump-beam is directed towards a biased PCA. The PCA is usually a gallium arsenide (GaAs) substrate, sandwiched between two electrodes. With sufficient bias voltage along with excitation of the semiconductor with femtosecond optical pulses with energy greater than its bandgap leads to emission of accelerated photo-carriers in the form of THz wave. The generated THz wave is detected using an EO zinc-telluride (ZnTe) crystal in time-step by introducing delay in the system. This delay is maintained using a mechanical translation stage for which the pump beam travels through a time-delay and the arrival of the THz wave to the ZnTe crystal is delayed by Δt relative to the probe-beam. This ensures step-by step sampling of the THz radiation intensity at the detector end. A detailed description of the THz-TDS measurement setup in the Antenna Lab at QMUL's THz laboratory is provided in Appendix A.

THz-TDS investigates the complex dielectric response of materials. In this section we report optical constants of a donor-acceptor organic system, a bulk-heterojunction formed by blending 5% PCBM with a matrix of 95% P3HT, using THz-TDS. With the THz-TDS measurement technique, the material under test is characterised using a comparison between a THz pulse that propagates through the sample and a THz pulse that propagates in the same propagation path with the sample absent. A femto-second class-4b laser produces 100 fs laser pulses with a repetition rate of 80 MHz. The THz-detector gets enough time to receive consecutive THz-pulses from the photoconductive antenna and the laser probe- beam, and they do not overlap in the crystal. The detector is connected to a lock-in-amplifier that inputs the electric field intensity across the sample

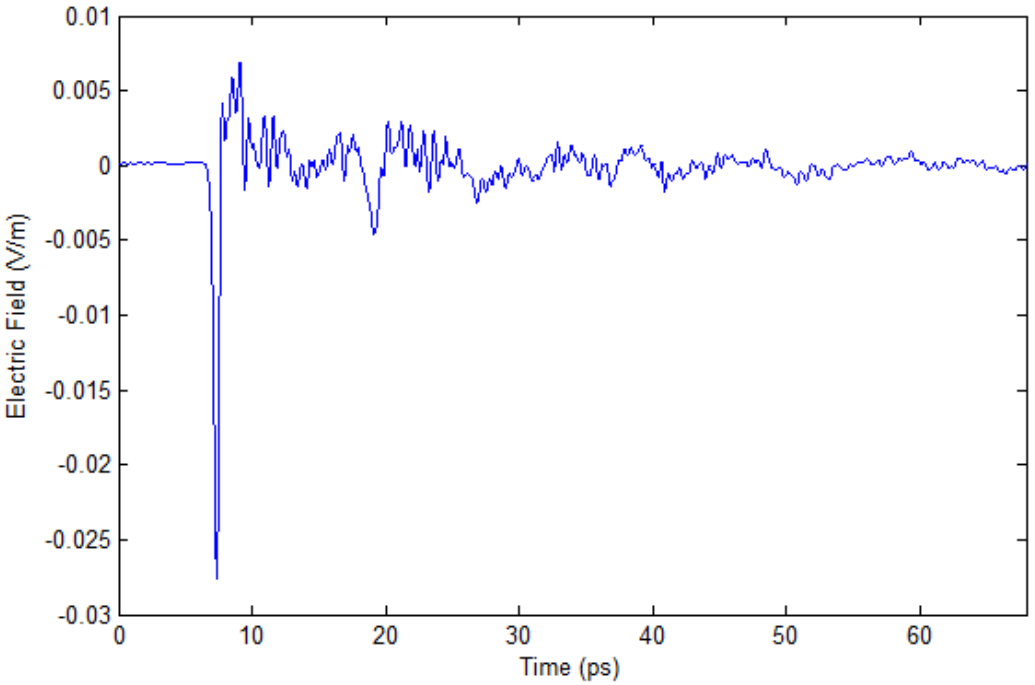

a)

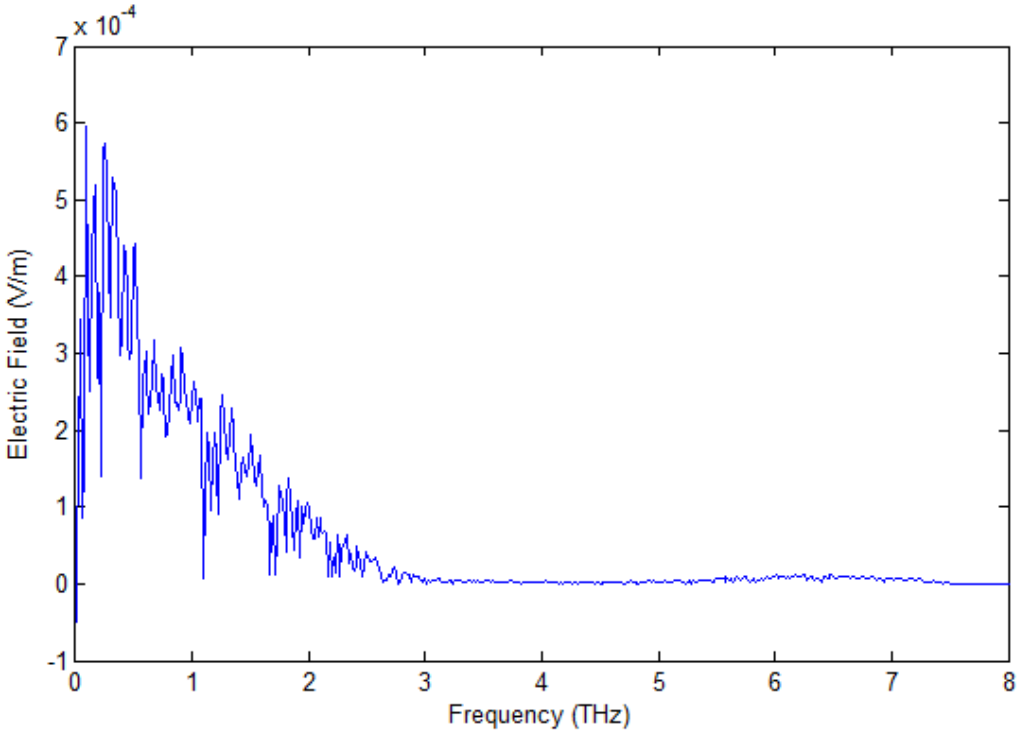

b)

Fig. 4.6. Display of the electric field magnitude of background (sample absent) measured in transmission mode using a Lab-view driven real-time THz-TDS system represented in a) time b) frequency.

plane in delay-space. A Lab-view driven real-time system is setup that displays the electric field magnitude against position of delay stage. In a single scan, a discrete THz waveform is obtained due to the step motion of the delay-stage. A discrete Fourier transform is then applied to the time-domain response to produce discrete amplitude and phase spectra. An example of the time-domain and frequency-domain response of the background (without sample) is shown in Fig. 4.6.

The sample on the TDS-bench acts as a Fabry-Perot resonator as the THz-pulse propagates through it, for which the detector receives multiple signals of the THz-pulse. The time-of-flight of the THz pulse to pass through the sample is tens of picoseconds. Isolation of the primary pulse from its multiple etalon reflections, propagating through the sample, is necessary for approximating the optical parameters of the material. However, lower refractive index materials weaken this analysis, as do thin (i.e. sub-mm) samples. This is because with low dielectric or thin materials the delay between the primary pulse and the immediate second reflection is very low. The analysing algorithm requires clear time-resolution between the primary pulse and its copies. Hence, the thickness of the sample is crucial while characterising materials using a THz-TDS system. Optical parameter extraction of very thin samples have a limit in TDS systems. In our case, the limitation of the system in terms of sample thickness is 3 µm (see Fig 4.7).

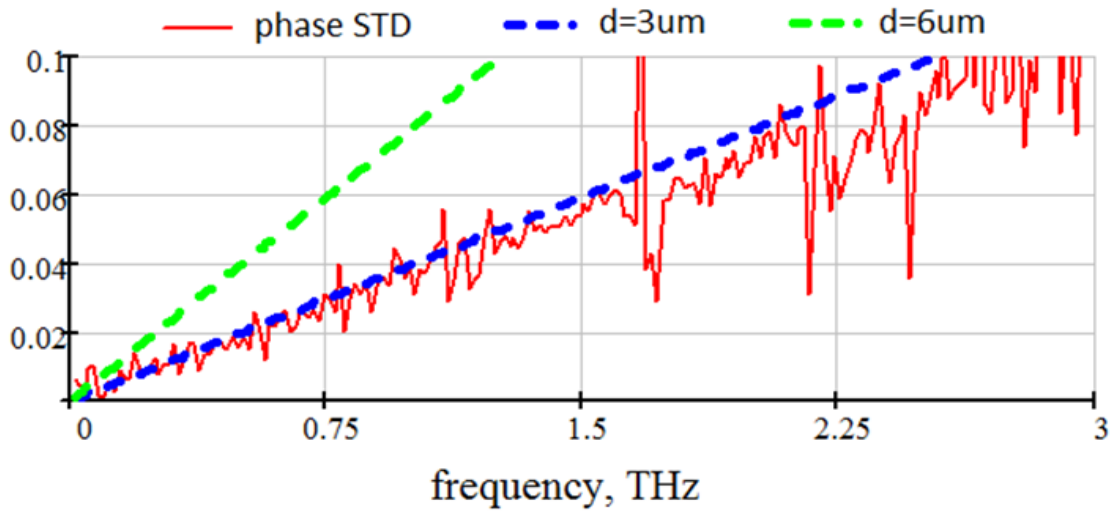

Fig. 4.7. Comparative analysis between the noise floor (phase) of the QMUL TDS system and the phase response of two standard samples (ptfe and tpx polymethylpentene) of varied thicknesses 3 and 6 µm, respectively.

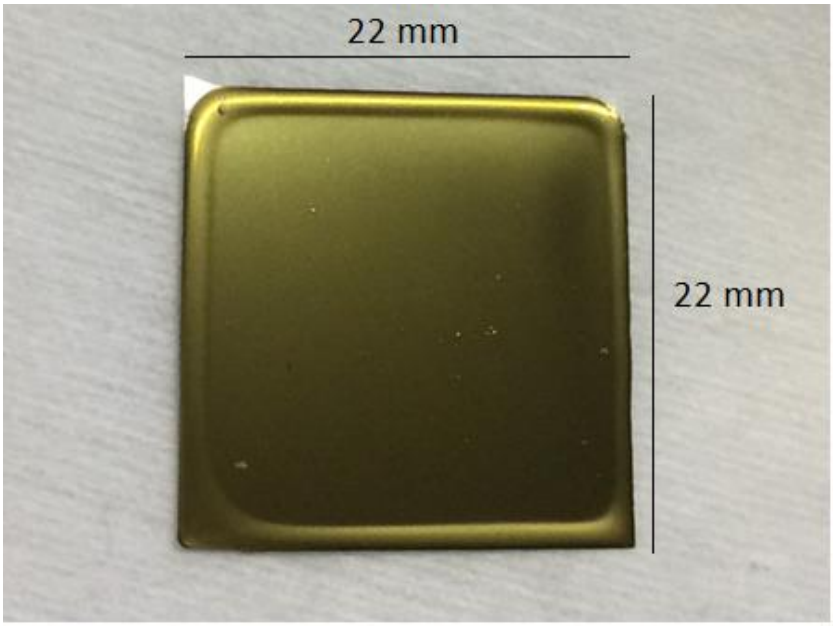

Fig. 4.8. Thin film of P3HT:PCBM blend deposited on a 105 μm glass slide.

In order to measure the dark and active-state dielectric constants of the blend (95% P3HT and 5% PCBM), it is dissolved in dichlorobenzene and the solution drop-cast onto 105 μm thick glass substrates. The solution is allowed to dry and the thickness of the blend residue is measured using a micrometre screw gauge. Using concentrations of 67 mg/ml and 8mg/ml thicknesses of 40 μm (sample 2) and 6 μm (sample 3) respectively are obtained. Fig. 4.8 shows a P3HT:PCBM thin-film deposited onto a glass substrate. The complex permittivity of the organic blend is estimated by detecting the THz electric field through the material under test (MUT) positioned at the beam focus of a THz-TDS. A theoretical transfer function $\widetilde{H}(\omega)$ is used to match the measured transfer function from the transmission response obtained from TDS measurements. This is expressed in (4.1) in the case of a single layer:

$$\widetilde{H}(\omega) = \tilde{t}_{12}(\omega)\tilde{t}_{21}(\omega)\exp\left(-\frac{i\omega d(\tilde{n}(\omega)-n_{air})}{c}\right).\sum_{k=0}^{m}\left[\tilde{r}^2(\omega)\exp\left(-\frac{i2d\omega\tilde{n}(\omega)}{c}\right)\right]^k. \quad (4.1)$$

where $\tilde{r}(\omega) = \frac{\tilde{n}(\omega)-n_{air}}{\tilde{n}(\omega)+n_{air}}$, $\tilde{t}_{12}(\omega) = \frac{2n_{air}}{\tilde{n}(\omega)+n_{air}}$, $\tilde{t}_{12}(\omega) = \frac{2\tilde{n}(\omega)}{\tilde{n}(\omega)+n_{air}}$ are the complex Fresnel coefficients at normal incidence; $\tilde{n}(\omega) = n(\omega) - ik(\omega)$ is the frequency dependant complex refractive index of the polymer film, *d* is the film thickness; m is the order of internal Fabry-Perot reflections. Since the transfer function takes into account internal reflections of the THz-pulse within the sample, the accuracy of the estimation of the optical constants is enhanced. The experimental transfer function, $\widetilde{H}(\omega)_{Exp}$, is matched to the theoretical transfer function, $\widetilde{H}(\omega)_{Theory}$, using regression fitting, and the

complex parameters of $\tilde{n}(\omega)$ of the sample extracted. The corresponding value of the real and imaginary part of complex permittivity can be found from the relationship between complex refractive index and complex permittivity: $\varepsilon'(\omega) = n(\omega)^2 - k(\omega)^2$ and $\varepsilon''(\omega) = 2n(\omega)\,k(\omega)$, where $n(\omega)$ is the refractive index, $k(\omega)$ is the extinction coefficient, $\varepsilon'(\omega)$ is the real part and $\varepsilon''(\omega)$ is the imaginary part of the complex permittivity. The sample plane is kept at 45º to the incident THz-pulse. This is to illuminate the MUT using LED white light source (see Fig. 4.9). Calculations for the transmission of the THz-pulse across the sample require consideration of the angle of the sample plane according to the following equation.

$$t_s = \frac{2n_1 cos\theta_i}{n_1 cos\theta_i + n_2 cos\theta_t} \tag{4.2}$$

where, θ_i is the incident angle to the sample plane and θ_t is the transmitted angle. The refractive index of the less dense medium is denoted by $n_1$and the denser by n_2. The thickness of the sample is also increased in the sample plane as by the factor

$$d_\varphi = \frac{d_0}{cos\varphi} \tag{4.3}$$

d_0 is the initial thickness of the perpendicular sample plane and d_φ is the thickness of the sample at 45° to the incident THz-pulse.

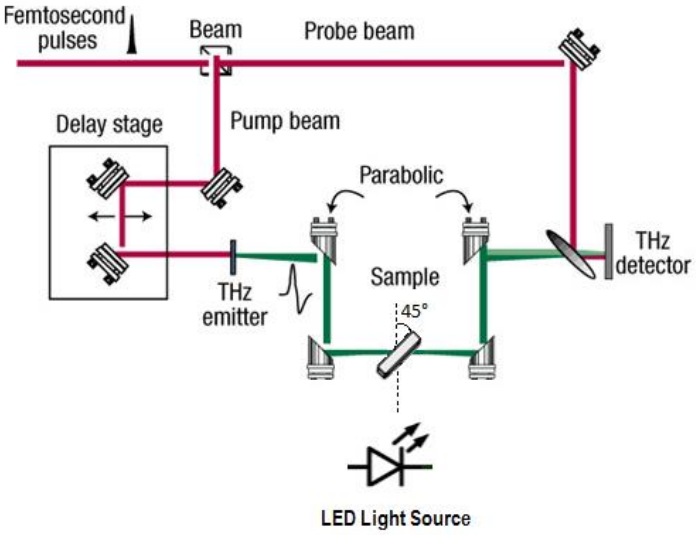

Fig. 4.9. Schematic diagram of the THz-TDS setup for measuring the dielectric constant of the optically-tuneable organic blend. The sample is positioned at 45º to the incident THz beam field to allow for optimum (non-impeding) illumination at the sample plane.

According to the phase response of a standard sample ($\varepsilon \approx 3.0$) shown in Fig. 4.8, it is expected that any sample with thickness above 3 μm measured using the THz-TDS should be above noise floor of the system. However, Fig. 4.10 shows negligible difference of the time- domain response of the thin film (6 μm in this case) organic blend between dark and active states. Both, 6 and 40 μm films show similar behaviour in time-domain response. The expected relative change in refractive index of the organic blend due to illumination is about 2%. Considering the current system configuration (scan-length and step-size) and sample thickness, such change in material properties triggers the temporal shift of the THz waveform (Δt=1fs for n=0.03 and thickness=10 μm) that is below the system resolution (for 1 μm step Δt=6.7 fs). For example, with a sample having a minimum film thickness of 67 μm the TDS system would be able to detect such small changes in the dielectric. Furthermore, it is also essential to realise that if the excitation-region layer diffuses to an effective depth of 67 μm, given the absorption depth of such photosensitive polymers is in the range of nanometres, there is a possibility of detecting such changes. An extensive research needs to be performed in order to precisely determine the active excitation-region depth of such photosensitive organic polymers, which is discussed as future work in Chapter 7.

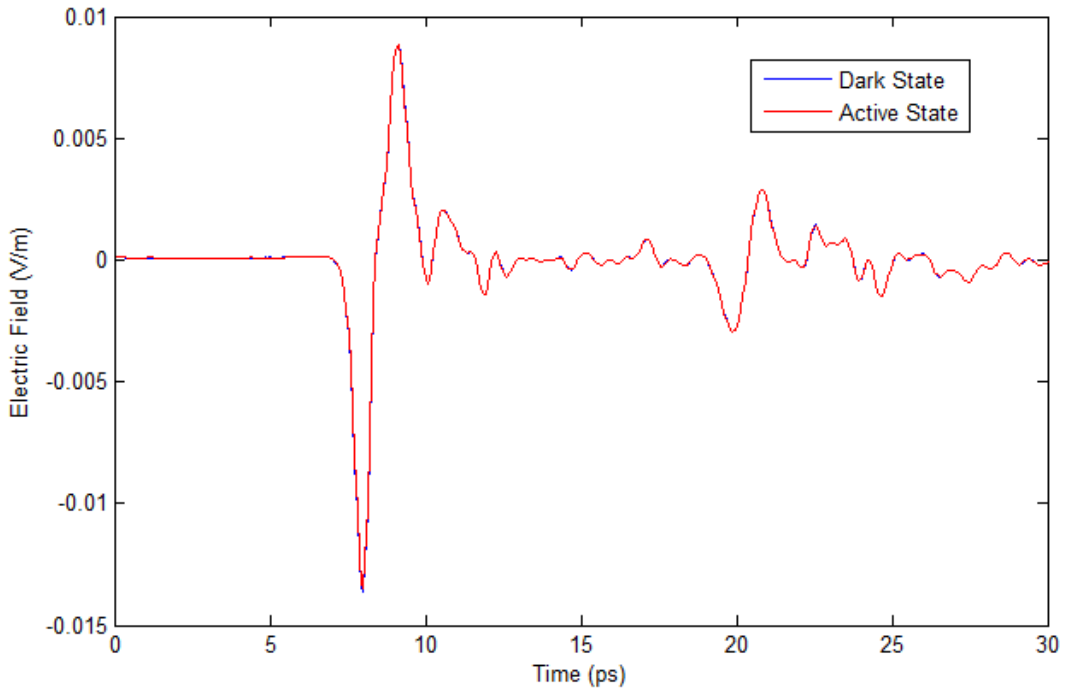

Fig. 4.10. Time-domain response of a thin film P3HT:PCBM blend in the dark and active states show no significant difference. This implies changes in the dielectric between dark and active states was not detected by the THz-TDS system.

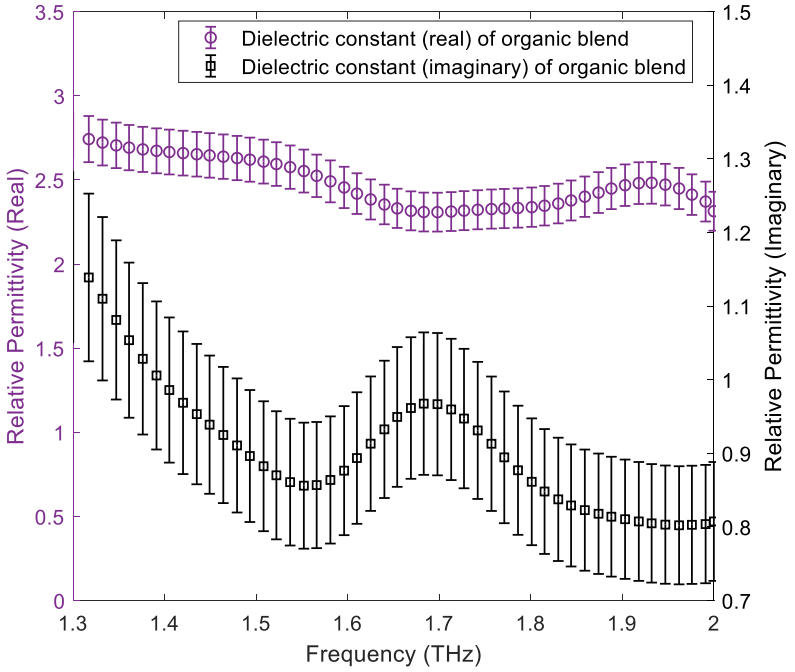

Fig. 4.11. Dispersive response of the organic blend (40 μm) in the THz frequency-domain (1.3 - 2 THz)

However, the dark dielectric constant of the polymer blend at THz frequencies has been precisely estimated using the THz-TDS (see Fig. 4.11). The MUT is positioned in the sample plane, i.e. at the focal point of the TDS system, and the transmission through the sample is received using the THz detector, which is connected to a lock-in-amplifier that measures the electric field intensity propagated through the sample plane in delay-space. A LabVIEW-driven real-time system is developed to display the electric field magnitude against position of the delay-stage. The electric field strength transmitted through the sample can be determined in the time-domain using a discretely moving delay stage. Fourier transformation of the detected time-domain electric field is used to determine the complex transmission through the sample in the frequency-domain. While extracting the dielectric constants of the organic blend, it is observed that Sample-2, with thickness 40 μm, provided a more expected dielectric constant value at THz frequencies and the traces were smoother due to an enhanced signal-to-noise ratio because of a higher sample thickness. Since the thickness detection limit of the THz-TDS for a material of dielectric constant around 3.0 is 3 μm, and the thickness of sample-3 is 6 μm, the measured transmission of sample-2 included noise, and resulted in unphysical values. The real part of the permittivity of the blend is estimated as 2.3 at 2-THz, which is close to the optical constant of (P3HT:$PC_{61}BM$) measured by Stelling et al at optical frequencies (ε=2.89 at 200 THz) [16, 42].

4.4 Dielectric spectroscopy of a low-loss photosensitive organic polymer blend using quasi-optical transmissometer

In this section the dielectric constants of the organic blend 95% P3HT:5% PCBM are precisely measured at sub-THz frequencies using a quasi-optical (QO) transmissometer. The use of such a polymer blend in EM applications is prominently dependent on the excitation region of the polymer in the active state. This is because this region contributes to the manipulation of EM waves with low absorption at sub-THz frequencies [43]. At sub-THz frequencies, small changes in the dielectric with a excitation-region depth of circa tens of microns are sufficient to manipulate the emerging wave of an antenna or lens, since the wavelength is smaller than that in the microwave frequency-domain. An optically-activated dynamic lens is one of the proposed applications for such materials [44]. The lens is used to dynamically control sub-THz transmission using optical illumination. The ease of device handling in terms of fabrication and illumination of the gantry for this lens provides added advantages over the current tuning mechanisms proposed for beam-control in quasi-optical (QO) systems [45, 46]. Operation of such dynamic lenses can prove to be highly beneficial for imaging, surveillance and remote sensing applications over the sub-THz frequency-domain. In order to investigate a potential application for such polymers in the field of electromagnetics, physical properties such as the dielectric constant, active-state dielectric constant and the excitation-region depth of the photosensitive polymer need to be precisely determined.

As discussed previously, QO transmissometer systems are often used to determine the dielectric constants of dispersive materials using transmission-only measurements. The schematic of a QO transmissometer is shown in Fig. 4.12a. The energies of the transmitted beams in these systems is brought to a focus onto the MUT positioned at the focal point, with its planar face normal to the incident beam. Ideally, the beam waist at the focal point completely covers the sample. The vector subtraction of the transmission response of the background (material absent) from the response of the MUT, results in the response of the material alone. This measured response, as a transfer function, can be matched with a theoretical transfer function. In the QO transmissometer system, the normalised transmission, in terms of scattering (S)-parameters, through the sample interface is measured using the PNA-X [47]. The transmission (S_{21}) derived from the ABCD matrix approach [48] is used to extract the real and imaginary parts of the complex

permittivity of the material. The ABCD matrix for a single layer with sample thickness d_s is given in (4.4).

$$\begin{bmatrix} A & B \\ C & D \end{bmatrix} = \begin{bmatrix} cos\left(\frac{\omega d_s\sqrt{\epsilon_r}}{c}\right) & jZ_1 sin\left(\frac{\omega d_s\sqrt{\epsilon_r}}{c}\right) \\ {}^{j}/_{Z}\, sin\left(\frac{\omega d_s\sqrt{\epsilon_r}}{c}\right) & cos\left(\frac{\omega d_s\sqrt{\epsilon_r}}{c}\right) \end{bmatrix}. \tag{4.4}$$

Z is the wave impedance of the material, ω is the angular frequency and c has its usual meaning as the speed of light in free-space. The ABCD transfer matrix can be used to estimate the transmittance of the material under test using the following equation.

$$S_{21} = \frac{2Z_0}{AZ_0 + B + CZ_0{}^2 + DZ_0}. \tag{4.5}$$

Z_0 is the wave impedance of free space. For an n-layered structure, the transfer matrix is expressed as

$$T_{total} = \begin{bmatrix} A_{total} & B_{total} \\ C_{total} & D_{total} \end{bmatrix} = \begin{bmatrix} A_1 & B_1 \\ C_1 & D_1 \end{bmatrix} \begin{bmatrix} A_2 & B_2 \\ C_2 & D_2 \end{bmatrix} \dots\dots\dots \begin{bmatrix} A_n & B_n \\ C_n & D_n \end{bmatrix} \tag{4.6}$$

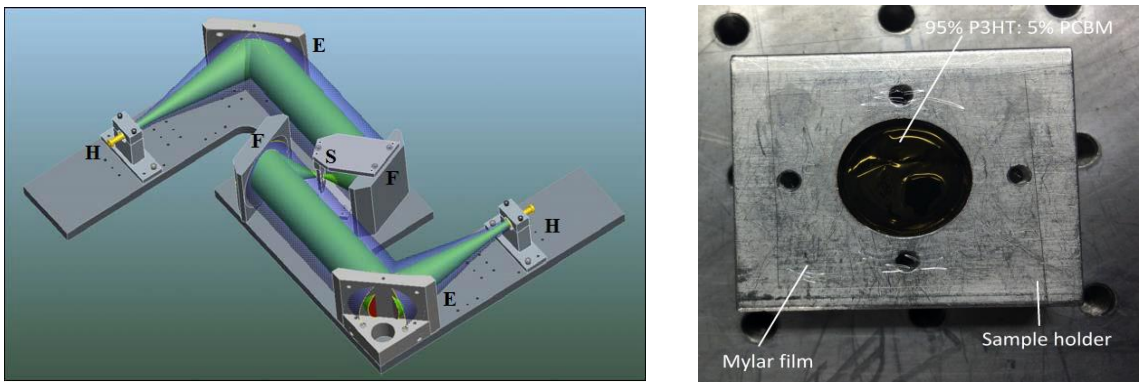

a) b)

Fig. 4.12. Schematic of a quasi-optical (QO) transmissometer system (H: feeding horns; E: elliptical mirrors; F: focusing mirrors b) Front view of the rectangular metallic sample holder (S) with sample (95% P3HT:5% PCBM) drop-casted onto a thin supporting Mylar film through the central cylindrical cut-out of the holder.

Initially, in order to test the dielectric response of the organic blend 95% P3HT: 5% PCBM, two solutions of 48.6 mg of P3HT: 2.4 mg of PCBM and 15 mg of P3HT:0.8 mg of PCBM along with 1.5 ml and 0.5 ml of organic solvent dichlorobenzene were drop-cast onto 10 μm thick Mylar films. The films were glued over a hole cut out of a rectangular slab of aluminium that served as a sample holder. The organic blend, supported by the Mylar film, and the metal holder are shown in Fig. 4.12b. The thickness of the organic blend developed on the Mylar film was measured to be 230 (sample 4) and 70 μm (sample 5) respectively using a micrometre screw gauge. An irradiance of 65mW/cm^2 (measured using a photo-diode tuned at 532 nm) and absorption area of 2.27 cm^2, constituted the active state response analysed.

The measured complex transmission of these organic blends and Mylar was normalised to background (sample absent). During post-processing, a two-layered structure model was used in this case to obtain a total ABCD matrix as the multiplication of the individual matrices for each layer treated as a transmission line. The total ABCD matrix for the two layers with thicknesses of Mylar and organic layer are individually considered as shown for an n-layered structure in (4.6). Figs. 4.13 and 4.14 shows dispersive estimates of real and imaginary dielectric response of a 230 μm (sample 4) and a 70 μm (sample 5) 95% P3HT: 5% PCBM organic blend respectively. The 'active' imaginary part of the permittivity is higher than for the off-state, since the conductivity increases with increase in the number of carriers. The polymer blends are observed to be more lossier in the active state with the imaginary part of the permittivity being at a mean value of 0.2 over the measured frequency-domain. An expected difference between the real part of the permittivity in dark and active states is observed. The mean values of the real part of the permittivity in the dark state for both the samples are 3.16 and 3.06 respectively. These match with the dark-state permittivity of P3HT stated in literature [9]. The average change in permittivity of the organic blends between active and dark states are estimated as 0.095 and 0.137. These values match with the predicted change in the dielectric constant of P3HT between dark and active states by Tang et al [11]

However, since the estimated dark dielectric constants have a difference of 17% in their values, it is evident that variation in thickness of individual samples are responsible for such variances. These blends are cast onto Mylar cast with higher concentrations, resulted in a non-uniform surface of the organic layer. This introduces variation in both real and imaginary parts of the dielectric constants due to thickness uncertainty. Hence, a more appropriate fabrication method for drop-casting the organic

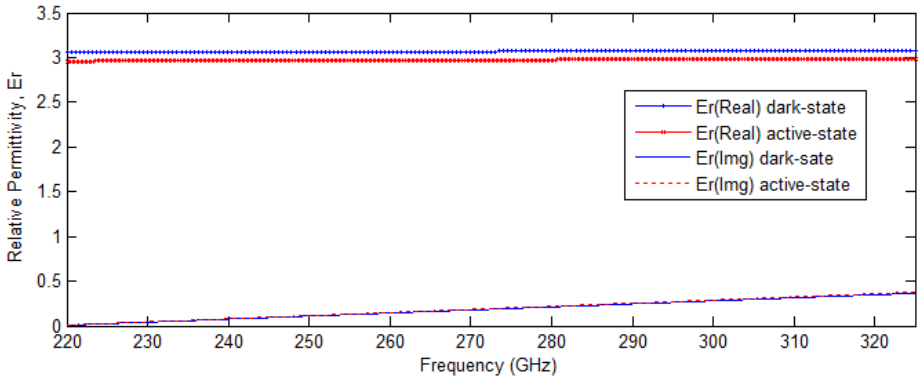

Fig. 4.13. Dispersive dielectric response of polymer blend (51mg of P3HT:PCBM + 1.5ml chloroform) with film thickness 230 µm showing the usual behaviour of the active-state real part of the dielectric constant being less and the imaginary part being greater than the dark-state one over the WR-3 waveguide band .

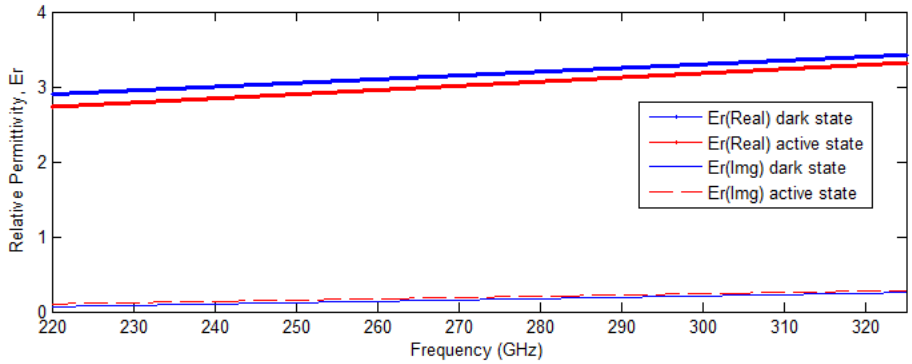

Fig. 4.14. Dispersive dielectric response of the second polymer blend (15.8mg of P3HT:PCBM + 0.5ml DCB) with film thickness 70 µm showing the same characteristics as Fig. 4.13 over the WR-3 waveguide band.

blend is chosen, where a thin glass is used as a substrate for the organic blend to be drop-cast on. The P3HT:PCBM solution is kept at 60°C for 3-4 hours to ensure complete dissolution which results in uniform deposition of the thin-films onto the glass substratesduring drop- casting. The solution is carefully drop-cast onto 105 µm thick glass slides, at one drop per second, until the surface tension produces a stable 0.5 ml drop.

As discussed in section 4.3, with concentrations of 67 mg/ml and 8mg/ml we obtain organic films of thickness 40 µm and 6 µm respectively. The drop-cast onto a glass substrate ensures development of a film after drying which is entirely uniform in depth. The organic blend thickness uncertainty after deposition across the 22 mm by 22mm glass substrate is estimated at ± 10%. Throughout the fabrication, the films are kept inside a nitrogen (N_2) glovebox to prevent exposing the samples to ambient air. It is observed that

the performance of the photosensitive organic polymers degrades in the presence of oxygen (O_2), light and water vapour (H_2O) [49]. The exposure of the sample to ambient air while taking free-space measurements can degrade the active-state permittivity of the organic polymer. Goris et al performed direct optical absorption measurements on fully encapsulated P3HT:PCBM blends [50]. Similarly, in this work, the drop-cast thin-films are sealed in 50 μm Nylon encapsulations, or pockets, under N_2. These samples (sample-6 and sample-7) are then used to measure the active-state dielectric constant (see Fig. 4.15a).

Since the organic blend is supported and encapsulated by glass and Nylon respectively, the dielectric loss of these materials is determined using the VNA-driven QO transmissometer. This is to ensure that the transmitted signal passing through the encapsulated blend has sufficient power at the receiving end of the QO transmissometer, and is above the noise floor of the system, for successful material characterisation. Fig. 4.15b shows the loss tangent of the supporting materials for the organic blend, the glass and the Nylon, in the sub-THz frequency-domain. The loss tangents of both the supporting materials show at least 40% of the incident power being delivered to the organic blend alone. This ensures that the received signal contains sufficient information about the organic blend for accurate determination of its physical properties.

Additionally, the phase response of the 105 μm glass substrates is checked before drop-casting the polymer solutions. Since the glass substrates are identical, it is possible to take relative measurements of the drop-cast organic blend and estimate its dark dielectric constant. The vector subtraction of the transmission response (S_{21}) of the glass substrate from the drop-cast blend and glass combination, results in the transmission response of the blend alone. The phase response of eight glass substrates before drop-casting is measured (see Fig. 4.16a) and yields a maximum standard deviation of the phase being less than 0.5°. This ensures the dark and active dielectric constant calculations of the organic blend is independent of the glass substrate.

It is observed that the post-processing algorithms fail to match the transfer function of the measured transmission of these samples, and further result in unphysical values of the dielectric constant for different thicknesses, when the sample interface at the focal point of the QO transmissometer is not absolutely normal to the incident Gaussian-beam. Fig. 4.16b shows the real and imaginary parts of the permittivity of the glass obtained by fitting the data in Fig. 14.6a (lower plot). Note that the fitting procedure

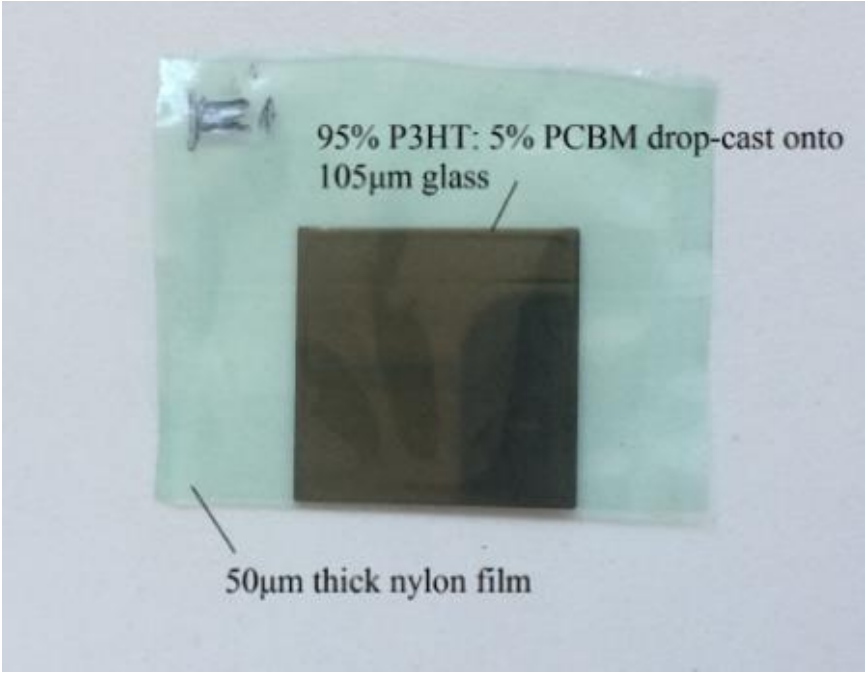

a)

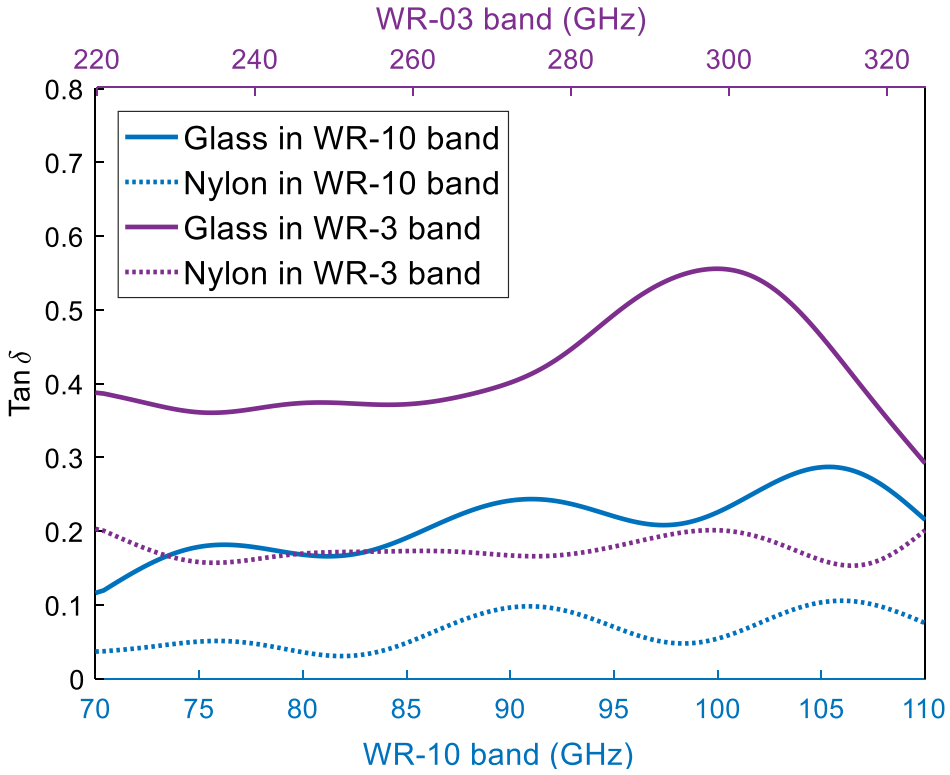

b)

Fig. 4.15. A prototype of the encapsulated organic blend 95% P3HT: 5% PCBM on 105 µm thick glass b) Dielectric loss tangent (tanδ) of the supporting materials: Nylon and glass in the sub-THz frequency-domain (WR-10: 75-110 GHz and WR-3: 220-325 GHz).

results in errors in the real and imaginary parts of the permittivity of ±3% and ±12%, respectively. Fig. 4.16c shows the magnitude and phase transmission results obtained using the QO method for a 40 μm thick organic layer in an encapsulated sample in the dark and under 60 $mWcm^{-2}$ white light illumination. Fig. 4.16d shows the real and imaginary dielectric constant values obtained by fitting the dark data for two organic samples (sample 6 and 7) of different thickness. During fitting, the only free parameter was the complex organic permittivity, since the organic layer thickness had been measured independently and the glass and Nylon layers were defined by previous measurements. The real part of the organic permittivity under no illumination from 75 to 105 GHz is shown in Fig.4.16d and appears to be frequency independent with an average value of 3.2 ± 0.3, with the two data sets from different thickness devices in agreement within fitting errors and data point scatter. The imaginary part of the permittivity in Fig. 4.16d does not display agreement between samples. For instance, the 40 μm data shows a peak at approximately 90 GHz which appears suppressed in the 6 μm (sample 7) data. We tentatively attribute this disagreement to a larger relative thickness variation (roughness) in the thinner sample.

With the intention of comparing the dielectric response of the organic blend in different frequency-domains, from sub-THz to THz, the transmission through sample-6 has been post-processed and represented in terms of real and imaginary parts of the permittivity, as a function of frequency (Fig. 4.17a). Fig. 4.17a shows the dispersive dielectric behaviour of sample-6 in the sub-THz frequency-domain. Comparison has been made for the optical constants of sample-6 extracted in the sub-THz as well as in the THz frequency-domain. In the THz frequency-domain, the extracted optical constants between 1.3 and 2 THz show the most stable response, without any fluctuations (see Fig. 4.11). The real part of the permittivity of the blend is also estimated as 2.85 and 2.30 at 300 GHz and 2 THz, respectively. The imaginary part of the permittivity of the blend, has also been observed to be higher in the THz region than the sub-THz frequency-domain (to compare the results see Fig. 4.11 and 4.17a).

The active-state dielectric constants of the organic blend are measured using the QO transmissometer in the sub-THz frequency-domain. The SUT, sample-6, in this case encapsulated, is essentially mounted at the focal point of the QO transmissometer at right angles to the incident Gaussian beam, by stretching it onto a sample holder. White-light illumination of irradiance, 60 $mWcm^{-2}$ is projected for 40 seconds from the side onto the

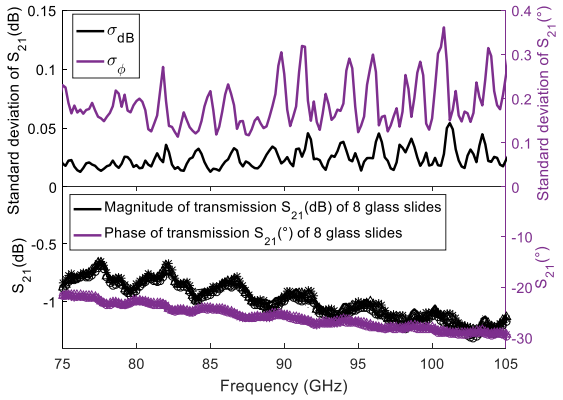

a)

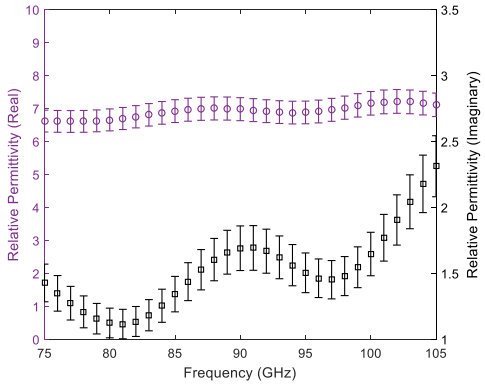

b)

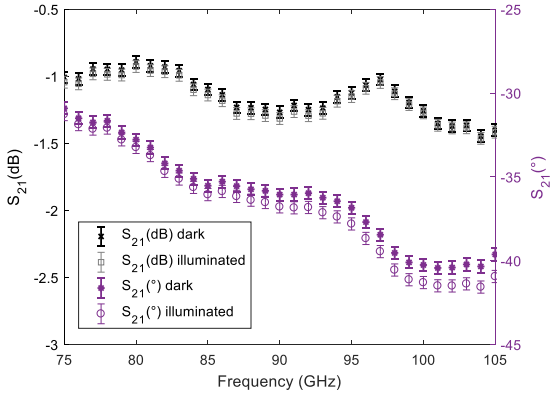

c)

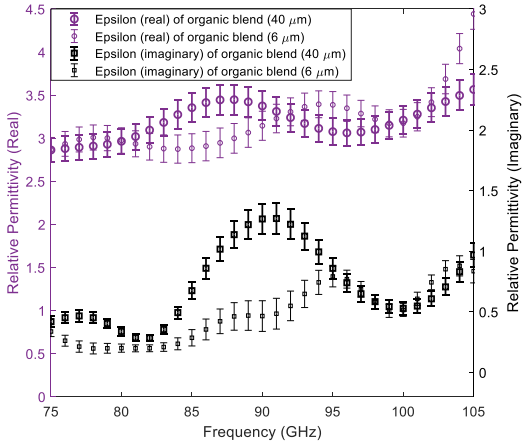

d)

Fig. 4.16. (a) Deviation in magnitude (dB) and phase (°) of transmission (S_{21}) of 8 glass slides of 105 µm thickness. (b) Dispersive response of a 105 µm thick glass slide in the sub-THz (WR-10) frequency domain. (c) Transmission response of a 40 µm organic blend (95% P3HT: 5% PCBM), encapsulated in Nylon (sample 6), in the dark and illuminated states. (d) Dispersive response of two organic blends (6 µm and 40 µm) under no illumination in the sub-THz (WR-10) frequency domain.

SUT. The active-state dielectric constants are estimated from the measured change in the complex transmission through the SUT for this duration. It is observed that the change in the phase of complex transmission through the sample reaches saturation after 40 seconds. When the illumination is turned off, the phase returns to its original position as in the dark state. The change in the complex transmission of the SUT is calculated by subtracting its transmission in the dark state from the active state. The complex change in dielectric constant $\Delta\varepsilon$ of the organic blend, is evaluated using the ABCD matrix transfer

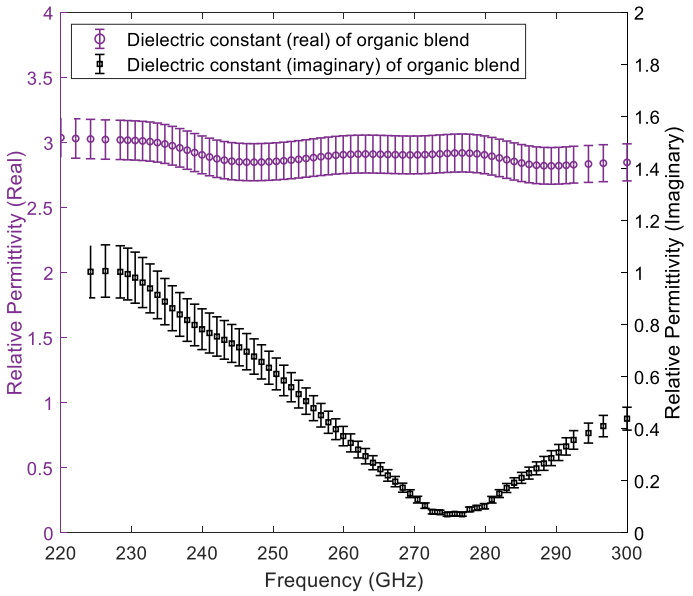

a)

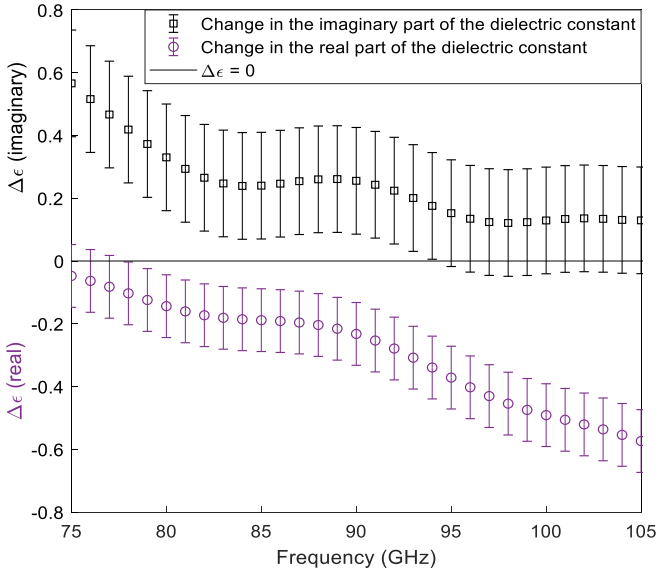

b)

Fig. 4.17. a) Dispersive response of the organic blend (sample 6) in the sub-THz (WR-3) and THz frequency-domains. The profiles of the curves show the real part of the dielectric constant to be uniform over the sub-THz and THz frequencies. The profile of the measured imaginary part, however, is non-uniform due to thickness variation in the sample b) Illumination-driven change in the real (Δε') and imaginary (Δε'') parts of the permittivity of sample-1 in the sub-THz (WR-10) frequency-domain. A change in the range of –0.05 to –0.55 in the imaginary part and +0.01 to +0.52 in the real part of the dielectric constant of the blend is observed.

function. The response of the change in the dielectric constant between dark and active states of the organic blend over the WR-10 frequency-domain is shown in Fig. 4.17b. The active-state real part of the dielectric constant is evaluated as 2.55 at 100 GHz. Any changes in the real or imaginary parts of the dielectric properties under illumination are evaluated using simple subtraction between dark and active state dielectric constants.

Precisely estimating the physical properties, i.e. the complex dielectric constant, change in the dielectric constant between dark and active states, and the excitation-region depth in organic semiconductor blends allows commercially available EM modelling software, like CST, to accurately model the excitation region of the polymer. This enables the software to evaluate the performance of optically-activated antennas or lenses made from such dielectric materials. Hence, as an application, dynamically controlling the EM behaviour of an incident beam-field of an antenna using such photosensitive organic polymers with white light, can significantly enhance existing technologies in THz optics.

4.5 Summary

In this chapter, characterisation of photosensitive semiconducting materials using EM transmission-only techniques have been thoroughly discussed. A novel matching technique using a microstrip transmission line and its transmission characteristics for estimating the dark and active state conductivities of a photosensitive semiconducting material at microwave frequencies has been demonstrated. Following that, two different free-space material characterisation setups, QO transmissometer and THz-TDS, were deployed for material characterisation using transmission-only configurations. The QO transmissometer system was used to cross-check the derived estimates of the optical constants measured in the THz frequencies using THz-TDS. The active state dielectric constants of the organic blend 95% P3HT: 5% PCBM were estimated using the QO transmissometer. Reversible and reproducible changes in the real and imaginary parts of the complex dielectric constant of the organic blend are measured in the range of –0.05 to –0.55 and +0.01 to +0.52 respectively, over the sub-THz frequency-domain. These dielectric changes coincide with photo-generated charge carrier densities of order 10^{15} $(cm)^{-3}$, measured in Chapter 3, under identical measurement conditions.

References

[1] A. Ahmed, I. A. Goldthorpe, and A. K. Khandani, "Electrically tunable materials for microwave applications," *Applied Physics Reviews,* vol. 2, Mar 2015.

[2] "Computer Simulation Technology," 2017 ed: Dassault Systemes.

[3] Rhode&Schwarz. (2012, Measurement of Dielectric Material Properties. 3-15. Available: https://www.rohde-schwarz.com/uk/applications/measurement-of-dielectric-material-properties-application-note_56280-15697.html

[4] I. Pupeza, R. Wilk, and M. Koch, "Highly accurate optical material parameter determination with THz time-domain spectroscopy," *Optics Express,* vol. 15, pp. 4335-4350, Apr 2 2007.

[5] S. Puthukodan, E. Dadrasnia, V. K. T. Vinod, H. K. Nguendon, H. Lamela, G. Ducournau, *et al.*, "Sub-THz characterisation of multi-walled carbon nanotube thin films using vector network analyser," *Electronics Letters,* vol. 50, pp. 297-298, Feb 13 2014.

[6] C. H. Lee, P. S. Mak, and A. P. Defonzo, "Optical Control of Millimeter-Wave Propagation in Dielectric Wave-Guides," *IEEE Journal of Quantum Electronics,* vol. 16, pp. 277-288, 1980.

[7] C. J. Panagamuwa, A. Chauraya, and J. C. Vardaxoglou, "Frequency and beam reconfigurable antenna using photoconducting switches," *IEEE Transactions on Antennas and Propagation,* vol. 54, pp. 449-454, Feb 2006.

[8] Y. Tawk, A. R. Albrecht, S. Hemmady, G. Balakrishnan, and C. G. Christodoulou, "Optically Pumped Frequency Reconfigurable Antenna Design," *IEEE Antennas and Wireless Propagation Letters,* vol. 9, pp. 280-283, 2010.

[9] V. Sathi, N. Ehteshami, and J. Nourinia, "New frequency-reconfigurable microstrip antenna composed of organic semiconductor polymer," *Organic Electronics,* vol. 13, pp. 1192-1196, Jul 2012.

[10] V. Sathi, N. Ehteshami, and J. Nourinia, "Optically Tuned Frequency-Reconfigurable Microstrip Antenna," *IEEE Antennas and Wireless Propagation Letters,* vol. 11, pp. 1018-1020, 2012.

[11] H. Y. Tang, R. S. Donnan, and T. Kreouzis, "An optically controlled phase shifter employing the organic semiconductor poly(3-hexylthiophene)," *Applied Physics Letters,* vol. 91, Nov 12 2007.

[12] T. I. Jeon, D. Grischkowsky, A. K. Mukherjee, and R. Menon, "Electrical and optical characterization of conducting poly-3-methylthiophene film by THz time-

domain spectroscopy," *Applied Physics Letters,* vol. 79, pp. 4142-4144, Dec 17 2001.

[13] E. Hendry, M. Koeberg, J. M. Schins, L. D. A. Siebbeles, and M. Bonn, "Free carrier photogeneration in polythiophene versus poly(phenylene vinylene) studied with THz spectroscopy," *Chemical Physics Letters,* vol. 432, pp. 441-445, Dec 11 2006.

[14] P. Parkinson, J. Lloyd-Hughes, M. B. Johnston, and L. M. Herz, "Efficient generation of charges via below-gap photoexcitation of polymer-fullerene blend films investigated by terahertz spectroscopy," *Physical Review B,* vol. 78, Sep 2008.

[15] P. D. Cunningham and L. M. Hayden, "Carrier dynamics resulting from above and below gap excitation of P3HT and P3HT/PCBM investigated by optical-pump terahertz-probe spectroscopy," *Journal of Physical Chemistry C,* vol. 112, pp. 7928-7935, May 29 2008.

[16] C. Stelling, C. R. Singh, M. Karg, T. A. F. Konig, M. Thelakkat, and M. Retsch, "Plasmonic nanomeshes: their ambivalent role as transparent electrodes in organic solar cells," *Scientific Reports,* vol. 7, Feb 15 2017.

[17] M. S. Hilario, B. W. Hoff, M. P. Young, and M. T. Langan, "W-Band Free-Space Dielectric Material Property Measurement Techniques for Beamed Energy Applications," presented at the 53rd AIAA Aerospace Sciences Meeting, Kissimme, Florida, 2015.

[18] E. Kemptner and S. Thurner, "Free space material characterization for microwave frequencies," presented at the 6th European Conference on Antennas and Propagation (EUCAP), Prague, Czech Republic, 2012.

[19] O. Buyukozturk, T. Y. Yu, and J. A. Ortega, "A methodology for determining complex permittivity of construction materials based on transmission-only coherent, wide-bandwidth free-space measurements," *Cement & Concrete Composites,* vol. 28, pp. 349-359, Apr 2006.

[20] S. Khanal, T. Kiuru, J. Mallat, O. Luukkonen, and A. V. Raisanen, "Measurement of Dielectric Properties at 75-325 GHz using a Vector Network Analyzer and Full Wave Simulator," *Radioengineering,* vol. 21, pp. 551-556, Jun 2012.

[21] C. D. Gamlath, D. M. Benton, and M. J. Cryan, "Microwave Properties of an Inhomogeneous Optically Illuminated Plasma in a Microstrip Gap," *IEEE Transactions on Microwave Theory and Techniques,* vol. 63, pp. 374-383, Feb 2015.

[22] M. N. Afsar, "Precision Millimeter-Wave Measurements of Complex Refractive-Index, Complex Dielectric Permittivity, and Loss Tangent of Common Polymers," *IEEE Transactions on Instrumentation and Measurement,* vol. 36, pp. 530-536, Jun 1987.

[23] J. Ji, C. Y. Luo, Y. K. Rao, F. R. Ling, and J. Q. Yao, "Investigation of optical pump on dielectric tunability in PZT/PT thin film by THz spectroscopy," *Optics Express,* vol. 24, pp. 15212-15221, Jul 11 2016.

[24] A. H. Boughriet, C. Legrand, and A. Chapoton, "Noniterative stable transmission/reflection method for low-loss material complex permittivity determination," *IEEE Transactions on Microwave Theory and Techniques,* vol. 45, pp. 52-57, Jan 1997.

[25] J. Bakerjarvis, E. J. Vanzura, and W. A. Kissick, "Improved Technique for Determining Complex Permittivity with the Transmission Reflection Method," *IEEE Transactions on Microwave Theory and Techniques,* vol. 38, pp. 1096-1103, Aug 1990.

[26] K. Sarabandi and F. T. Ulaby, "Technique for Measuring the Dielectric-Constant of Thin Materials," *IEEE Transactions on Instrumentation and Measurement,* vol. 37, pp. 631-636, Dec 1988.

[27] U. C. Hasar, "Permittivity Measurement of Thin Dielectric Materials from Reflection-Only Measurements Using One-Port Vector Network Analyzers," *Progress in Electromagnetics Research-Pier,* vol. 95, pp. 365-380, 2009.

[28] U. C. Hasar, "Unique Retrieval of Complex Permittivity of Low-Loss Dielectric Materials From Transmission-Only Measurements," *IEEE Geoscience and Remote Sensing Letters,* vol. 8, pp. 562-564, May 2011.

[29] B. Yang, R. J. Wylde, D. H. Martin, P. Goy, R. S. Donnan, and S. Caroopen, "Determination of the Gyrotropic Characteristics of Hexaferrite Ceramics From 75 to 600 GHz," *IEEE Transactions on Microwave Theory and Techniques,* vol. 58, pp. 3587-3597, Dec 2010.

[30] W. F. Sun, B. Yang, X. K. Wang, Y. Zhang, and R. Donnan, "Accurate determination of terahertz optical constants by vector network analyzer of Fabry-Perot response," *Optics Letters,* vol. 38, pp. 5438-5441, Dec 15 2013.

[31] E. K. Kowalczuk, R. D. Seager, and C. J. Panagamuwa, "Investigating Factors Affecting Photoconductive Microwave Switch Performance using 3D EM Simulation," *2015 Loughborough Antennas & Propagation Conference (Lapc),* 2015.

[32] H. S. Su, I. Shoaib, X. D. Chen, and T. Kreouzis, "Optically Tuned Polarisation Reconfigurable Antenna (Invited)," *2012 IEEE Asia-Pacific Conference on Antennas and Propagation (Apcap)*, pp. 265-+, 2012.

[33] R. L. Haupt, J. Flemish, and D. Aten, "Adaptive Nulling Using Photoconductive Attenuators," *IEEE Transactions on Antennas and Propagation*, vol. 59, pp. 869-876, Mar 2011.

[34] J. R. Flemish and R. L. Haupt, "Optimization of a Photonically Controlled Microwave Switch and Attenuator," *IEEE Transactions on Microwave Theory and Techniques*, vol. 58, pp. 2582-2588, Oct 2010.

[35] A. Andy, P. Alizadeh, K. Z. Rajab, T. Kreouzis, and R. Donnan, "An Optically-Switched Frequency Reconfigurable Antenna for Cognitive Radio Applications," *2016 10th European Conference on Antennas and Propagation (Eucap)*, 2016.

[36] P. Alizadeh, A. S. Andy, C. Parini, and K. Z. Rajab, "A Reconfigurable Reflectarray Antenna in Ka-Band Using Optically Excited Silicon," *2016 10th European Conference on Antennas and Propagation (Eucap)*, 2016.

[37] KeysightTechnologies, "N5230C PNA-L Network Analyzer [10MHz-20GHz]."

[38] B. Yang, X. K. Wang, Y. Zhang, and R. S. Donnan, "Experimental characterization of hexaferrite ceramics from 100 GHz to 1 THz using vector network analysis and terahertz-time domain spectroscopy," *Journal of Applied Physics*, vol. 109, Feb 1 2011.

[39] N. Katzenellenbogen and D. Grischkowsky, "Electrical Characterization to 4 Thz of N-Type and P-Type Gaas Using Thz Time-Domain Spectroscopy," *Applied Physics Letters*, vol. 61, pp. 840-842, Aug 17 1992.

[40] T. I. Jeon, D. Grischkowsky, A. K. Mukherjee, and R. Menon, "Electrical and optical characterization of conducting polymers by THz time-domain spectroscopy," *Synthetic Metals*, vol. 135, pp. 451-452, Apr 4 2003.

[41] R. A. Lewis, *Terahertz Physics*. NY: Cambridge University Press, 2012.

[42] Refractive Index database [Online]. Available: https://refractiveindex.info/?shelf=other&book=P3HT-PC61BM&page=Stelling

[43] A. S. Andy, O. Sushko, T. Kreouzis, and R. S. Donnan, "Optically-Tunable Organic Semiconductor Heterojunction P3HT-PCBM for Millimeter-wave Applications," *2015 40th International Conference on Infrared, Millimeter and Terahertz Waves (Irmmw-Thz)*, 2015.

[44] A. S. Andy, J. W. E. Kneller, O. Sushko, R. Dubrovka, T. Kreouzis, and R. S. Donnan, "Dynamic organic lens using photosensitive semiconductor

(P3HT:PCBM) for millimetre-wave applications," *2017 42nd International Conference on Infrared, Millimeter, and Terahertz Waves (IRMMW-THz)*, 2017.

[45] T. F. Gallacher, R. Sondena, D. A. Robertson, and G. M. Smith, "Optical Modulation of Millimeter-Wave Beams Using a Semiconductor Substrate," *IEEE Transactions on Microwave Theory and Techniques*, vol. 60, pp. 2301-2309, Jul 2012.

[46] L. J. Cheng and L. Liu, "Optical modulation of continuous terahertz waves towards cost-effective reconfigurable quasi-optical terahertz components," *Optics Express*, vol. 21, pp. 28657-28667, Nov 18 2013.

[47] KeysightTechnologies, "N5244A PNA-X Microwave Network Analyzer, 43.5 GHz."

[48] D. M. Pozar, *Microwave Engineering*. New Jersey: J. Wiley, 2005.

[49] S. Khelifi, K. Decock, J. Lauwaert, H. Vrielinck, D. Spoltore, F. Piersimoni, *et al.*, "Investigation of defects by admittance spectroscopy measurements in poly (3-hexylthiophene):(6,6)-phenyl C-61-butyric acid methyl ester organic solar cells degraded under air exposure," *Journal of Applied Physics*, vol. 110, Nov 1 2011.

[50] L. Goris, A. Poruba, L. Hod'akova, M. Vanecek, K. Haenen, M. Nesladek, *et al.*, "Observation of the subgap optical absorption in polymer-fullerene blend solar cells," *Applied Physics Letters*, vol. 88, Jan 30 2006.

Chapter 5 Optically-Activated Antennas Using Photosensitive Semiconducting Materials

Based on the operating mechanisms in an optically-activated reconfigurable antenna as discussed in Section 2.3 of Chapter 2, in this chapter discussion is made of the design and analysis of these microstrip-based antennas. The concept of frequency or phase-shifting using photoconductivity in microstrip-based antennas, to attain reconfigurability, has been demonstrated in several previous works [1-3]. In microwave frequencies, the applications of such antennas lie in GSM and WiMAX applications, where these antennas fulfil the multiband and beam-steering requirements. Others have demonstrated the use of optically-tuneable semiconducting materials in waveguide fed arrays at mm-wave frequencies [4, 5]. These antenna arrays have the potential for use in indoor, radar, imaging, and wireless telecommunications applications.

Although, these optically-activated reconfigurable antennas, reported to-date, have demonstrated performances similar to those obtained using electronically-switched reconfigurable antennas, sources of light for illuminating semiconducting materials in such designs, lack practicality. However, these sources do allow Si to operate with excellent on-state characteristics. Consequently, some authors report the use of an optical fibre cable, connected to a laser source, to illuminate the Si switch, by drilling a hole through the substrate and ground plane [6]. However, this illuminating technique increases fabrication complexity of the reconfigurable antenna. A few designs reported in the literature have suggested the use of IR-LEDs as a source of illumination and stated that the maximum output radiance of such LEDs is sufficient for the Si switch to operate as a photoconductive switch [7, 8]. Hence, in order to demonstrate a more practical approach towards attaining reconfigurability using such designs, we have used a medium-resistivity silicon (Si) in a reconfigurable antenna design and illuminated it using an IR-

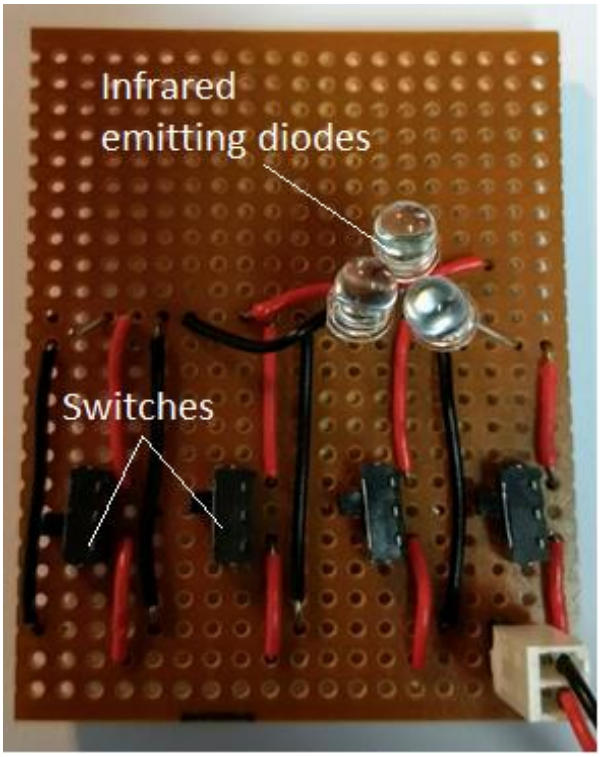

Fig. 5.1. Portable light source with three IREDs and a switching circuitry for turning them on and off individually. The three IREDs together produces a maximum output power of 280 mW at 1mm from a standard photo-detector (power meter).

LED light source (see Fig. 5.1). As discussed in Chapter 3, the performance of a photoconductive switch can be analysed using the measured transmission response of the switch in a microstrip transmission line, the physical properties of the Si switch in the active state is used in a model of an optically-activated antenna and the performance evaluated using an electromagnetic (EM) modelling software CST [9]. A practical application of such a setup has also been proposed in this chapter in Section 5.1.

Another issue in optically-activated antennas using inorganic semiconducting materials is with the fabrication of the photoconductive switches or substrates. Inorganic semiconducting materials, such as Si, are brittle by nature and are quite difficult to cut and fabricate. Additionally, in order to attach them to a metal patch or a transmission line, a metallic glue, such as silver epoxy, is required. As a result, there is a constant hunt for flexible organic materials to replace these conventional semiconductors. Photosensitive organic semiconductors such as poly(3-hexylthiophene), or P3HT, are light weight, flexible, non-brittle, and can be triggered by using white-light LED light source. The fabrication of such materials is very easy. Processes such as spin-coating, drop-casting and spray-coating are used to deposit such polymers onto substrates. Hence the feasibility

of a practical application of such materials is more likely. In Section 5.2 of this chapter we discuss the possibilities of designing an optically-activated phased array using photosensitive organic semiconductors for beam-steering applications.

5.1 Optically-Switched Frequency Reconfigurable Antenna for Cognitive Radio Applications

The recent rise in the number of services supported by wireless communication system has placed demand for efficient use of the radio spectrum. Cognitive radio is a useful and intelligent way of increasing channel efficiency of a wireless system [10]. This type of smart radio is capable of sensing an idle frequency, and then switching to a particular operating frequency for transmission or reception. Hence this intelligent mechanism can be used to allocate individual users to specific frequency bands that are not in use. The sensing unit of the cognitive radio is used to detect idle channels available for use throughout its operating band whereas a frequency reconfigurable unit is used to switch individual operating frequencies for broadcasting [11]. Hence the proposed cognitive radio here are comprised of an ultra-wide band scanning unit and an optically-controlled reconfigurable antenna. Frequency reconfigurability in a cognitive radio system can be achieved using either electronic, mechanical or optical switches. One or many switches can be used in the reconfigurable antenna design to switch between several different narrow-band resonant frequencies. Electronic switches such as PIN-diodes and FETs require biased voltage lines to activate them, which in turn interfere with the radiating wave of the antenna. Additionally, mechanical switches are very complicated to fabricate and tends to be heavy, hampering flexibility of design. Optical switches on the other hand provide immunity from electromagnetic interference since there is high isolation between the controlling signal and the radiating signal of the antenna. In addition, they are light weight and have very high switching speeds between on and off states [12].

An optically-switched cognitive radio essentially consists of an ultra-wide band (UWB) scanning-unit, and an optically-switched reconfigurable antenna unit. Reconfigurability in these antennas is achieved with the use of optical switches, namely Si. A novel antenna with a reconfigurable ground plane is designed and reported in this chapter. With the use of a rectangular block of Si, the length of the ground plane of an antenna can be altered and by changing the area of the ground plane, the operating frequency of the antenna can be controlled. The initial idea, as discussed in Chapter 3,

was to use medium-resistivity Si and extract the dark-state conductivity (5 Sm^{-1}) and active state (70 Sm^{-1}) values and input them in the modelled reconfigurable ground. However, in the active state of the antenna, the reconfigurable ground has to attain high conductivity ($\sigma \geq 150$ Sm^{-1}) to behave like a metal and reduce loss due to absorption. As a result, the reconfigurable ground was modelled as high-resistivity Si (dark-state σ: 4.25 x 10^{-4} Sm^{-1}; active state σ: 168 Sm^{-1}) in CST. These estimated values were obtained from Gamlath *et al.* [13].

An UWB antenna was designed by modifying the well-known PICA (Planar inverted cone antenna) antenna (see Fig. 5.2a). The bottom layer of the PICA antenna is a partial ground. The feedline of the antenna is a microstrip line and the substrate used is Taconic (TLY-5). Fig. 5.3 shows the antenna return loss and depicts the antenna frequency sensing domain [2.6 − 8 GHz]. Fig. 5.4 on the other hand shows the maximum gain of the antenna throughout the frequency-domain [2 − 9 GHz]. In addition, the E- and H-plane farfield radiation patterns of the UWB antenna show an omni-directional nature.

The optically-switched reconfigurable unit is a narrow-band antenna with resonant frequencies at 3.9 and 6.2 GHz for the dark and active states of the antenna respectively. The narrow band antenna was modified based on existing omni-directional reconfigurable antennas reported in [11]. The antenna was modified using CST Studio Suite by designing a diamond-shaped patch in the top layer, fed via a microstrip line; the bottom layer being a partial ground (12 mm x 24 mm). The dimensions of the reconfigurable antenna design in shown in Fig. 5.2b. The reconfigurable ground is constructed with a 4.5 mm x 24 mm

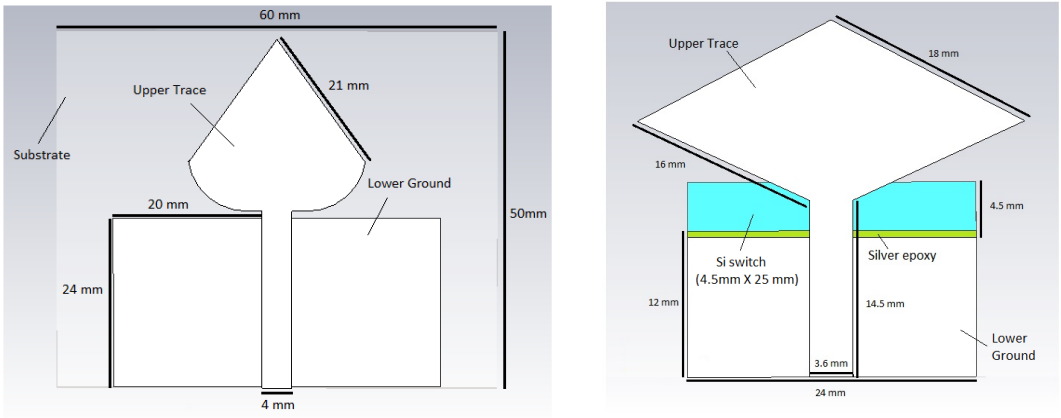

a) b)

Fig. 5.2. Prototype of an a) UWB antenna operating from 2.6 to 8 GHz b) diamond-shaped frequency-switched antenna with an optically-reconfigurable ground (blue block). Tuneability of the reconfigurable ground is attained with the using of the IREDs shown in Fig. 5.1.

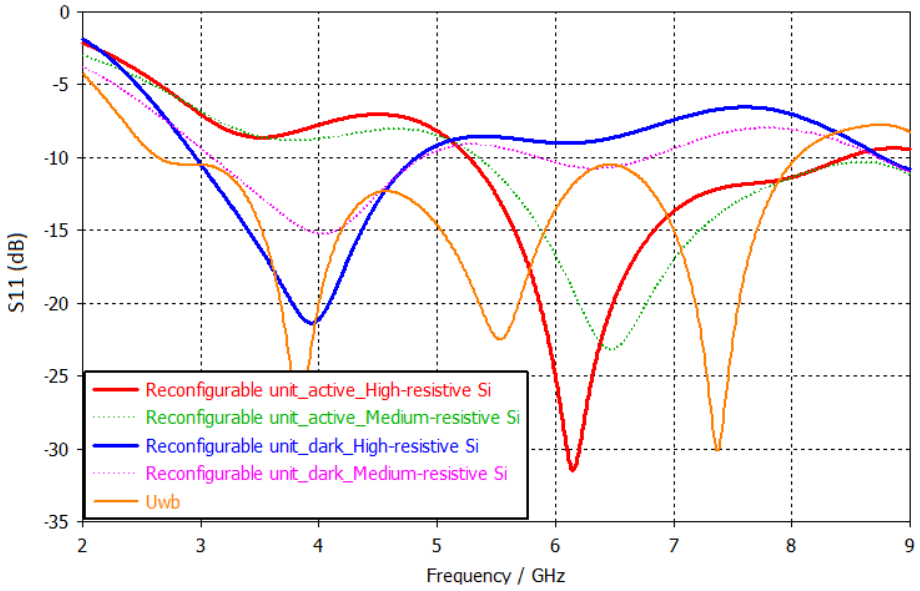

Fig. 5.3. Simulated return loss measurement of the UWB scanning antenna, and optically-switched reconfigurable antenna at dark and active states. The UWB antenna shows a wide-band characteristics from 2.7 to 8 GHz and the reconfigurable antenna switches its operating frequency from 3.9 GHz in the dark-state to 6.2 GHz in the active state.

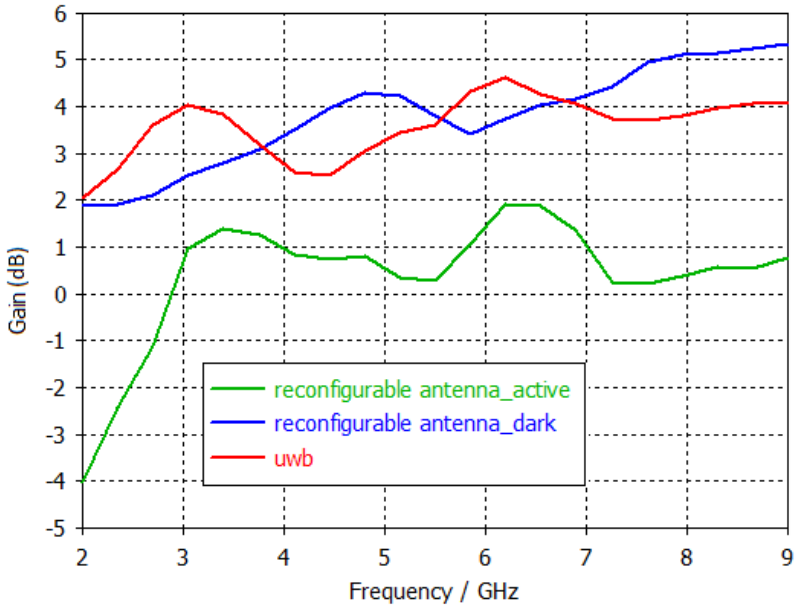

Fig. 5.4. Maximum Gain of the UWB scanning antenna, and the optically-switched reconfigurable antenna at dark and active states throughout the frequency-domain [2-9 GHz]. The gain of the UWB antenna is sufficient for channel sensing throughout its operating frequency-domain. The dark-state gain of the reconfigurable antenna is higher than the active-state gain because the reconfigurable antenna loses power due to increase in losses of the Si switch in its active state.

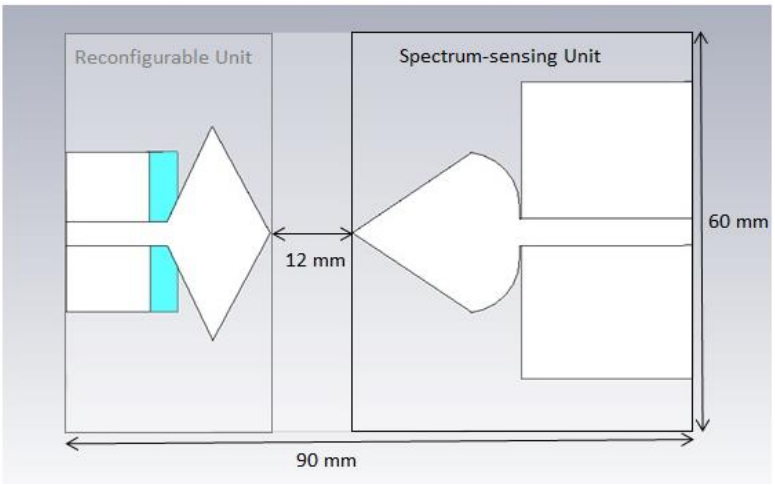

Fig. 5.5. Prototype of the optically-switched cognitive radio system. The sensing unit (UWB antenna) continuously senses the available channels and the reconfigurable unit (optically-switched reconfigurable antenna) switches to the operating bands (3.9 and 6.2 GHz in this case).

x 0.38 mm rectangular slab of high-resistivity Si attached to the partial ground of the reconfigurable antenna. The Si switch (see Fig. 5.5) is positioned on the edge of the ground plane using silver epoxy.

CST Studio Suite was used to account for the change in conductivity of the plasma layer of the ground-plane Si switch. In dark-state operation of the antenna, the Si behaves as dielectric and the effective length of the conducting partial ground plane remains at 12mm. However, active state Si behaves as a metal (168 Sm^{-1}) due to excess electrons being generated, and extends the partial ground to a longer length (16 mm). The change in length causes the resonant frequency of the antenna to shift from 3.9 to 6.2 GHz. In the fabricated prototype of such a reconfigurable antenna, the array of LEDs will be placed 1mm away from the reconfigurable ground plane, keeping the whole system compact. Construction of the optically-switched cognitive radio requires inclusion of both the scanning and the reconfigurable unit in the same antenna substrate, but the two antennas are fed with two different feeds. The coupling between the two units is kept below -20 dB by ensuring a distance of 12 mm between tips of the spade-shaped and the diamond-shaped structures. The optically-switched cognitive radio system is shown in Fig. 5.5.

Firstly, the operating frequency of the reconfigurable antenna for dark and active states falls within the operating band of the UWB-sensing unit, providing the functionality of a cognitive radio. Secondly, the dispersive gain graph shows that the gain of the UWB antenna is sufficient for channel sensing throughout its operating frequency-domain. The dark-state gain of the reconfigurable antenna is higher than the active-state gain because,

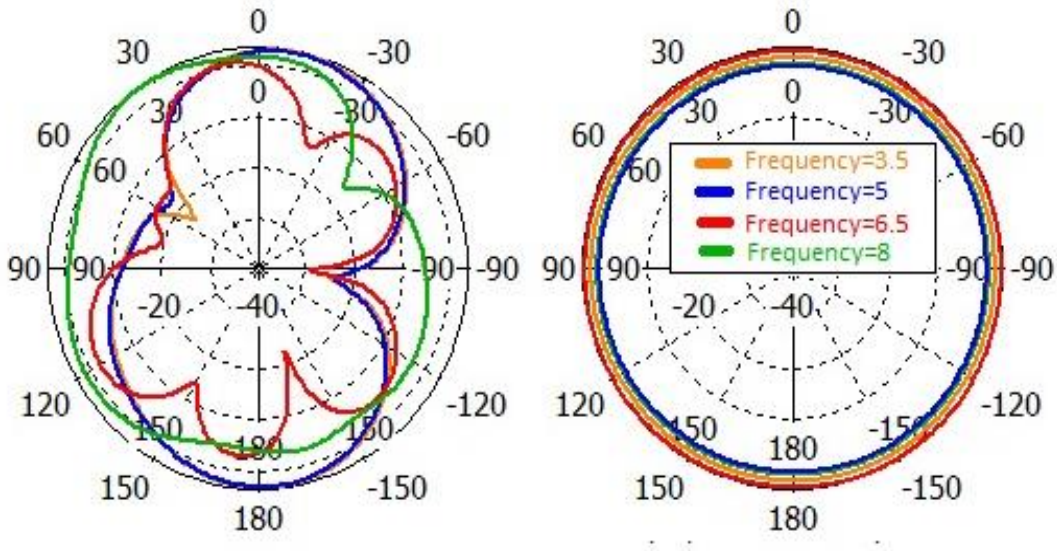

a) b)

Fig. 5.6. a) Simulated E-Plane (X-Y) radiation pattern of the UWB sensing antenna b) H-plane (X-Z) radiation pattern of the sensing antenna. The radiation pattern of the UWB shows an omni-directional nature for certain frequencies (3.5, 5 6.5 and 8 GHz) in the frequency-domain [2-9 GHz].

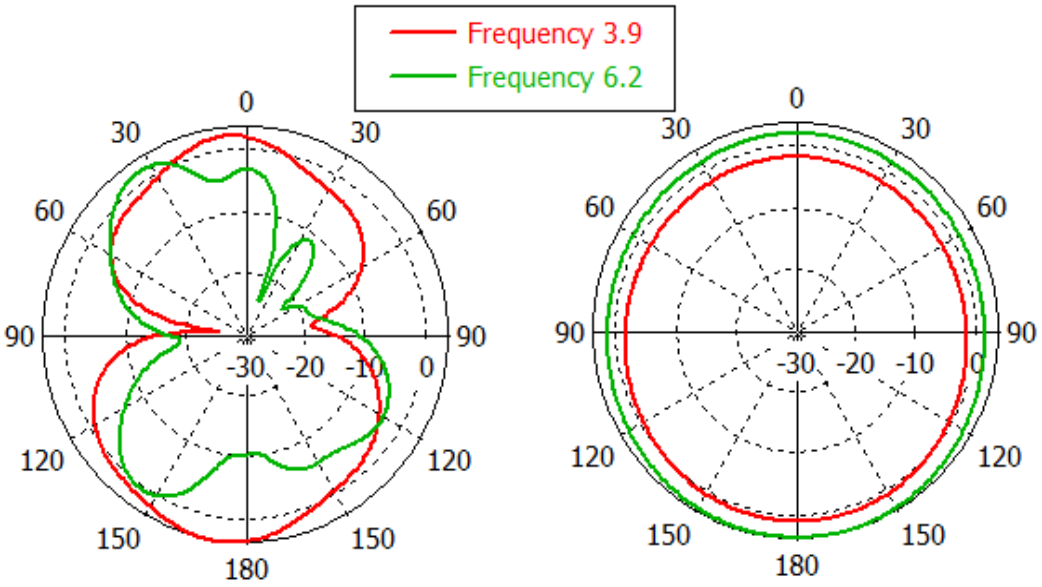

a) b)

Fig. 5.7. a) Simulated E-Plane (X-Y) radiation pattern of the optically-switched reconfigurable antenna for dark (3.9 GHz) and active (6.2 GHz) states b) H-plane (X-Z) radiation pattern of the optically-switched reconfigurable antenna for dark (3.9 GHz) and active (6.2 GHz) states.

in its active state, the reconfigurable antenna loses power due to increase in losses of the Si switch. The normalized farfield polar plots of both prototypes- (UWB and reconfigurable), show radiation pattern of a dipole antenna in both active and dark states (see Fig. 5.6-5.7). This confirms the omni-directional nature of both the antennas.

An optically-switched cognitive radio has been modelled and simulation results reported. The active state in the optically-switched transmission line with a medium-resistivity Si switch was initiated with the use of an array of LED light sources (880 nm). This arrangement of light source can be used to pump the reconfigurable ground of a fabricated prototype. As reported in Chapter 3 the conductivity of the medium-resistivity Si in the dark and active states has been estimated by matching simulated with measured transmission results of the optically-switched transmission line. Similarly, for future work, the conductivity of any photosensitive semiconducting crystalline material in both the dark and active states can be estimated and then input to the modelled cognitive radio system, in order to evaluate the performance of the system. This sort of performance evaluation using a modelled system, provides a feasibility check on the expected output of such designs.

5.2 Optically-activated phase shifter for antenna beam steering

The use of photosensitive organic semiconductors in EM applications was first proposed by Tang et al [14]. It was demonstrated that a 9°±1° phase shift using a simple transmission line structure and an 18°±1° phase shift is achievable using a meandering conductor strip transmission line. White-light irradiance was used to trigger the photosensitive organic semiconductor substrate of these transmission lines. These findings led to a conclusion that it is possible to manipulate EM waves using such photosensitive organic semiconducting materials. In order to demonstrate an application of such a behaviour, an optically-activated two-element patch antenna array was designed with integrated optically-controlled phase-shifters. The phase shifting of such an antenna is derived from optically-induced generation of photo-excited states in the organic that translate into an effective dielectric response. This response can be engineered to induce a differential phase offset between microstrip antenna circuit elements.

Poly (3-hexyltiophene) (P3HT) is an organic-semiconductor whose dielectric response varies with irradiance due to its optical absorption properties and moderately high mobility of induced charge carriers. As explained in Chapter 3, by adding an n-type polymer PCBM to P3HT, the organic nature of P3HT is distorted. This enables

dissociation of free electrons easily, since the recombination process of an excited electron from conduction band to valence band is to somewhat restricted. As a result more photo-generated carriers are expected in the active region of a P3HT:PCBM blend compared to neat P3HT. These organic polymers, although powdery in form, can still be spray-coated onto any hard surface when dissolved with organic solvents.

The electron-hole excitation region generated in the organic semiconductor layer due to external illumination spreads throughout the dielectric layer of the substrate. Consequently, this induces a complex permittivity shift in the illuminated region, which attains a different value to that of the region left un-illuminated. This phenomenon can be best explained using classical electron-hole plasma theory demonstrated in Section 3.1 of Chapter 3, although there is no plasma region in organics. Here an analogy between the electron-hole excitation region in organics has been made with the plasma region of inorganic semiconductors. The generation of free carriers in a photo-sensitive material in turn leads to an effective change in the permittivity of the active region as per (3.19). Hence when the organic layer is illuminated with differential illumination, what is observed is a relative phase shift between two regions, namely the activated and dormant patch. As a result factors such as propagation, signal velocity and impedance in the active region will be different to the dormant. This change in velocity of the electromagnetic wave propagating in the excitation region causes the beam to swing.

There are different techniques for impedance matching of microstrip antennas to a transmission line. These methods are readily deployed in antenna designs and have been proven to obtain maximum power transfer. One of these methods is single stub-matching or tuning, which works with the simple principle of having an open or short circuited length in parallel or series with the transmission line at a given distance from the load [15]. This concept was used to design the two-element patch antenna along with a Wilkinson power divider to split the power equally among the two arms of the power divider. A micro-milling machine was used to fabricate the antenna array [16]. After that, the antenna array was coated with P3HT:PCBM using spray-coating technique in the School of Physics and Astronomy at QMUL.

The primitive mechanism of the antenna array is used to exemplify a phase difference at the output due to the difference in permittivity of the organic semiconducting material during illumination. The prototype two-element antenna array was designed using CST. The real antenna was fabricated on FR-4 substrate with a dielectric constant

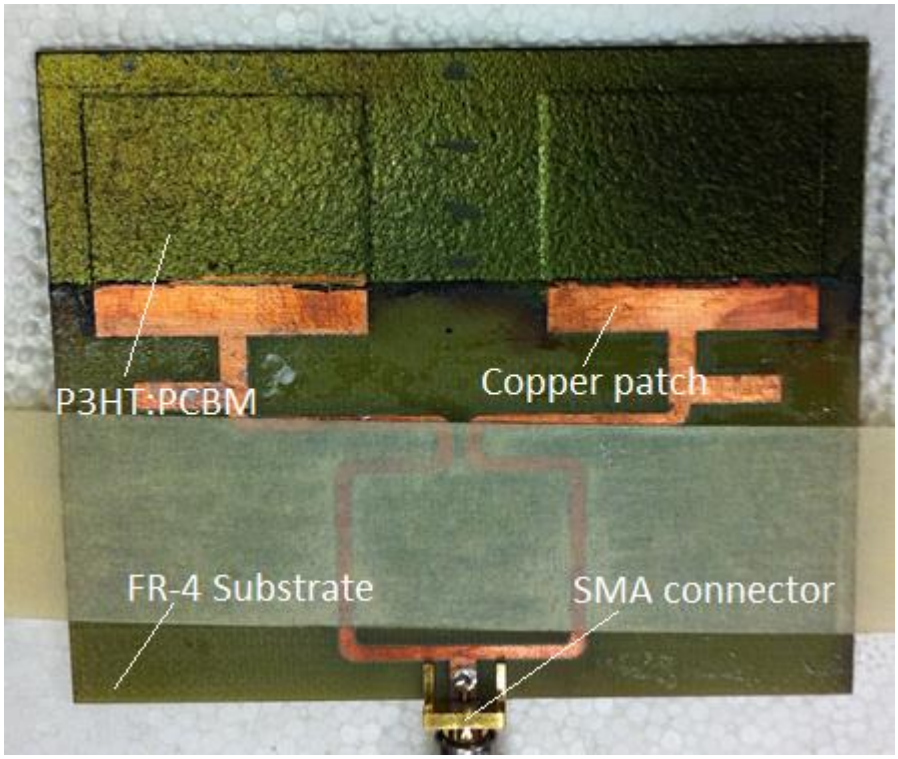

Fig. 5.8. Fabricated two-element patch antenna array on FR-4 substrate with P3HT:PCBM spray-coated over an area of 25.12 x 91.79 mm^2.

of 4.3 according to the prototype design in CST. The patches were then coated with the P3HT:PCBM blend over an area of 25.12 x 91.79 mm^2. P3HT was spray-coated onto the patches and left to dry for two days inside a vacuum chamber in darkness. Fig. 5.8 shows the fabricated prototype of the optically-activated antenna array. S_{11} measurements were recorded using a PNA-L [17] and far-field radiation patterns of the antenna were measured inside the anechoic chamber in the Antenna Laboratory.

The ratio of 0.95:0.5 P3HT: PCBM was used and the blend was treated with an organic solvent dichlorobenzene to promote efficient dissolving. In order to dissolve lumps of P3HT quickly, the solution was placed on a hot plate at 90°C. The P3HT:PCBM blend was placed in small vials and an air brush was used to accurately aim the spraying onto the desired area. The even spraying of the mixture led to a more uniform thickness of the organic layer. Once the 910mg (95%:5% P3HT:PCBM) mixture was deposited onto the desired region of the patch antenna the thickness of the P3HT layer was measured. The thickness was measured at different points on the desired region by making small scratches through the substrate using the profilometer [18]. The depth of the blend varied from ~ 55 to 65 µm. The density of P3HT is estimated to be 1.1g cm^{-3} [19]. With an area of deposition of around 25.12 x 91.79 mm^2 and 0.91g mass of

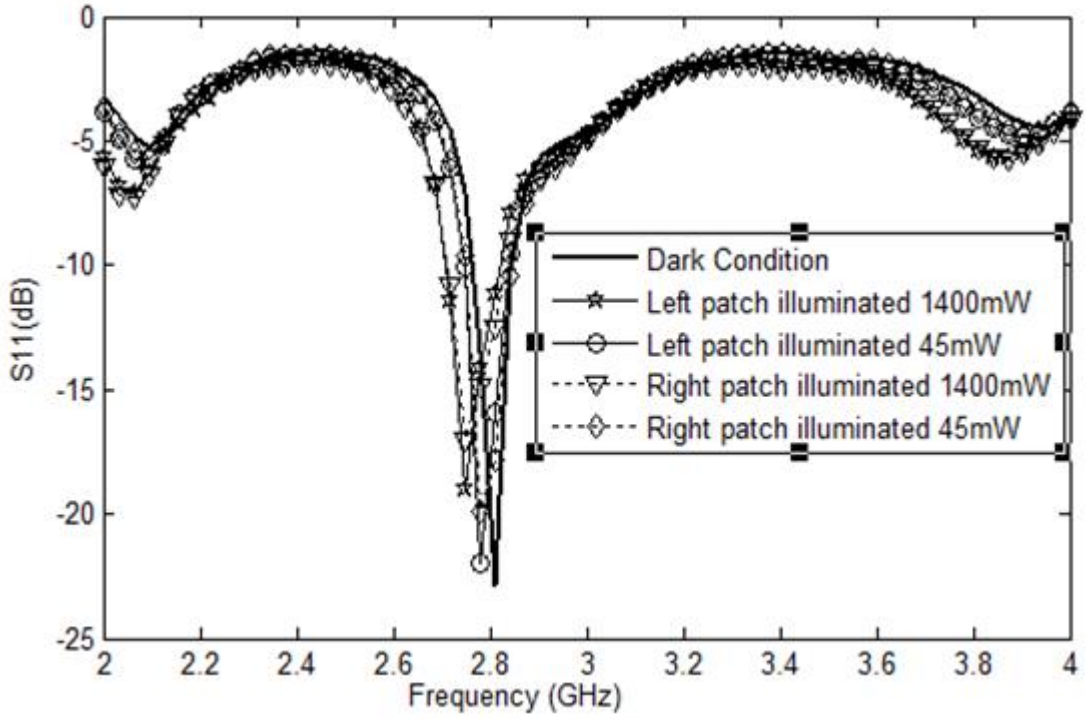

Fig. 5.9. Return loss measurements of the fabricated antenna with varied illumination intensities. Noticeable shifts in the resonant frequency of the two-element patch antenna array is observed when an intensity of 1.4 W (over an area of 9.62 cm^2) is applied on the left or right patch independently.

P3HT:PCBM a thickness of roughly 0.4 mm was estimated. A final thickness 60 µm was achieved as a result of loss due to spillage.

The return loss (S11) of the fabricated two-element patch antenna array was measured at different illumination intensities using a PNA-L. The antenna array was illuminated using a high intensity illumination source (visible light) Spectralux 6000 [19]. The return loss has been analysed by considering the effect of external irradiance on the impedance of the antenna by changing the intensity from 45 mW to 1.4 W over an area of 9.62 cm^2. At high intensities of light above 1W, there was significant shift in the resonant frequency of the antenna as shown in Fig. 5.9. It is observed that throughout this range of irradiance, the antenna is impedance matched.

The computational analysis of the two-element antenna design was performed using CST. The impedance of the antenna structure was matched at -25 dB after taking into consideration the organic layer to be deposited onto the patches. In order to investigate the behaviour of the P3HT illumination in CST, data from previous work was used [20]. Empirical values of $\varepsilon_r = 3.0$, $\tan\delta = 0.02$ for dormant conditions and $\varepsilon_r = 2.72$,

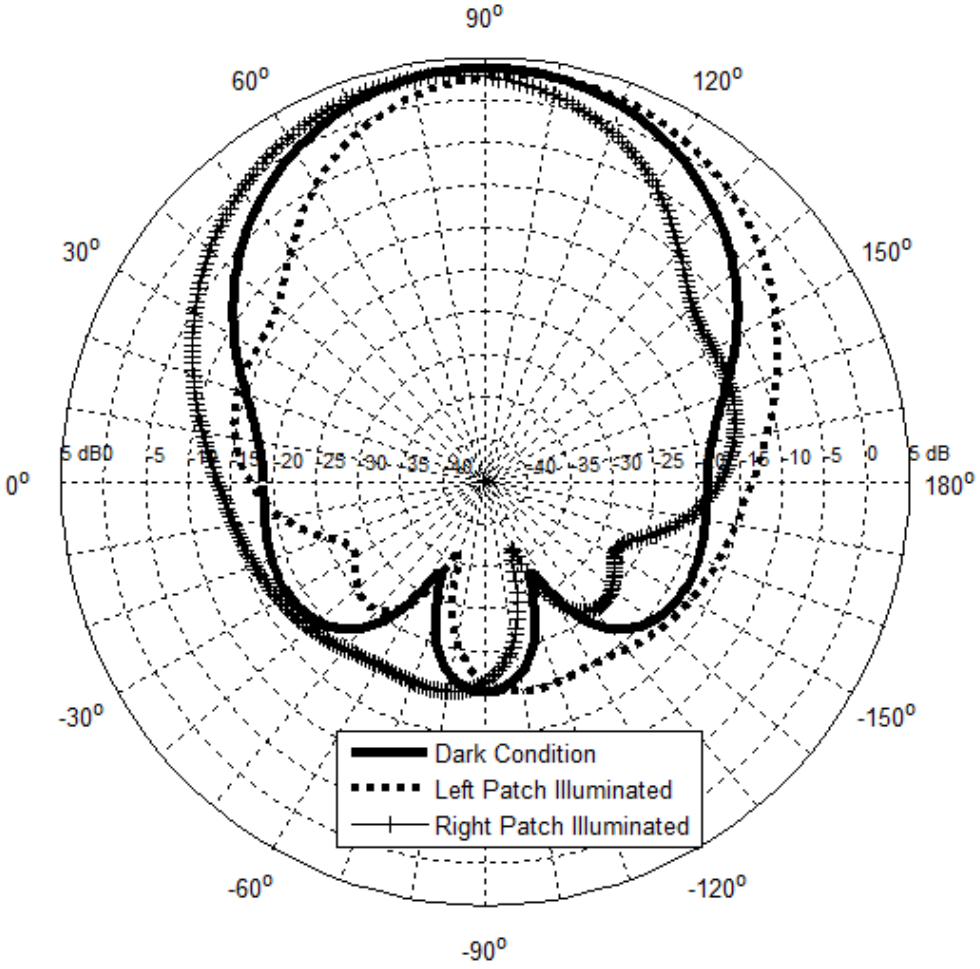

Fig. 5.10. Farfield pattern of the prototype two-element antenna array simulated using CST showing a symmetrical beam steer of 11° for both illumination conditions (right and left).

tanδ = 0.12 for illumination were inputs. Fig. 5.10 shows the comparison of the beam steer between three illumination conditions, namely: dormant (or dark) (ε_{left} = 3.0| ε_{right} = 3.0), right illuminated (ε_{left} = 3.0| ε_{right} = 2.72), and left illuminated (ε_{left} = 2.72| ε_{right} = 3.0). A symmetrical beam steer of 11° was observed for both illumination conditions (right and left) from the farfield radiation pattern in CST.

During farfield radiation pattern measurements, four different illumination conditions were analysed and compared. The farfield radiation patterns of the two-element antenna were obtained in an anechoic chamber. Illumination of the patches was facilitated by optical fibre cable. An irradiance of 65mW was obtained inside the anechoic chamber using the fibre optic cable during farfield measurements. Fig. 5.11a and b shows no beam steer for the dark state and normal room light conditions, whereas there were 8 and 22° change in the radiation pattern at both left and right illumination conditions shown in Fig 5.11 c) and d) respectively. An asymmetric shift in the beam radiation pattern was

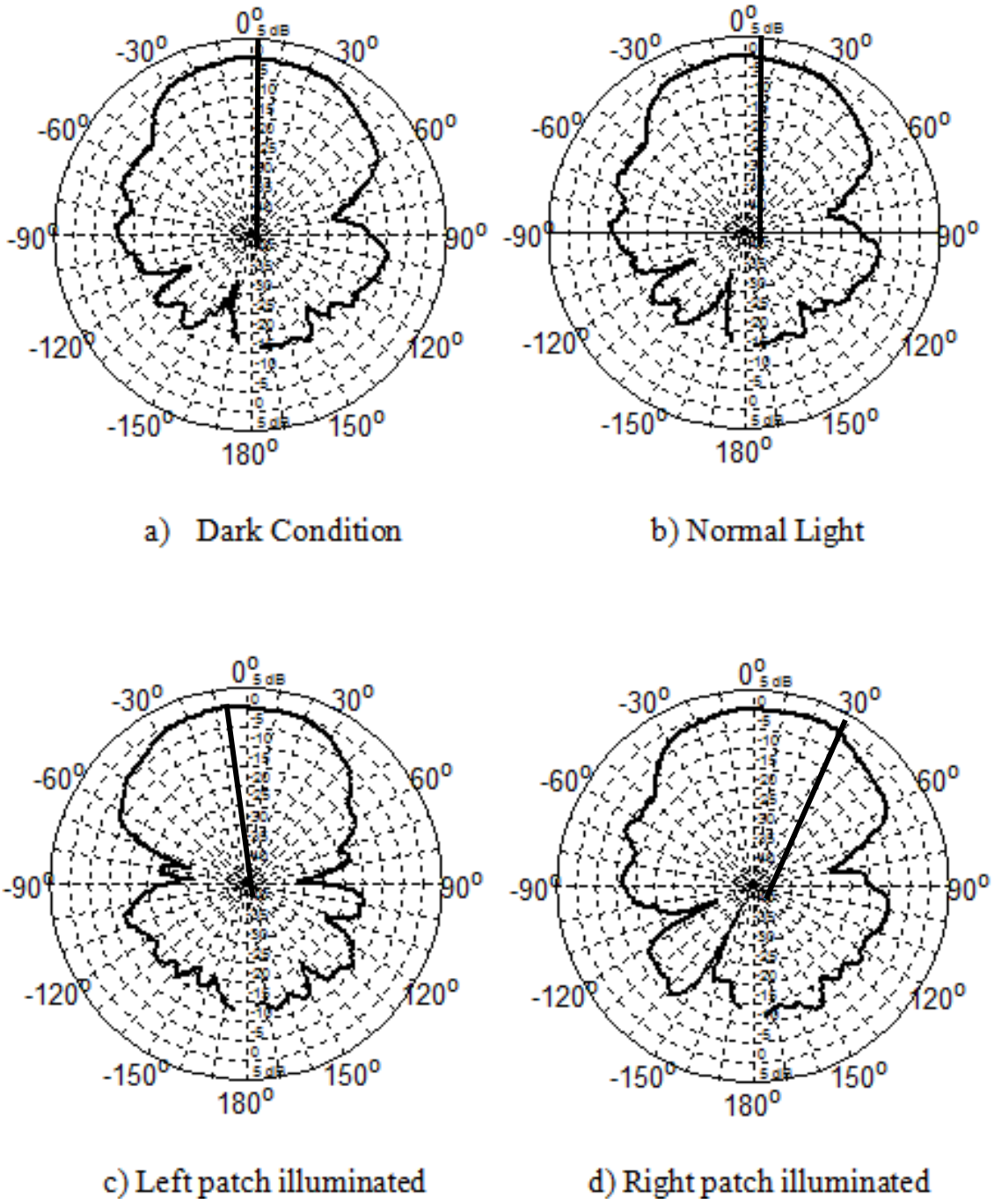

Fig. 5.11. Measured radiation patterns of the two-element patch antenna array under a) Dark condition (beam steer 0º off beam-axis) b) Normal Light condition (beam steer 0º off beam-axis) c) Left patch illuminated condition (beam steer 8º off beam-axis) d) Right patch illuminated condition (beam steer 22º off beam-axis).

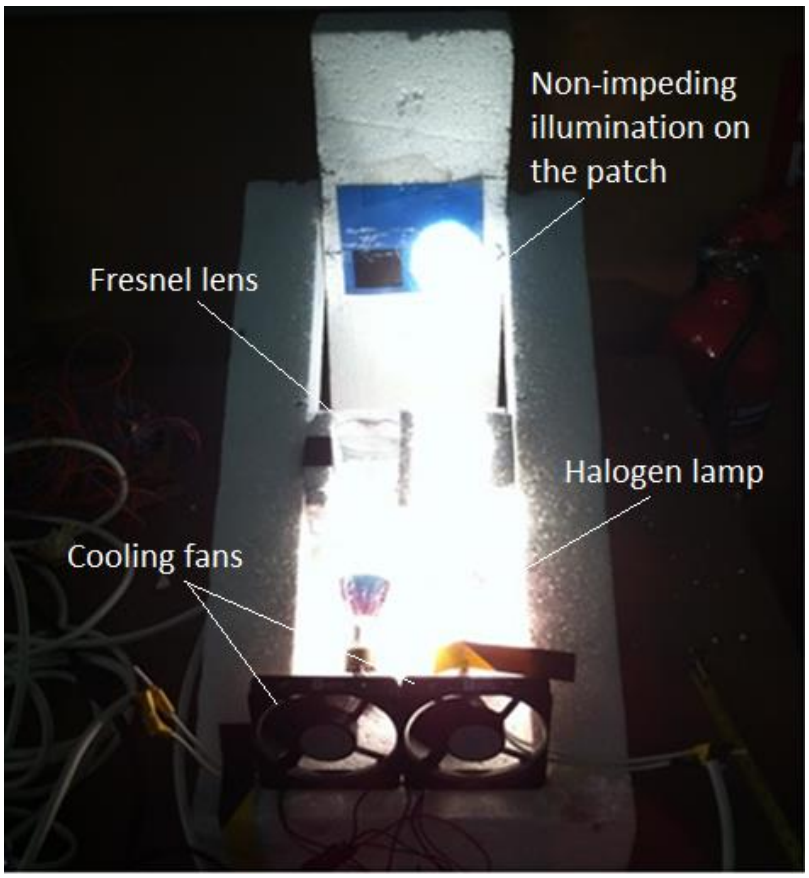

Fig. 5.12. Fabricated Styrofoam gantry for precise positioning of the antenna and halogen lamps for optimum illumination onto the patches of the two-element patch antenna array.

observed with 22º for right patch illumination and 8º for left patch. This difference was mainly accounted for non-optimum illuminating setup.

Keeping in mind the need for an appropriate gantry for optimum illumination for the patches, a Styrofoam gantry was constructed as shown in Fig. 5.9. Two identical Halogen lamps with power ratings of 40W were used as light sources. Two fans were installed in the structure to avoid over heating of the halogen lamps. The lamps were positioned equidistant from two Fresnel lenses installed in between the lamps and the antenna patches. The positioning of the lenses was such that the focal point of the lenses was located at the patches. In addition, since Fresnel lenses were used, they ensured that light from the source were collimated at the patches.

The distance between the patch and the halogen lights was kept constant as shown in Fig. 5.12, and the position of the Fresnel lenses was adjusted to find the optimum distance of the lens from the lamps. The irradiance at the patches was measured using a photo-detector at 532 nm wavelength. At a distance 13.5 cm between the lamps and the

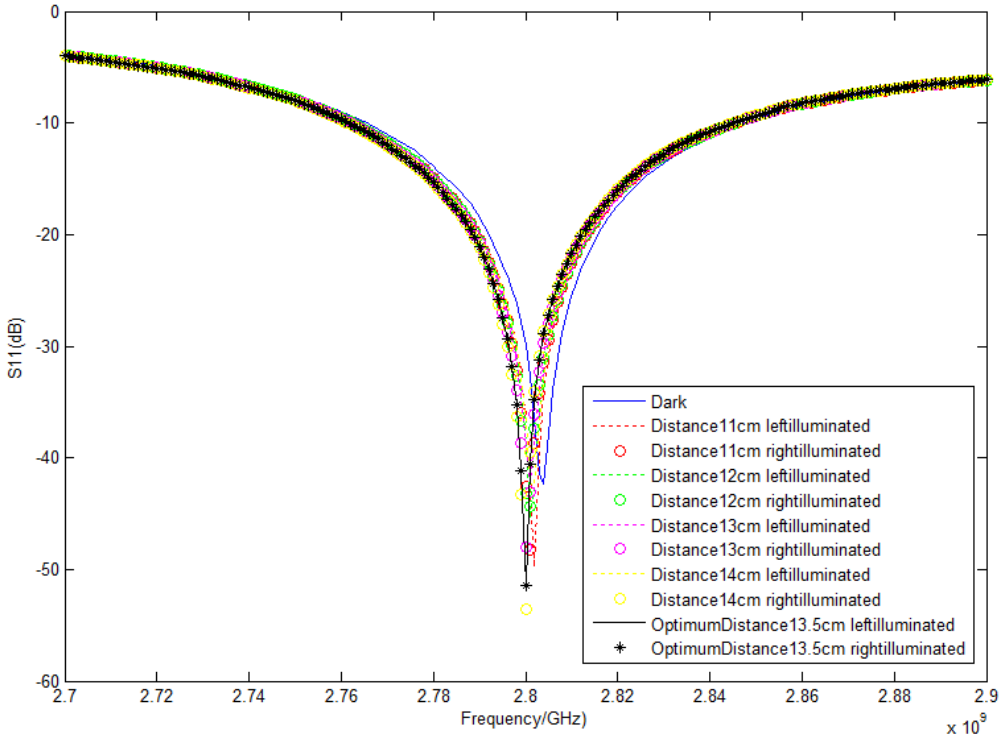

Fig. 5.13. Return loss measurements of the two-element patch antenna array depicting the shift in its resonant frequency at varying intensities (as a function of distance). The maximum shift in the resonant frequency of the antenna array was observed with illumination at a distance of 13.5 cm from the halogen light source.

lenses, and 8.5 cm between the lenses and the patches, a maximum of 165 mW irradiance was measured for both incident light sources. The return loss of the two-element patch antenna array was measured at different distances of the lens from the source. The return loss measurements also proved the fact that at the optimum distance between the source and the light, i.e. when the focal point is at the patches, the maximum frequency shift is observed (see Fig. 5.13).

The return loss measurements have shown a respectable impedance-matched condition for both off (dormant/dark) and on (optimum right & left-illuminated conditions) states. Thereafter the farfield radiation pattern measurements were taken in the anechoic chamber and results obtained as depicted in Fig 5.14. The Cartesian plot of the farfield radiation patterns of the antenna array show almost no significant difference between the off-state and on-state (both right illuminated and left illuminated). This observation is explained by comparing the return loss plots Fig. 5.9 and Fig 5.13. In Fig 5.9, firstly it is seen that for a wide range of irradiance being used (upto 1 W, which is impractical for use while measuring the radiation pattern), the light source is a heavy and bulky metallic structure. Secondly, in Fig 5.13, the highest optical (measured at λ =532

nm) power at 13.5cm distance between the lenses and the lamps was recorded as 165 mW and the resultant shift in frequency was only 4MHz.

Thus arises a question, how could there be a beam steer as shown in Fig. 5.11? Hence, further higher power LED lamps were used in the Styrofoam gantry setup with cooling fans to keep them at constant operating temperature for optimum illumination. However, there was still no significant beam steer. An impeding illuminating setup (see Fig. 5.15) was certainly the reason behind the non-uniform beam steer. In addition, thickness of P3HT:PCBM achieved in this work was around 60 µm, whereas Sathi et al [20] have demonstrated the use of 100 µm thickness deposition of P3HT. One reason for no beam steer could be due to the thickness of deposition being not sufficient to shift the main beam off boresight, provided the tuneability of such polymers is very small ($\Delta\varepsilon \approx 0.1$). Additionally, in Figs. 5.9 and 5.13., the resonant frequency of the antenna shows a red shift. Whereas according to the equation $f_0 = c/\lambda\sqrt{\varepsilon}$, where f_0 is the resonant frequency of the radiating element, λ is the wavelength in the substrate, ε the permittivity of the substrate and c having the usual meaning of speed of light, a change in the dielectric constant from ε_r=3.0 to 2.9 should result in a blue shift. This shows the dominance of thermal effect on the resonant frequency shift.

Another reason is that, in this work, the P3HT:PCBM layer was coated on top of the antenna patches for the ease of spray coating. In the modelled design, in CST, it was observed that this unconventional way of depositing a superstrate on top of the patches doesn't result in a significant beam steer of the antenna. The simulated beam steer in Fig. 5.10 resulted from modelling the organic layer below the patches. However, fabricating such a layer between the patch and the substrate is not practical. Also illuminating a layer of organic semiconductor underneath the patches is extremely challenging. As a solution, a concept of a novel antenna array using a transparent (to visible light) substrate and a ground plane was developed. In this way, it was ensured, that the organic layer could be illuminated from underneath through the transparent ground plane and substrate. The main intension of such an investigation was to determine the optimum excitation-region depth at which a minimum useful beam steer is observed using such low-tuneable dielectrics in microwave frequencies.

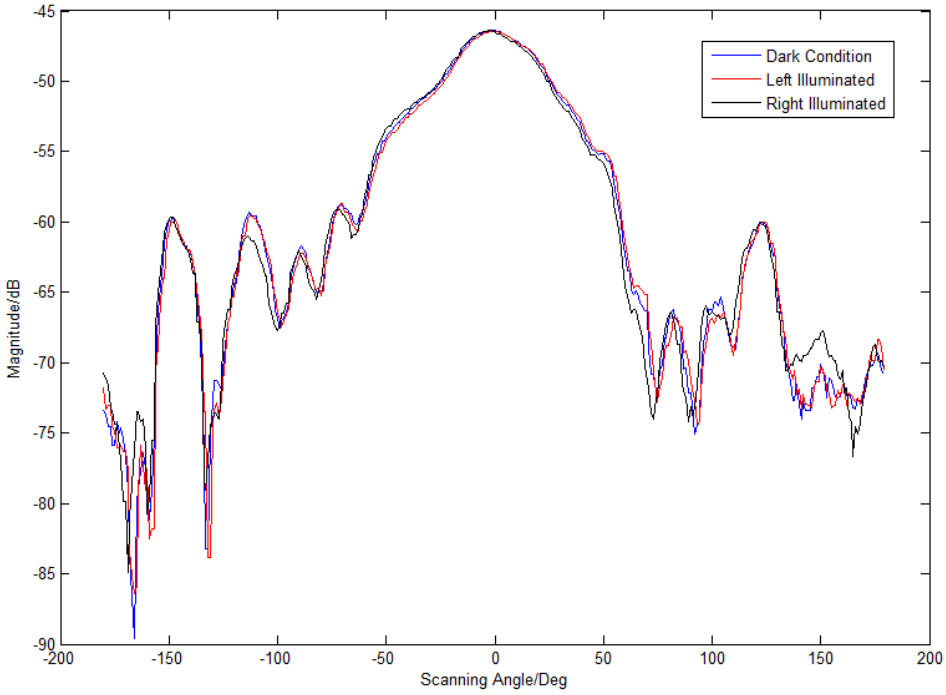

Fig. 5.14. Cartesian plot of the measured farfield radiation pattern of the two-element patch antenna array with right and left patch lit conditions. With the use of the high-power LED light source the right and left patch lit conditions did not result in any significant beam steer.

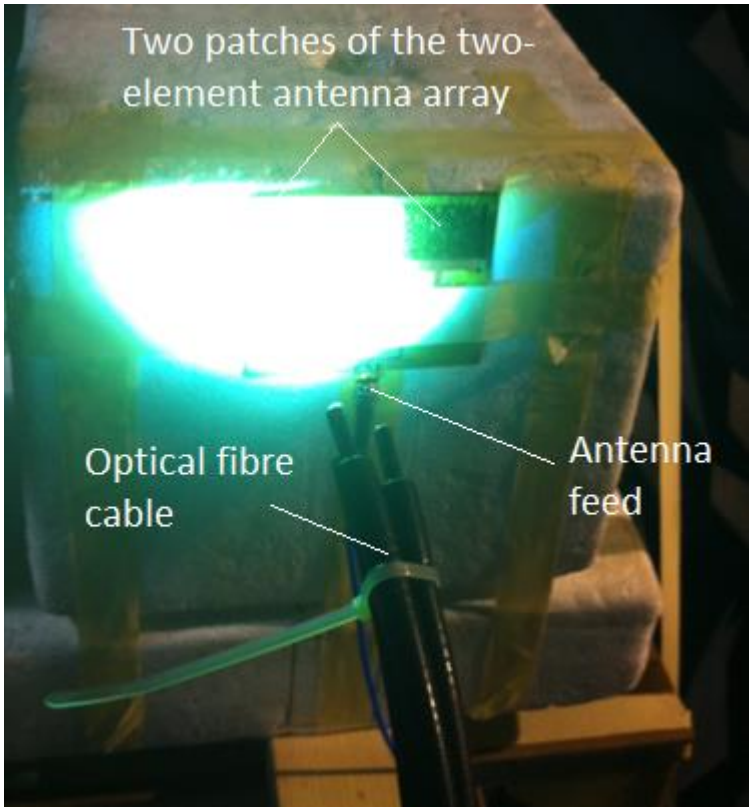

Fig. 5.15. Impeding illumination setup using an optical cable during far-field radiation pattern measurements.

5.3 Optically activated antenna array on glass substrate

A different design approach for an optically-activated phase-shifter can be considered, where the dielectric material for the design is glass instead of FR-4. A thin layer of ITO (indium-tin oxide), which is optically transparent, serves as the ground plane and due to its moderately low electrical resistance it acts as reflector to microwave and Sub-THz frequencies [4]. As depicted in the schematic view of the antenna design in Fig. 5.16, P3HT:PCBM is deposited onto the glass substrate. While fabricating such a design the patch-array and the transmission lines have to be vacuum deposited onto the drop-casted P3HT:PCBM layer. This system is expected to radiate at lower frequencies compared to the previous design because of the effective dielectric constant of glass and P3HT:PCBM is higher than FR-4. However, the measured results of such a design are more likely to match with the simulation results from CST, as in this design P3HT:PCBM is modelled as a substrate rather than a superstrate.

In order to optimally illuminate the organic polymer layer on a substrate, a substrate transparent to white light, sodalime glass, was chosen. The schematic of the layers of the modelled antenna array is shown in Fig.5.16. The substrate of the antenna is

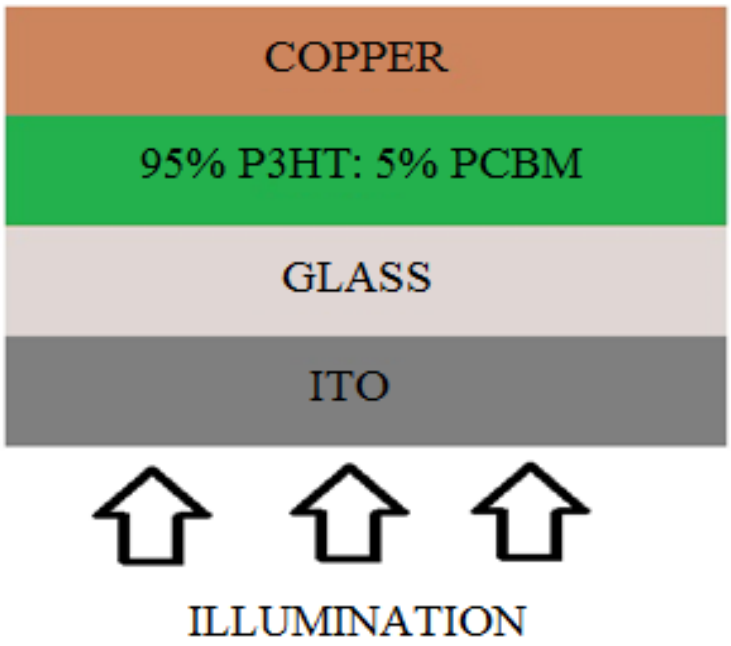

Fig. 5.16. Schematic diagram of the optically-activated antenna. It comprises of 4 layers: copper, organic (95% P3HT: 5% PCBM), sodalime glass, and indium tin oxide (ITO). The glass and ITO are transparent to visible light allowing white-light to reach the organic layer. The top layer (copper) represents the patches and the transmission line of the antenna array.

composed of two layers, the first being the optically-transparent glass substrate and the second the organic polymer. The ground of the antenna is modelled using indium tin oxide (ITO). This is because ITO is a highly regenerate n-type semiconductor, which is transparent to visible light and has a very low resistivity, therefore acting as a reflector at microwave frequencies.

A quasi-optical (QO) transmissometer driven by a PNA-X [21] is used to characterise the organic polymer blend in its dark and active states. The calibrated complex transmission across the sample is measured, which, together with the thickness of the sample and ABCD matrix theory, as described in Section 4.4 of Chapter 4, is used to extract the real and imaginary part of the complex permittivity of the material under test. Estimates of the real and imaginary parts of the complex permittivity of the P3HT:PCBM heterojunction in dark and active states is evaluated. The dark permittivity of the organic blend was estimated at 3.0 and the change, $\Delta\varepsilon$, was estimated at 0.1. In Chapter 4 it was shown how precise measurements of the organic blend under illumination can lead to frequency-dependant dielectric changes of up to 0.7. However, in S-Band, it is very challenging to develop a measurement system for measuring the dark and active dielectric constants of this type of photosensitive material. This is because the beam-waist at these frequencies is extremely large and requires a large sample size and illuminating area. This is why the real and imaginary part of the complex permittivity of the organic blend are estimated at a frequency much higher than the operating frequency (S-Band) of the modelled antenna. In order to test a feasibility check of the effect $\Delta\varepsilon$ has on the beam pattern of the modelled antenna at S-band, these estimates are used while modelling the organic layer in CST.

The complex permittivity of sodalime glass is measured using a split−cylinder resonator [22] driven by a PNA-L. The resonator is designed to resonate at 10 GHz in free-space. The thickness of the glass is measured using a micrometre screw gauge as is 1.11 mm. Depending on the thickness and the dielectric of sample under test, the resonator shifts to a single resonating frequency at the fundamental mode. At the resonant frequency of 8.4 GHz, the real part of sodalime permittivity is estimated to be 6.82 (± 5%) and its loss tangent to be 0.0053 (±2%). These values are used to model the substrate in CST. The dielectric response is extrapolated to S-Band (see Fig. 5.17).

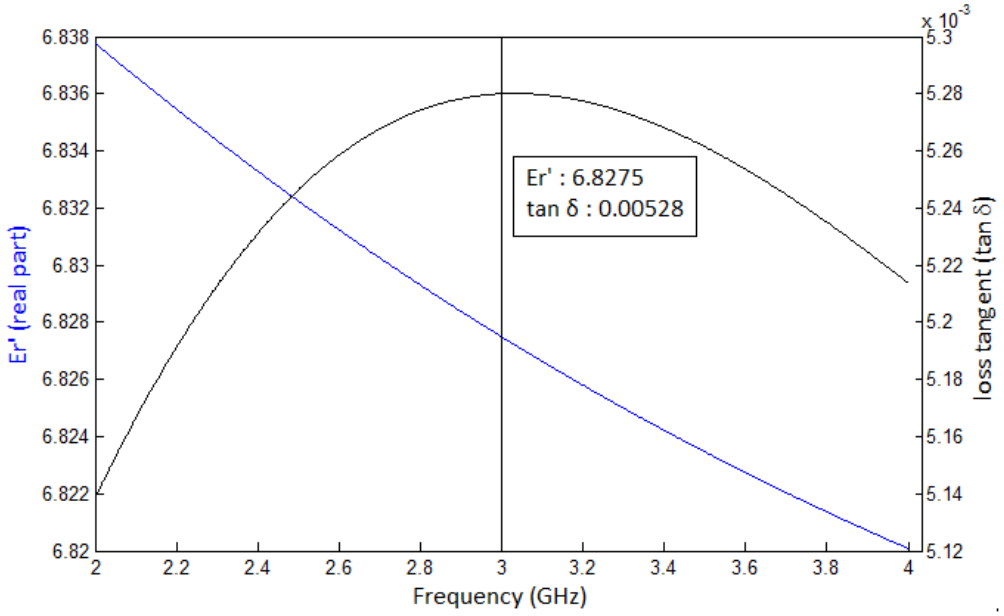

Fig. 5.17. Measured dielectric response of sodalime-glass over S-band using a Split-Cylinder Resonator and extrapolated using CST.

In order to promote accurate modelling of the ITO ground layer in CST, the conductivity of ITO is measured. Measurement of ITO conductivity involved measuring resistivity of ITO using the well-known four-point probe method. This method works with four equi-distant, linear probe points. ITO-coated sodalime glass is used in the antenna design as a substitute to the conventional dielectric-copper model. The thickness of the ITO coating on the glass-substrate is measured by etching and forming a pattern of ITO on the glass substrate to measure the difference between the two layers. ITO thickness is measured using a profilometer to be 110 nm. For a sample thickness w much smaller than the probe separation s, resistivity, ρ, of the sample can be directly calculated by $\rho = (\pi/\ln 2)\, w\, (V/I)$. The measured resistivity was measured to be 1.5×10^{-6} Ω m. A more detailed description of the four-point-probe method is provided in Appendix C.

A two-element patch antenna array for S-band application was designed using CST. The substrate of the antenna array is modelled as a multi-layered structure with the organic polymer layer stacked on top of the soda-lime glass sample. The antenna design was selected from previous work (section 5.2), and modified according to the new substrate definition. The modelled structure consists of four layers; copper, organic polymer, sodalime-glass and ITO, respectively. The substrates and ground plane are modelled using the measured parameters. Measured values of conductivity and thickness of ITO are used to model the ground plane.

The organic layer on the glass-substrate was modelled using a thickness of 0.36 mm, a minimum depth at which a significant beam steer is observed. This layer was placed on top of the glass, covering the whole area (70 x 90 mm^2). The metal patch array was modelled on top of the P3HT:PCBM layer. The return loss of the modelled antenna is analysed (see Fig. 5.18). In the dark-state of the antenna, the impedance is matched at –30 dB. The left and right side illuminating conditions are modelled by changing the dielectric properties of the respective side. Measured values of $\varepsilon_r = 3.0$, $\tan\delta = 0.06$ for dark conditions and $\varepsilon_r = 2.9$, $\tan\delta = 0.089$ for illumination are considered as inputs. Both the right-illuminated and left-illuminated conditions show impedance matching.

Under left-illuminated condition, as the phase of excitation advances, the surface current distribution at the left patch is different from the right, and vice versa for the right-illuminated condition. This demonstrates the fact that there is an uneven distribution in the magnitude of the surface current density vector among the patches during illumination due to the phase lag. A symmetrical beam steer of 5° off boresight was observed for both illuminated conditions from the simulated farfield radiation pattern (see Fig. 5.19). Figs. 5.20a and b shows the surface current distribution of the two-element patch antenna array for left-patch illuminated and right-patch illuminated conditions at 3 GHz, respectively.

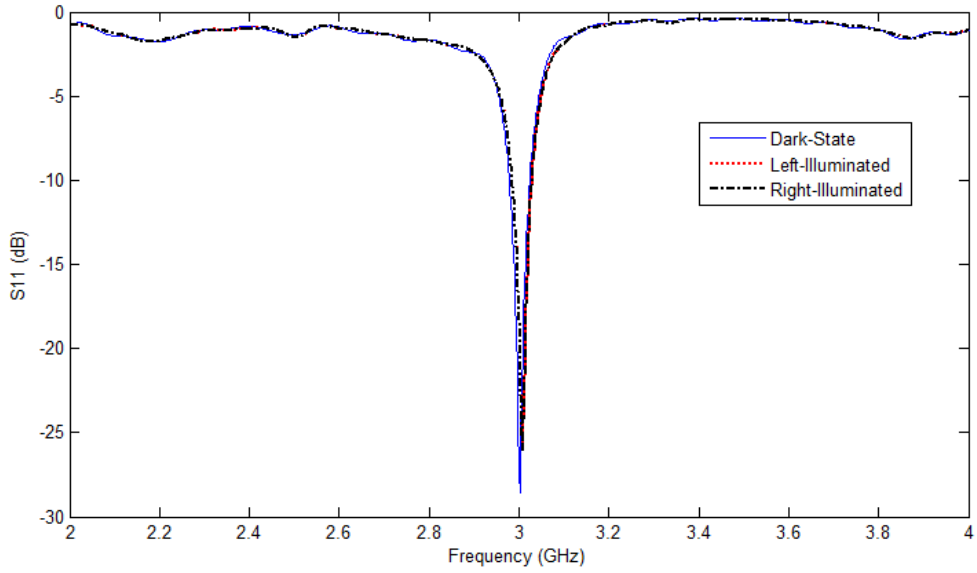

Fig. 5.18. Simulated return loss of the two-element patch antenna array showing the dark and active state resonant frequencies.

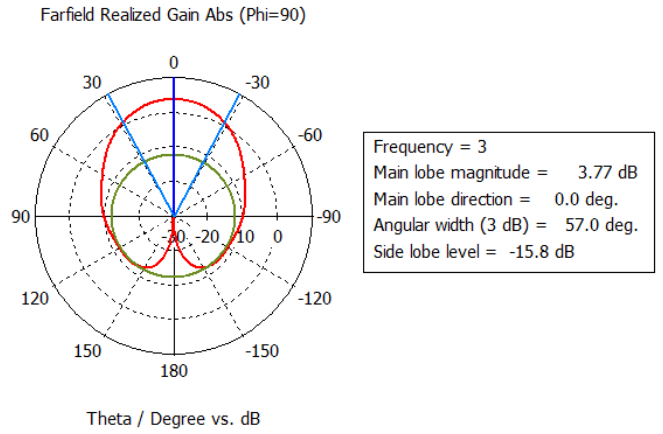

a)

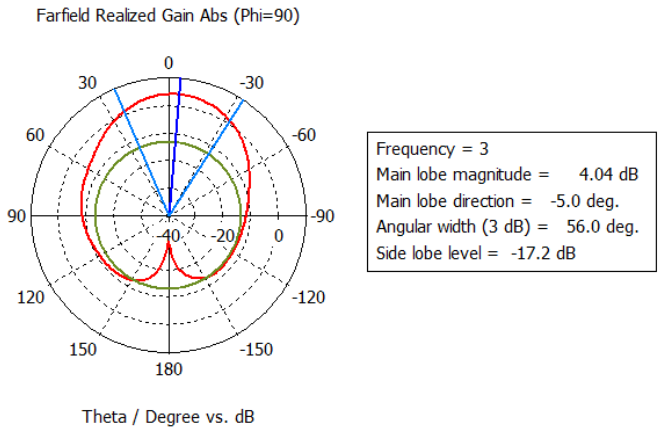

b)

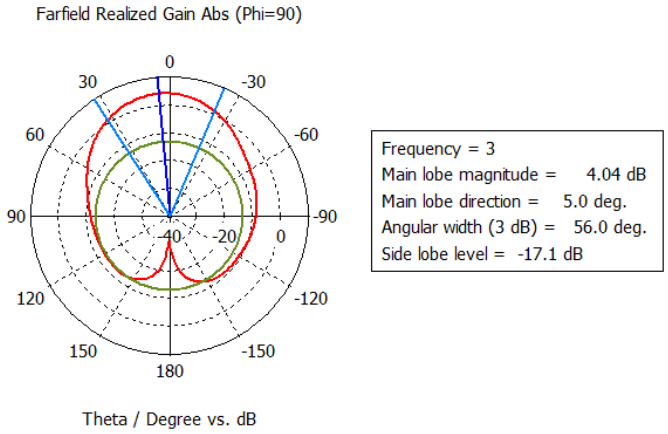

c)

Fig. 5.19. Simulated farfield radiation pattern of the modelled antenna: (a) dark-state; (b) left-illuminated condition; (b) right-illuminated condition. A symmetrical beam steer of 5º off boresight is observed in both the illuminated conditions.

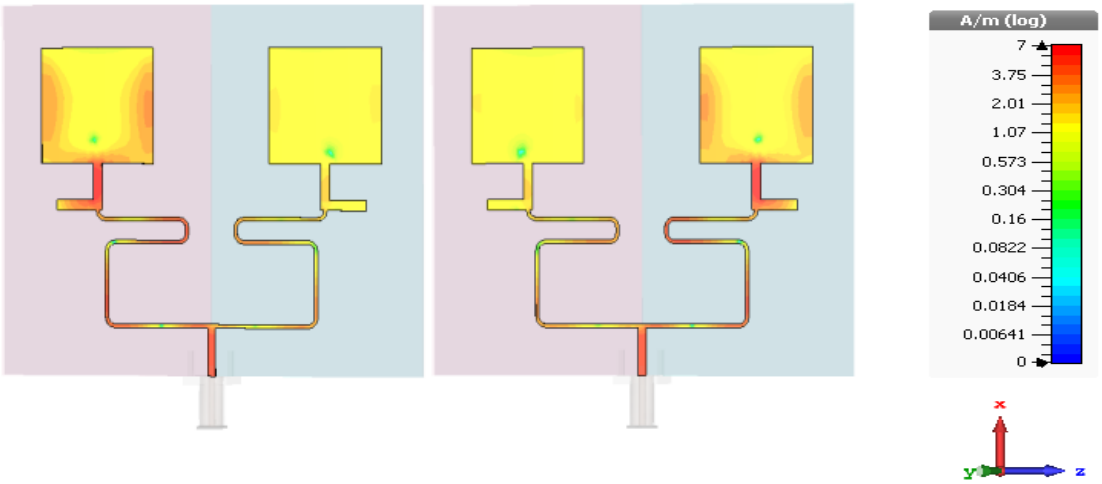

a) b)

Fig. 5.20. Simulated average surface current distributions at 3 GHz: (a) left-side illuminated condition; (b) right-side illuminated condition. Uneven distribution in the magnitude of the surface current density vector among the patches results during illumination due to the phase lag.

Although the complex permittivity measurements for the organic polymer blend were taken at a much higher frequency compared to the operating frequency of the modelled device, it gave an estimate of the change is permittivity between dark and active states. This provided the data input required to show the proof-of-concept for beam steering with such a phase-shifting device. In addition, the antenna design also demonstrated that with a small change in the real part of the permittivity of the substrate it is possible to generate a significant beam steer (5° in this case), using an effective phase-shifting design.

5.4 Summary

In conclusion, this chapter details development of the illumination techniques in the designs of the existing optically-activated antennas using inorganic semiconductors and employment of photosensitive organic semiconductors in antenna engineering to generate beam steer. A novel optically-switched cognitive radio system has been designed, and the reconfigurability of such a system is brought about by using illumination from a portable array of LED light source (880 nm). Such a system is suggested for use in practical applications due to its light-weight and compactness. In addition, a performance comparison has been made between two systems using medium-resistivity and high-resistivity Si as the reconfigurable ground. It has been established that the system requires a transition of conductivity from 4.25×10^{-4} Sm^{-1} to 168 Sm^{-1} to perform efficiently as a cognitive radio.

The possibility of an application using photosensitive organic semiconductors in optically-activated antennas have been discussed in detail in this chapter. A novel optically-activated antenna array using photo-activated organic semiconductor blend (P3HT: PCBM) has been presented. The primary objective of the proposed design was to justify the concept of beam steering using a photo-sensitive tuneable dielectric material. The optically-tuneable organic polymer was characterised using a QO transmissometer. The proposed design generated a 5° beam steer off boresight at S-band. A potential future application for the proposed system is the employment of the device for point-to-point beam alignment for detection and steering in data-centre high-capacity communication links.

References

[1] C. J. Panagamuwa, A. Chauraya, and J. C. Vardaxoglou, "Frequency and beam reconfigurable antenna using photoconducting switches," *IEEE Transactions on Antennas and Propagation,* vol. 54, pp. 449-454, Feb 2006.

[2] Y. Tawk, A. R. Albrecht, S. Hemmady, G. Balakrishnan, and C. G. Christodoulou, "Optically Pumped Frequency Reconfigurable Antenna Design," *IEEE Antennas and Wireless Propagation Letters,* vol. 9, pp. 280-283, 2010.

[3] H. S. Su, I. Shoaib, X. D. Chen, and T. Kreouzis, "Optically Tuned Polarisation Reconfigurable Antenna (Invited)," *2012 IEEE Asia-Pacific Conference on Antennas and Propagation (Apcap),* pp. 265-+, 2012.

[4] M. R. Chaharmir, J. Shaker, M. Cuhaci, and A. R. Sebak, "Novel photonically-controlled reflectarray antenna," *IEEE Transactions on Antennas and Propagation,* vol. 54, pp. 1134-1141, Apr 2006.

[5] I. F. da Costa, S. A. Cerqueira, D. H. Spadoti, L. G. da Silva, J. A. J. Ribeiro, and S. E. Barbin, "Optically Controlled Reconfigurable Antenna Array for mm-Wave Applications," *IEEE Antennas and Wireless Propagation Letters,* vol. 16, pp. 2142-2145, 2017.

[6] Y. Tawk, S. Hemmady, C. G. Christodoulou, J. Costantine, and G. Balakrishnan, "A Cognitive Radio Antenna Design Based on Optically Pumped Reconfigurable Antenna System (OPRAS)," *2011 IEEE International Symposium on Antennas and Propagation (Apsursi),* pp. 1116-1119, 2011.

[7] R. L. Haupt, J. Flemish, and D. Aten, "Adaptive Nulling Using Photoconductive Attenuators," *IEEE Transactions on Antennas and Propagation*, vol. 59, pp. 869-876, Mar 2011.

[8] J. R. Flemish and R. L. Haupt, "Optimization of a Photonically Controlled Microwave Switch and Attenuator," *IEEE Transactions on Microwave Theory and Techniques*, vol. 58, pp. 2582-2588, Oct 2010.

[9] "Computer Simulation Technology," 2017 ed: Dassault Systemes.

[10] J. Mitola, "Cognitive Radio Architecture Evolution," *Proceedings of the IEEE*, vol. 97, pp. 626-641, Apr 2009.

[11] Y. Tawk and C. G. Christodoulou, "A New Reconfigurable Antenna Design for Cognitive Radio," *IEEE Antennas and Wireless Propagation Letters*, vol. 8, pp. 1378-1381, 2009.

[12] S. Pendharker, R. K. Shevgaonkar, and A. N. Chandorkar, "Optically Controlled Frequency-Reconfigurable Microstrip Antenna With Low Photoconductivity," *IEEE Antennas and Wireless Propagation Letters*, vol. 13, pp. 99-102, 2014.

[13] C. D. Gamlath, D. M. Benton, and M. J. Cryan, "Microwave Properties of an Inhomogeneous Optically Illuminated Plasma in a Microstrip Gap," *IEEE Transactions on Microwave Theory and Techniques*, vol. 63, pp. 374-383, Feb 2015.

[14] H. Y. Tang, R. S. Donnan, and T. Kreouzis, "An optically controlled phase shifter employing the organic semiconductor poly(3-hexylthiophene)," *Applied Physics Letters*, vol. 91, Nov 12 2007.

[15] D. M. Pozar, *Microwave Engineering*. New Jersey: J. Wiley, 2005.

[16] LPKF(PhotoMatX60) [Online]. Available: http://www.lpkf.com/products/rapid-pcb-prototyping/circuit-board-plotter/protomat-x60.htm

[17] Keysight Technologies N5230C PNA-L Microwave Network Analyzer [Online]. Available: https://www.keysight.com/en/pd-1350041-pn-N5230C/pna-l-microwave-network-analyzer?cc=US&lc=eng

[18] Dektak Profilometer [Online]. Available: https://www.bruker.com/products/surface-and-dimensional-analysis/stylus-profilometers/dektak-xt/overview.html

[19] Spectralux 6000 [Online]. Available: http://www.omc-uk.com/lighting/lighting-components/spectralux-light-engines

[20] V. Sathi, N. Ehteshami, and J. Nourinia, "New frequency-reconfigurable microstrip antenna composed of organic semiconductor polymer," *Organic Electronics*, vol. 13, pp. 1192-1196, Jul 2012.

[21] KeysightTechnologies N5244A PNA-X Microwave Network Analyzer, 43.5 GHz [Online]. Available: https://www.keysight.com/en/pdx-x201767-pn-N5244A/pna-x-microwave-network-analyzer-435-ghz?cc=US&lc=eng

[22] Keysight Technologies 85072A 10-GHz Split Cylinder Resonator [Online]. Available: https://www.keysight.com/en/pd-1078775-pn-85072A/10-ghz-split-cylinder-resonator?cc=US&lc=eng

Chapter 6 Optically-Tuneable Dynamic Organic Lens and its Applications

Lensing for microwave and millimetre-wave applications work in the similar principles as optics. Lenses operating at microwave or millimetre-wave are mainly referred to as quasi-optical (QO) phase-correction devices. These lenses have been used to convert spherical phase fronts into planar fronts across an aperture to enhance directivity of the beam of the source. Similarly, they can also be used to converge plane waves into a single point. A lensing configuration has a primary feed and focusing elements (i.e. the lens) shown in Fig. 6.1. A microwave dielectric lens consists of two surfaces providing two degrees of freedom, where amplitude and phase distributions of the incident electromagnetic wave over the aperture can be controlled. These dielectric lenses abide by the laws of refractive in optics (Snell's law). Several application-driven designs of microwave and millimetre wave lenses have been reported in literature [1-5].

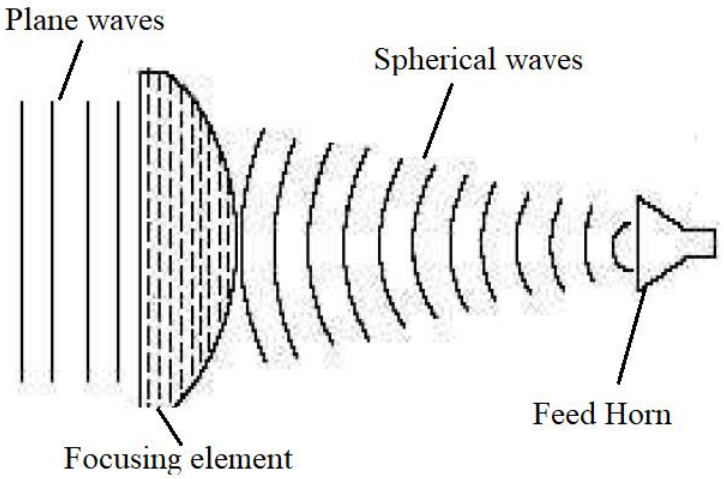

Fig. 6.1. Lensing configuration with a primary feed (horn antenna) and focusing element (lens).

Dynamic operation of millimetre-wave beams provides improved reliability, speed and flexibility to several electromagnetic applications. These applications include imaging, remote sensing and beam reconfiguration in antenna arrays and quasi-optical systems [1]. However, these applications require beam-controlling devices, and in this frequency regime either the performance of current electronic-based methods is poor, or the cost of fabricating such devices is very high. Several tuneable lenses for a wide range of applications have been reported in literature [6-9]. However, most of these either impractical or are difficult to fabricate.

Optically-tuneable lenses reported to-date have the advantages of comparatively easier fabrication and being dynamically tuneable in response to optical illumination [10, 11]. Further, flat lenses particularly, in comparison to the conventional curved lenses, reduces overall volume of the lens thereby enabling more compact packaging [12]. An optically-tuneable lens, for example, is used in beam-steering applications; by altering relative permittivity of the lens material from point-to-point across its face, according to how a pattern of light is designed to shine on it. As explained in detail in Chapters-2 and 3 concerning the principle of operation of such lenses, their applications can span from beam-alignment in quasi-optical systems to dynamic beam scanning in millimetre wave (mm-wave) radar systems. Dynamic beam scanning or beam steering as shown by Gallacher et al depicts that different illuminating patterns can be used to project onto the lens face and steer the main beam of the antenna off boresight [6]. Changing the illuminating pattern alters the mainlobe of the transmitting antenna assembly, allowing for dynamic beamforming. Hence, this sort of QO dynamic lens gives rise to the concept of mm-wave dynamic beamforming.

The optically-tuneable, organic, dynamic lens reported in this chapter demonstrates the possibilities of controlling the incident Gaussian beam at a lens surface. By allowing spatially-continuous variations in the relative permittivity of the organic layer of the lens, the EM behaviour of the incident beam from a high-gain horn antenna can be controlled. The spatially-continuous variation in the relative permittivity in turn is controlled by projecting a graduated illumination pattern onto the optically-tuneable organic lens. The tuneable organic layer is comprised of an organic heterojunction P3HT-PCBM that generates electron-hole pairs when excited with white-light.

The photo-injected organic dynamic lens creates an excitation region where illuminated, whereas the non-illuminated region remains unperturbed. This change in the

distribution of the electron-hole pairs in the excitation region can be examined using a near-field electric field monitor. The near-field probe measures the complex electric field at a particular distance from the surface under test, to provide a map of the field distribution in space. The near-field measurement system is used to verify the operation as well as the limitation of the dynamic organic lens. The pattern of mm-wave electric field distribution emerging from the lens is expected to be similar to the visible light pattern shone onto it.

6.1 Near-field Antenna Measurements

The near-field region of an antenna is defined as within 1 to 3 wavelengths (λ) from the antenna aperture (see Fig. 6.2a). This region is again subdivided into the reactive near-field, and the radiating near-field or Fresnel region. Beyond the near-field region of the antenna is the far-field or Fraunhofer region, calculated to commence $2D^2(\lambda)^{-1}$ from the radiating aperture; D being the aperture diameter. The near field is sampled outside the evanescent or reactive near-field region, which starts $\lambda(2\pi)^{-1}$ from the conductive surface of the antenna. The radiating near-field region, lies between the evanescent region and 3λ from the source aperture. This is the useful region where near-field measurements can be transformed to its conjugate far-field equivalent via a 2D Fourier transform. The near-field measurement system operates by measuring the phase front of the antenna under test (AUT) and then mathematically transforming the phase front into the equivalent far-field spectrum [13]. In practice, an electric-field probe is moved across a plane area in space to sample the signal from the incident horn (while compensating for Doppler shift due to motion of probe).

The near-field system measures the amplitude and phase of the electromagnetic field of the AUT. The probes used in a near-field measurement system are used to measure the phase-front the near-field of the AUT. The concept behind near-field measurements can be well understood by looking at how a lens antenna transmits energy along the propagation path of an electromagnetic wave (see Fig. 6.2b). In Fig. 6.2b the energy is given to be travelling to the right from the lens structure. The energy is shown as a phase-front by identifying lines of equal phase angle at a given time. Now an important point to note here is that a single moving probe is sufficient to get the same spatial information as that with four moving probes. Conventionally, planar near-field measurement systems operate using a single probe, sampling the amplitude and phase of the near-field wave of the AUT at regular intervals over a planar surface. The near-field

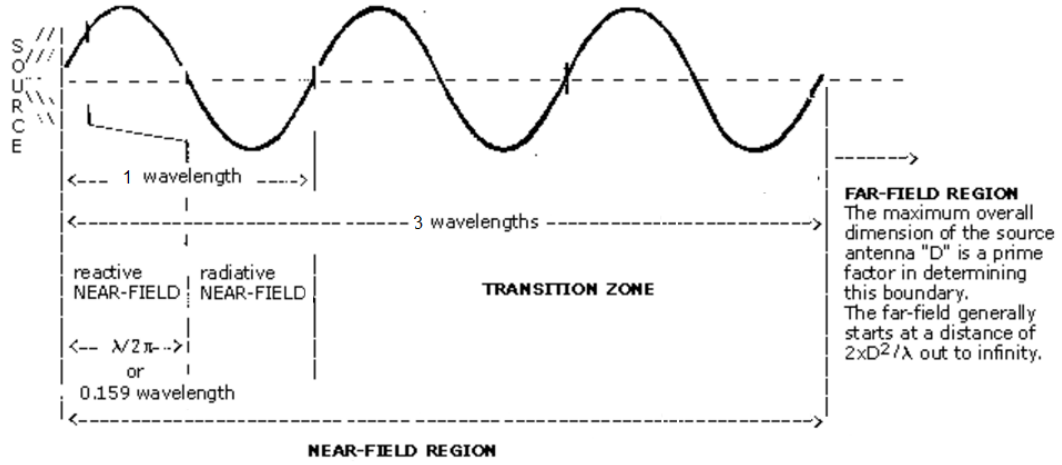

a)

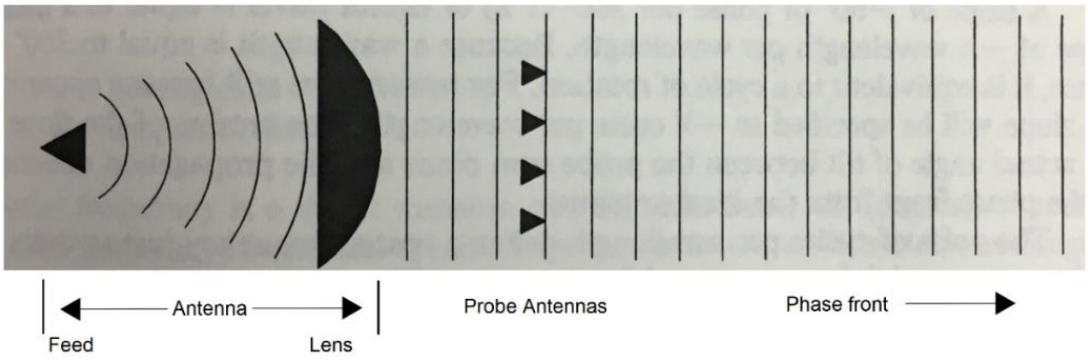

b)

Fig. 6.2. Field regions of a typical antenna (source), reproduced from [14]. The reactive near-field, the radiative near-field and the far-field region exists at a distance of $\lambda(2\pi)^{-1}$, $\lambda(2\pi)^{-1}$ to 1λ, and $2D^2\,\lambda^{-1}$ respectively from the source antenna.b) Ideal case of a lens antenna with a planar phase front and four probe antennas, reproduced from [13]. This is how a lens antenna transmits energy along the propagation path of an electromagnetic wave.

probe is normal to the aperture plane of the AUT and kept at a few wavelengths from it. An electrically-small, low gain, and low scattering cross-section antenna is commonly used as the near-field probe [15]. The measurements are typically made on a lattice corresponding to a rectangular Cartesian grid along paths parallel with the x-and y axes of the antenna (see Fig. 6.3).

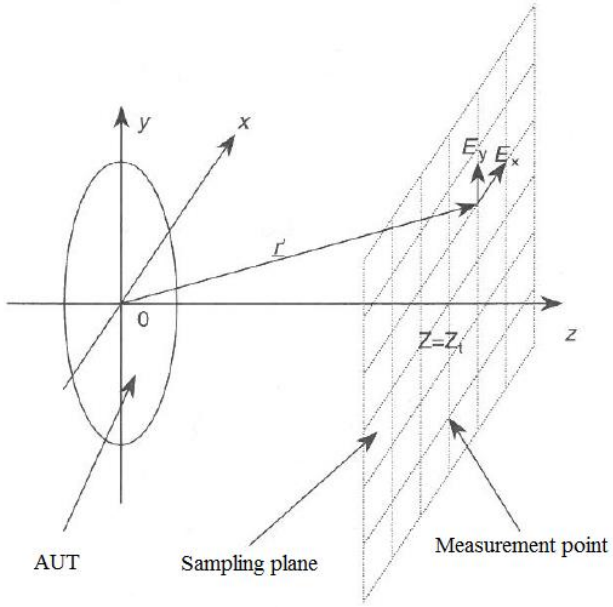

Fig. 6.3. Coordinate system for planar Near-field scanning, reproduced from [15]. The sampling plane shows how the probe translates in x and y direction and detects the spatial electric field components (E_y and E_x) of the antenna under test (AUT).

6.2 Dynamic Organic Lens

The organic lens strucutre is fabricated using sodalime glass as the substrate to support the organic film drop-cast onto it. An organic solution is developed using 95% P3HT :5% PCBM organic polymer along with the organic solvent, dichlorobenzene. The fully dissolved organic polymer is drop-cast onto the glass substrate and allowed to dry in a glove-box at room temperature. A thickness of 40 µm for the polymer is estimated using a micormetre screw gauge. Fig. 6.4 shows the dimensions and layers of the organic

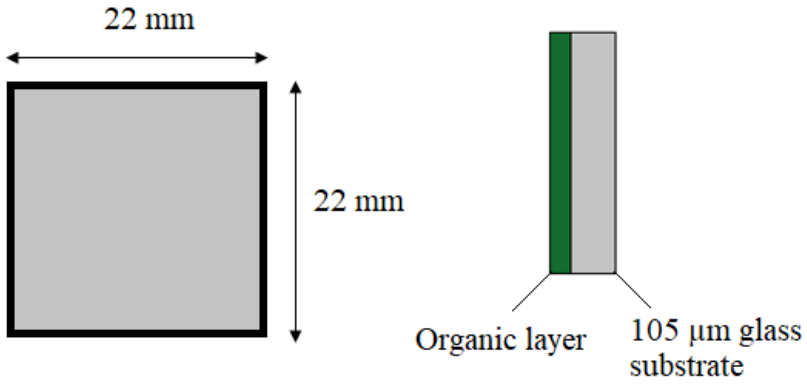

Fig. 6.4. Dimensions and thicknesses of the individual layers of the organic lens.

lens strucuture. To avoid exposure of the organic polymer to air, the drop-cast polymer is encapsulated within a 50 μm thick nylon film under N_2 inside the glove box.

In order to make the lens dynamic, an external illumination using a LED lamp is applied. A maximum irradiance of 60 $mWcm^{-2}$ is obtained at the sample plane, recorded using a power-meter operating at 532 nm. A Fresnel lens is used to collimate the beam from the LED lamp across the lens plane. For simplicity the projected light pattern is chosen to be of dark and light rings. Since the organic polymer is a photosensitive material (as per, (3.19)), the effective permittivty of the illuminated region is expected to change, relative to the dark ring regions. Hence the electromagnetic wave propagating through this graduated region is expected to undergo changes in magnitude, but mostly in phase. This is because the real part of the dielectric constant is expected to change by at least 0.1, while negligably for the imaginary part (as described in Chapter -4).

6.3 Electromagnetic modelling of the dynamic organic lens

Fig. 6.5 represents the experimental setup to determine the performance of the dynamic organic lens. In order to perform a rigorous numerical analysis of such a dynamic lens, a model of the entire setup is built using the commercially available software CST [16]. A feasibility test is performed to check whether it is possible to obtain a pattern from the spatial electric field distribution across the lens plane as that projected by the patterned light source. For this, the dynamic lens is positioned in front of a modelled WR-3 waveguide horn and field monitor is set to calculate the complex electric field across the lens plane. In order to account for the effect of differential illumination ($\lambda = 532$ nm) from the LED light source onto the lens plane in the software, concentric light and dark rings are defined. The illuminated regions represented a permittivity ($\varepsilon_{r\,active} = 2.9$) which is less than the non-illuminated regions ($\varepsilon_{r\,dark} = 3.0$). This information is taken from characterisation of the organic polymer in both illuminated and non-illuminated states on a quasi-optic bench in the WR-3 waveguide band [17]. The excitation-region depth in the illuminated state is estimated to be 100 μm.

The simulated electric field results were based on measured change in the complex permittivity of the organic polymer in the active state. The illumination intensity at the sample plane of the LEDs is measured to be 60 $mWcm^{-2}$ using a photodetector. The phase distribution in the active state shows a significant difference to that in the dark state. This is due to the change in the complex permittivity between the dark and photo-active region,

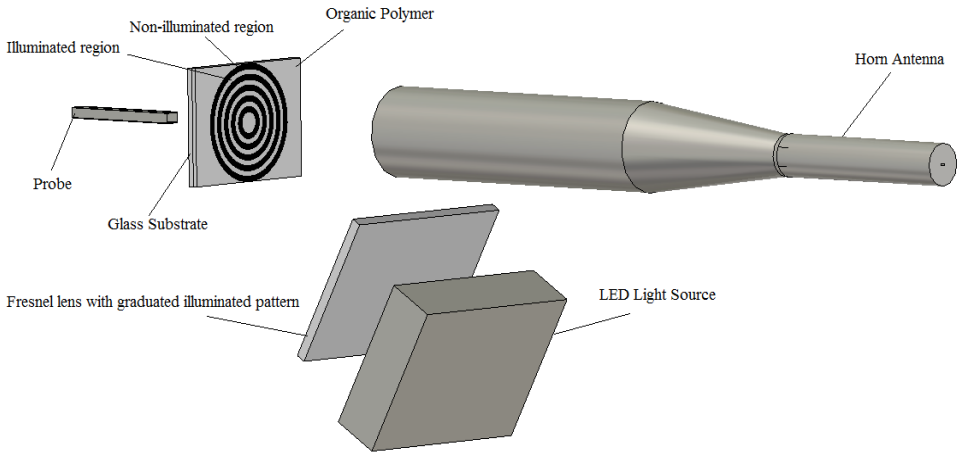

Fig. 6.5. Near-field measuring system of the optically-activated dynamic lens using a WR-3 horn antenna and a spatially translated probe.

leading to a change in phase of the same incident wave at a particular position of the lens. This is depicted in the false colour 2D plot of the spatial change in phase distribution of the electric field across the lens (Fig. 6.6). The phase distribution in the active state shows a distinct difference to that in the dark state because of the change in the complex permittivity between the dark and photo-active regions.

The simulated spatial electric field distribution across the lens plane is evaluated in the WR-3 waveguide band (300 GHz). However, demonstrating such an observation in reality requires measuring of the electric field distribution across the lens plane using a WR-03 waveguide probe. Due to the unavailability of such a probe in our antenna lab, the characterisation of the dynamic lens is performed in the WR-10 waveguide band. As a result, following the investigation in the WR-03 waveguide band, a numerical analysis is carried out in the WR-10 waveguide band. The transmission and detection of the WR-10 horn antenna and the waveguide probe is measured and analysed. The planar near-field region of a standard WR-10 horn antenna is measured using a NSI-MI Scanner [18], by keeping the probe 3λ away from the horn. Using the near-field measurements of the AUT, and Fourier transform, it is possible to evaluate the far-field performance. Fig. 6.7 shows the H-plane far-field radiation pattern of the standard horn. It is observed that the measured radiation patterns, with the near field scanned at 3λ away, agrees with the simulated far-field radiation pattern in CST. The standard field scanning distance of the AUT using the NSI scanner in our antenna lab is 3-5λ for the best results of far-field radiation pattern.

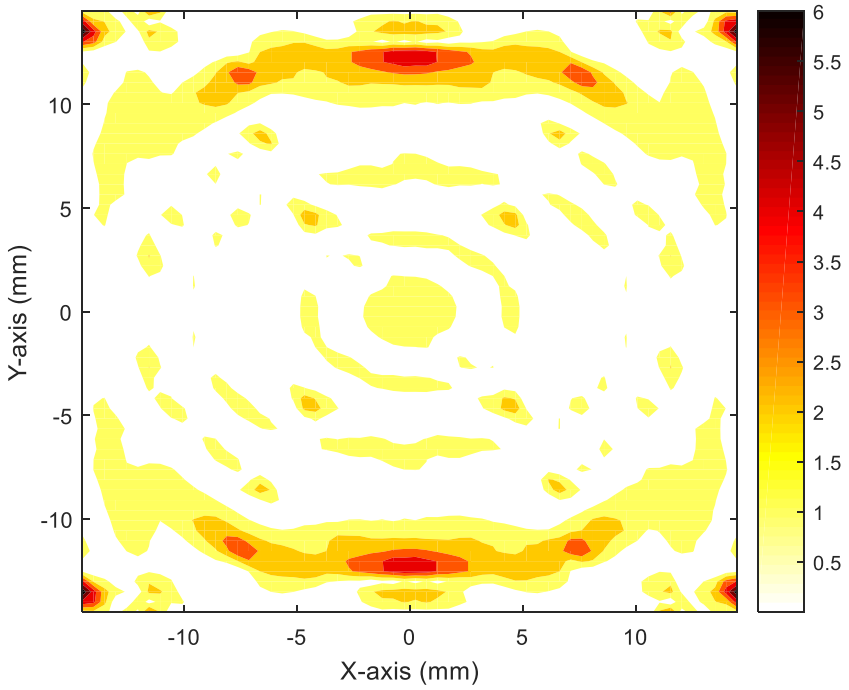

Fig. 6.6. Simulated spatial change in phase (º) distribution of the electric field across the dynamic organic lens face between dark and active states at operating frequency 300 GHz.

In the setup, shown in Fig. 6.5, the dynamic lens is placed at the far-field of the transmitting horn antenna. The calculated far-field distance and the 3 dB beamwaist in the far-field of the standard horn antenna at 100 GHz is 10.5 cm and 6 cm respectively. As a result, the dynamic lens with dimensions, 22 mm × 22 mm, is kept at the far-field distance so that the 3 dB beamwaist of the standard horn completely covers the lens area. In this investigation, the far-field of the standard horn is considered from 10.5 cm to infinity. The dynamic lens, as a result, is positioned at a distance of 10.5 cm or further from the standard horn aperture. In CST, the far-field monitor is moved to 10.5 cm from the antenna and the far-field radiation pattern analysed. Fig. 6.7 shows that the comparison between the measured H-plane radiation pattern and the simulated radiation patterns with a horn-to-probe distance of 10.5 cm. It is observed that the simulated results at such a distance (10.5 cm) in CST do not match with the measured results. This is because the post-processed far-field radiation patterns from the NSI-MI scanner yields an accurate Fourier transform of the near-field of the AUT, when the scanning distance is 3-5λ away from the AUT. However, in this case, the probe is placed 12cm away from the standard horn. However, the simulated radiation patterns are matched with that of the measured by moving the probe closer to the AUT. At a lens-to-horn distance of 5 cm, the simulated H-plane radiation pattern matches with that of the measured radiation pattern (see Fig 6.8).

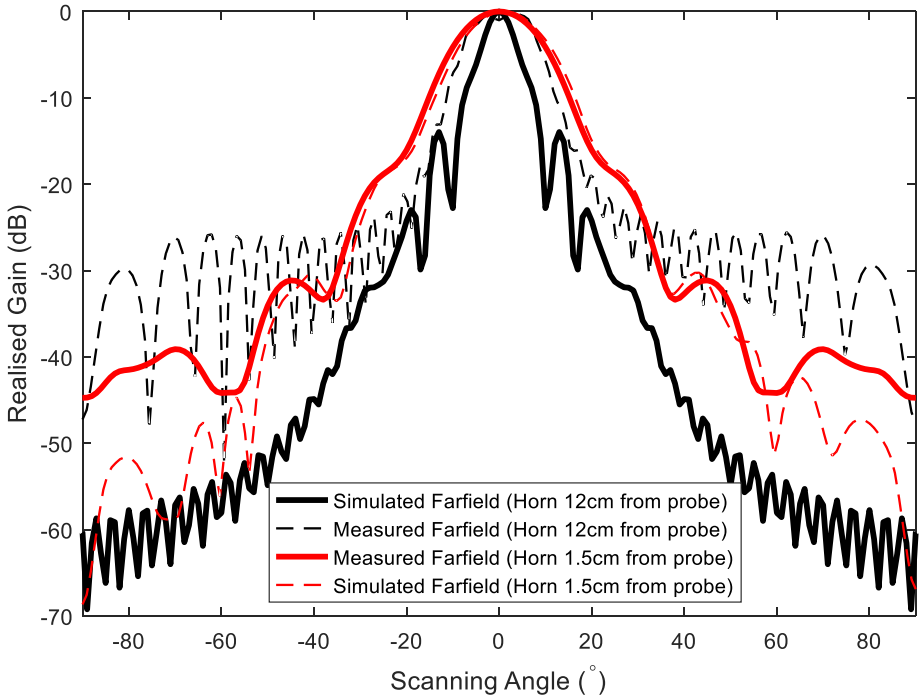

Fig. 6.7. Comparison between measured (using NSI scanner) and simulated (using CST) far-field radiation pattern of a standard WR-10 (75 – 110 GHz) horn antenna.

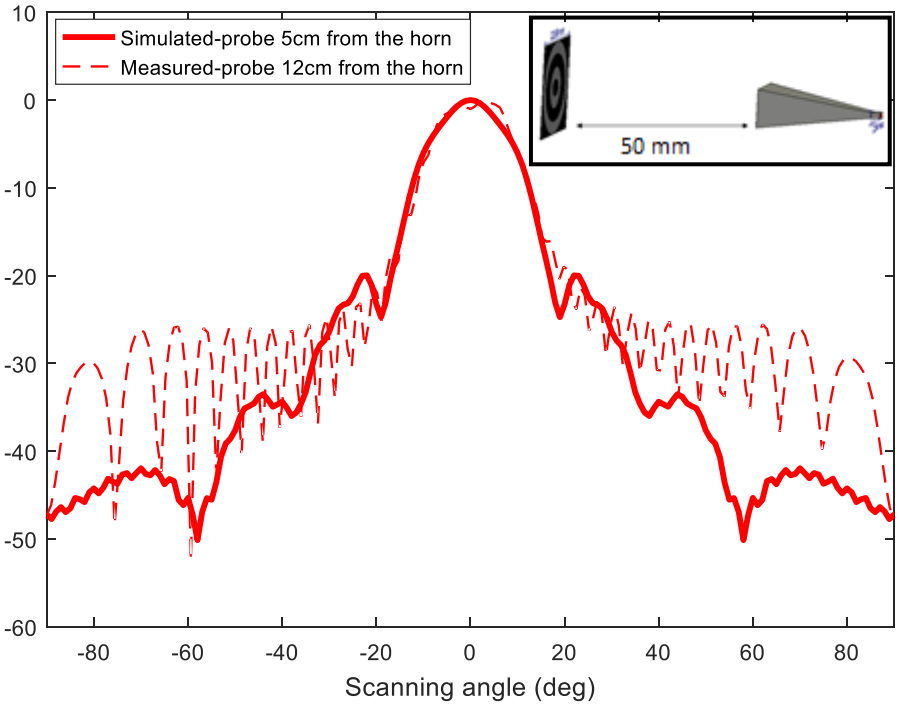

Fig. 6.8. Matched simulated far-field radiation pattern to the measured radiation pattern of a standard WR-10 (75 – 110 GHz) horn antenna with horn and probe separation of 12cm. In the simulation the horn and lens separation was 5 cm as shown in the inset of this figure.

The lens-to-horn distance of 5 cm is taken as a standard for analysing the performance of the dynamic organic lens. Four different illumination patterns were chosen and the spatial complex electric field across the lens plane is evaluated at different distances using CST. The illuminated regions represented a permittivity ($\varepsilon_{r\ active} = 2.9$) and the non-illuminated regions ($\varepsilon_{r\ dark} = 3.0$) as used for the WR-03 waveguide band case. For each of the illumination patterns, the electric field across the planar organic lens is determined at multiples of the wavelength of operation. In this case the frequency of operation is chosen as 100 GHz ($\lambda = 3$ mm). Fig. 6.9 shows the four illumination patterns used in CST to evaluate the performance of the dynamic organic lens. The complex electric field at probing distances λ, 2λ, 3λ, 4λ and 5λ is determined using the electric field monitor in CST.

In order to look at the spatial electric field distribution in phase across the lens plane, a post-processing algorithm is chosen to plot the phase distribution of the complex electric field in space. Since the WR-10 horn antenna is vertically polarised, the electric field E_y (vertical component), is approximated as the total electric field across the lens

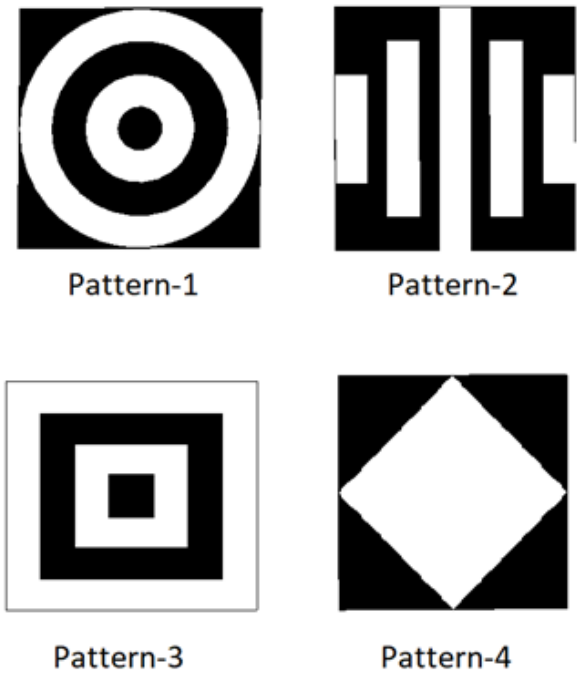

Fig. 6.9. Four illumination patterns used to demonstrate the dynamic behaviour of the organic lens. The patterns were chosen based on the wavelength of operation of the dynamic organic lens (i.e. $\lambda = 3$ mm). It is expected to observe a similar pattern in the spatial electric field distribution across the organic lens as that projected by the illuminating source.

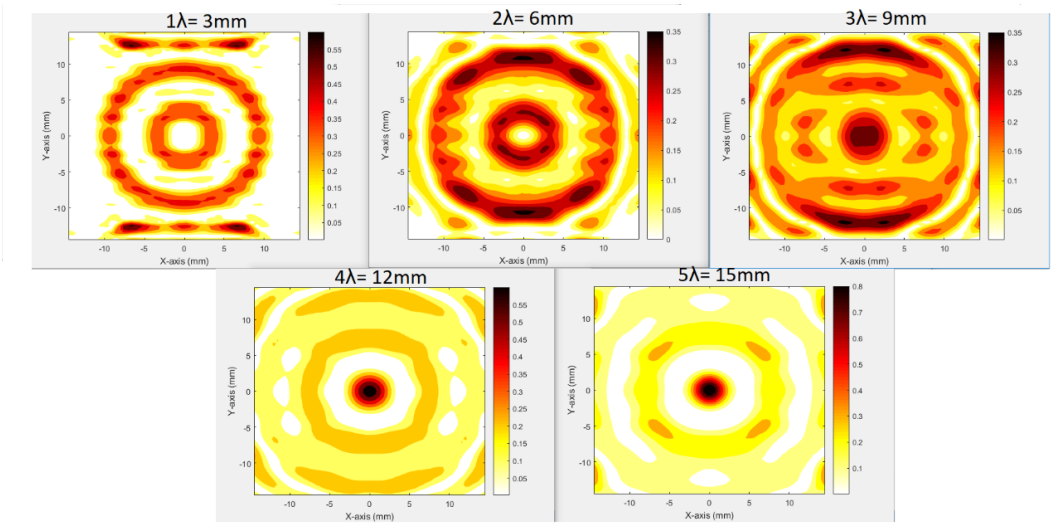
1λ= 3mm
2λ= 6mm
3λ= 9mm
4λ= 12mm
5λ= 15mm
X-axis (mm)
Y-axis (mm)

a)

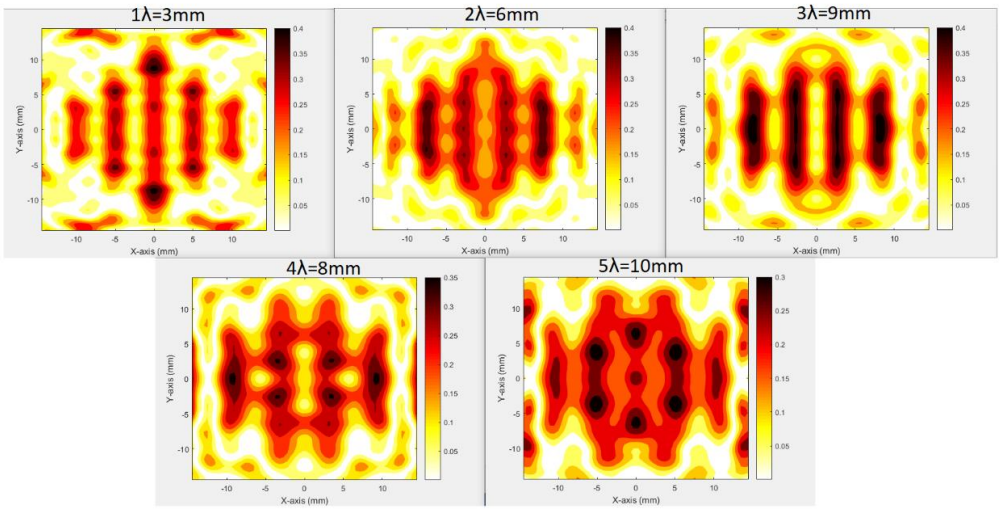
1λ=3mm
2λ=6mm
3λ=9mm
4λ=8mm
5λ=10mm
X-axis (mm)
Y-axis (mm)

b)

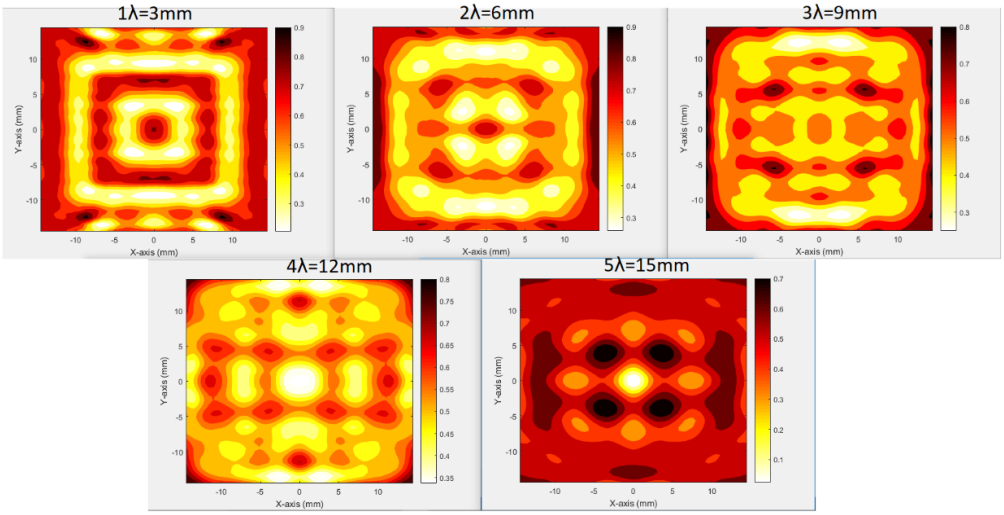
1λ=3mm
2λ=6mm
3λ=9mm
4λ=12mm
5λ=15mm
X-axis (mm)
Y-axis (mm)

c)

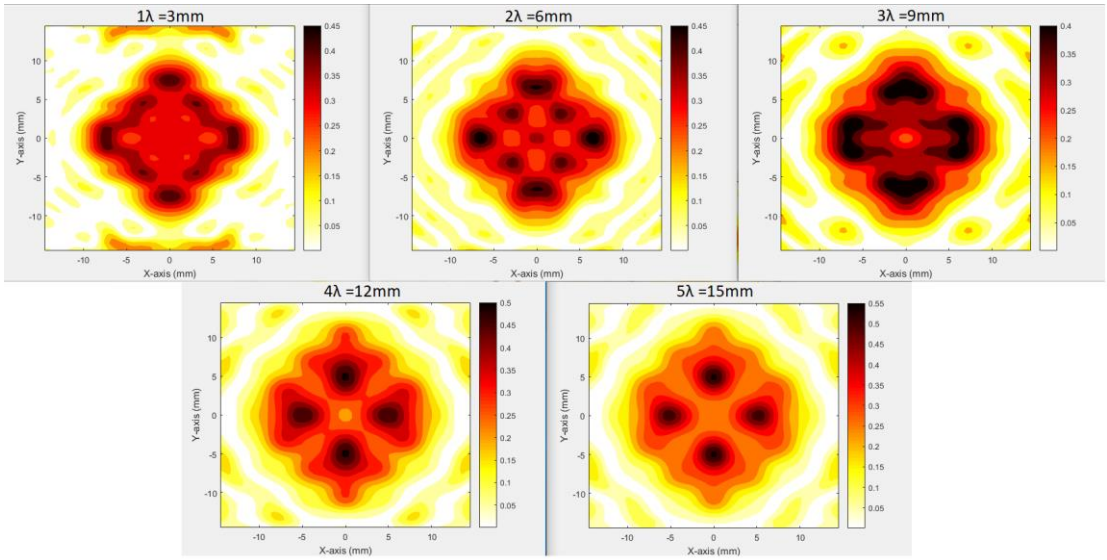

d)

Fig. 6.10. Simulated spatial phase distribution of the complex electric field between dark and active states of the lens using a) Pattern-1 b) Pattern-2 c) Pattern-3 d) Pattern-4 at different probing distances λ, 2λ, 3λ, 4λ, 5λ.

plane and converted to polar form to extract the phase. It is expected that the spatial change in phase of the complex electric field, across the lens plane between dark (non-illuminated) and active (illuminated) states of the lens, would show the same pattern as that projected by the illuminating source. Fig. 6.10 shows the post-processed results of the spatial distribution of the change in phase of the complex electric field across the lens plane at different probing distances. It is observed image reconstruction of the illumination pattern projected onto the lens is possible by taking a simple vector subtraction of the dark complex electric field from the active complex electric field. The resolution of the image is found to be higher with reduction in the probing distance. For all the patterns, the image is more vivid in the case where the probing distance is kept at one wavelength (λ =3mm). Such an observation demonstrates that the probing distance, when measuring the complex electric field across the lens plane using the NSI scanner, should be at least one wavelength away to acquire a high resolution image of the illumination pattern. As a result, the measurements of the organic lens is carried out at a distance less than one wavelength of the operating frequency. However, during measurements, other factors such as the instrument noiseshould also be considered in order to observe a clear image of the projected illumination pattern from the measured near-field across the dynamic organic lens.

6.4 Illuminating projection for the dynamic organic lens

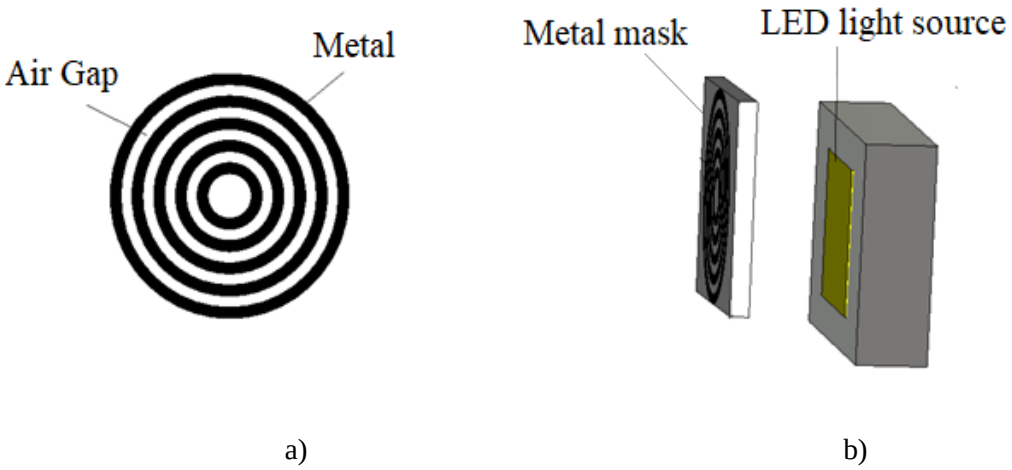

a) b)

Fig. 6.11. a) Illuminated projection pattern showing the illuminated and non-illuminated regions. b) Setup showing the how the illumination pattern is projected from the LED light source via the metal mask.

Based on the numerical analysis performed using the four different illumination patterns on the dynamic organic lens, four distinct patterned metal masks were fabricated using a computer numerical control (CNC) machine [19]. These masks had patterns made of alternate air-gap and metal regions, allowing full illumination on some regions and no illumination onto others. An example of such a design is shown in Fig. 6.11a. These designs were modelled using CST and input to the CNC machine, using 1mm diameter drill bits to fabricate them onto 0.5 mm thick copper. Fig. 6.11b shows how these patterned masks are mounted onto the LED light source. The dimensions of the patterns are made comparable to the led square surface area (25 mm × 25 mm). This resulted in exposure of the illumination onto the patterned area of the mask only. The patterned output from the mask is brought to focus or in other words, collimated, onto the organic lens using a Fresnel pre-lens.

Four different illumination pattern masks were fabricated as shown in Fig. 6. 12. During measurements of the organic lens, these masks were screwed onto the LED light surface area, holding them firm and stable for uniform illumination. The irradiance received from each of the illumination patterns were recorded using a photodetector operating at a wavelength of 532 nm. The results from the photodetector at the organic lens plane is tabulated in Table. 6-1. From the table it is evident that the power at the sample plane using patterned illumination is lower than the power used to observe the

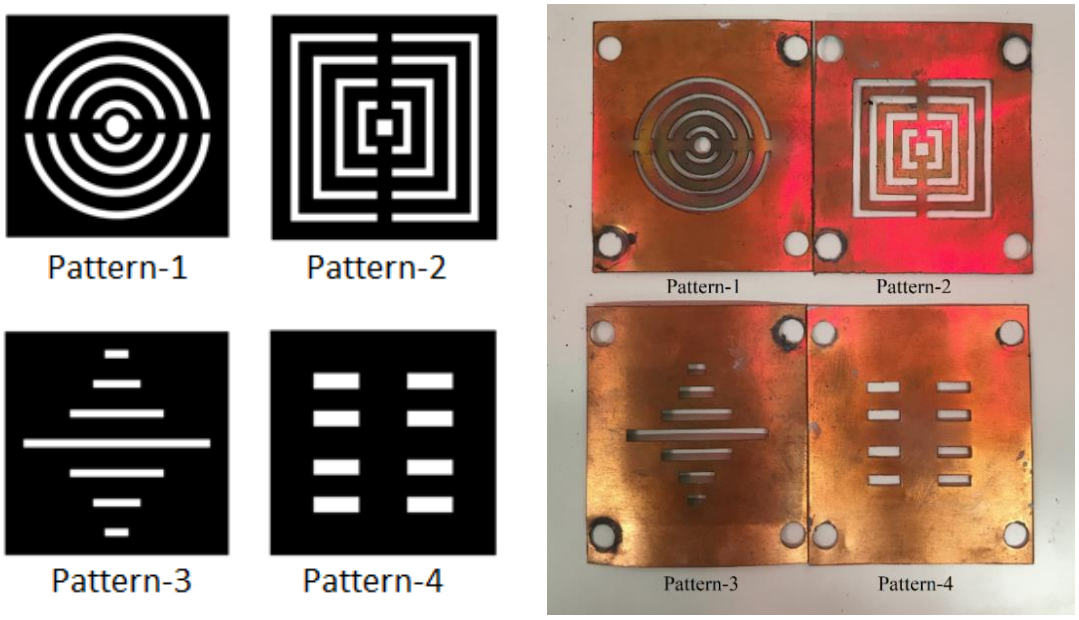

a) b)

Fig. 6.12. a) Four different illumination patterns to be projected onto the dynamic organic lens chosen as per ease of fabrication of the metal masks. b) Fabricated metal masks based on the four chosen illumination patterns shown in a).

Table. 6.1. Measured irradiances of four different patterned illumination at the dynamic organic lens measurement plane.

Patterns	Irradiance ($mWcm^{-2}$)
1	18
2	23
3	26
4	16
Full illumination (without pattern)	60

tuneable change of the organic polymer using the quasi-optical (QO) transmissometer in Chapter 4. However, in order to establish the proof-of-concept of the operating mechanism of the dynamic organic lens in practice, the near-field of the lens with the four different patterned illumination is sensed using the NSI scanner.

6.5 Performance analysis of the fabricated organic lens

The dynamic organic lens is fabricated as explained in Section 6.2. During measurements, the lens is mounted between a WR-10 standard horn antenna and a waveguide probe using a Teflon lens holder. The illumination at the organic lens plane is obtained with the use of a LED light source, kept at a 45º angle, followed by a Fresnel lens to focus the illumination onto the organic lens surface (see Fig. 6.13a). The entire illumination setup is kept below the beam axis of the horn antenna and the waveguide probe. An illuminating pattern cast onto the organic lens, mounted using a Teflon holder, is shown in Fig. 6.13b.

Throughout the measurements, the WR-10 horn antenna is kept at a distance of 10.5 cm, i.e., in the far-field, away from the organic lens. From the simulation results it is evident that sensing of the organic lens is best when the probing distance is kept at 1λ or less. The WR-10 horn antenna with a rectangular aperture area of 12.40 mm × 9 mm is used at the transmitting end of the system to throw a sub-THz beamfield onto the organic lens. The beam-waist in the far-field of the transmitting beam is calculated as 60 mm and the far-field of the horn is estimated at 105 mm from the aperture plane. On the transmit side of the lens, a near-field probe is positioned as the receiver for sampling the electric field distribution emerging from the organic lens. The probe is moved spatially in two dimensions, keeping the distance in the direction of wave propagation fixed at 1mm (λ/3) from the lens plane.

The background phase noise of the measurement system is firstly measured before evaluating the dynamic operation of the organic lens. Keeping the organic lens in the measurement plane, the change in phase between two successive measurements is evaluated. Three different measurements of the near-field of the organic lens without any illumination is taken. The change in phase of the electric field across the lens plane between these measurements is evaluated. This change in phase between individual measurements give rise to the system noise. Fig. 6.14 shows the spatial distribution of this phase noise across the organic lens plane. The change in phase noise in space is evaluated by taking vector subtraction of the phase of the electric field at each measured point. It is observed that the change in phase follows a uniform pattern. A maximum change in phase of the system, due to noise, is measured to be 1.4º. Four different projected illumination patterns on the organic lens represented its active state. As explained in section 6.4, the four patterns of illumination had different projection

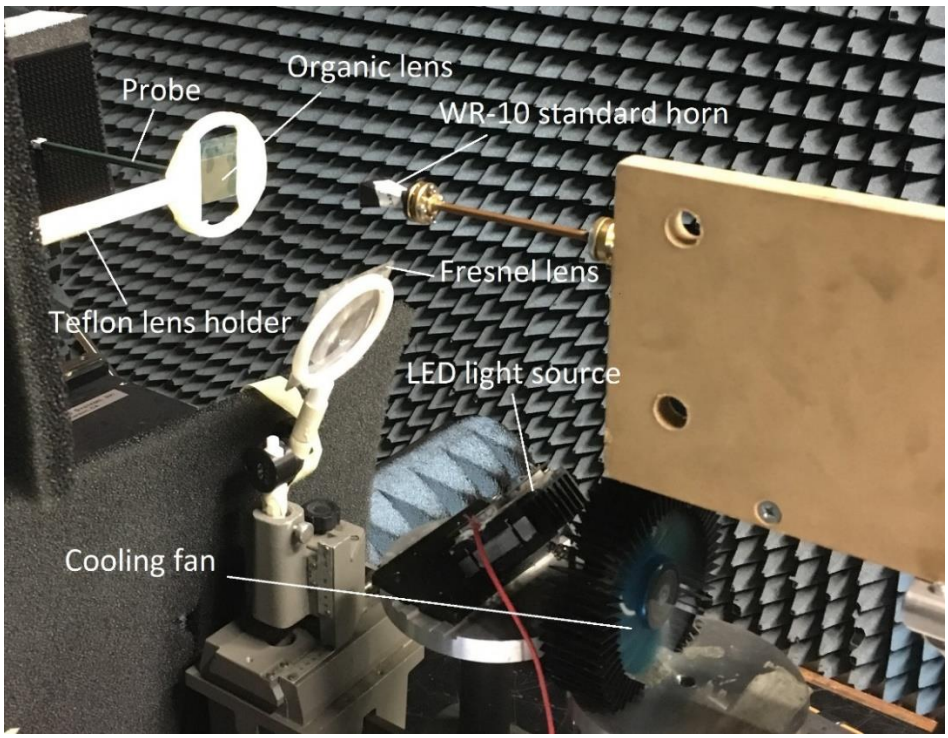

a)

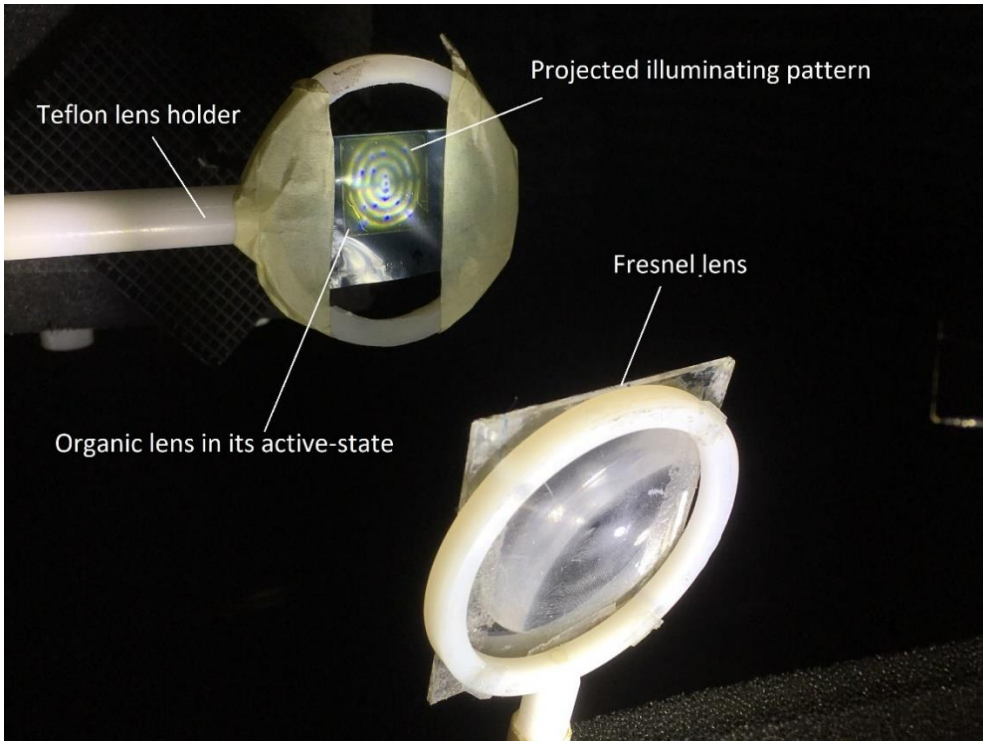

b)

Fig. 6.13. a) Measurement setup of the dynamic organic lens using the NSI-MI scanner. b) Illumination pattern (Pattern-1) projected at the organic lens plane to photo-induce electron-hole pairs in the illuminated regions.

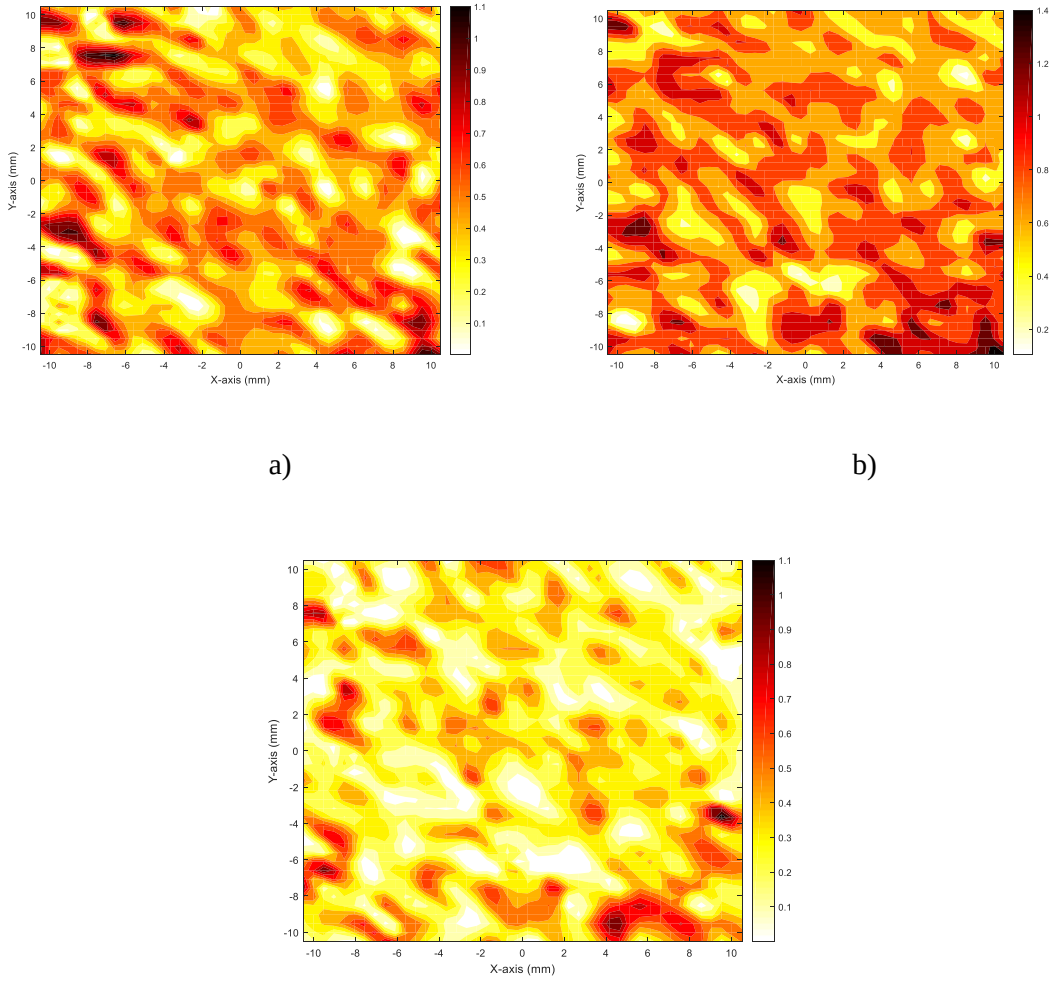

Fig. 6.14. Three different measurements of the organic lens without illumination taken showing the change in phase of the complex electric field across the lens plane between a) measurement-1 and measurement-2 b) measurement-2 and measurement-3 c) measurement-1 and measurement-3.

radiances. The near-field across the lens plane at a probing distance of 1 mm is measured using the NSI scanner. The vector subtraction of the complex electric field across the lens between its illuminated and non-illuminated states is expected to produce a pattern correlated to that projected. Fig. 6.15 shows the measured spatial change in the phase of the complex electric field across the organic lens between its illuminated and non-illuminated states at different frequencies. It is observed that the change in electric field distribution in phase doesn't quite display the pattern expected to be observed. However, when these results are compared with those of the background, i.e., noise floor, as shown in Fig. 6.14, a significant difference is seen in the pattern observed between them.

The reason for this observation resulted due to two major reasons. First, the patterned light projection onto the organic lens was not sufficient to observe the patterned distribution of electron-hole pairs with the measurement system used. The observed dielectric changes from the QO transmissometer measurements were obtained at higher irradiances. The irradiances shown in Table 6.1 shows the evidence that the irradiances achieved at the sample plane in the NSI measurements were much lower than the irradiance used to measure the dielectric changes using QO transmissometry. Secondly, the change in phase in the complex electric field observed from the NSI measurements was very close to the noise floor of the measurement system. As a result the dominant effect of the electron-hole pair patterns was obscured by the phase-noise. Additionally, the illumination pattern did not have absolute dark and light regions. The margin between light and dark was blurred. This was initially assumed to be negligible. Hence, with the use of brighter illumination patterns onto the lens, more sharp images are expected to be seen. On the other hand, a more advanced measurement setup, with lower background noise, can also resolve this issue. An electro-optic probe, field-scanning system at THz frequencies, could be used to observe such small dielectric changes in terms of imaging.

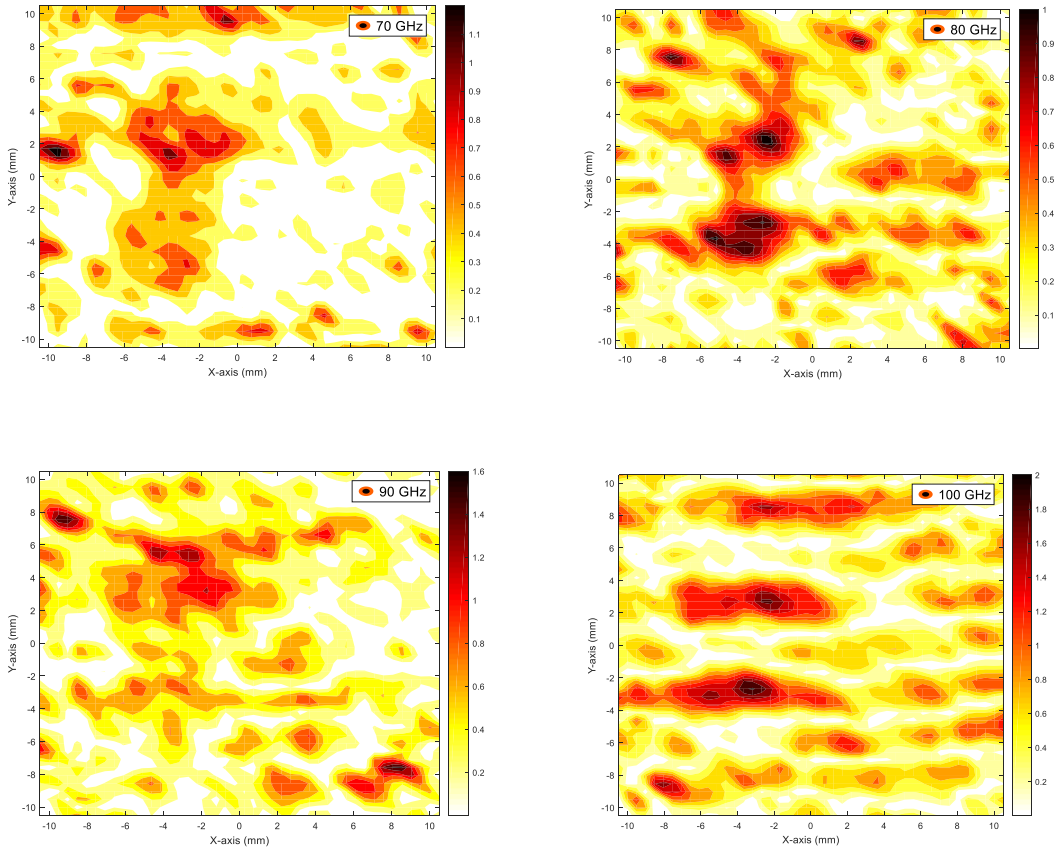

a) Pattern-1

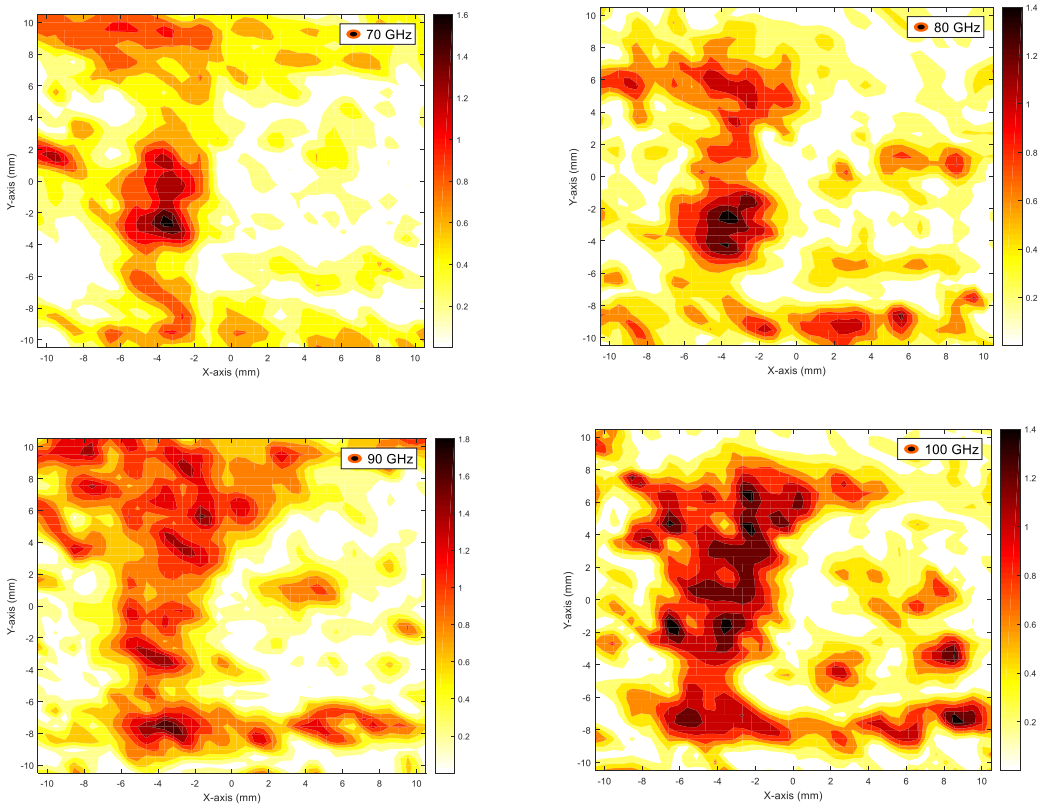

b) Pattern-2

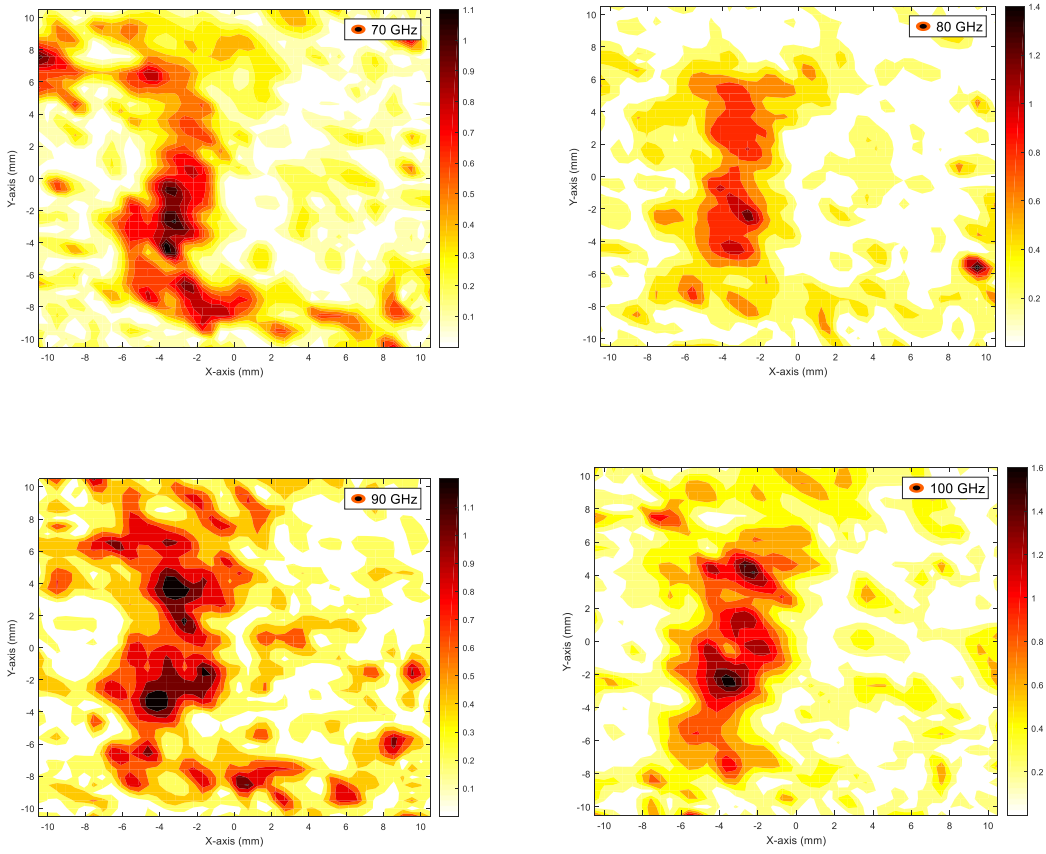

c) Pattern-3

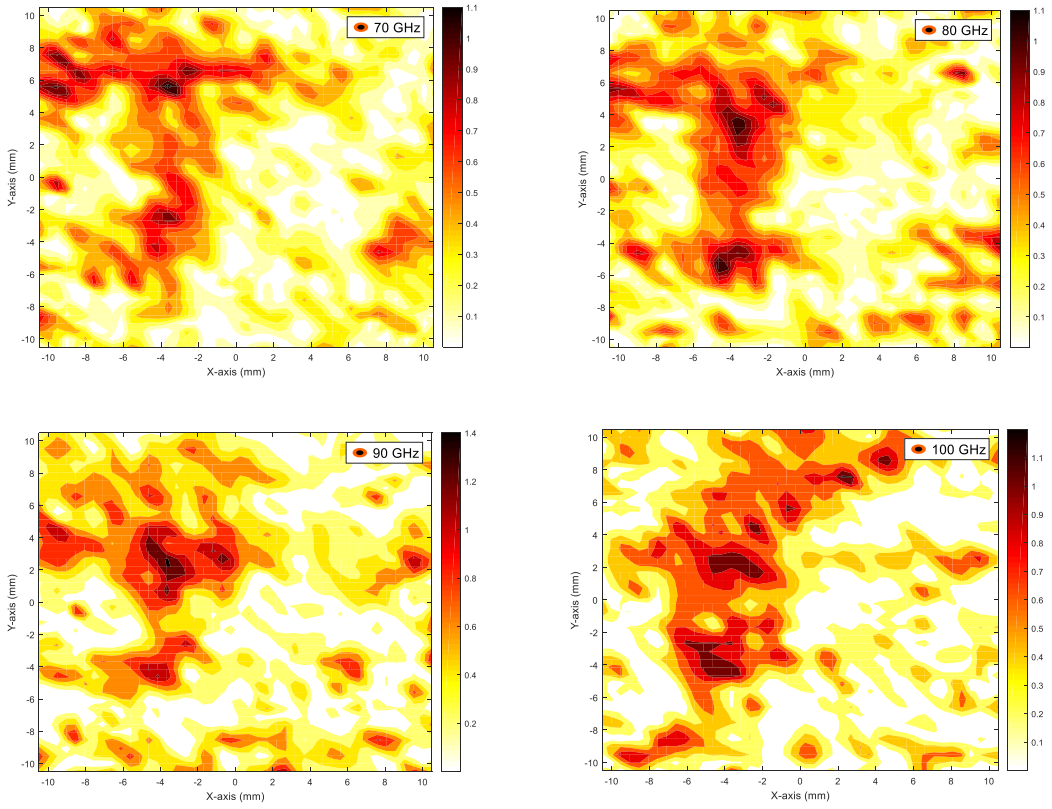

d) Pattern-4

Fig. 6.15. Spatial distribution of the change in phase of the electric field across the organic lens between illuminated and non-illuminated conditions using illumination patterns: a) Pattern-1 b) Pattern-2 c) Pattern-3 d) Pattern-4

6.6 Summary

In this chapter, the concept of a novel dynamic organic lens has been reported and its performance evaluated using numerical analysis as well as measurements. The performance of the lens has been analysed using an NSI planar scanner. Using numerical analysis it has been shown that a photo-sensitive planar lens is able to output a pattern, in terms of its spatial complex electric field distribution, when triggered with patterned illumination. From measured results, however, exact projected pattern in the output was not clearly seen, mainly because the change in phase of the complex electric field across the lens plane was very close to the noise floor of the measurement system. Possible solutions for observing images created by such small dielectric changes are to increase the irradiance onto the patterned illumination and measuring the response using a low-noise, i.e., more sensitive, system such as an electro-optic probe in THz frequencies.

References

[1] D. F. Filipovic, S. S. Gearhart, and G. M. Rebeiz, "Double-Slot Antennas on Extended Hemispherical and Elliptic Silicon Dielectric Lenses," *IEEE Transactions on Microwave Theory and Techniques,* vol. 41, pp. 1738-1749, Oct 1993.

[2] T. N. Ngoc, N. Delhote, M. Ettorre, D. Baillargeat, L. Le Coq, and R. Sauleau, "Design and Characterization of 60-GHz Integrated Lens Antennas Fabricated Through Ceramic Stereolithography," *IEEE Transactions on Antennas and Propagation,* vol. 58, pp. 2757-2762, Aug 2010.

[3] M. Liang, W. R. Ng, K. H. Chang, K. Gbele, M. E. Gehm, and H. Xin, "A 3-D Luneburg Lens Antenna Fabricated by Polymer Jetting Rapid Prototyping," *IEEE Transactions on Antennas and Propagation,* vol. 62, pp. 1799-1807, Apr 2014.

[4] H. F. Ma and T. J. Cui, "Three-dimensional broadband and broad-angle transformation-optics lens," *Nature Communications,* vol. 1, Nov 2010.

[5] C. Mateo-Segura, A. Dyke, H. Dyke, S. Haq, and Y. Hao, "Flat Luneburg Lens via Transformation Optics for Directive Antenna Applications," *IEEE Transactions on Antennas and Propagation,* vol. 62, pp. 1945-1953, Apr 2014.

[6] T. F. Gallacher, R. Sondena, D. A. Robertson, and G. M. Smith, "Optical Modulation of Millimeter-Wave Beams Using a Semiconductor Substrate," *Ieee Transactions on Microwave Theory and Techniques,* vol. 60, pp. 2301-2309, Jul 2012.

[7] J. W. Zhong, N. An, N. B. Yi, M. X. Zhu, Q. H. Song, and S. M. Xiao, "Broadband and Tunable-Focus Flat Lens with Dielectric Metasurface," *Plasmonics,* vol. 11, pp. 537-541, Apr 2016.

[8] B. F. Zhu, G. B. Ren, M. J. Cryan, C. L. Wan, Y. X. Gao, Y. Yang, *et al.*, "Tunable graphene-coated spiral dielectric lens as a circular polarization analyzer," *Optics Express,* vol. 23, pp. 8348-8356, Apr 6 2015.

[9] Y. S. Lu, H. G. Tu, Y. Xu, and H. R. Jiang, "Tunable dielectric liquid lens on flexible substrate," *Applied Physics Letters,* vol. 103, Dec 23 2013.

[10] L. J. Cheng and L. Liu, "Optical modulation of continuous terahertz waves towards cost-effective reconfigurable quasi-optical terahertz components," *Optics Express,* vol. 21, pp. 28657-28667, Nov 18 2013.

[11] S. Busch, B. Scherger, M. Scheller, and M. Koch, "Optically controlled terahertz beam steering and imaging," *Optics Letters*, vol. 37, pp. 1391-1393, Apr 15 2012.

[12] D. N. Black and J. C. Wiltse, "Millimeter-Wave Characteristics of Phase-Correcting Fresnel Zone Plates," *Ieee Transactions on Microwave Theory and Techniques*, vol. 35, pp. 1122-1129, Dec 1987.

[13] D. Slater, *Near-field Antenna Measurements* Boston, MA: Artech House 1991.

[14] Electromagnetic Radiation: Field Memo [Online]. Available: https://www.osha.gov/SLTC/radiofrequencyradiation/electromagnetic_fieldmemo/electromagnetic.html#section_1

[15] S. Gregson, J. McCormick, and C. Parini, *Principles of Planar Near-field Antenna Measurements*. London, UK: Institute of Engineering and Technology, 2007.

[16] "Computer Simulation Technology," 2017 ed: Dassault Systemes.

[17] A. S. Andy, O. Sushko, T. Kreouzis, and R. S. Donnan, "Optically-Tunable Organic Semiconductor Heterojunction P3HT-PCBM for Millimeter-wave Applications," *2015 40th International Conference on Infrared, Millimeter and Terahertz Waves (Irmmw-Thz)*, 2015.

[18] NSI-MI Planar Scanner [Online]. Available: https://www.nsi-mi.com/

[19] LPKF ProtoMat M60 [Online]. Available: http://www.lpkfusa.com/downloads/support/docs/man_m60.pdf

Chapter 7 Conclusion and Future Work

7.1 Conclusion

For the last two decades, several contributions have been made regarding the use of tuneable materials in antenna engineering. These materials have been selected based on their efficiency, flexibility in fabrication, and the cost of production. In addition, the means by which these materials attain tuneability, i.e., how they are activated is also of great importance when designing a tuneable microwave, millimetre-wave (mm-wave) or terahertz (THz) device. This is because the controlling arrangement in the system can impede the transmission or radiation of the device. As a result, optically-activated tuneable devices stand out as the optimal solution for isolating the controlling signals from the radiating wave of these devices, especially in mm-wave and THz frequencies.

Optical switches, in addition, provide faster switching speed compared to the conventional electronic switches. These switches are photonically excited, and tend to have high reliability. However, these optical switches are mainly silicon (Si)-based and are challenging to incorporate in an antenna design. In addition, they require high power infrared illumination to control their tuneability. These drawbacks make use of inorganic semiconductors in an antenna system inflexible and therefore impractical. As a result, there is a constant search for an enhanced semiconductor material to replace Si.

Organic semiconductors are an ideal candidate to replace the high mobility inorganic semiconductors. Although, the switching speed of organic semiconductors are not as high as that of their inorganic counterparts, due to their inherent low carrier mobility, other advantages such as mechanical flexibility, ease of fabrication, and low fabrication cost make them potential candidates for use as tuneable materials in antenna engineering. The primary organic semiconductor chosen in this research is poly(3-hexylthiophene) or, P3HT. In addition, band-gap engineering has been performed, to

increase the tuneability of the base polymer, by doping the p-type base polymer, P3HT, with an n-type dopant, phenyl-C61-butyric-acid-methyl ester (PCBM). The carrier mobility and the change in the carrier concentration in the active state of the blend has been measured to be 2×10^{-4} $cm^2V^{-1}s^{-1}$ and 10^{15} cm^{-3}, respectively. The change in the carrier concentration of the blend due to optical excitation provides sufficient information that there is a measurable change in the dielectric constant of the polymer.

In order to estimate the dielectric changes of the organic blend due to optical excitation a free-space transmission-only measurement technique is considered. This technique can be used to characterise any photosensitive semiconducting material. Two different free-space measurement setups, quasi-optical (QO) transmissometer and THz-TDS, have been deployed for the material characterisation of the organic blend using transmission-only configurations. The QO transmissometer system is used to cross-check the derived estimates of the optical constants measured in the THz frequencies using THz-TDS. Reversible and reproducible changes in the real and imaginary parts of the complex dielectric constant of the organic blend are measured in the range of –0.05 to –0.55 and +0.01 to +0.52, respectively, over the sub-THz frequency-domain.

The use of optically-tuneable semiconducting materials, both organic and inorganic, have been effectively demonstrated in novel reconfigurable antenna designs. Firstly, an optically-switched cognitive radio has been proposed, and the reconfigurability of such a system is brought about by using illumination from a relatively portable array of LED light source (880 nm). The cognitive radio comprises of an ultra-wideband (UWB) antenna as well as an optically-switched frequency reconfigurable antenna. Such a system is suggested for use in practical applications due to its lightweight and compactness. In addition, the conductivity of a medium-resistivity Si in the dark and active states has been estimated by matching simulated with measured transmission results of the optically-switched transmission line. A performance comparison has been conducted between the two systems using the medium-resistivity and high-resistivity Si as the reconfigurable ground. It has been established that the system requires a transition of conductivity from 4.25×10^{-4} Sm^{-1} to 168 Sm^{-1}, in order to perform efficiently as a cognitive radio.

Secondly, a novel optically-activated antenna array using photo-activated organic semiconductor blend (P3HT: PCBM) has been presented. In order to demonstrate the tuneability of the organic heterojunction, P3HT:PCBM, a two-element patch antenna

array has been enveloped with the organic blend layer and optical illumination (532 nm) is used to steer the main beam on the antenna array off boresight. Illumination of the organic layer is directed from the front-end, failing to ensure a non-impeding condition during measurements. As a result, a multi-layered model of an antenna array comprising of copper, organic blend, sodalime glass ITO (indium tin oxide) is proposed. Glass and ITO, being transparent to visible light, allow optimum illumination of the organic layer. The primary objective of the proposed design has been to justify the concept of beam steering functionality using the photo-sensitive organic blend. With the estimates of the change in dielectric from the QO transmissometer measurements, the proposed design generated a 5° beam steer off boresight at S-band. A potential future application of the proposed system is the employment of the device for point-to-point (P2P) beam alignment for detection and steering in data-centre high-capacity communication links.

Lastly, an organic lens whose action may be dynamically adjusted has been designed, and its principle of operation assessed numerically, as well as measurements using a NSI planar scanner. During the numerical analysis, the measured estimates of the complex permittivity of the organic blend in active and dark states have been used, in order to model the excited and non-excited regions in the organic lens. Analysis of the phase distribution of the electric field across the face of the plane organic lens has also been carried out, and a similar pattern is further observed in the spatial phase-distribution of the lens plane in the active state, as that projected by the illuminating source. From the measured results, however, exact projected pattern in the output has not been clearly observed, mainly due to the change in phase of the complex electric field across the lens plane being very close to the noise floor of the measurement system. Possible solutions to observe the images created by such small dielectric changes include the increase in the irradiance onto the patterned illumination, as well as the response measurement using a low-noise (i.e., more sensitive) system, such as an electro-optic probe in THz frequencies.

7.2 Future Work

Future research work in this area primarily incorporates the thorough investigation on the practical applications of the discussed photosensitive semiconducting materials. New photosensitive organic polymers or blends, need to be appropriately manufactured, in order to result in the increase of the tuneability in the real part of the dielectric constant. Different concentrations of donor-acceptor system also need to be investigated keeping in mind that the change in the imaginary part of the dielectric constant stays as low as

possible. It is already shown that the small dielectric changes in the dielectric constant of the organic polymers would be beneficial for applications at THz frequencies. Devices that require the beam steering or impedance matching could attain sufficient tuneability with the employment of such polymers in the design at THz frequencies. Moreover, following is the list of areas where the intended future work can be effectively deployed.

(i) Determination of excitation-region depth of optically-tuneable organic semiconductor heterojunctions for THz-applications

In order to estimate the excitation-region depth of a photosensitive organic polymer, several samples of the polymer with varied thicknesses, *t*, is required (e.g., *t* = 1–50 μm). During excitation-region depth determination of the organic polymer, the spatial variation in thickness in individual samples must be uniform. The results obtained using the QO transmissometer in this research, for thin samples resulted in unphysical values of the dielectric change. Uniform sample thickness along the sample area through which the sub-THz beamfield passes is required to successfully estimate the change in the dielectric constant in thin samples. A graph of $\Delta\varepsilon$ versus organic film thickness is expected to saturate after certain thickness of the organic film. This is because as the thickness of the sample increases, the effect of $\Delta\varepsilon$ on the sub-THz beam will become recessive. Hence, the respective thickness for which $\Delta\varepsilon$ shows a point of saturation in the curve should be considered as the excitation-region depth.

(ii) Characterisation of other tuneable organic polymers using the QO transmissometer

The organic polymer blend P3HT:PCBM has been characterised at WR-10 and WR-3 waveguide bands using the QO transmissometer. The average dynamic tuning in the dielectric constant of the polymer blend has been estimated at 0.1. However, there are other tuneable organic polymers such as Polytriarylamine (PTAA) and PEDOT:PSS that needs to be characterised using the already established transmission-only measurement configurations. The base polymer P3HT should be blended with higher concentrations (10%, 20%, etc). However, heed should be paid not to increase the imaginary part of the dielectric constant so that the losses at THz frequencies remain minimum. The mechanical flexibility analysis of these photosensitive organic semiconductors also needs to be implemented. The performance of organic polymers due to mechanical flexibility can be investigated using the QO tranmissometer, as well.

(iii) Optically-tuneable dynamic organic lens

The measured spatial change in the phase of the complex electric field across the dynamic organic lens between its illuminated and non-illuminated states displayed blurry patterns of the projection. The dominant effect of the electron-hole pair patterns was obscured by the phase-noise. With the use of brighter illumination patterns, i.e., using a higher power LED light source onto the lens, more sharp images are expected to be seen. Additionally, a more advanced measurement setup, with lower background noise, can also resolve this issue. An electro-optic probe, field-scanning system at THz frequencies, could be used to observe such small dielectric changes in terms of imaging.

(iv) Non-linear sub-THz QO devices

The low loss light-sensitive organic blend (P3HT:PCBM), having small excitation-region depth (i.e., < 100 μm) is an ideal candidate for use in THz frequencies, since the excitation-region depth is comparable to the wavelength of the EM wave. Hence, at active state, the change in phase of the polymer dielectric can contribute to the matching of the impedance of non-linear QO multipliers (free-space frequency multiplication devices). Using a variable intensity light source, it is then possible to adjust the impedance of these multipliers in an array arrangement by tuning the dielectric of the light-sensitive polymer coated on each of the elements. Due to the use of the tuneable filter in the form of the light-sensitive polymer (P3HT:PCBM), the impedance of the array is better matched, consequently resulting in the enhancement of the overall system efficiency.

APPENDIX A. THz-TDS

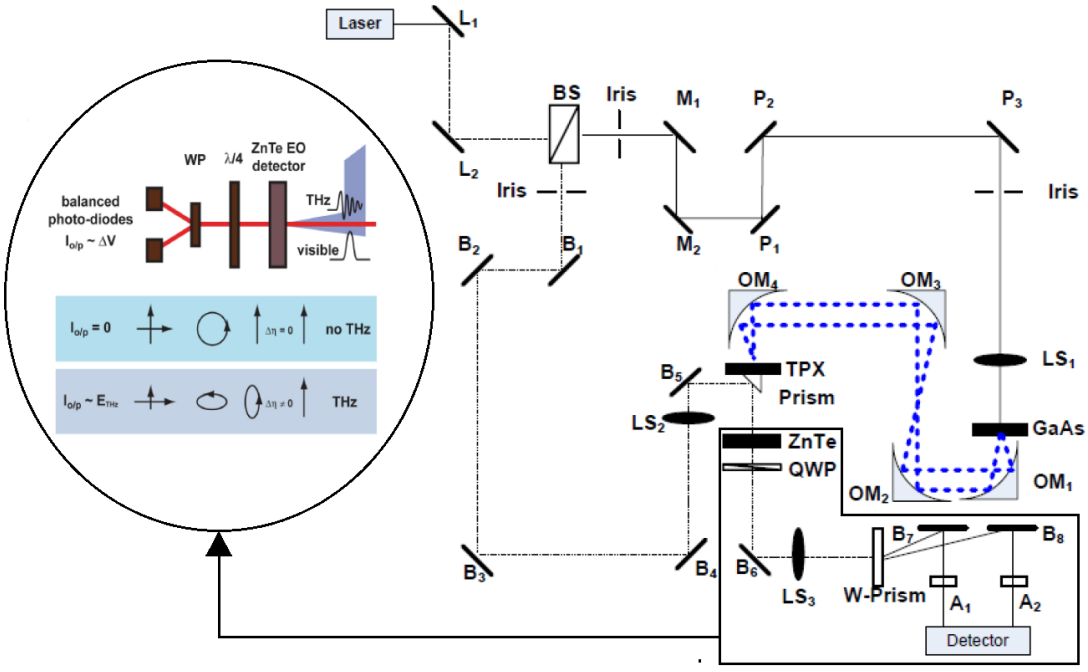

Fig. A-1 Schematic diagram of the THz-TDS setup operating in the transmission mode configured in QMUL THz laboratory. L, P, B are flat reflecting mirrors, M – flat mirrors of delay stage, LS – focusing lenses, A – attenuators, BS – beam splitter, QWP – quarter-wave plate, OM – off-axis parabolic mirrors. The THz beam path is marked blue and the black solid line shows in detail the THz-wave detection in the circular subset.

The THz-TDS measurement setup in the Antenna Lab at QMUL's THz laboratory is shown in Fig. 4.6 [42]. The TDS setup consists of a pulsed titanium-Sapphire femto-second laser, a GaAs PCA (THz emitter), a beam splitter, off-axis parabolic mirrors, a ZnTe crystal (THz-detector) and a lock-in-amplifier connected to the detector. The TDS system, in the THz-lab, is a Lab-VIEW driven real-time system that displays the electric field intensity against the position of the delay-stage. At the detector end, shown in the subset of Fig. 4.6, the THz radiation causes birefringence in the 2mm thin ZnTe crystal plate. This is caused due to the well-known Pockel effect of EO crystals [43]. The birefringence hence produces a cross-polarisation component in the ZnTe crystal. In absence of the THz wave, the orthogonal polarisation components of the probe beam passing through the ZnTe crystal is balanced. As a result of the change in the refractive index of the crystal caused by the THz wave, the probe beam passing through the crystal is modulated, in terms of polarisation. A quarter wave plate is positioned after the ZnTe crystal to change the polarisation for the probe beam to elliptical. A Wollaston prism, that

essentially resolves the two orthogonal wave components, splits the elliptically polarised probe beam into two wave components and is received by the 2-port photo-detector. The balanced photo-detectors receive the two wave components separately and measures the intensity difference between these components. The difference between the two detected intensities is proportional to the amplitude of the THz electric field. The variation in the arrival time of the probe beam, i.e., repetitive sampling of the signal, creates a discrete periodic THz waveform. A discrete Fourier transform reconstructs the time-domain response into a discrete amplitude and phase spectra.

APPENDIX B. Cleaning Procedure

Detail of the cleaning procedure of any substrate before polymer deposition is as follows:

1) Clean the substrate using detergent and tap water.
2) Immerse the substrate into a beaker containing distilled water and half teaspoon of detergent. Place the beaker in an ultrasonic bath for 20 mins as shown in Fig. B-1. This is to remove any dirt on the substrate.
3) Place the substrate inside a beaker filled with only distilled water this time and put the beaker in the ultrasonic bath for 5 minutes. Repeat this process twice. In total the substrate should be bathed every 5 minutes thrice, each time replacing the dirty distilled water. This is to remove any detergent sticking to the substrate.
4) Now, place the substrate inside a beaker filled with acetone and place them in the ultrasonic bath for 5 mins. Do this twice.
5) Finally, place the substrate inside a beaker filled with chloroform and place them in the ultrasonic bath for 5 mins. Do this twice as well. Once this is done, dry the substrate using an air gun. This ensures removal of any chloroform residue on the substrate.

Fig. B-1. An Ultrasonic Cleaner for cleaning substrates.

APPENDIX C. Four-Point Probe Method

This method involves four probes arranged in a line in such a way that they are equidistant from each other (see Fig. C-1a). The two outer points represent the dipole, and the two inner, the current, I, measured using an ammeter. In the calculation of the resistivity of the material under test, the voltage, V, between the two inner probes can be measured using a voltmeter. For a sample thickness w much smaller than the probe separation s, resistivity of the sample can be easily calculated using the equation,

$$\rho = \frac{\pi}{\ln(2)} \mathrm{w} \left(\frac{V}{I}\right) \qquad \text{C-1}$$

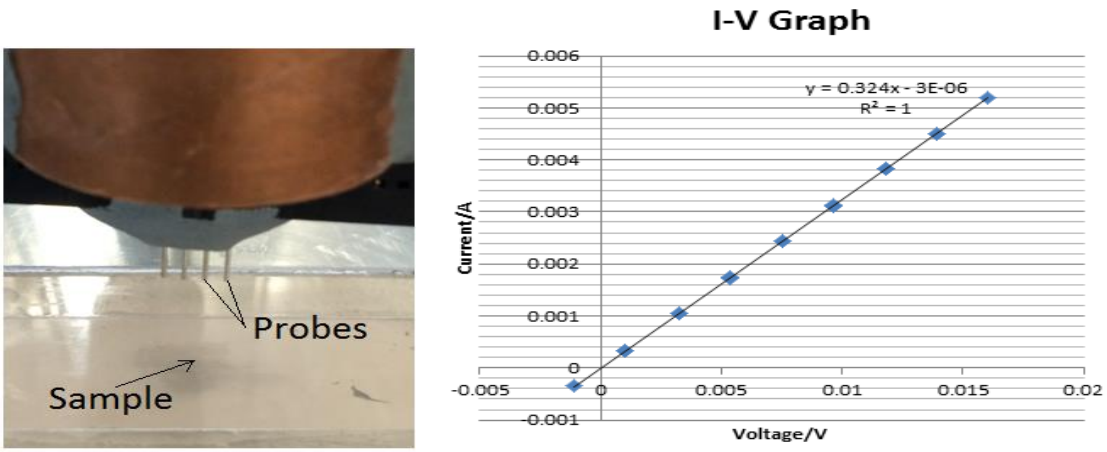

a) b)

Fig. C-1 a) Four-point probe method used to measure the current and voltage across the probes that are in contact with indium-tin-oxide (ITO). b) Measured I-V characteristics of ITO.

The resistivity of ITO is calculated as the product of the inverse of the gradient of the I-V curve (see Fig. C-1b) and $\frac{\pi}{\ln(2)}$w, where w is measured using a Profilometer as 110 nm. The conductivity is measured using ρ^{-1} t 6.5×10^5 Sm^{-1}.

APPENDIX D. RF Terminologies

D.1 Microstrip line

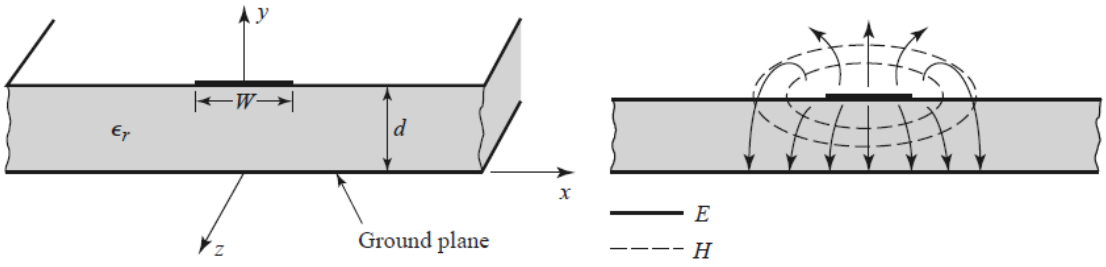

a) b)

Fig. D-1. Microstrip transmission line. a) Schematic b) Electric and magnetic fields [reproduced from Microwave Engineering, D.M Pozar]

Microstrip line is a transmission line that is commonly used in both passive and active microwave devices. Fig. D-1a shows the geometry of the microstrip line where a conductor with a width of W printed on a thin, grounded dielectric substrate of thickness d and relative permittivity ε_r. Fig. D-1b shows the electric and magnetic field lines emerging from the conductor. To match the impedance of this type of transmission line to the source at a particular frequency, the width of the line, thickness of the substrate and the relative permittivity of the substrate is tuned. The optimum width of a microstrip transmission line for a particular input impedance (source) at a particular frequency can be calculated using the following online source: [http://www.emtalk.com/mscalc.php].

D.2 Co-planar waveguide

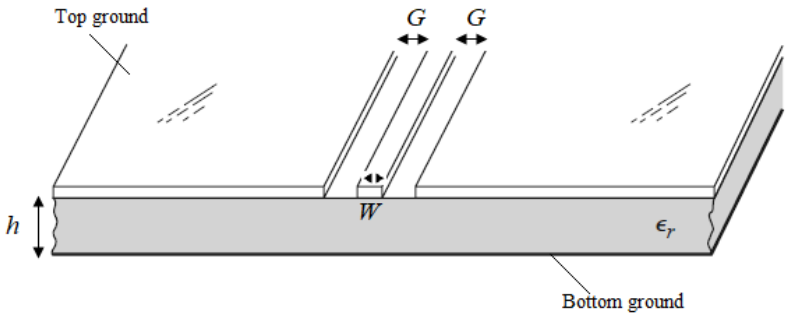

Fig. D-2. Coplanar waveguide geometry [reproduced from Microwave Engineering, D.M Pozar]

The coplanar waveguide another type pf planar transmission line. The geometry of coplanar waveguide is shown in Fig. D-2, where where a conductor with a width of *W* printed on a thin, dielectric substrate of thickness *d* and relative permittivity ε_r grounded on both sides (top and bottom). Unlike microstrip line this structure has a top ground plane, for which there are two gaps, *G*, in the design. To match the impedance of this type of transmission line to the source at a particular frequency, the width of the line, width of the two gaps (symmetrical in most cases), thickness of the substrate and the relative permittivity of the substrate is tuned. The optimum width (*W*) and gap size (*G*) of a microstrip transmission line for a particular input impedance (source) at a particular frequency can be calculated using the following online source: [https://www.microwaves101.com/calculators/864-coplanar-waveguide-calculator]

D.3 Scattering-parameters (S-parameters)

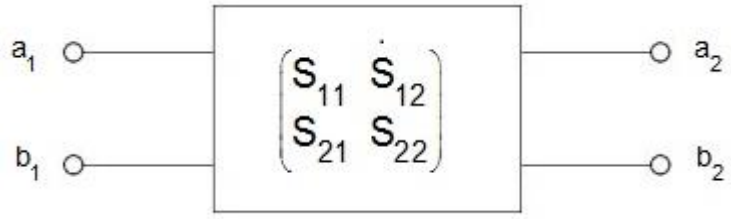

Fig. D-3. A two port network.

The scattering parameters are best understood using a two-port network. The relation between the reflected, incident power and the scattering matrices is given by the following:

$$\begin{pmatrix} b_1 \\ b_2 \end{pmatrix} = \begin{pmatrix} S_{11} & S_{12} \\ S_{21} & S_{22} \end{pmatrix} \begin{pmatrix} a_1 \\ a_2 \end{pmatrix}$$

Expanding the matrices we get

$$b_1 = S_{11}a_1 + S_{12}a_2$$

and

$$b_2 = S_{21}a_1 + S_{22}a_2$$

These equations relate the reflected and incident power of the waves from ports 1 and 2 in terms of the network's individual S-parameters ($S_{11}, S_{12}, S_{21}, and\ S_{22}$). If the incident power is supplied to port 1(b_1) there will be reflected waves from port want and transmitted waves at port 2 (b_2). However, when port 2 is terminated with a matched load

to the input, according to the maximum power transfer theorem, b_2 will be totally absorbed making a_2 equal to zero. Now defining the incident voltage as $a_1 = V_1^+$and $a_2 = V_2^+$with the reflected waves being $b_1 = V_1^-$and $b_2 = V_2^-$. Similarly, if port 1 is terminated in the system then $a_1$becomes zero.

$$S_{11} = \frac{b_1}{a_1} = \frac{V_1^-}{V_1^+},\ S_{21} = \frac{b_2}{a_1} = \frac{V_2^-}{V_1^+},\ S_{12} = \frac{b_1}{a_2} = \frac{V_1^-}{V_2^+},\ S_{22} = \frac{b_2}{a_2} = \frac{V_2^-}{V_2^+}$$

where the S-parameters have generic description as follows:

S_{11}: input port voltage reflection coefficient

S_{12}: reverse voltage gain

S_{21}: forward voltage gain

S_{22}: output port voltage reflection coefficient